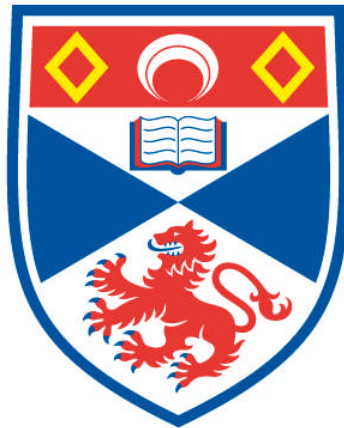


# **SELF-ASSEMBLED MONOLAYERS OF THIOLATES AS TEMPLATES FOR MICRO/NANO FABRICATION**

**Cai Shen**

**A Thesis Submitted for the Degree of PhD  
at the  
University of St Andrews**



**2008**

**Full metadata for this item is available in  
Research@StAndrews:FullText  
at:**

**<http://research-repository.st-andrews.ac.uk/>**

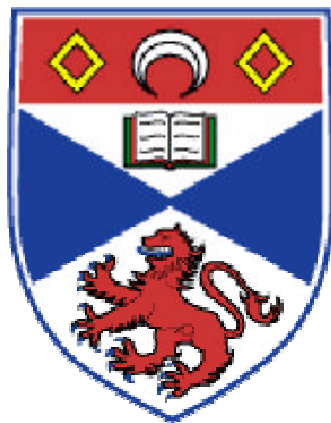
**Please use this identifier to cite or link to this item:**

**<http://hdl.handle.net/10023/603>**

**This item is protected by original copyright**

**This item is licensed under a  
Creative Commons License**

**Self-assembled Monolayers of Thiulates as Templates  
for Micro/Nano Fabrication**



A thesis submitted for the degree of Ph. D.

by

Cai Shen

Supervised by Dr. Manfred Buck

University of St. Andrews

August, 2008

## Abstract

Self-assembled monolayers (SAMs) were investigated with regard to their application as templates to control processes down to the nanometre length scale. With applications of SAM for electrochemical nanotechnology in mind, the range of aspects studied comprises patterning on different length scales, behaviour of SAMs under the conditions of electrochemical metal deposition, and the influence of the head and tail groups on formation and structure of SAMs.

On a micrometre scale, laser scanning lithography (LSL) was used to pattern SAM covered Au surfaces. With this technique, localized regions of a SAM are desorbed by scanning the focal spot of a laser beam. Thermal desorption occurs as a result of the high substrate temperature produced by the laser pulses. Patterns with line width as small as 0.9  $\mu\text{m}$  were produced by LSL. It is demonstrated that SAM can not only be patterned by laser radiation but can also be rendered more passive as revealed by electrochemical metal deposition. Such blocking effect is explained by annealing of defects upon irradiation at the appropriate laser energy. This effect can block deposition of bulk copper particles, but does not prevent the underpotential deposition. Based on this passivation effect, large passivation areas can be created, which can be used as substrate for further nano/micro fabrication. The combination of SAM patterning and electrochemical metal deposition was also demonstrated to be an effective way to prepare superhydrophobic surfaces, exhibiting a contact angle of  $165^\circ$  (water droplet).

Aiming for the generation of smaller structures, scanning tunneling microscopy (STM) is used as a tool to pattern SAMs. Several phenomena observed in STM based manipulation of SAMs are addressed. The first one is sweeping effect. Deposited metal particles on top of SAM and SAMs are swept by STM tip by choosing appropriate I/V parameters. The closer the tip (higher current, lower bias), the more effective it is. Molecularly resolved images confirm that after sweeping, the scanned area is still

covered by SAM molecules. This is explained by diffusion. The sweeping process can be repeated, thus, resulting in a layer by layer etching. The second effect is field-induced desorption. Applying a positive voltage (2.5 – 5V), a SAM is damaged beneath the area of the tip. The damage depends not only on the bias applied, but also on the current setpoint right before applying the bias. The third effect is nanografting. Nanografting was observed that a SAM having a stronger assembling ability can replace the weaker one (matrix layer) in hexadecane solution by STM scanning under normal I/V parameters combination that are usually used for imaging. It is found that longer chain can replace the shorter chain thiol, alkanethiol can replace biphenyl thiol. This method can be applied to pattern SAM.

Defects (punched holes) were created purposely on the SAMs covered Au surface and *in situ* STM was used to investigate the process of Under-Potential Deposition (UPD) and bulk metal deposition. Bulk metal deposition on punched holes depends on the size. Small scale patterning by punching is sufficient for applications based on UPD but not for bulk metal deposition.

Several SAMs assembled on Au(111) surface (1-mercaptoundecanoic acid (MUA), Dodecyl Thiocyanate (C12SCN) and bis(pyrazol-1-yl)pyridine-substituted thiol (bpp-SH) and thiocyanate (bpp-SCN)) were investigated with the aim to expand the type of SAMs that can be used as template for further application, such as metal coordination. High quality thiolate monolayers formed by cleavage of the S-CN bond can be obtained on Au(111). Thus, organothiocyanates appear to be a promising alternative to thiols. Well-ordered MUA monolayers are formed in a few hours at the temperature range of 323-363 K by Physical Vapour Deposition (PVD). Self-assembled monolayers of bpp-SH and bpp-SCN on Au(111)/mica were studied with STM. Preparation conditions such as temperature, solvent, and contamination affect the formation of SAMs on Au(111) much more than other common thiols such as alkanethiols and biphenylthiols.

## Acknowledgements

First and foremost I would like to express my immense gratitude to my supervisor Dr. Manfred Buck, whose enthusiasm for science has been an inspiration and whose encouragements have been tremendously valuable. Thanks for his patience in the days when experiment did not work and thanks for his quick-sighted way in spotting the “useless” data that turn out to be exciting in the end. Thanks for his personal character that have influenced me strongly and will be wealth for my whole life.

I would like to thank Dr. Christophe Silien, Dr. Rafael Madueno, Dr. Iza Cebula and Dr. Minna Räisänen for their helpful and stimulating discussions. In particular, Dr. Christophe Silien’s help on various technical aspects about STM has been much appreciated. I would also like to thank Nelly Bonnet and Francis McCarthy for all kinds of help. Thanks to Professor Neville Richardson and Dr Richard Baker, who were my first year report assessors and gave me valuable advices. Thanks to Dr. Chris Baddeley’s support with IR spectroscopy. Thanks to the whole Surface Science group who have fostered a pleasant and co-operative working environment and organized several enjoyable social events over the past three years. Thanks to Michael Zharikov, Tobias Weidner, Marco Haryono, Andreas Grohmann, and Nirmalya Ballav and James Wilton-Ely for providing chemicals, NEXAFS and XPS measurement along with helpful discussions. Thanks to the technical staff, Iain Paterson (undergraduate laboratories), George Anthony and Robert E. Cathcart (mechanical workshop), Andrew P. Watson, Colin Millar, Jim R. Bews, Derek Waddell and Marjory B. Parker, and to the general office staff, especially Carolyn McAllister for invaluable support.

Thanks to my friends in and out of the chemistry department who have made the past three years an enjoyable time. Also, I would like to thank my parents and the rest of my family for all of their belief, encouragement and support for my entire time at University.

Finally, I would express my immense gratitude to EaStCHEM for financially supporting these three years at the University of St Andrews.

## Declarations

I, Cai Shen, hereby certify that this thesis, which is approximately 36,000 words in length, has been written by me, that it is the record of work carried out by me and that it has not been submitted in any previous application for a higher degree.

*date*

*signature of candidate*

I was admitted as a research student in September, 2005 and as a candidate for the degree of Doctor of Philosophy in September, 2005; the higher study for which this is a record was carried out in the University of St Andrews between 2005 and 2008.

*date*

*signature of candidate*

I hereby certify that the candidate has fulfilled the conditions of the Resolution and Regulations appropriate for the degree of Doctor of Philosophy in the University of St Andrews and that the candidate is qualified to submit this thesis in application for that degree.

*date*

*signature of supervisor*

In submitting this thesis to the University of St Andrews I wish access to it to be subject to the following conditions: for a period of 1 year from the date of submission, the thesis shall be made available for use only with the consent of the Head of the School in which the work was carried out.

I understand, however, that the title and abstract of the thesis will be published during this period of restricted access; and that after the expiry of this period the thesis will be made available for use in accordance with the regulations of the University Library for the time being in force, subject to any copyright in the work not being affected thereby, and a copy of the work may be made and supplied to any bona fide library or research worker, that my thesis will be electronically accessible for personal or research use, and that the library has the right to migrate my thesis into new electronic forms as required to ensure continued access to the thesis. I have obtained any third-party copyright permissions that may be required in order to allow such access and migration.

*date*

*signature of candidate*

*date*

*signature of supervisor*

## List of Abbreviations

AFM	Atomic Force Microscopy
BP0	4'-Methyl-biphenyl-4-thiol
BP1	(4'-Methyl-biphenyl-4-yl)-methanethiol
BP2	2-(4'-Methyl-biphenyl-4-yl)-ethanethiol
BP3	3-(4'-Methyl-biphenyl-4-yl)-propane-1-thiol
BP4	4-(4'-Methyl-biphenyl-4-yl)-butane-1-thiol
BP5	5-(4'-Methyl-biphenyl-4-yl)-pentane-1-thiol
BP12	12-(4'-Methyl-biphenyl-4-yl)-dodecane-1-thiol
bpp-SH	bis(pyrazol-1-yl)pyridine-substituted thiol
bpp-SCN	bis(pyrazol-1-yl)pyridine-substituted thiocyanate
C12SH	Dodecanethiol
C12SCN	Dodecyl thiocyanate
DMF	N,N-Dimethylformamide
DT	(4'-Mercaptomethyl-biphenyl-4-yl)-methanethiol
ECSTM	Electrochemical Scanning Tunnelling Microscopy
ESCA	Electron Spectroscopy for Chemical Analysis
IRRAS	Infrared Reflection Absorption Spectroscopy
LSL	Laser Scanning Lithography
MC4	Butanethiol
MC6	Hexanethiol
MC10	Decanethiol
MC11	Undecanethiol
MC14	Tetradecanethiol
MC18	Octadecanethiol
MC22	Docosane thiol
MUA	Mercaptoundecanoic acid
MHA	Mercaptohexadecanoic acid
$\mu$ CP	Microcontact Printing
NEXAFS	Near Edge X-ray Absorption Fine Structure
NSOM	Near-Field Scanning Optical Microscopy
OPD	Over-Potential Deposition
PTCDA	Perylene-3,4,9,10-tetracarboxylic dianhydride
PVD	Physical Vapour Deposition
SAM(s)	Self-Assembled Monolayer(s)
SPM	Scanning Probe Microscopy
SPL	Scanning Probe Lithography
STM	Scanning Tunnelling Microscopy
UPD	Under-Potential Deposition
XPS	X-ray Photoelectron Spectroscopy

---

## Table of Contents

<b>Chapter 1 Research Background.....</b>	<b>9</b>
<b>1.1 Introduction.....</b>	<b>9</b>
<b>1.2 Brief Introduction to Self-Assembled Monolayers .....</b>	<b>11</b>
1.2.1 Self-Assembled Monolayers .....	11
1.2.2 The Au(111) Surface.....	13
1.2.3 Self-Assembled Monolayers of Alkanethiol on Gold .....	14
1.2.4 Self-Assembled Monolayer of Biphenyl Based Thiols on Gold .....	19
1.2.5 Defects in SAMs .....	22
<b>1.3 SAM Patterning .....</b>	<b>23</b>
1.3.1 Microcontact Printing .....	23
1.3.2 Scanning Probe Lithography.....	25
1.3.3 Photolithography.....	27
1.3.4 E-Beam Lithography .....	29
1.3.5 Laser Beam Lithography .....	30
<b>1.4 Electrochemistry .....</b>	<b>32</b>
1.4.1 Electrochemistry Basic Principles.....	32
1.4.2 Cyclic Voltammetry.....	33
1.4.3 Metal Deposition.....	34
<b>1.5 Scanning Tunnelling Microscopy .....</b>	<b>36</b>
<b>1.6 IRRAS, XPS and NEXAFS Spectroscopy .....</b>	<b>39</b>
1.6.1 Infrared Reflection Absorption Spectroscopy.....	39
1.6.2 XPS and NEXAFS Spectroscopy .....	39
<b>Chapter 2 Experimental Section .....</b>	<b>49</b>
<b>2.1 Substances and Sample Preparation.....</b>	<b>49</b>
<b>2.2 Laser system.....</b>	<b>51</b>
<b>2.3 Electrochemistry .....</b>	<b>53</b>
<b>2.4 STM Measurements.....</b>	<b>55</b>
2.4.1 ECSTM Setup .....	55
2.4.2 STM Tip Preparation .....	57
2.4.3 PicoLITH.....	57
<b>2.5 XPS and NEXAFS Measurements .....</b>	<b>58</b>
<b>2.6 IRRAS Measurements .....</b>	<b>59</b>
<b>2.7 Contact Angle Measurements .....</b>	<b>59</b>
<b>Chapter 3 Self-assembled Monolayers as Templates for Micro/Nano Fabrication .....</b>	<b>61</b>

---

<b>3.1 Introduction.....</b>	<b>61</b>
<b>3.2 Laser Scanning Lithography .....</b>	<b>62</b>
3.2.1 STM Investigation of Laser-Patterned Surfaces.....	62
3.2.2 LSL Repeatability .....	66
3.2.3 Lift Off.....	67
3.2.4 Conclusion.....	69
<b>3.3 Laser-Induced Passivation .....</b>	<b>69</b>
3.3.1 Introduction.....	69
3.3.2 Passivation Effect.....	70
3.3.3 Passivation Lines .....	72
3.3.4 Large Area Passivation.....	74
3.3.5 STM investigation of Laser Passivated Surfaces .....	78
3.3.6 Application of Passivation .....	79
3.3.7 Conclusion.....	80
<b>3.4 Superhydrophobic Surface Built from SAM Templates .....</b>	<b>81</b>
3.4.1 Introduction.....	81
3.4.2 Experimental.....	81
3.4.3 Results and Discussion.....	83
3.4.4 Conclusion.....	84
<b>Chapter 4 SAM Manipulation and Modification by STM.....</b>	<b>87</b>
<b>4.1 Introduction.....</b>	<b>87</b>
<b>4.2 Sweeping Effect.....</b>	<b>88</b>
4.2.1 STM Modification of Electrodeposited Metal Clusters on SAMs .....	88
4.2.1.1 Alkane thiol SAMs .....	88
4.2.1.2 Other SAMs .....	92
4.2.2 Sweeping Effect at the Nanoscale .....	94
4.2.1.1 Sweeping on Cu Deposited SAM Surfaces .....	94
4.2.1.2 Sweeping on SAM Surfaces .....	100
4.2.3 Discussion.....	101
4.2.4 Conclusions.....	103
<b>4.3 Displacement Patterning .....</b>	<b>104</b>
4.3.1 Introduction.....	104
4.3.2 Patterning by Punching Mode .....	105
4.3.3 Nanografting .....	110
4.3.3.1 Nanografting on Uniform SAMs .....	110
4.3.3.2 Patterned SAMs by Nanografting.....	116
4.3.3.3 Discussion.....	118
4.3.3.4 Conclusion.....	122
<b>4.4 Metal Deposition on STM Modified SAMs .....</b>	<b>123</b>
4.4.1 Introduction.....	123
4.4.2 Results and Discussion.....	124
4.4.3 Conclusions.....	131

---

<b>Chapter 5 Self-Assembled Monolayers .....</b>	<b>137</b>
<b>General.....</b>	<b>137</b>
<b>5.1 Self-Assembled Monolayers of Dodecyl Thiocyanate .....</b>	<b>137</b>
5.1.1 Introduction.....	137
5.1.2 Results and Discussion.....	138
5.1.2.1 STM characterization .....	138
5.1.2.2 XPS and NEXAFS Spectroscopy .....	146
5.1.2.3 IRRAS characterization .....	148
5.1.3 Conclusion.....	149
<b>5.2 Self Assembled Monolayers of MUA Prepared by Physical Vapour Deposition .....</b>	<b>150</b>
5.2.1 Introduction.....	150
5.2.2 Results and Discussion.....	150
5.2.2.1 STM and contact angle characterizations .....	150
5.2.2.2 Electrochemical characterization .....	154
5.2.2.3 IRRAS characterization .....	155
5.2.2.4 XPS and NEXAFS Spectroscopy .....	156
5.2.3 Conclusion.....	158
<b>5.3 Bis(pyrazol-1-yl)pyridine-terminated SAMs on Au(111) .....</b>	<b>159</b>
5.3.1. Introduction.....	159
5.3.2 STM characterization of bpp-SH.....	160
5.3.3 STM characterization of bpp-SCN.....	163
5.3.4 Conclusions.....	168
<b>Chapter 6 Conclusions .....</b>	<b>173</b>

# Chapter 1 Research Background

## 1.1 Introduction

One important issue in nanotechnology is the reduction of feature size and the corresponding increase in pattern/device density. This has been demonstrated to be the most productive way to develop more efficient and faster electronic devices. Micro/Nano metal structures in general, and electrode structures, in particular are very important in the field of molecular electronics, micro and nano electromechanical systems, and sensors. When dealing with nano-scale structures, there are many challenges such as the generation of such small dimensions, bridging of the gap between the nanoscopic length scale and dimensions accessible externally, and of fabrication processes which allow routine generation of structures that are not limited by reliability and cost.

Different concepts are currently pursued which either involve well established lithographic techniques such as electron and ion beam lithography<sup>1,2</sup> or the exploration of alternative approaches based on scanning probe techniques, and contact printing.<sup>3,4</sup> Limitations in resolution, definition of patterns, scalability to large areas and complexity of the process are typical problems. Intensive worldwide activities are trying to find suitable processes meeting as many challenges as possible.<sup>5-8</sup>

The past decade has witnessed the rapid development of a variety of strategies and techniques to pattern organic thin films. Self-assembled monolayers (SAMs, see section 1.2) are one of the most promising organic thin layers that can be used for micro/nano fabrications. Patterned SAMs have attracted tremendous interest because of their utility as templates for directing the selective adsorption and growth of metals and as resists for pattern transfer. Recently, our research group developed a scheme to generate metal microstructures by template-directed electrometallization.<sup>9</sup> The scheme is promising for micro and nano-fabrication. It is shown in Figure 1.1. Patterned SAMs

(two different types of SAMs with different blocking behavior against electrochemical Cu deposition) are produced. These two types of molecules play two roles in this fabrication process. First, they act as a template to direct electrochemical metal deposition. By changing a SAM structure, one can change the blocking behavior. Consequently, a patterned SAM consisting of two types of molecules sufficiently different in their blocking behavior can be used for selective metal deposition.

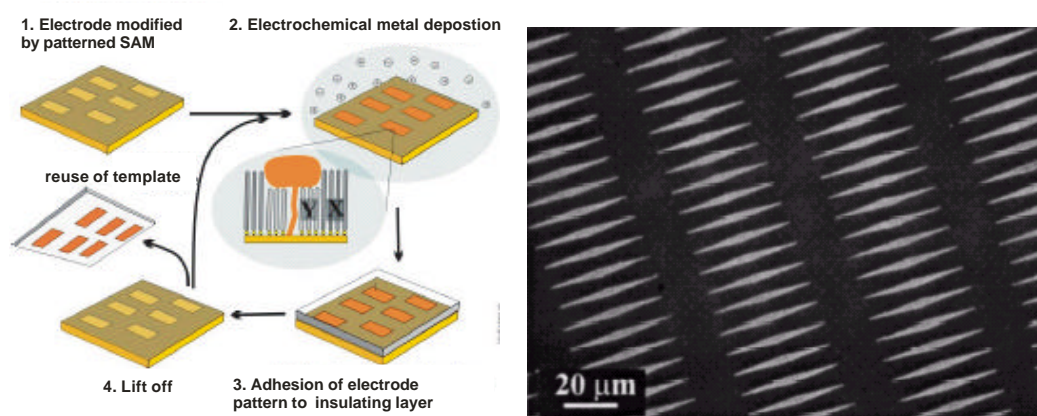


**Figure 1.1 left; Electrode pattern produced by electrodeposition and lift off. A Au electrode is modified by a patterned SAM (1). It is repeatedly used in a production cycle, starting with selective electrochemical metal deposition (2). An insulating substrate is then brought into contact (3). Lift off of the substrate (4). Leaves the template behind for the next cycle. X and Y symbolise thiols which differ in their electrochemical blocking behaviour. Right, optical micrograph of a copper pattern (bright areas) on glass produced by selective copper deposition and lift-off.<sup>9</sup>**

Since a variety of techniques can be used to pattern SAMs, structures on lengthscales ranging from microscopic to nanoscopic dimensions can be defined. The second role of the patterned SAM is to reduce adhesion of the metal deposit to the substrate,<sup>10</sup> which ensures that the electrochemically deposited metal pattern can be transferred to an insulating substrate. The most obvious advantage of this technology is that, once the patterned substrate is produced, it can be repeatedly used, which makes the process simple and rapid. However, the applicability of the process depends on the achievable contrast in the metal deposition and, in particular, on the quality of the pattern transfer during steps 3 and 4. Furthermore, the deterioration of the patterned SAM during the various steps is a crucial issue as this limits the number of deposition and lift-off cycles.

The goal of this project is to explore how this scheme can be carried forward towards nanometer dimensions. Based on patterned self-assembled monolayers which serve as templates to control electrodeposition this work aims for the further development of this process which promises a routine and simple generation of metal patterns that can be freely defined.

Another issue of this thesis is to understand the self-assembly behavior of SAMs and to develop new type of SAMs with different functional group and different properties (i.e. for metal coordination) which will be used as templates for further patterning. So, in this thesis, we also discuss several new SAMs/new preparation methods on Au(111) substrates.

## 1.2 Brief Introduction to Self-Assembled Monolayers

### 1.2.1 Self-Assembled Monolayers

Self-assembled monolayers (SAMs) are molecular assemblies that are formed spontaneously by the immersion of an appropriate substrate into a solution of an active surfactant in a solvent.<sup>11,12</sup> There are several types of SAMs: organosilane on hydroxylated surfaces ( $\text{SiO}_2$  on Si,  $\text{Al}_2\text{O}_3$  on Al, glass, etc.);<sup>13</sup> phosphates/phosphonates on Ti/metal oxide surfaces;<sup>14-16</sup> alkanethiols or aromatic thiols on gold,<sup>5,11,17</sup> silver,<sup>18</sup> and copper;<sup>19</sup> dialkyl disulfides on gold;<sup>20</sup> alcohols and amines on platinum;<sup>21,22</sup> and carboxylic acids on aluminum oxide or silver.<sup>23</sup>

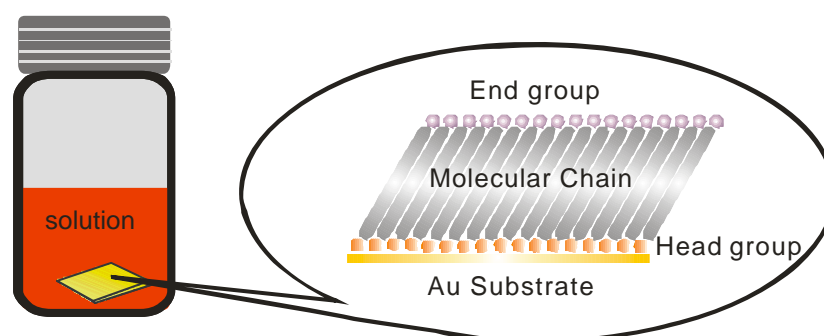


Figure 1.2 Schematic of SAMs on Au assembled from solution.

Self-assembling surfactant molecules can be divided into three parts.<sup>12</sup> The first part is the head group. For thiols on Au, it is a sulfur atom chemically bonded to the surface. The energy of such chemisorption is 40-45 kcal/mol.<sup>12,24</sup> The second part is the molecular chain, which can be used to tailor the SAMs properties by changing the type and length of the chain. The third part is the terminal functional group, which can be hydrophobic/hydrophilic,<sup>25-27</sup> bio-active<sup>28,29</sup> or other special functional groups.<sup>30-33</sup> Figure 1.2 shows a schematic view of SAMs on gold surface.

Among various SAMs, organosulfur molecules on metal surfaces are the ones studied most. In 1983, Nuzzo and Allara discovered that dialkyldisulfides (RS-SR) can form oriented monolayer on gold surface.<sup>34</sup> Later, it was found that sulfur compounds can coordinate not only to gold, but also to other metals, such as silver, copper and platinum. However, the overwhelming majority of work done to date has used gold substrates. There are several reasons why gold is a good choice as a substrate for studying SAMs.<sup>8,11,13,35,36</sup> It is easy to prepare thin films by physical vapour deposition, sputtering, or electrodeposition. Vapour deposited Au on mica with well-defined <111> oriented crystallites as well as Au single crystals are commercially available. Gold is also easy to pattern with a combination of lithographic tools, such as photolithography, micromachining, and chemical etchants. Moreover, gold is inert and is commonly used for spectroscopies and analytical techniques, such as quartz crystal microbalances, plasmon spectroscopy, and ellipsometry.<sup>37,38</sup>

SAMs on gold are easy to prepare both by deposition from the gas phase and in liquid environments. For liquid environments, in general, alkanethiol adsorption on gold is prepared from low-concentration solutions (1 mM or less) of thiols or disulfides (the S-S bond breaks during adsorption). The solvents are chosen depending on the nature of the thiol. The adsorption starts with an initial physisorption, followed by chemisorption on the Au surface through the S-heads (which finishes in several minutes), and finally it takes several hours to form ordered domains.<sup>39-41</sup> During physisorption, the alkanethiol molecule binds to the Au surface through sulfur atom and then it loses the mercaptane H atom, transforming from alkanethiol to alkanethiolate.

The increasing surface coverage results in the nucleation of domains that finally form close packed structure and cover the entire gold surface.

### 1.2.2 The Au(111) Surface

Au single crystal has a face centred cubic (*fcc*) lattice with a bond distance of 2.88 Angstroms (Å). The (111) surface is obtained by cutting the Au in such a way that the surface plane intersects the *x*, *y* and *z* axes at the same value. Figure 1.3 illustrates the Au *fcc* unit cell structure and Au(111) cut from the *fcc* crystal lattice.

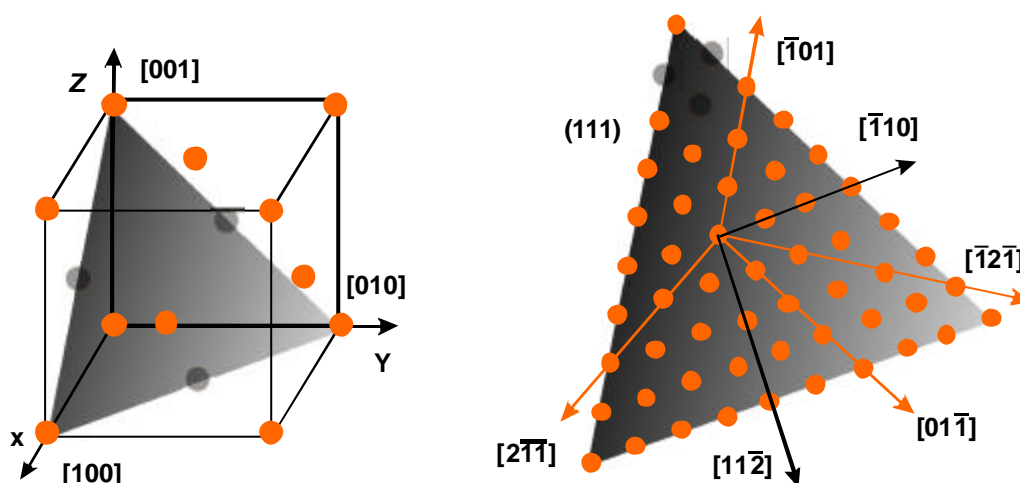


Figure 1.3 Au *fcc* unit cell structure (left) and Au(111) surface (right). Au Atoms are not drawn to scale.

The Au(111) surface is energetically unfavourable, and naturally (or under flame annealing) reconstructs to a  $(23 \times \sqrt{3})$  unit cell.<sup>42-46</sup> The reconstruction forms a herringbone shape and results in a ~4.2% uniaxial (along  $\langle \bar{1}10 \rangle$  directions) contraction on the surface relative to the bulk layers. Figure 1.4 illustrates the Au(111) surface reconstruction. The surface consists of hexagonally close-packed (*hcp*) and face-centered cubic (*fcc*) regions connected by transitional bridge sites elevated ~0.2 Å relative to the *fcc* regions.

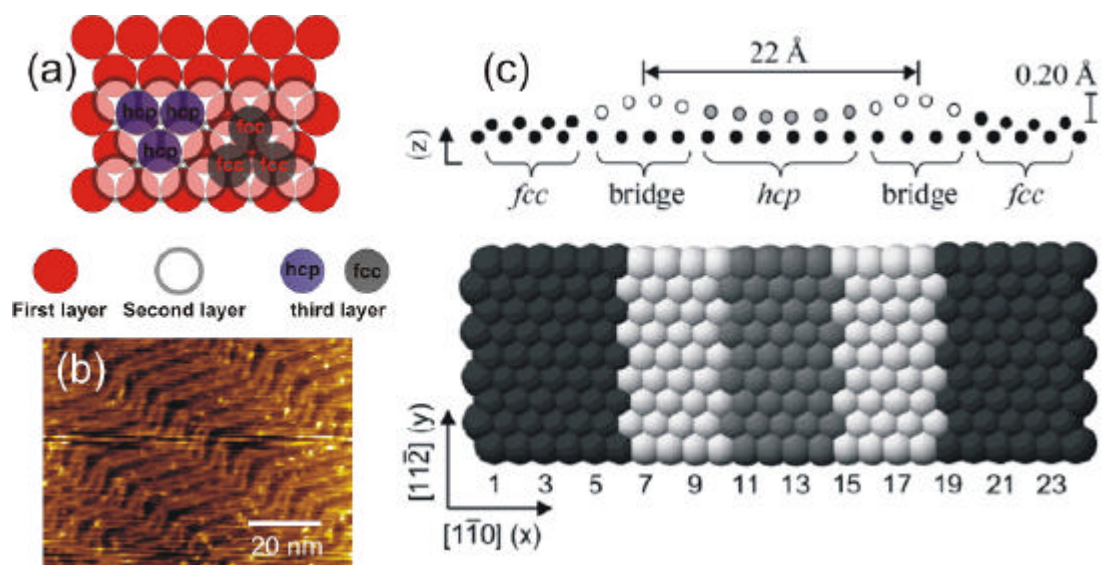


Figure 1.4 Au(111) adopts a  $23 \times 3$  surface reconstruction in order to reduce surface free energy. The surface consists of hexagonally close-packed (*hcp*) and face-centered cubic (*fcc*) regions (a) connected by transitional bridge sites elevated  $\sim 0.2$  Å relative to the *fcc* regions (c)<sup>43</sup>. (b) STM image of Au(111) reconstruction prepared by flame annealing, ( $I = 9$  nA,  $V = 0.05$  V).

### 1.2.3 Self-Assembled Monolayers of Alkanethiol on Gold

Two types of organosulfur molecules are of particular interest to us: alkanethiols and biphenyl thiols. These two types of SAMs form ordered structures on Au(111) and have obvious contrast against electrochemical Cu deposition, which allow the selective Cu deposition on patterned areas (see sections 1.1, 1.3.2, 1.3.3, and 2.3).

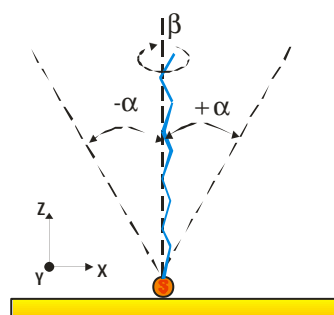


Figure 1.5 Schematic of one long-chain alkanethiol adsorbed on Au surface.<sup>5</sup>

As shown in Figure 1.5, there are two parameters describing the orientation of the molecules of alkanethiolate adsorbed on Au surface: the tilt angle of the molecule away

from the surface normal ( $a$ ) and the twist angle ( $b$ ), which describes the rotation of the C-C-C bond plane relative to the plane formed by the surface normal and the tilted chain.

There are two different structures of SAMs depending on their coverage on the surface: striped structures (low-coverage phase) and close packed structures (high-coverage phase). Striped structures can be obtained by using a very dilute solution of SAM.<sup>47</sup> It can also be found on the surface of vacuum annealed solution-grown SAM.<sup>48</sup> For these structures the molecules lie down flat on the surface in various arrangements.<sup>11,48-52</sup>

The common structure of the high-coverage phases on Au(111) surface is  $\sqrt{3} \times \sqrt{3}$  R30° (R30° means the lattice rotated 30 degree compared to the Au(111) surface lattice).<sup>53,54</sup> A c(4×2) superlattice is also confirmed by many researchers.<sup>55,56</sup>

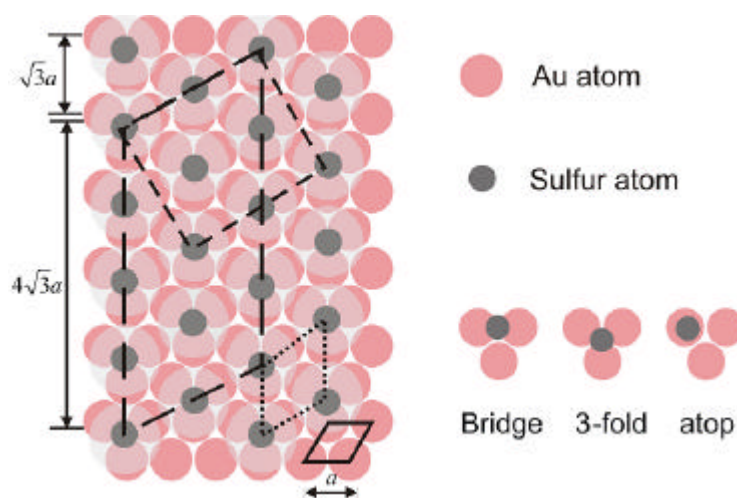


**Figure 1.6** Schematic diagram depicting the arrangement of alkanethiol on Au(111). Three structures are presented:  $\sqrt{3} \times \sqrt{3}$  R30° (marked by dotted line),  $2\sqrt{3} \times 3$  (marked by short dash lines), and c(4×2) (marked by long dash lines). Light gray circles indicate the projected area occupied by each alkane chain. Sulfur atoms were positioned in the 3-fold hollow sites.  $a = 2.88 \text{ \AA}$ .<sup>5</sup> For simplicity, the position of sulfur atom is arbitrarily chosen.

Figure 1.6 shows a schematic of the SAM structure with the sulfur atoms positioned in the 3-fold hollow sites of the gold lattice. The  $\sqrt{3} \times \sqrt{3}$  R30° structure is marked by dotted line. The superlattice structure c(4×2) is marked by lines with long dashes. An equivalent  $2\sqrt{3} \times 3$  unit cell is marked by lines with short dashes. Although the

S-adsorption position in 3-fold hollow sites has been proposed originally, recent experiments and calculations strongly suggested that the thiol is not adsorbed on a bulk terminated Au surface. For example, Molina and Hammer point out that a bridge site is the most stable location on the honeycomb structure (one gold atom missing for every three in the outermost Au layer) and atop position for the inverted-honeycomb structure (with two gold atoms missing for every three) when a defect Au(111) surface instead of a perfect surface was considered.<sup>57</sup> Kondoh and Ohta found that methylthiolate ( $\text{CH}_3\text{S}$ ) occupy atop sites on Au(111) with a S-Au distance of  $2.42 \pm 0.03 \text{ \AA}$ .<sup>58</sup> Maksymovych proposed a new structural model for the lowest-coverage SAM of alkanethiols on Au(111) where pairs of RS species bond via one Au adatom (RS-Au-SR), on the basis of STM measurements and density-functional theory calculations.<sup>59</sup> The result agrees with Woodruff and Wang's findings. They proposed that alkylthiolate SAMs on Au(111) involve Au-thiolate moieties, rather than thiulates bonded directly to atomically flat substrate.<sup>60,61</sup> Moreover, two-site adsorption is also possible as proposed by Torrelles et al.<sup>62</sup>

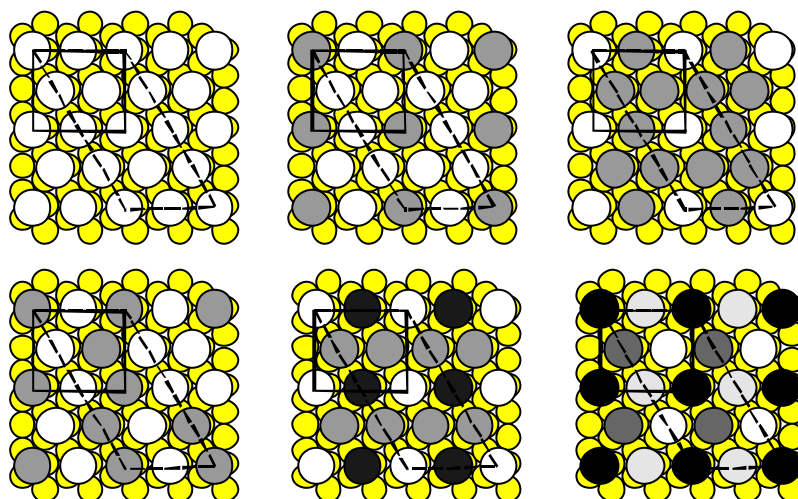


**Figure 1.7** The two structures of MC12 on Au(111) :  $2\sqrt{3} \times 3$  structure (solid rectangular) and  $c(4 \times 2)$  superlattice (dash rectangular).<sup>63</sup> From upper left to lower right are *a* phase, *b* phase, *g* phase, *d* phase, *e* phase, and *x* phase. The darkness shows the height differences. For the *x* phase, there are 4 different height in the  $c(4 \times 2)$  superlattice.<sup>63</sup>

Six phases have been reported regarding the  $c(4 \times 2)$  superlattices based on the assumption that the sulfur atom is in the 3-fold position.<sup>63</sup> Figure 1.7 shows these structural differences. It has been suggested that such difference is due to the

inequivalent bonding site (on-top, three-fold, bridge site), which results in different tunneling current and different twists of the molecular chains.<sup>64-66</sup> However, it has been shown by Riposan and Liu that these contrast transitions originate from probing the corresponding local density of states (LDOS) of each molecule and not from the reorientation of the alkanethiol chains.<sup>67</sup> They observed systematic, reversible, and reproducible contrast transitions with bias and current.

In reality, arrangements of SAMs on substrates are not perfect as what we saw from the above. Figure 1.8 shows STM images of undecanethiol (MC11) SAMs on Au(111).

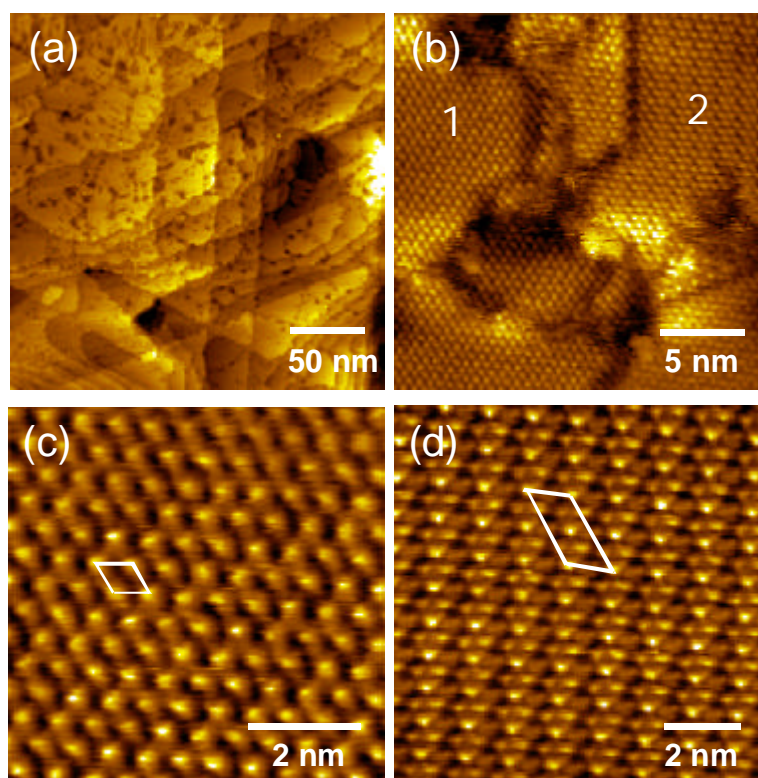


**Figure 1.8** STM images of MC11/Au(111) prepared at 72 °C for 8 hours. (a) A 250 × 250 nm image showing etched pits (vacancy islands). (b) Image showing domain boundaries and vacancy islands. Structures 1 and 2 are shown in (c) and (d), respectively. (c)  $3 \times 3$  structure. (d)  $4 \times 2$  superstructure.

As shown in the large scale image (a), the surface has many “pits”, which is characteristic of alkanethiol assembled on Au(111) (also see section 1.2.5). These are formed during the self-assembly process when thiols lift off the Au atoms (also see discussions in 1.3.4). High resolution images (b-d) show the MC11 SAM at molecular

resolution. In (b) two different structures are seen to coexist. Molecular domains are usually small, about several to tens of nanometers depending on the temperature of preparation; (c) shows the  $\sqrt{3} \times \sqrt{3}$  structure, and (d) shows the  $4 \times 2$  superstructure.

Thermal annealing can cause the fusion of small domains into larger ones (Ostwald ripening effect).<sup>68,69</sup> Regular stripe structures spaced  $\sim 3$ -6 nm are running across the surface as shown in Figure 1.9. The depression of these defect lines are only about 1–2 Å, which result from the rearrangement of SAMs in order to release stress coming from the mismatch of SAM lattice and substrate.

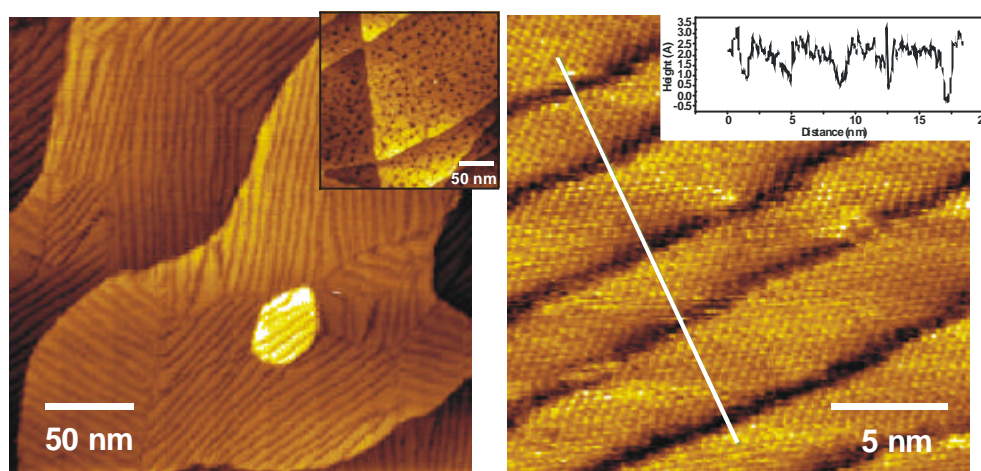


**Figure 1.9** STM images of MC12 annealed for 10 h at 393 K in N<sub>2</sub> atmosphere. The inset STM image shows MC12 prepared at 345 K.

The structure of thiol SAMs is balanced by several factors: (1) intermolecular interactions (e.g., van der Waals), (2) corrugation potential of the interaction between sulfur and substrate,<sup>70</sup> (3) inclination of the molecules. As a result, an average spacing of adsorption sites of 5 Å and the optimum vander Waals distance of  $\sim 4.1$  Å yields a tilt of the hydrocarbon chains by about 30° away from the surface normal on Au(111). However, the angle is smaller (0 - 15°) on silver even though the lattice constant of silver (2.89 Å) is almost the same as gold (2.88 Å). An opposite odd-even effect was found for alkanethiols. Orientation of terminal methyl group is significantly different for odd and even numbers of methylene units. The effect on gold is opposite to that on silver, which is due to the  $sp^3$  hybridization (C-S-Au angle is  $\sim 104^\circ$ ) on gold and  $sp$ -hybridization (C-S-Ag angle is  $\sim 180^\circ$ ) on silver.<sup>71,72</sup> Figure 1.10 shows the odd-even

effect in *n*-alkanethiol monolayers on Ag and Au surfaces.

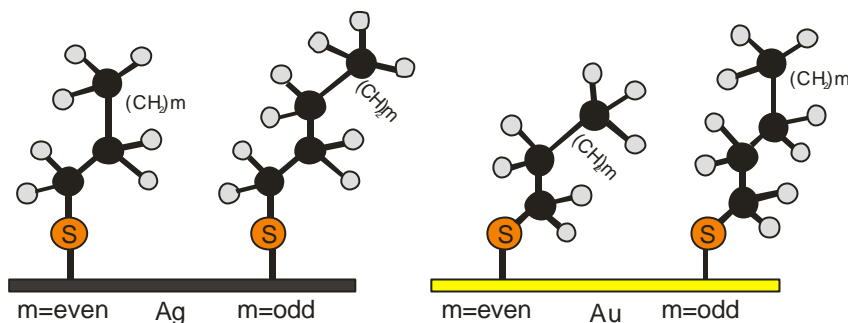


Figure 1.10 Odd-even effect in *n*-alkanethiol SAMs on Ag and Au surfaces.<sup>71</sup>

### 1.2.4 Self-Assembled Monolayer of Biphenyl Based Thiols on Gold

One shortcoming of alkanethiol SAMs is thermal disorder that leads to ‘gauche’ defects, and thus surface disorder. Sum-frequency generation spectroscopy<sup>73</sup> showed that the SAM surface structure is perturbed when it interacts strongly with another phase, e.g. hexane. Thus, surface reorganization must be considered, especially when very polar end-groups (e.g. hydroxyl) are present.<sup>74</sup> Perturbation can be significant, and will not necessarily be confined to the surface. Consequently, surface technologies using alkanethiol SAMs will not be stable enough to allow reproducible, and systematic studies of wettability or other properties.<sup>75</sup> To overcome this shortcoming, Ulman and coworkers have synthesized several 4’-substituted-4-mercaptobiphenyls.<sup>75-78</sup> However, low quality SAMs were formed from these purely aromatic thiols. Rong, et al. investigated a similar system, however with a decisive difference in structure. They studied a series of biphenyl thiols ( $\text{CH}_3\text{-C}_6\text{H}_4\text{-C}_6\text{H}_4\text{-(CH}_2\text{)}_m\text{SH}$ , BPm)<sup>72</sup> which as shown in Figure 1.11, have  $\text{CH}_2$  groups between the aromatic unit and the thiol head group.

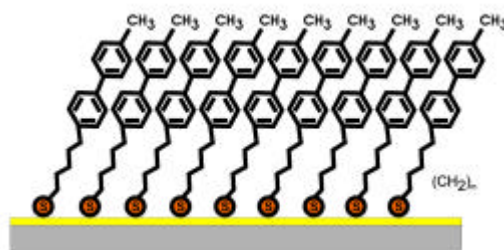


Figure 1.11 Schematic of BPm SAM.

These SAMs turn out to be of very high structure quality.<sup>79-81</sup> The introduction of alkane spacer chain between biphenyl group and sulfur atom provides higher stability than other biphenyl-based SAMs.<sup>75</sup> This was explained by the alkane spacer being able to cope with mismatch between the lattice of aromatic groups and the substrate lattice. Misfit between lattice of SAM and substrate gives rise to stress, which is resolved by introducing defects in the monolayer.<sup>82</sup> However, the combination of aliphatic and aromatic moieties provides additional degrees of freedom, such as conformational ones to release stress.<sup>83</sup> BPm SAMs have been investigated by a number of surface spectroscopies and STM. Fundamental aspects of SAMs were revealed<sup>72,80,84,85</sup> and provide the basis for our research project due to their many advantages such as thermal stability and large domains (exceeding  $10^5 \text{ nm}^2$ ).<sup>79,84</sup>

Similar to alkanethiols an odd-even effect is also observed in BPm SAMs, that is, for  $m = \text{odd}$  on Au and  $m = \text{even}$  on Ag, the arrangement of the aromatic moieties agrees well with the bulk structure of biphenyl, and the bonding of the thiols to the substrate is in agreement with an  $\text{sp}^3$  hybridization of the sulfur on Au and  $\text{sp}$  on Ag, respectively. For  $m = \text{even}$  on Au and  $m = \text{odd}$  on Ag, biphenyl moieties adopt a significantly more canted orientation, which means that the BP unit is too large to fit to a  $\sqrt{3} \times \sqrt{3}$  structure for Au, resulting in a lower coverage (about 10 – 15%).<sup>86-88</sup> Figure 1.12 illustrates the odd-even effect in BPm SAMs on Au. This odd-even effect in the coverage is in sharp contrast with alkanethiols, which do not show coverage difference.

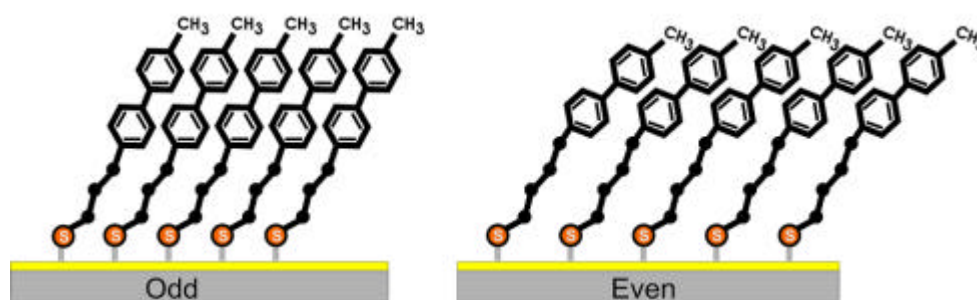
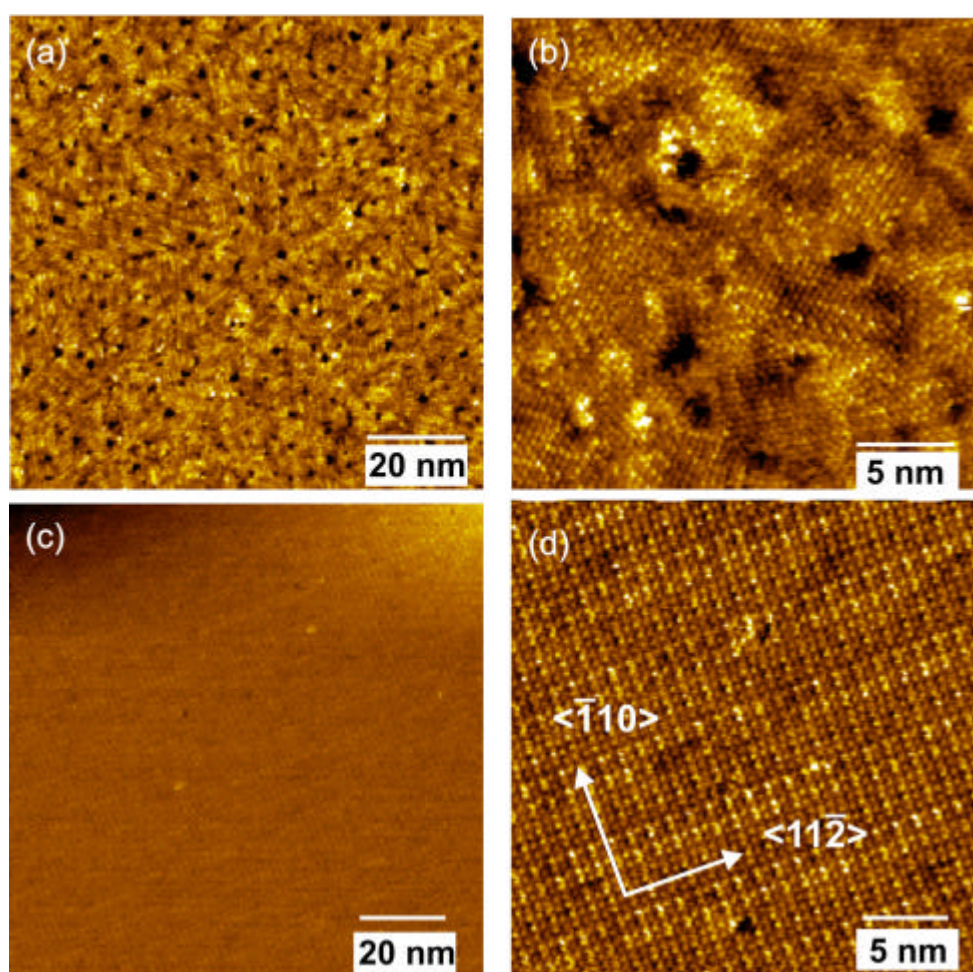


Figure 1.12 BPm SAMs on Au for odd and even methylene units ( $m$ ).

Thus, for BPm on Au, the number of methylene units in the alkane spacer determines the orientation of aromatic units<sup>72,79</sup>. As a consequence, for  $m = \text{odd}$ , a denser packing

can be realized. For  $m = \text{even}$ , although it is not as dense as  $m = \text{odd}$  when prepared at room temperature, it has phase transition when prepared at elevated temperature.<sup>79-81</sup>

Figure 1.13 shows STM images of a BP2 SAM prepared at room temperature and at high temperature. For room temperature preparation (Figure 1.13a, b), the surface is full of etch pits, and the surface has a unit cell structure of  $5\sqrt{3} \times 3$ . After annealing at 428 K for 10 hours, the etch pits are essentially eliminated and large domains are formed as shown in Figure 1.13 (c). The structure exhibits a rectangular  $2\sqrt{3} \times 2$  unit cell with line defects running exclusively along the  $\langle 11\bar{2} \rangle$  direction.<sup>81</sup>



**Figure 1.13** STM images of BP2 prepared at room temperature overnight (a, b), and after annealing at 428 K for 10 hours.

The difference of phase transitions observed between odd BPm and even BPm was explained in terms of intermolecular interactions, coverage, and bending potential (Au-S-C).<sup>80</sup> For BPm ( $m = \text{odd}$ ), they prefer high coverage as the energies of all those

three factors are driven toward a minimum. However, for BP $m$  ( $m = \text{even}$ ), there is competition between these three factors. As a result, even-numbered BP $m$  can have different structures with similar energies. Nevertheless, this high temperature phase BP2 is an extremely good template for patterning and further micro/nano fabrication due to its stability, high order and large domains.

### 1.2.5 Defects in SAMs

Several factors can affect the quality of thiol SAMs: the crystallinity and the roughness of the Au substrate, as well as its cleanness, the nature of the thiol molecule (hydrocarbon chain length, terminal group functionality, etc.), the temperature at which the thiol is adsorbed, the solvent used (ethanol, methanol, toluene, hexane, water, etc), the immersion time, and the concentration of adsorbate. These factors make the idea of a perfect self-assembled monolayer unrealistic.

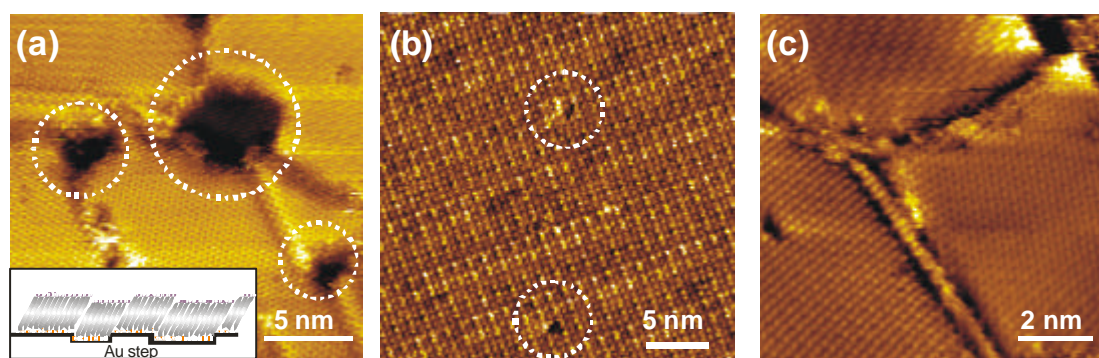


**Figure 1.14** STM images showing the typical defects in SAMs (MC11 (images a and c), BP2 (image b)): (a) Vacancy Au islands, the inset shows the cartoon of Au vacancy islands. (b) Molecular defects. (c) Domain boundaries.

There are several typical defects of SAMs on Au(111) as shown in Figure 1.14: (1) vacancy Au islands produced during the self-assembly process, (2) molecular defects, where molecules are absent or disordered, and (3) domain boundaries, where the molecules exhibit disorder.<sup>17,50</sup> Large dark regions in Figure 1.14(a) are not SAM defects. It has been demonstrated by STM and AFM that, in addition to well-ordered domains, gold 2D vacancy islands of monatomic depth ( $\sim 2.5 \text{ \AA}$  for Au(111)) whose

bottoms are covered by alkanethiolate molecules. These pits were formed from the dissolution of Au atoms during the adsorption of alkanethiols.<sup>\*55,89</sup> In addition to vacancy islands, the gold surface has other structural defects, like steps in the mica substrate and in the case of polycrystalline Au films, intergrain boundaries. For many applications, the quality of SAMs prepared under normal conditions (immersion at room temperature over night) is enough. For others, such as in the fields of electronics and electrochemistry, defects are a problem and improving the SAM quality is crucial. An example will be presented in chapter 3 where a new method of laser-induced passivation will be discussed.

### 1.3 SAM Patterning

It is important to pattern SAMs in order to understand the fundamental interactions or organization of mixed monolayer on metal surfaces. Using different functional groups or using mixed component of SAMs, nanoparticles, proteins, and other nanodevices can be attached to the surface, which can lead to potential applications.<sup>90-94</sup>

There are several types of patterning technologies based on SAM, such as microcontact printing, scanning probe lithography, photolithography/particle beam lithography and laser lithography. Each type of patterning technology has advantages and disadvantages.<sup>5,8</sup>

#### 1.3.1 Microcontact Printing

Soft lithography is using soft materials such as flexible elastomeric polymers in order to transfer and fabricate features into and onto a substrate.<sup>5</sup> Many examples of soft lithography techniques are described in the literature, such as microcontact printing ( $\mu$ CP),<sup>95-97</sup> micromolding in capillaries (MIMIC),<sup>98-100</sup> and microtransfer molding ( $\mu$ TM).<sup>98,101-104</sup>

---

\* For sample prepared in vacuum, the restructuring of SAM/Au interface also results in such pits.

Microcontact printing is a simple method for patterning SAMs on metal surfaces that is operationally like printing ink with a rubber stamp on paper. SAMs form in the regions of contact between a patterned elastomeric stamp, which was wetted with a reactive chemical ‘ink’ consisting of SAMs, is ‘printed’ on the bare surface of a metal, metal oxide, or semiconductor. Figure 1.15 shows a schematic view of the use of  $\mu$ CP to deposit two types of molecules onto a gold surface. When forming patterned SAMs on gold surface, the stamp is typically left in contact with the surface for a short time (seconds to minutes) before it is removed.

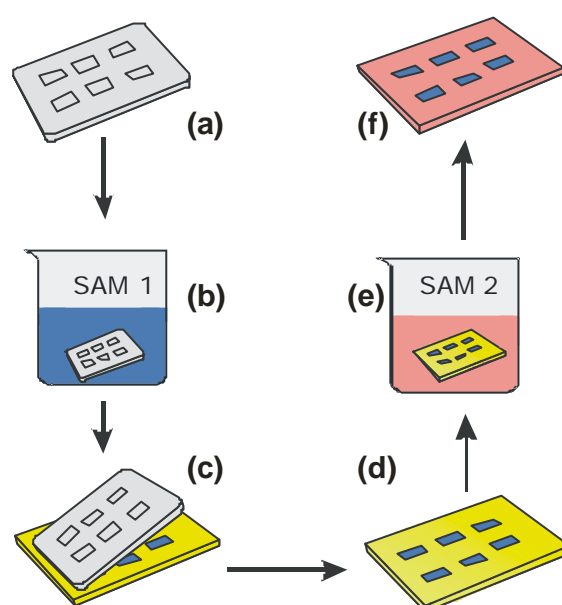


**Figure 1.15** A schematic view of microcontact printing. (a) a PDMS mold prepared from a pattern. (b) the PDMS mold is immersed into SAM solution 1. (c) the PDMS mold with the “ink”- SAM is gently pressed onto the Au surface. (d) a pattern with a single SAM covers the Au surface. (e) the Au substrate is immersed into a second SAM solution 2 to fill the bare area. (f) a pattern with two-types of SAMs is formed.

Although this process is simple, several parameters affect the lateral resolution. These include the type of molecules, concentration in the ink, the type of solvent, the duration of contact, and the pressure applied. Studies show that the mass transport of thiols during  $\mu$ CP includes the following processes: diffusion of ink from stamp to interface; diffusion away from the edges of the stamp and across the Au surface/vapor transport through gas phase. The first mechanism is important for the formation of SAMs in areas where the stamp is in contact with the surface. The second mechanism is

important for understanding the diffusion of SAMs into areas that are not in contact with the stamp. These processes lead to lateral distortions of the pattern and limit the resolution.<sup>5</sup>

It has been shown that the lateral mobility increases if no molecule is used to fill the empty spaces, a process called backfilling. To avoid this problem, a so-called microdisplacement printing was proposed by P. S. Weiss et al.<sup>105</sup> They used a preassembled monolayer to protect the surface. Such preassembled layer is easy to be replaced by other SAMs used. However, the limitation in the choice of the preassembled layer (typically adamantanethiol) and the extent to which the replacement can be completed hinder the resolution and further application, such as electrochemical deposition.

In summary,  $\mu$ CP is a very versatile and powerful tool in micro/sub-micro range fabrication. It has the advantage of large area printing, can be applied to curved surface of stamp or substrate. However, the diffusion and the alignment precision as well as the stability of stamp also limit the achieved resolution. The common feature can be obtained are usually in the range of several micrometers, although sub-micrometer resolution can also be achieved.<sup>106-108</sup>

### 1.3.2 Scanning Probe Lithography

Scanning Probe Microscopy (SPM) has two roles in the field of nanotechnology. The first one is to 'see' molecules in a straightforward way. The second one is to manipulate atoms/molecules on the surface with the tip. This technology is referred to as scanning probe lithography (SPL), which include atomic force microscopy (AFM) and scanning tunnelling microscopy (STM lithography is addressed in Chapter 4)

By applying a relatively large force load, the AFM tip can remove the SAMs, which is usually called nanoshaving.<sup>6,109-111</sup> The method was developed by Xu and Liu.<sup>112,113</sup> In this method, a matrix layer is imaged by the AFM tip under a low load, and is switched to modifying mode (high load) once an area chosen for patterning. The

molecules are removed and replaced by other molecules. The AFM tip was then used to image the pattern by using a low load. Lines of 10 nm width with a separation of 20 nm were demonstrated. Island of about 32 molecular of MC18 was patterned in a MC10 matrix.<sup>114</sup>

When using current sensing AFM, voltage can be applied between tip and conductive/semi-conductive substrates. This allows oxidizing local area<sup>115-118</sup> (most works were based on the substrate of silicon, which can be oxidized to  $\text{SiO}_2$ . However, SAMs modified surfaces can also be oxidized).<sup>119</sup> The mechanism is proposed to be that water meniscus forms a bridge due to capillary condensation between tip and sample. It is hence an electrochemical process.

“Dip-Pen” nanolithography (DPN)<sup>120-122</sup> is a variation of scanning probe lithography (direct-write) proposed by Jaschke<sup>123</sup> and developed by Mirkin and his coworkers.<sup>120</sup> The concept of DPN is that the printing of molecules is analogous to writing with an ink. Patterns of different sizes can be achieved by allowing molecules to diffuse to the substrate by holding a molecules-loaded probe in contact with the surface shown in Figure 1.16. Although this lithography is direct and of high resolution, the moving distance of the tip is limited, hence the efficiency is low compared to microcontact printing technique.

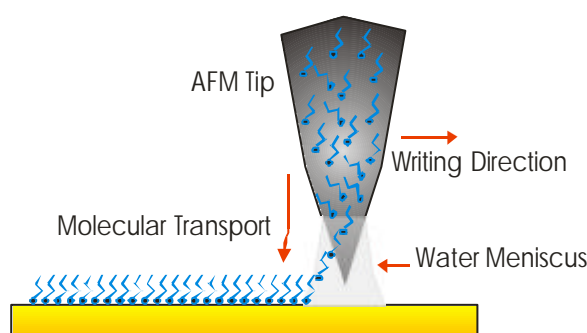


**Figure 1.16 Schematic representation of DPN.**<sup>120</sup>

To increase patterning speed, Mirkin and co-workers<sup>124,125</sup> described a massively parallel method to pattern large areas with 80-100 nm features arranged in complex patterns within 30 minutes, which is 55000 times faster than single tip patterning (see

Figure 1.17).

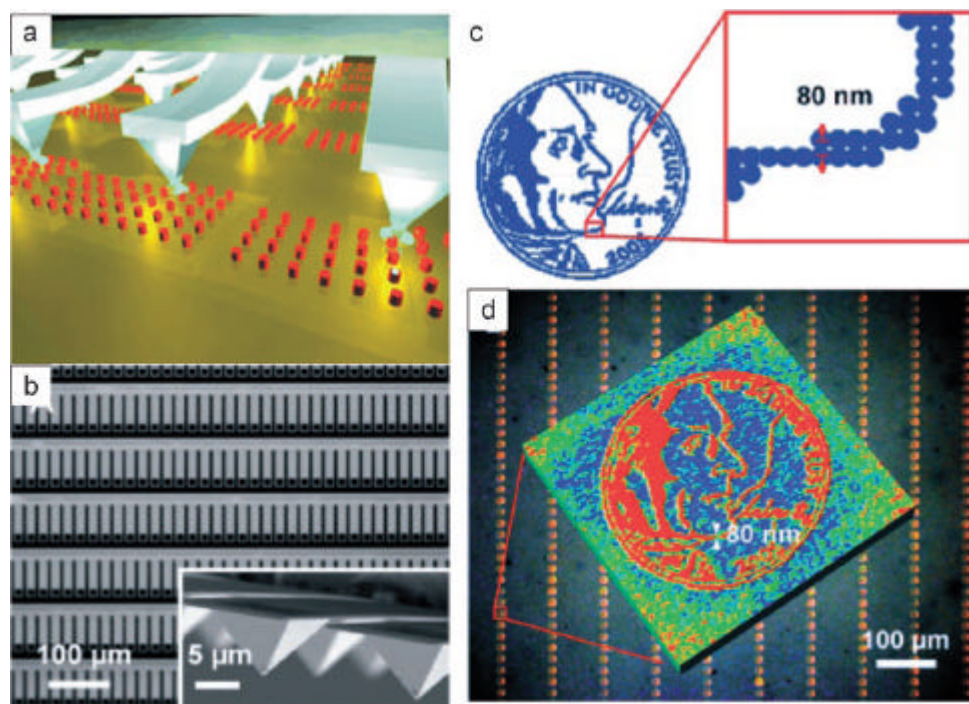


**Figure 1.17** Massively parallel DPN (a) artist's impression of the arrays of cantilevers (shown in part b) writing nanoscale features. (c) and (d) demonstration of the formation of complex features using 80-nm-diameter dots.<sup>124,126</sup> (reproduced from ref<sup>124</sup>).

It is also possible to use a heated AFM cantilever with a tip coated by a solid “ink”.<sup>121,127</sup> When the tip is warm enough, the ink melts and flows onto the substrate. No deposition occurs when the tip is cold. It is hence possible to avoid unintended deposition due to diffusion of ink. The method is also useful for transporting materials that are solids at room temperature like polymers.

Other effects are also used for AFM patterning, for example, by using catalyst functionalized AFM tip, chemical reaction can be produced in a confined space, thus patterning and functionalizing can happen at the same time.<sup>128-130</sup>

### 1.3.3 Photolithography

Photolithography is one of the most developed (and commercially available) technologies for patterning.<sup>131</sup> It is also known as optical lithography. In the past several decades, it has been the mainstream technology for high-volume manufacturing in the

semiconductor industry. The principle is simple: light passes through a mask, which contains the desired pattern, causing photoresist to be removed by subsequent treatment. The pattern was then used for further treatment, such as etching and more complicated fabrication.

Irradiation of a SAM with UV light through a pattern of apertures leads to photooxidation of the SAM in exposed area. Oxidized species can later be removed by rinsing in polar solvent, such as water or ethanol. The exposed area can be filled by a second SAM of interest by immersion into the respective solution.<sup>132</sup> Figure 1.18 shows a simple example of photolithography.

The maximum resolution of in standard photolithography is determined by the optical elements of the system, with the minimum feature size  $\lambda/2$  of the light source, which is the diffraction limit. The lateral optical resolution is related to the light wavelength ( $\lambda$ ), and to the numerical aperture (NA):

$$\Delta x = k \frac{\lambda}{NA} = k \frac{\lambda}{n \sin \theta} \quad (1-1)$$

where  $k$  is a process factor determined by the different optical system, with a physical limit of 0.25.<sup>133</sup>  $n$  is the index of refraction of the medium in which the lens is working, and  $\theta$  is the half-angle of the maximum cone of the light that can enter the lens. The maximum values of the NA can be achieved at the present is 0.93 for dry and 1.35 for water immersion lenses.<sup>134,135</sup>

To overcome the optical diffraction limit, a fiber-based Near Field Scanning Optical Microscopy (NSOM) can be used by working with an aperture brought very close to a surface. The resolution is a function of the aperture size of the fibre tip, regardless of the wavelength of the light source.<sup>7,136,137</sup> Structures with dimensions as small as 9 nm ( $\sim \lambda/30$ , which is approximately 15 times smaller than the conventional diffraction limit.) were created on SAM/Au surface by Leggett et. al. by using a NSOM coupled with a 244 nm light source.<sup>138</sup>

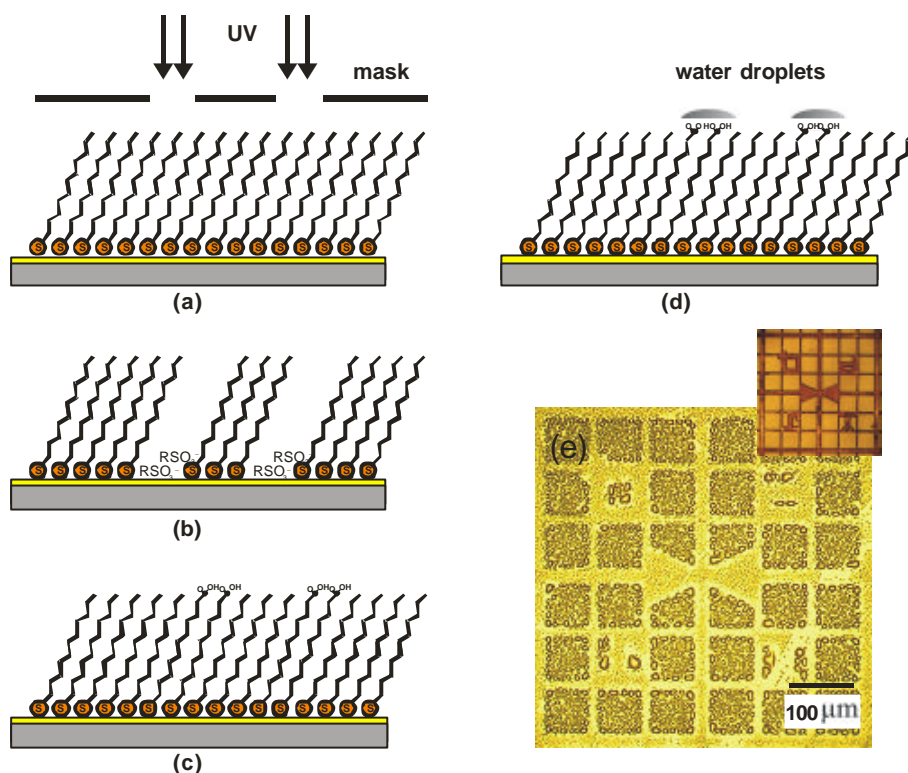


**Figure 1.18** Schematic diagram showing the sequence of steps in forming a pattern (hydrophobic/hydrophilic) by photolithography. (a) UV light passes mask and irradiates a hydrophobic SAM (MC11). (b) Exposed areas are oxidized to  $\text{RSO}_3^-$  species. (c) A hydrophilic SAM (MUA) formed on the irradiated area. (d) Water condensation formed on pattern SAMs. The inset is a copper grid serving as mask.

### 1.3.4 E-Beam Lithography

Electrons can also generate patterns in SAMs. Low energy beams of electrons in the range of 10-100 eV can induce chemical changes in SAMs, such as cleavage of bonds (C-S and C-H), formation of C=C bonds, cross-linking of adjacent molecules, fragmentation of molecules, and conformational disorder.<sup>139-141</sup>

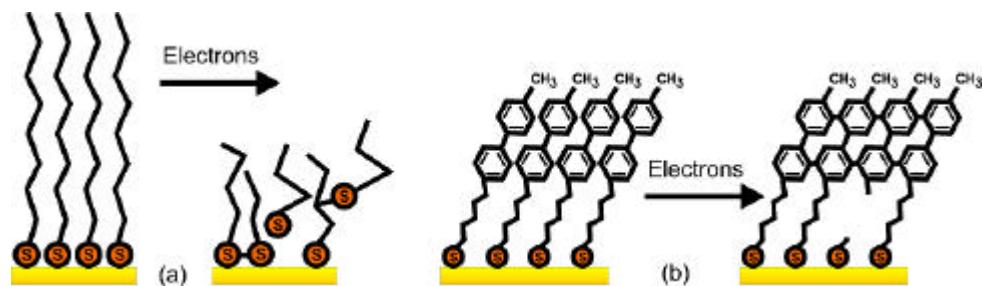


**Figure 1.19** Schematic of electron-induced destruction and disorder in aliphatic (a) and aromatic self-assembled monolayers (b). They can be used as positive and negative resist, respectively.

Upon irradiation, alkanethiol SAMs become disordered and more prone to desorption and C-C bond cleavage, which damages the SAM and makes the underlying gold film susceptible to corrosion by wet chemical etchants. This type of SAMs can be used as positive resist.<sup>142</sup> However, SAMs of biphenyl thiols undergo cross-linking reactions after cleavage of the C-H bonds on the aromatic rings. These modified areas provide better resistance against etchants.<sup>78,143-145</sup> Thus, this type of SAMs can be used as negative resists. Figure 1.19 shows a schematic of electron-induced changes in aliphatic and aromatic self-assembled monolayers. Cross-linked biphenyl SAMs also exhibit an extremely high thermal stability, which can be useful for ‘thermal desorption lithography’.<sup>146</sup>

The resolution of E-beam lithography is limited by the spot size of the electron beam, which is determined by the forward scattering of electrons in resists and backward scattering from the substrate.<sup>147</sup> Thin resists like SAMs can help to improve the attainable resolution since they reduce the scattering of electrons.<sup>148</sup> In principle, E-beam lithography can produce line widths of 10 nm or smaller (for a JBX 5500 FS lithography tool, a minimum line width of 10 nm can be obtained)<sup>149</sup>. However, compared to photolithography, E-beam lithography is slow and not suitable for high-volume manufacturing since the beam has to be scanned across the surface and the pattern generation is serial. Also, like high-end photolithography equipment, advanced E-beam writing systems are expensive.

### 1.3.5 Laser Beam Lithography

It is known that the Au-S bond is unstable at elevated temperature, and SAMs can desorb from the gold surface.<sup>11</sup> Mass spectroscopy of alkanethiol SAMs thermally desorbed shows that the molecules desorb as dialkyl-disulfide dimers. The signal associated with the dialkyl-disulfide increases in magnitude with increasing temperature.<sup>150</sup> All these experiments show that desorption of SAMs from Au is a temperature-enhanced reaction. The activation energy is estimated at 32 kcal/mol.<sup>150</sup> It

is believed that localized heating can also break up Au-S bonds and produce bare Au regions of gold through laser irradiation. A second alkanethiol with different terminal group or chain length can then be assembled into these bare regions. A laser beam is an excellent tool for precise localized heating since it causes activation or acceleration of endothermic chemical reactions. The desired pattern can be produced by relative movement of laser beam and substrate.

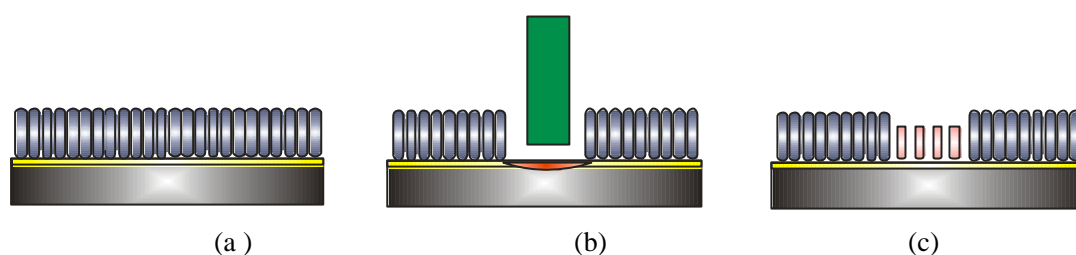


**Figure 1.20** Schematic of laser scanning lithography procedure. (a) Initial homogeneous SAM, (b) laser Irradiation, (c) adsorption of another SAM on the Au-exposed area.

As shown in Figure 1.20, the laser patterning procedure is a simple three-step process: first, a homogeneous SAM is formed on the substrate surface; second, the pattern is created with the laser; and finally, a different SAM grows on the irradiated area or metal is deposited directly.

It is noncontact, flexible, and can be applied to other systems such as SAMs on silicon or even on polymeric substrates. Resolution is determined by the laser spot size, which depends on the laser source and the focus system. The resolution is typically in the micrometer region. Shadnam and Amirfazli showed the feasibility of laser patterning by using a 488 nm continuous-wave Ar laser and wrote lines with widths of 28-170  $\mu\text{m}$ .<sup>151</sup> Balgar et al. showed that by using a 10 W, 458 nm continuous-wave Ar laser, structures with a lateral resolution of 500 nm can be prepared routinely.<sup>152</sup> Chang et al. demonstrated that sub-micro line width as small as 250 nm can be obtained by a pulsed laser coupled with near-field scanning optical microscopy.<sup>153</sup>

## 1.4 Electrochemistry

### 1.4.1 Electrochemistry Basic Principles

In electrochemistry, the electrode/electrolyte interface is considerably different to those in solution. Strong interactions happen between the ions/molecules in solution and the electrode surface under potential control. This give rise to a region called “electric double layer”. This is an important issue in electrochemistry.<sup>154</sup>

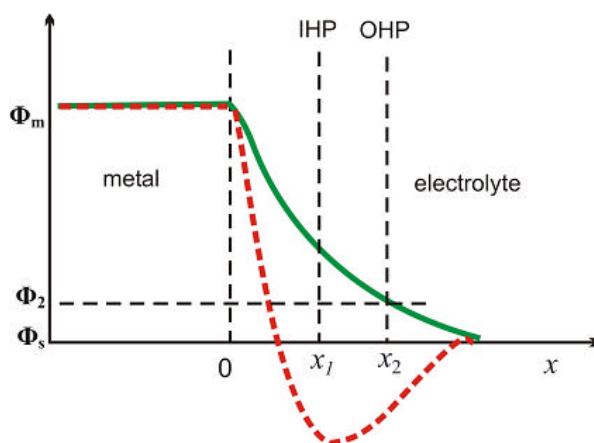


**Figure 1.21** Model of metal/electrolyte double layer interface. Potential distribution across the electrochemical interface for a purely electrostatic interaction between solvated ions and the metallic surface (solid line) and for the case of specifically adsorbed ions (dash line gray). Position  $x_1$  and  $x_2$  correspond to the IHP and OHP respectively.  $F_s$  is the solution potential,  $F_m$  is the metal surface potential, and  $F_2$  is the potential at  $x_2$  with respect to the bulk solution.<sup>154,155</sup>

There are several ‘layers’ that make up the double layer. The inner layer (the layer closest to the electrode) contains solvent molecules and other species (ion or molecules) that are specifically adsorbed. This inner layer is also called the compact, Helmholtz, or Stern layer (see Figure 1.21), which includes two parts: inner Helmholtz plane and outer Helmholtz plane. The electrical centre of the specifically adsorbed ions is called the inner Helmholtz plane (IHP, position  $x_1$  in Figure 1.21). The centre of solvated ions which can only approach the metal to a distance  $x_2$  is called the outer Helmholtz plane (OHP).<sup>154</sup> The interaction between the solvated ions and the charged metal involves only long-range electrostatic forces. This interaction is essentially independent of the chemical properties of the ions. These ions are nonspecifically adsorbed and are distributed in a three-dimensional region called the diffuse layer, which extends from

the OHP into the bulk of the solution. Because the chemical interaction between specifically adsorbed ions and the metal surface can result in more charge to be accumulated at the surface than required by electrostatics. Counter charges are brought into the double layer for compensation. Consequently, specifically adsorbed ions cause a steeper potential gradient (close to metal surface) than the non-specifically adsorbed ions.<sup>155</sup> The potential profile across the double-layer region is shown in Figure 1.21.

Two types of processes can occur at the electrode surface, Faradaic and nonfaradaic. In Faradaic processes, charges are transferred across the metal-solution interface. This electron transfer causes oxidation or reduction. In nonfaradaic processes, adsorption and desorption can occur. The structure of the electrode-solution interface can be changed by changing potential or solution composition. Arrangements of molecules on metal surfaces can be controlled by changing the potential.<sup>156,157</sup>

## 1.4.2 Cyclic Voltammetry

Cyclic voltammetry (CV) is one of the most commonly used techniques in electrochemistry. It is based on a linear potential waveform, i.e., the potential is changed as a linear function of time. It involves measuring the current while scanning the potential of the working electrode, where redox reactions (adsorption/desorption) are happening. The combination of the current/time curve and potential/time curve is how a CV curve is obtained as shown in Figure 1.22.

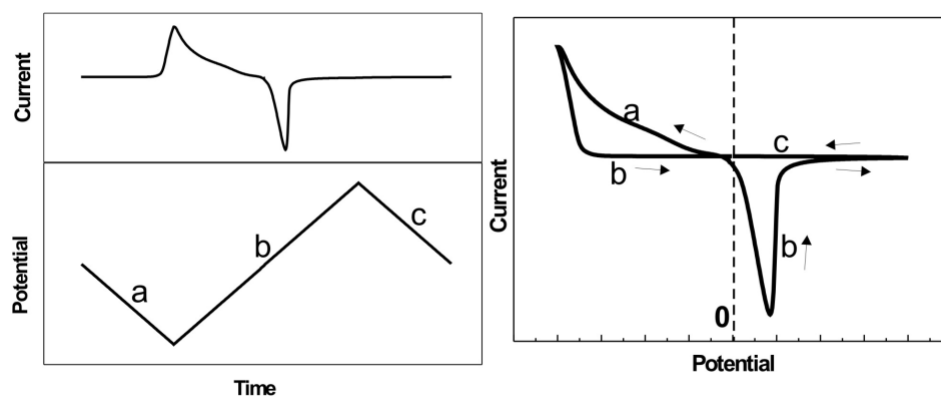
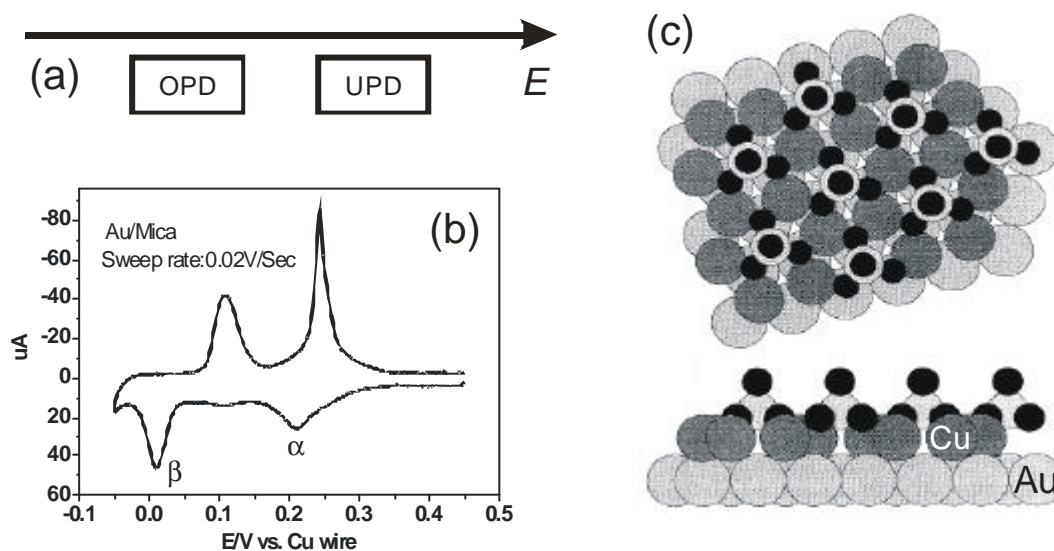


Figure 1.22 Combination of current/time curve and potential/time curve generates a CV.

### 1.4.3 Metal Deposition

There are several ways to deposit metal on the substrate, such as physical vapour deposition (PVD)<sup>158-160</sup>, chemical vapour deposition (CVD),<sup>161</sup> electroless plating,<sup>162-164</sup> and electrochemical deposition.<sup>155,165-168</sup> Electrochemical deposition has several advantages such as selective deposition and control of rate via the potential. There are two deposition processes which can happen during metal deposition: bulk deposition or overpotential deposition (OPD) and underpotential deposition (UPD).



**Figure 1.23** (a) UPD happens in a potential more positive than the OPD. (b) CV showing deposition and desorption of Cu UPD. The pair of deposition peaks corresponds to a two step deposition process: a  $\sqrt{3} \times \sqrt{3} R30^\circ$  honeycomb structure with copper coverage of 0.67 and sulfate anions occupying the centers of the honeycomb with the coverage of 0.33 after the first deposition peak (a), and a  $(1 \times 1)$  structure with copper coverage of 1 after the second deposition peak (b). (c)<sup>172</sup> Surface structure of Cu UPD on Au(111) after the first UPD peak. Sulfate anions occupying the centers of the honeycomb of Cu UPD.

Underpotential deposition (UPD) refers to electrodeposition of a monolayer of a metal A on a substrate metal of B at potentials that can be significantly less negative than that for deposition of A on A.<sup>169</sup> UPD happens in a potential region positive of the respective Nernst potential. This is because of the interactions between adatom-substrate are stronger than the interactions between adatom species.<sup>170</sup> Thus, a UPD monolayer is formed before bulk deposition starts. UPD of Cu on Au surface has

been studied extensively over the past, among which, the Cu UPD on Au(111) is one of the most widely studied systems. The cyclic voltammogram of Figure 1.23 shows characteristic voltammetric features of Cu UPD.<sup>171</sup> The pair of deposition peaks  $\alpha$  and  $\beta$  correspond to a two step deposition process: that is a  $\sqrt{3} \times \sqrt{3}$  R30° honeycomb structure with copper coverage of 0.67 and sulfate anions occupying the centers of the honeycomb with the coverage of 0.33 after the first deposition peak ( $\alpha$ ) and a (1×1) structure with copper coverage of 1 after the second deposition peak ( $\beta$ ).<sup>172,173</sup>

On a bare Au surface, the driving force for UPD is the strong interactions between adatom and substrate. On a SAM modified Au electrode, the higher stability of Cu-S versus Au-S provides an additional driving force for forming a UPD of Cu between the substrate and SAM.<sup>174,175</sup> However, a SAM modified electrode can block UPD and bulk metal deposition. However, if the chain is too short or if there are defects in the SAM, blocking is insufficient and UPD/metal deposition can happen on the substrate, although in a much slower way (reorientation of SAM can happen during this process).<sup>174,176</sup> Moreover, the terminal groups of SAMs also affect the penetration of metal ions.<sup>177</sup>

The OPD is determined by the Nernst equation:

$$E = E_0 + RT / nF \ln a_{m^{n+}} / a_m \quad (1 - 2)$$

Where  $E_0$  is the standard potential of the  $m / m^{n+}$  redox couple,  $a_{m^{n+}}$  and  $a_m$  are the activities of the metal ion and metal, and  $a_m$  is defined as 1.  $n$  is the number of electrons per ion, and  $F$  is the Faraday constant.

The presence of a SAM on metal surface can significantly block bulk metal deposition.<sup>165,178,179</sup> This blocking behaviour shows a chain length dependence (see section 2.3) which can be used for selective metal deposition.

## 1.5 Scanning Tunnelling Microscopy

The Scanning Tunneling Microscope (STM) was invented by G. Binnig and W. Rohrer at the IBM Zurich Research Laboratory in 1982 and was honoured by the Nobel Prize in physics in 1986.<sup>180,181</sup> It has become an important tool in surface science for analysis of conducting and semi-conducting materials in real space.

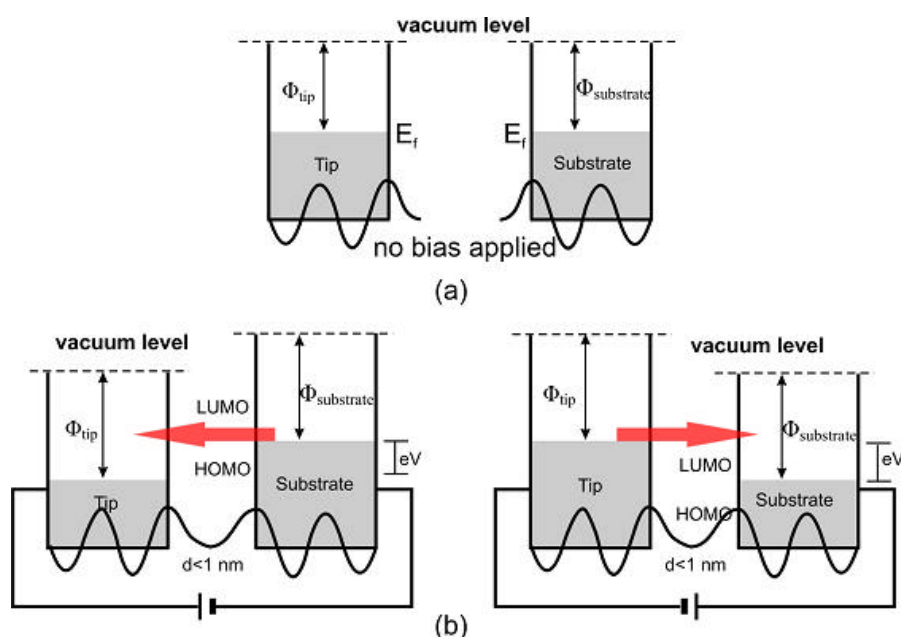


**Figure 1.24** (a) Electrons can traverse the forbidden region and reappear on the other side of the barrier if the barrier with potential energy larger than the kinetic energy of the electrons; (b) If the distance between the two electrodes is close enough ( $< 1 \text{ nm}$ ), and if a bias is applied, the overlapped electron wavefunction permits quantum mechanical tunneling and a current will flow across the barrier.<sup>182</sup>

STM is based on a quantum mechanical phenomenon known as tunneling.<sup>183,184</sup> In tunneling, a particle, in this case an electron, can jump from the STM tip to the sample or vice versa. The space between the tip and the sample forms a barrier. If the distance between the two is small enough, electrons will tunnel from one electrode to the other. If no voltage is applied between the tip and the sample, electrons will tunnel in both directions and no net current will flow. Only when a voltage is applied, can electrons tunnel from the lower voltage to the higher one and a current can be measured.

The quantum mechanical effect of tunneling is shown in Figure 1.24. The wavefunctions at the Fermi level exponentially leak out of the metal with an inverse decay length of

$$k = \hbar^{-1}(2m\mathbf{f})^{1/2} \quad (1 - 3)$$

Where  $m$  is the mass of electron and  $\mathbf{f}$  is the tunneling barrier height. If the two metals are brought in close contact and if a small voltage is applied between them, a tunneling current can be generated which is

$$I \propto U \exp(-2kd) \quad (1 - 4)$$

Where  $d$  is the distance between the conductors. This equation indicates that the tunneling current is exponentially dependent on the distance between the conductors.

Both positive and negative bias voltages can be applied to the tip (sample). When the tip is positive (sample negative), electrons will tunnel from the occupied states of sample to the unoccupied states of the tip. When the tip is negative (sample positive), electrons will tunnel from the occupied states of the tip to the unoccupied states of the sample.

In understanding the lateral resolution of STM, S-wave tip model was proposed by Tersoff and Hamann to replace the unknown electric structure of the tip.<sup>184</sup> They proposed that the tunnelling rate is proportional to the local electronic density of states at the center of curvature of the tip, and the effective lateral resolution is related to the tip radius  $R$  and the vacuum gap distance  $d$  as  $[(2\text{\AA})(R+d)]^{1/2}$ . However, this model fails in explaining the observed atom-resolved image because it models the tip as a macroscopic continuum. Chen proposed that d-band metal is required to achieve atomic resolution by taking account the actual electronic states of the tip.<sup>185</sup> He explained the difference between the S-wave shape model and his model by a reciprocity principle (interchanging the electronic state of the tip and the sample state, the image should be the same). As shown in Figure 1.25, higher resolution can be obtained by using a  $dZ^2$  wave tip.

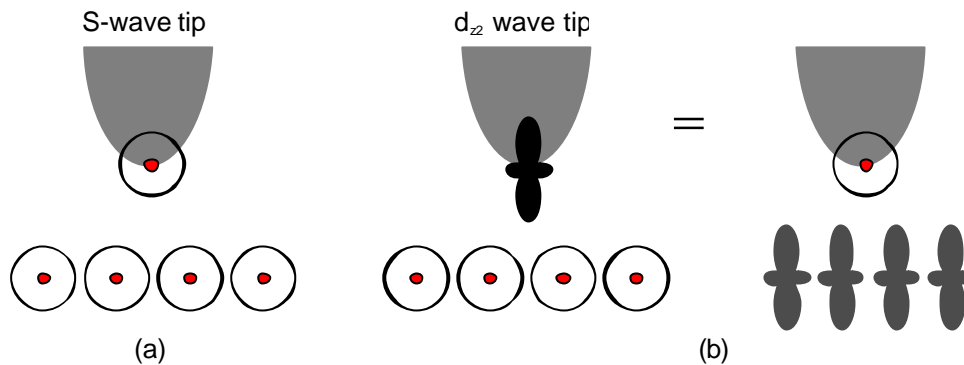


Figure 1.25 Higher resolution can be obtained by using a  $dz^2$  wave tip in comparison to a S-wave tip.<sup>185</sup>

There are several modes of operation for STM as seen in Figure 1.26: (1) Constant current mode. The tip is vertically adjusted by using a feedback loop and the current is kept constant. As the current is exponential to the distance  $d$  between tip and sample, the tip is sensitive to surface topography. Thus, topographic images of the surface can be generated by recording the vertical position of the tip. As the scanning is slow in this mode, drift in  $xy$  plane (sample surface) is possible. (2) Constant height mode. In this mode the vertical position of the tip is kept constant and the tunneling current is monitored. This can be done by using a disabled feedback. This mode can only be applied to atomically flat surfaces.

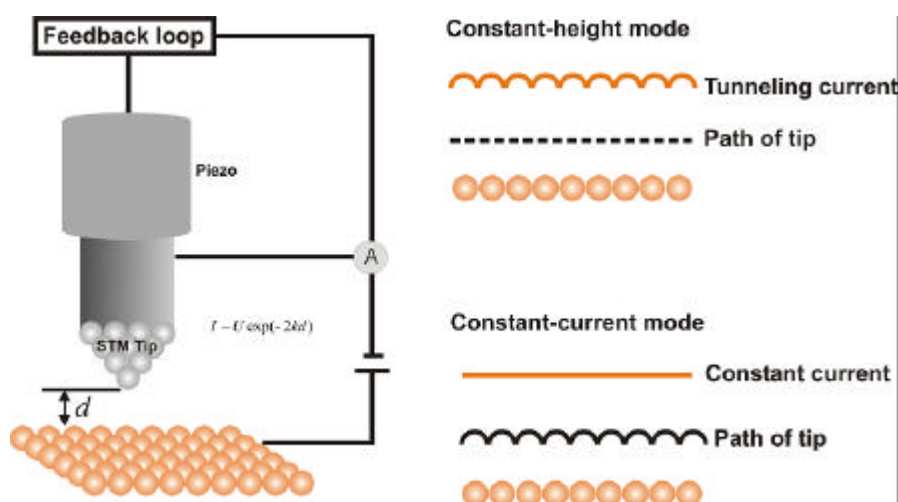
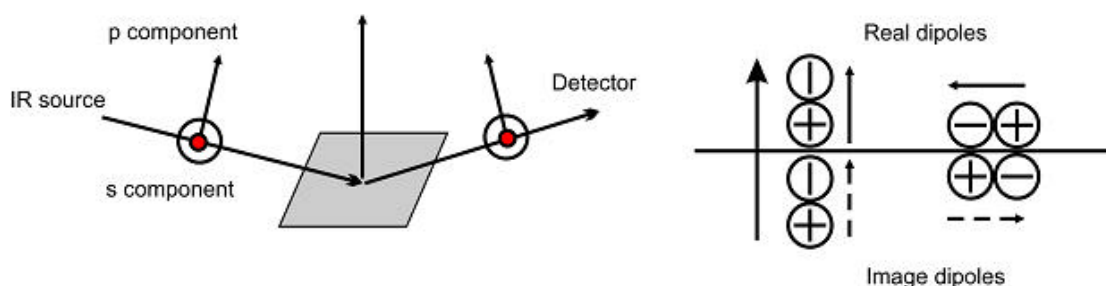


Figure 1.26 Principle of STM. There are two working modes: constant height mode and constant current mode.

## 1.6 IRRAS, XPS and NEXAFS Spectroscopy

### 1.6.1 Infrared Reflection Absorption Spectroscopy

Infrared Reflection Absorption Spectroscopy (IRRAS) can be used to study SAMs where the IR beam is specularly reflected from the front face of substrate.<sup>186,187</sup> An IR beam can be resolved into p- and s- polarized components in which the electric vector is parallel and perpendicular to the plane of incidence, respectively. Polarisation modulation IRRAS (PMIRRAS) using a polarizer to create p-polarised light (see Figure 1.27 (left)). It is only those vibrations of the adsorbed molecules, whose dipole change has a component perpendicular to the surface are active (see Figure 1.27(right)). The advantage of PMIRRAS over the conventional IRRAS is that PMIRRAS is independent on the adsorption of gas/water. Consequently the disturbing factors of water vapor and CO<sub>2</sub> can be eliminated.



**Figure 1.27 IRRAS and surface dipole selection rule. It is only those vibrations of the adsorbed molecules, whose dipole change has a component perpendicular to the surface are active.**

### 1.6.2 XPS and NEXAFS Spectroscopy

X-ray photoelectron spectroscopy (XPS), also known as Electron Spectroscopy for Chemical Analysis (ESCA) is an important surface analysis technique that measures the elemental composition, chemical state and electronic state of the elements. It measures the kinetic energy (KE) and number of electrons that escape from the top 1-10 nm of a material by irradiating the surface with X-rays. Each element has a characteristic set of XPS peaks at characteristic binding energy (BE) values, which

correspond to the electron configuration of the electrons within the atoms, e.g., 1s, 2s, 2p, etc. A quantitative analysis is possible via the number of detected electrons in each of the characteristic peaks, i.e., the concentration of the element is related to the intensity of the peaks.

Near Edge X-ray Absorption Fine Structure (NEXAFS)<sup>188</sup> probes the absorption of electromagnetic radiation by excitation of core electrons into unoccupied molecular orbitals or continuum states (see Figure 1.28). It was developed in the 1980s, mainly in order to resolve the structure and orientation of low-Z ( $Z$  is the atomic number) molecules bonded to surfaces. Opposite to XPS, where the source energy is fixed and the electron intensity is measured as a function of electron kinetic energy, in NEXAFS the x-ray energy is tunable and the absorbed x-ray intensity is measured (or the Auger electron yield / total electron yield is measured).

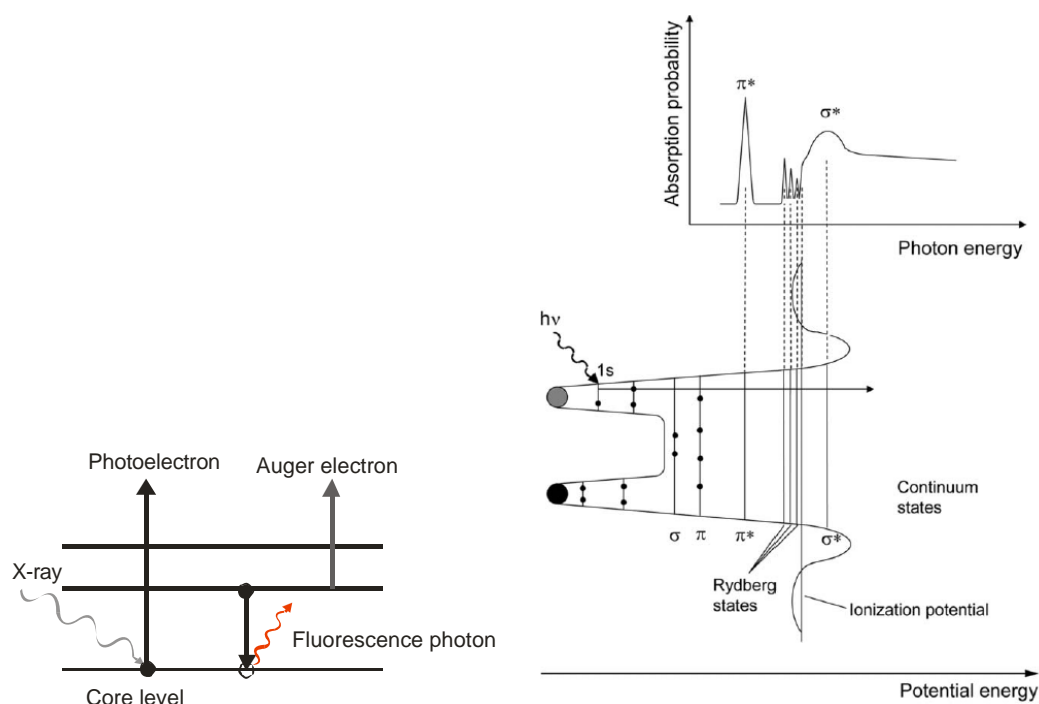


**Figure 1.28** Energy diagram of the photoabsorption process. The absorption results in a photoelectron and a core hole, which is subsequently filled by the emission of a fluorescence photon or an Auger electron (left). Schematic potential and corresponding NEXAFS Kshell spectrum of a diatomic molecular (sub) group (right).<sup>188</sup>

One great asset of NEXAFS spectroscopy is its ability to obtain information on the molecular orientation. An example is shown in Figure 1.29 for the benzene molecule.

When the electric field vector  $E$  is aligned along the surface normal (grazing incidence), peaks due to the out-of-plane  $p$  orbitals will be seen and when  $E$  is parallel to the surface resonances (normal incidence) due to the in-plane  $s$  orbitals are dominant.



**Figure 1.29** Illustrative depictions of angular dependence of NEXAFS resonances for a lying-down benzene molecule adsorbed on surface. The  $p^*$  resonance is maximized at grazing incidence (left); the  $s^*$  is maximized at normal incidence (right).<sup>189</sup>

In an experiment, spectra are usually recorded at several different angles of X-ray incidence (ranging from grazing incidence to normal incidence), and the intensities are compared to reveal the orientation of molecules.

## References

- (1) Cai, Y. G.; Ocko, B. M. *Journal of the American Chemical Society* 2005, 127, 16287-16291.
- (2) Choi, J.; Lee, K.; Janes, D. B. *Nano Letters* 2004, 4, 1699-1703.
- (3) Schaper, C. D. *Nano Letters* 2003, 3, 1305-1309.
- (4) Loo, Y. L.; Lang, D. V.; Rogers, J. A.; Hsu, J. W. P. *Nano Letters* 2003, 3, 913-917.
- (5) Love, J. C.; Estroff, L. A.; Kriebel, J. K.; Nuzzo, R. G.; Whitesides, G. M. *Chemical Reviews* 2005, 105, 1103-1169.
- (6) Gates, B. D.; Xu, Q. B.; Stewart, M.; Ryan, D.; Willson, C. G.; Whitesides, G. M. *Chemical Reviews* 2005, 105, 1171-1196.
- (7) Leggett, G. J. *Chemical Society Reviews* 2006, 35, 1150-1161.
- (8) Smith, R. K.; Lewis, P. A.; Weiss, P. S. *Progress in Surface Science* 2004, 75, 1-68.
- (9) Thom, I.; Hahner, G.; Buck, M. *Applied Physics Letters* 2005, 87, 024101.
- (10) Azzaroni, O.; Schilardi, P. L.; Salvarezza, R. C. *Electrochimica Acta* 2003, 48, 3107-3114.
- (11) Schreiber, F. *Progress in Surface Science* 2000, 65, 151-256.
- (12) Ulman, A. *An Introduction to Ultrathin Organic Films*. Academic Press, 1991.
- (13) Senaratne, W.; Andruzzi, L.; Ober, C. K. *Biomacromolecules* 2005, 6, 2427-2448.
- (14) Tosatti, S.; Michel, R.; Textor, M.; Spencer, N. D. *Langmuir* 2002, 18, 3537-3548.
- (15) Spori, D. M.; Venkataraman, N. V.; Tosatti, S. G. P.; Durmaz, F.; Spencer, N. D.; Zurcher, S. *Langmuir* 2007, 23, 8053-8060.
- (16) Hofer, R.; Textor, M.; Spencer, N. D. *Langmuir* 2001, 17, 4014-4020.
- (17) Schonenberger, C.; Jorritsma, J.; Sondaghuethorst, J. A. M.; Fokkink, L. G. J. *Journal of Physical Chemistry* 1995, 99, 3259-3271.
- (18) Laibinis, P. E.; Whitesides, G. M.; Allara, D. L.; Tao, Y. T.; Parikh, A. N.; Nuzzo, R. G. *Journal of the American Chemical Society* 1991, 113, 7152-7167.
- (19) Meyers, R. A. *Encyclopedia of Analytical Chemistry* 1999, 1-26.
- (20) Heister, K.; Allara, D. L.; Bahnck, K.; Frey, S.; Zharnikov, M.; Grunze, M. *Langmuir* 1999, 15, 5440-5443.
- (21) Romeo, R.; Arena, G.; Scolaro, L. M.; Plutino, M. R.; Bruno, G.; Nicolo, F. *Inorganic Chemistry* 1994, 33, 4029-4037.
- (22) Fried, I.; Meyerste.D *Journal of Electroanalytical Chemistry* 1971, 29, 429-438.
- (23) Node, M.; Nishide, K.; Ochiai, M.; Fujii, K.; Fujita, E. *Journal of Organic Chemistry* 1981, 46, 5163-5166.
- (24) Dubois, L. H.; Zegarski, B. R.; Nuzzo, R. G. *Journal of the American Chemical Society* 1990, 112, 570-579.
- (25) Lu, P.; Walker, A. V. *Langmuir* 2007, 23, 12577-12582.
- (26) Arima, Y.; Iwata, H. *Journal of Materials Chemistry* 2007, 17, 4079-4087.
- (27) Gosvami, N.; Lau, K. H. A.; Sinha, S. K.; O'Shea, S. J. *Applied Surface Science* 2006, 252, 3956-3960.
- (28) Tyan, Y. C.; Liao, J. D.; Jong, S. B.; Liao, P. C.; Yang, M. H.; Chang, Y. W.; Klauser, R.; Himmelhaus, M.; Grunze, M. *Journal of Materials Science-Materials in Medicine* 2005, 16, 135-142.
- (29) Valiokas, R.; Klenkar, G.; Tinazli, A.; Reichel, A.; Tampe, R.; Piehler, J.; Liedberg, B.

- Langmuir* 2008, 24, 4959-4967.
- (30) Ciszek, J. W.; Keane, Z. K.; Cheng, L.; Stewart, M. P.; Yu, L. H.; Natelson, D.; Tour, J. M. *Journal of the American Chemical Society* 2006, 128, 3179-3189.
- (31) Albrecht, T.; Moth-Poulsen, K.; Christensen, J. B.; Guckian, A.; Bjor nholm, T.; Vos, J. G.; Ulstrup, J. *Faraday Discussions* 2006, 131, 265-279.
- (32) Tuccitto, N.; Torrisci, V.; Cavazzini, M.; Morotti, T.; Puntoriero, F.; Quici, S.; Campagna, S.; Licciardello, A. *Chemphyschem* 2007, 8, 227-230.
- (33) Auditore, A.; Tuccitto, N.; Marzanni, G.; Quici, S.; Puntoriero, F.; Campagna, S.; Licciardello, A. *Chemical Communications* 2003, 2494-2495.
- (34) Nuzzo, R. G. A., D. L. *J. Am. Chem. Soc.* 1983, 105, 4481.
- (35) Kramer, S.; Fuierer, R. R.; Gorman, C. B. *Chemical Reviews* 2003, 103, 4367-4418.
- (36) Schreiber, F. *Journal of Physics-Condensed Matter* 2004, 16, R881-R900.
- (37) Brogan, K. L.; Wolfe, K. N.; Jones, P. A.; Schoenfish, M. H. *Analytica Chimica Acta* 2003, 496, 73-80.
- (38) Rickert, J.; Weiss, T.; Kraas, W.; Jung, G.; Gopel, W. *Biosensors & Bioelectronics* 1996, 11, 591-598.
- (39) Bain, C. D.; Troughton, E. B.; Tao, Y. T.; Evall, J.; Whitesides, G. M.; Nuzzo, R. G. *Journal of the American Chemical Society* 1989, 111, 321-335.
- (40) Hahner, G.; Woll, C.; Buck, M.; Grunze, M. *Langmuir* 1993, 9, 1955-1958.
- (41) Himmelhaus, M.; Eisert, F.; Buck, M.; Grunze, M. *Journal of Physical Chemistry B* 2000, 104, 576-584.
- (42) Vanhove, M. A.; Koestner, R. J.; Stair, P. C.; Biberian, J. P.; Kesmodel, L. L.; Bartos, I.; Somorjai, G. A. *Surface Science* 1981, 103, 218-238.
- (43) Schneider, K. S.; Nicholson, K. T.; Fosnacht, D. R.; Orr, B. G.; Holl, M. M. B. *Langmuir* 2002, 18, 8116-8122.
- (44) Woll, C.; Chiang, S.; Wilson, R. J.; Lippel, P. H. *Physical Review B* 1989, 39, 7988-7991.
- (45) Narasimhan, S.; Vanderbilt, D. *Physical Review Letters* 1992, 69, 1564-1567.
- (46) Barth, J. V.; Brune, H.; Ertl, G.; Behm, R. J. *Physical Review B* 1990, 42, 9307-9318.
- (47) Yamada, R.; Uosaki, K. *Langmuir* 1997, 13, 5218-5221.
- (48) Xiao, X. D.; Wang, B.; Zhang, C.; Yang, Z.; Loy, M. M. T. *Surface Science* 2001, 472, 41-50.
- (49) Qian, Y. L.; Yang, G. H.; Yu, J. J.; Jung, T. A.; Liu, G. Y. *Langmuir* 2003, 19, 6056-6065.
- (50) C. Vericat, M. E. V. a. R. C. S. *Physical Chemistry Chemical Physics* 2005, 6, 568.
- (51) Poirier, G. E.; Fitts, W. P.; White, J. M. *Langmuir* 2001, 17, 1176-1183.
- (52) Darling, S. B.; Rosenbaum, A. W.; Wang, Y.; Sibener, S. J. *Langmuir* 2002, 18, 7462-7468.
- (53) Dubois, L. H.; Nuzzo, R. G. *Annual Review of Physical Chemistry* 1992, 43, 437-463.
- (54) Dubois, L. H.; Zegarski, B. R.; Nuzzo, R. G. *Journal of Chemical Physics* 1993, 98, 678-688.
- (55) Poirier, G. E. *Langmuir* 1997, 13, 2019-2026.
- (56) Camillone, N.; Chidsey, C. E. D.; Liu, G.; Scoles, G. *Journal of Chemical Physics* 1993, 98, 4234-4245.
- (57) Molina, L. M.; Hammer, B. *Chemical Physics Letters* 2002, 360, 264-271.
- (58) Kondoh, H.; Iwasaki, M.; Shimada, T.; Amemiya, K.; Yokoyama, T.; Ohta, T.; Shimomura, M.; Kono, S. *Physical Review Letters* 2003, 90, 066102.

- (59) Maksymovych, P.; Sorescu, D. C.; Yates, J. T. *Physical Review Letters* 2006, 97, 146103.
- (60) Yu, M.; Bovet, N.; Satterley, C. J.; Bengio, S.; Lovelock, K. R. J.; Milligan, P. K.; Jones, R. G.; Woodruff, D. P.; Dhanak, V. *Physical Review Letters* 2006, 97, 166102.
- (61) Wang, Y.; Hush, N. S.; Reimers, J. R. *Journal of the American Chemical Society* 2007, 129, 14532-14533.
- (62) Torrelles, X.; Vericat, C.; Vela, M. E.; Fonticelli, M. H.; Millone, M. A. D.; Felici, R.; Lee, T. L.; Zegenhagen, J.; Munoz, G.; Martin-Gago, J. A.; Salvarezza, R. C. *Journal of Physical Chemistry B* 2006, 110, 5586-5594.
- (63) Lussem, B.; Muller-Meskamp, L.; Karthaus, S.; Waser, R. *Langmuir* 2005, 21, 5256-5258.
- (64) Delamarche, E.; Michel, B.; Gerber, C.; Anselmetti, D.; Guntherodt, H. J.; Wolf, H.; Ringsdorf, H. *Langmuir* 1994, 10, 2869-2871.
- (65) Roper, M. G.; Skegg, M. P.; Fisher, C. J.; Lee, J. J.; Dhanak, V. R.; Woodruff, D. P.; Jones, R. G. *Chemical Physics Letters* 2004, 389, 87-91.
- (66) Li, B.; Zeng, C. G.; Li, Q. X.; Wang, B.; Yuan, L. F.; Wang, H. Q.; Yang, J. L.; Hou, J. G.; Zhu, Q. S. *Journal of Physical Chemistry B* 2003, 107, 972-984.
- (67) Riposan, A.; Liu, G. Y. *Journal of Physical Chemistry B* 2006, 110, 23926-23937.
- (68) Delamarche, E.; Michel, B.; Kang, H.; Gerber, C. *Langmuir* 1994, 10, 4103-4108.
- (69) Poirier, G. E.; Tarlov, M. J. *Journal of Physical Chemistry* 1995, 99, 10966-10970.
- (70) Ulman, A. *Chemical Reviews* 1996, 96, 1533-1554.
- (71) Walczak, M. M.; Chung, C. K.; Stole, S. M.; Widrig, C. A.; Porter, M. D. *Journal of the American Chemical Society* 1991, 113, 2370-2378.
- (72) Rong, H. T.; Frey, S.; Yang, Y. J.; Zharnikov, M.; Buck, M.; Wuhn, M.; Woll, C.; Helmchen, G. *Langmuir* 2001, 17, 1582-1593.
- (73) Ong, T. H.; Ward, R. N.; Davies, P. B.; Bain, C. D. *Journal of the American Chemical Society* 1992, 114, 6243-6245.
- (74) Evans, S. D.; Sharma, R.; Ulman, A. *Langmuir* 1991, 7, 156-161.
- (75) Kang, J. F.; Liao, S.; Jordan, R.; Ulman, A. *Journal of the American Chemical Society* 1998, 120, 9662-9667.
- (76) Kang, J. F.; Ulman, A.; Liao, S.; Jordan, R. *Langmuir* 1999, 15, 2095-2098.
- (77) Felgenhauer, T.; Rong, H. T.; Buck, M. *Journal of Electroanalytical Chemistry* 2003, 550, 309-319.
- (78) Felgenhauer, T.; Yan, C.; Geyer, W.; Rong, H. T.; Golzhauser, A.; Buck, M. *Applied Physics Letters* 2001, 79, 3323-3325.
- (79) Cyganik, P.; Buck, M. *Journal of the American Chemical Society* 2004, 126, 5960-5961.
- (80) Cyganik, P.; Buck, M.; Strunskus, T.; Shaporenko, A.; Wilton-Ely, J. D. E. T.; Zharnikov, M.; Woll, C. *Journal of the American Chemical Society* 2006, 128, 13868-13878.
- (81) Cyganik, P.; Buck, M.; Strunskus, T.; Shaporenko, A.; Witte, G.; Zharnikov, M.; Woll, C. *Journal of Physical Chemistry C* 2007, 111, 16909-16919.
- (82) Kafer, D.; Witte, G.; Cyganik, P.; Terfort, A.; Woll, C. *Journal of the American Chemical Society* 2006, 128, 1723-1732.
- (83) Cyganik, P.; Buck, M.; Wilton-Ely, J. D. E. T.; Woll, C. *Journal of Physical Chemistry B* 2005, 109, 10902-10908.
- (84) Cyganik, P.; Buck, M.; Azzam, W.; Woll, C. *Journal of Physical Chemistry B* 2004, 108,

- 4989-4996.
- (85) Zharnikov, M.; Frey, S.; Rong, H.; Yang, Y. J.; Heister, K.; Buck, M.; Grunze, M. *Physical Chemistry Chemical Physics* 2000, 2, 3359-3362.
- (86) Long, Y. T.; Rong, H. T.; Buck, M.; Grunze, M. *Journal of Electroanalytical Chemistry* 2002, 524, 62-67.
- (87) Lussem, B.; Muller-Meskamp, L.; Karthaus, S.; Homberger, M.; Simon, U.; Waser, R. *Journal of Physical Chemistry C* 2007, 111, 6392-6397.
- (88) Su, G. J. J.; Aguilar-Sanchez, R.; Li, Z. H.; Pobelov, I.; Homberger, M.; Simon, U.; Wandlowski, T. *Chemphyschem* 2007, 8, 1037-1048.
- (89) Zhang, J. D.; Chi, Q. J.; Ulstrup, J. *Langmuir* 2006, 22, 6203-6213.
- (90) Lin, H. Y.; Chen, H. A.; Lin, H. N. *Analytical Chemistry* 2008, 80, 1937-1941.
- (91) Lee, W.; Lee, D. B.; Oh, B. K.; Lee, W. H.; Choi, J. W. *Enzyme and Microbial Technology* 2004, 35, 678-682.
- (92) Sung, I. H.; Yang, J. C.; Kim, D. E.; Shin, B. S. *Wear* 2003, 255, 808-818.
- (93) Chena, F. C.; Lin, Y. K.; Ko, C. J. *Applied Physics Letters* 2008, 92, 023307.
- (94) Li, S. P.; Russell, D. M.; Newsome, C. J.; Kugler, T.; Shimoda, T. *Applied Physics Letters* 2006, 89, 122105.
- (95) Quist, A. P.; Pavlovic, E.; Oscarsson, S. *Analytical and Bioanalytical Chemistry* 2005, 381, 591-600.
- (96) Yan, X.; Yao, J. M.; Lu, G. A.; Chen, X.; Zhang, K.; Yang, B. *Journal of the American Chemical Society* 2004, 126, 10510-10511.
- (97) Sharpe, R. B. A.; Burdinski, D.; Huskens, J.; Zandvliet, H. J. W.; Reinhoudt, D. N.; Poelsema, B. *Journal of the American Chemical Society* 2005, 127, 10344-10349.
- (98) Geiger, G. *American Ceramic Society Bulletin* 1996, 75, 27-27.
- (99) Wu, X. S.; Jin, B. K.; He, P. S. *Chinese Journal of Chemical Physics* 2003, 16, 406-410.
- (100) Tolinski, M. *Plastics Engineering* 2005, 61, 14-16.
- (101) Jin, B. K.; Wu, X. S.; He, P. S.; Pan, L. J. *Chinese Journal of Polymer Science* 2003, 21, 303-308.
- (102) Deng, T.; Ha, S.; Thomas, E. L. *Abstracts of Papers of the American Chemical Society* 2002, 224, U462-U462.
- (103) Heule, M.; Gauckler, L. J. *Advanced Materials* 2001, 13, 1790-1793.
- (104) Kim, E.; Xia, Y. N.; Whitesides, G. M. *Journal of the American Chemical Society* 1996, 118, 5722-5731.
- (105) Dameron, A. A.; Hampton, J. R.; Smith, R. K.; Mullen, T. J.; Gillmor, S. D.; Weiss, P. S. *Nano Letters* 2005, 5, 1834-1837.
- (106) Choi, K. M.; Rogers, J. A. *Journal of the American Chemical Society* 2003, 125, 4060-4061.
- (107) Csucs, G.; Kunzler, T.; Feldman, K.; Robin, F.; Spencer, N. D. *Langmuir* 2003, 19, 6104-6109.
- (108) Michel, B.; Bernard, A.; Bietsch, A.; Delamarche, E.; Geissler, M.; Juncker, D.; Kind, H.; Renault, J. P.; Rothuizen, H.; Schmid, H.; Schmidt-Winkel, P.; Stutz, R.; Wolf, H. *Ibm Journal of Research and Development* 2001, 45, 697-719.
- (109) Kenseth, J. R.; Harnisch, J. A.; Jones, V. W.; Porter, M. D. *Langmuir* 2001, 17, 4105-4112.
- (110) Liu, G. Y.; Xu, S.; Qian, Y. L. *Accounts of Chemical Research* 2000, 33, 457-466.
- (111) Garno, J. C.; Yang, Y. Y.; Amro, N. A.; Cruchon-Dupeyrat, S.; Chen, S. W.; Liu, G. Y.

- Nano Letters* 2003, 3, 389-395.
- (112) Xu, S.; Liu, G. Y. *Langmuir* 1997, 13, 127-129.
- (113) Xu, S.; Miller, S.; Laibinis, P. E.; Liu, G. Y. *Langmuir* 1999, 15, 7244-7251.
- (114) Liu, G. Y.; Amro, N. A. *Proceedings of the National Academy of Sciences of the United States of America* 2002, 99, 5165-5170.
- (115) Sugimura, H.; Hanji, T.; Hayashi, K.; Takai, O. *Advanced Materials* 2002, 14, 524-526.
- (116) Sugimura, H.; Nakagiri, N. *Journal of the American Chemical Society* 1997, 119, 9226-9229.
- (117) Suez, I.; Rolandi, M.; Backer, S. A.; Scholl, A.; Doran, A.; Okawa, D.; Zettl, A.; Frechet, J. M. J. *Advanced Materials* 2007, 19, 3570-3573.
- (118) Lee, W.; Kim, E. R.; Lee, H. *Langmuir* 2002, 18, 8375-8380.
- (119) Maoz, R.; Frydman, E.; Cohen, S. R.; Sagiv, J. *Advanced Materials* 2000, 12, 725-731.
- (120) Piner, R. D.; Zhu, J.; Xu, F.; Hong, S. H.; Mirkin, C. A. *Science* 1999, 283, 661-663.
- (121) Salaita, K.; Wang, Y. H.; Mirkin, C. A. *Nature Nanotechnology* 2007, 2, 145-155.
- (122) Liu, J. F.; Miller, G. P. *Journal of Physical Chemistry C* 2007, 111, 10758-10760.
- (123) Jaschke, M.; Butt, H. J. *Langmuir* 1995, 11, 1061-1064.
- (124) Salaita, K.; Wang, Y. H.; Fragala, J.; Vega, R. A.; Liu, C.; Mirkin, C. A. *Angewandte Chemie-International Edition* 2006, 45, 7220-7223.
- (125) Lenhert, S.; Sun, P.; Wang, Y. H.; Fuchs, H.; Mirkin, C. A. *Small* 2007, 3, 71-75.
- (126) Huck, W. T. S. *Angewandte Chemie-International Edition* 2007, 46, 2754-2757.
- (127) Nelson, B. A.; King, W. P.; Laracuenta, A. R.; Sheehan, P. E.; Whitman, L. J. *Applied Physics Letters* 2006, 88, 033104.
- (128) Davis, J. J.; Coleman, K. S.; Busuttill, K. L.; Bagshaw, C. B. *Journal of the American Chemical Society* 2005, 127, 13082-13083.
- (129) Peter, M.; Li, X. M.; Huskens, J.; Reinhoudt, D. N. *Journal of the American Chemical Society* 2004, 126, 11684-11690.
- (130) Blackledge, C.; Engebretson, D. A.; McDonald, J. D. *Langmuir* 2000, 16, 8317-8323.
- (131) Ito, T.; Okazaki, S. *Nature* 2000, 406, 1027-1031.
- (132) Hutt, D. A.; Cooper, E.; Parker, L.; Leggett, G. J.; Parker, T. L. *Langmuir* 1996, 12, 5494-5497.
- (133) Totzeck, M.; Ulrich, W.; Gohnermeier, A.; Kaiser, W. *Nature Photonics* 2007, 1, 629-631.
- (134) Rubingh, R.; Moers, M.; Suddendorf, M.; Vanoppen, P.; Kisteman, A.; Thier, M.; Blahnik, V.; Piper, E. *Proceedings of SPIE-The International Society for Optical Engineering* 2005, 681-692.
- (135) Klerk, J. d.; Wagner, C.; Droste, R.; Levasier, L.; Jorritsma, L.; Setten, E. v.; Kattouw, H.; Jacobs, J.; Heil, T. *Proceedings of SPIE-The International Society for Optical Engineering* 2007, 65201Y1.
- (136) Betzig, E.; Trautman, J. K. *Science* 1992, 257, 189-195.
- (137) Sun, S. Q.; Chong, K. S. L.; Leggett, G. J. *Nanotechnology* 2005, 16, 1798-1808.
- (138) Montague, M.; Ducker, R. E.; Chong, K. S. L.; Manning, R. J.; Rutten, F. J. M.; Davies, M. C.; Leggett, G. J. *Langmuir* 2007, 23, 7328-7337.
- (139) Weimann, T.; Geyer, W.; Hinze, P.; Stadler, V.; Eck, W.; Golzhauser, A. *Microelectronic Engineering* 2001, 57-8, 903-907.
- (140) Zharnikov, M.; Geyer, W.; Golzhauser, A.; Frey, S.; Grunze, M. *Physical Chemistry*

- Chemical Physics* 1999, *1*, 3163-3171.
- (141) Zharnikov, M.; Frey, S.; Heister, K.; Grunze, M. *Langmuir* 2000, *16*, 2697-2705.
- (142) Muller, H. U.; Zharnikov, M.; Volkel, B.; Schertel, A.; Harder, P.; Grunze, M. *Journal of Physical Chemistry B* 1998, *102*, 7949-7959.
- (143) Golzhauser, A.; Geyer, W.; Stadler, V.; Eck, W.; Grunze, M.; Edinger, K.; Weimann, T.; Hinze, P. *Journal of Vacuum Science & Technology B* 2000, *18*, 3414-3418.
- (144) Volkel, B.; Kaltenpoth, G.; Handrea, M.; Sahre, M.; Nottbohm, C. T.; Kuller, A.; Paul, A.; Kautek, W.; Eck, W.; Golzhauser, A. *Surface Science* 2005, *597*, 32-41.
- (145) Geyer, W.; Stadler, V.; Eck, W.; Zharnikov, M.; Golzhauser, A.; Grunze, M. *Applied Physics Letters* 1999, *75*, 2401-2403.
- (146) Turchanin, A.; El-Desawy, M.; Golzhauser, A. *Applied Physics Letters* 2007, *90*, 053102.
- (147) Sondaghuethorst, J. A. M.; Vanhelleputte, H. R. J.; Fokkink, L. G. J. *Applied Physics Letters* 1994, *64*, 285-287.
- (148) Jung, Y. J.; La, Y. H.; Kim, H. J.; Kang, T. H.; Ihm, K.; Kim, K. J.; Kim, B.; Park, J. W. *Langmuir* 2003, *19*, 4512-4518.
- (149) <http://www.jeol.com/PRODUCTS/SemiconductorEquipment/ElectronBeamLithography/JBX5500FS/tabid/481/Default.aspx>.
- (150) Nishida, N.; Hara, M.; Sasabe, H.; Knoll, W. *Japanese Journal of Applied Physics Part 1-Regular Papers Short Notes & Review Papers* 1996, *35*, 5866-5872.
- (151) Shadnam, M. R.; Kirkwood, S. E.; Fedosejevs, R.; Amirfazli, A. *Langmuir* 2004, *20*, 2667-2676.
- (152) Balgar, T.; Franzka, S.; Hartmann, N.; Hasselbrink, E. *Langmuir* 2004, *20*, 3525-3527.
- (153) Chang, W.; Choi, M.; Kim, J.; Cho, S.; Whang, K. *Applied Surface Science* 2005, *240*, 296-304.
- (154) Bard, A. J.; Faulkner, L. R. *Electrochemical Methods*, 1981.
- (155) Kolb, D. M. *Angewandte Chemie-International Edition* 2001, *40*, 1162-1181.
- (156) Seo, K.; Borguet, E. *Journal of Physical Chemistry C* 2007, *111*, 6335-6342.
- (157) Zhang, J. D.; Demetriou, A.; Welinder, A. C.; Albrecht, T.; Nichols, R. J.; Ulstrup, J. *Chemical Physics* 2005, *319*, 210-221.
- (158) Ohgi, T.; Sheng, H. Y.; Dong, Z. C.; Nejoh, H.; Fujita, D. *Applied Physics Letters* 2001, *79*, 2453-2455.
- (159) Ohgi, T.; Sheng, H. Y.; Nejoh, H. *Applied Surface Science* 1998, *132*, 919-924.
- (160) Speets, E. A.; Dordi, B.; Ravoo, B. J.; Oncel, N.; Hallback, A. S.; Zandvliet, H. J. W.; Poelsema, B.; Rijnders, G.; Blank, D. H. A.; Reinhoudt, D. N. *Small* 2005, *1*, 395-398.
- (161) Choi, H. G.; Amara, J. P.; Swager, T. M.; Jensen, K. F. *Langmuir* 2007, *23*, 2483-2491.
- (162) Hsu, C. H.; Yeh, M. C.; Lo, K. L.; Chen, L. J. *Langmuir* 2007, *23*, 12111-12118.
- (163) Xia, Y. A.; Venkateswaran, N.; Qin, D.; Tien, J.; Whitesides, G. M. *Langmuir* 1998, *14*, 363-371.
- (164) Moran, C. E.; Radloff, C.; Halas, N. J. *Advanced Materials* 2003, *15*, 804-807.
- (165) Gilbert, S. E.; Cavalleri, O.; Kern, K. *Journal of Physical Chemistry* 1996, *100*, 12123-12130.
- (166) Schneeweiss, M. A.; Hagenstrom, H.; Esplandiu, M. J.; Kolb, D. M. *Applied Physics a-Materials Science & Processing* 1999, *69*, 537-551.
- (167) Ivanova, V.; Baunach, T.; Kolb, D. A. *Electrochimica Acta* 2005, *50*, 4283-4288.

- (168) Hugelmann, M.; Hugelmann, P.; Lorenz, W. J.; Schindler, W. *Surface Science* 2005, 597, 156-172.
- (169) Herrero, E.; Buller, L. J.; Abruna, H. D. *Chemical Reviews* 2001, 101, 1897-1930.
- (170) Jennings, G. K.; Laibinis, P. E. *Journal of the American Chemical Society* 1997, 119, 5208-5214.
- (171) Schneeweiss, M. A.; Kolb, D. M. *Physica Status Solidi a-Applied Research* 1999, 173, 51-71.
- (172) Toney, M. F.; Howard, J. N.; Richer, J.; Borges, G. L.; Gordon, J. G.; Melroy, O. R. *Physical Review Letters* 1995, 75, 4472-4475.
- (173) Shi, Z. C.; Lipkowsky, J. *Journal of Electroanalytical Chemistry* 1994, 365, 303-309.
- (174) Silien, C.; Buck, M. *Journal of Physical Chemistry C* 2008, 112, 3881-3890.
- (175) Jennings, G. K.; Laibinis, P. E. *Langmuir* 1996, 12, 6173-6175.
- (176) Epple, M.; Bittner, A. M.; Kuhnke, A.; Kern, K.; Zheng, W. Q.; Tadjeddine, A. *Langmuir* 2002, 18, 773-784.
- (177) Zhu, Z. H.; Daniel, T. A.; Maitani, M.; Cabarcos, O. M.; Allara, D. L.; Winograd, N. *Journal of the American Chemical Society* 2006, 128, 13710-13719.
- (178) Cavalleri, O.; Gilbert, S. E.; Kern, K. *Surface Science* 1997, 377, 931-936.
- (179) Hagenstrom, H.; Schneeweiss, M. A.; Kolb, D. M. *Langmuir* 1999, 15, 7802-7809.
- (180) Binnings, G.; Rohrer, H.; Gerber, C.; Weibel, E. *Physical Review Letters* 1982, 49, 57-61.
- (181) Bai, C. *Scanning Tunneling Microscopy and Its Application*; Springer, 2000.
- (182) <http://www.chemistry.uoguelph.ca/educmat/chm729/STMpage/stmtutor.htm>
- (183) Razavy, M. *Quantum Theory of Tunneling*; World Scientific, 2003.
- (184) Tersoff, J.; Hamann, D. R. *Physical Review B* 1985, 31, 805-813.
- (185) Chen, C. J. *Physical Review Letters* 1990, 65, 448-451.
- (186) Methivier, C.; Beccard, B.; Pradier, C. M. *Langmuir* 2003, 19, 8807-8812.
- (187) Anderson, M. R.; Evaniak, M. N.; Zhang, M. H. *Langmuir* 1996, 12, 2327-2331.
- (188) Hahner, G. *Chemical Society Reviews* 2006, 35, 1244-1255.
- (189) Stohr, J. *NEXAFS Spectroscopy*; Springer: Berlin, 1992.

## Chapter 2 Experimental Section

### 2.1 Substances and Sample Preparation

We use Au on silicon (Au/Si), which consists of a 100 nm gold film evaporated onto silicon with a 5 nm titanium interlayer to enhance Au adhesion. Mica substrates with an epitaxial Au(111) layer 300 nm thick were also used. These substrates were purchased from Georg Albert PVD, Germany. Since organic molecules from the environment are easily adsorbed onto the Au surfaces, which contaminate the Au surface, typically, two major pretreatments can be used: (1) exposure to a strong oxidant, including piranha solution and oxygen plasma. However, these treatments leave a surface oxide, which can affect the properties of SAMs. Another surface cleaning method is flame annealing, which is frequently used to clean the Au substrate. In this project, we use flame annealing for cleaning the surface of Au/Mica. Au/Si substrates were used as received. Figure 2.1 shows a Au(111) surface on a mica substrate after flame annealing.

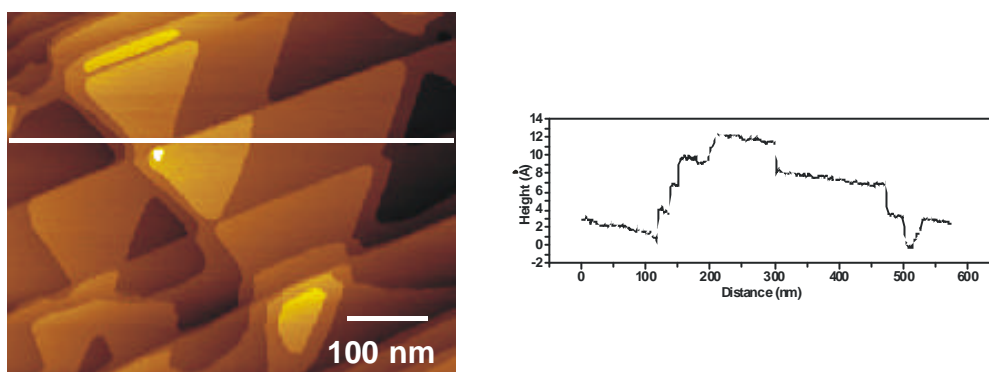


**Figure 2.1** STM image showing Au(111) on Mica surface. The line profile reveals Au steps, each step is about 2.5 Å.

Hexanethiol (96%) (MC6) was purchased from ACROS, undecanethiol (98%) (MC11), dodecanethiol (98%) (C12SH), mercaptoundecanoic acid (90%) (MUA) and mercaptohexadecanoic acid (90%) (MHA) were purchased from Aldrich. Tetradecanethiol (98%) (MC14) and octadecanethiol (95%) (MC18) were purchased from Fluka, dodecyl thiocyanate (97%) (C12SCN) as purchased from Alfa Aesar. All

biphenyl based thiols were available from a previous PhD work.<sup>1</sup> Bpp-SH and bpp-SCN were synthesized and provided by Marco Haryono and Andreas Grohmann, Berlin. Hexadecane (99%) was purchased from Aldrich and used as received. Ethanol (absolute) was analytical reagent grade (Fisher Scientific) and N,N-Dimethylformamide (DMF) was 99.9+% HPLC grade (Aldrich). Perylene-3,4,9,10-tetracarboxylic dianhydride (PTCDA) (> 98%, Aldrich) was used as received. Dodecane thiol was used as received, dodecyl thiocyanate was applied both as purchased and after purification. In the purification of C12SCN procedure (this work was done by James Wilton-Ely), one major peak was identified by UV (retention time 21.9 mins) with two minor but significant UV-active impurities (11.0 and 27.4 mins) present. A Dionex HPLC machine was used with a P60 pump with UVD 340V UV detector (UV at 240 nm) and a Phenomenex Jupiter 10  $\mu\text{m}$  Proteo 90 Å column, dimensions 250 x 21.2 mm, at a flow rate of 8 mL/min. Solvents: A = H<sub>2</sub>O, B = MeCN; t = 0, 40% A; t = 5, 40% A; t = 10, 0% A; t = 30, 100% A.

SAMs were prepared from either liquid or vapour phase. SAM solutions were prepared in ~ 1 mM concentration (unless mentioned otherwise) in ethanol solution (except mentioned) at various temperatures over night (see Fig. 2.2). After removal from the solution, samples were rinsed with pure ethanol and dried in a nitrogen stream.

Preparations from vapour phase were performed by putting a substrate into a vial (loaded with powder of respective thiol), and filling it with nitrogen before sealing tightly (see Fig.2.2).

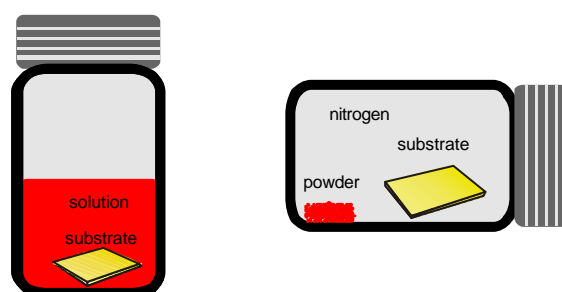


**Figure 2.2** Schematic illustration of SAMs preparation from solution and vapour phase.

For precoating with PTCDA the substrate was immersed into a saturated solution of

PTCDA in DMF for 5 minutes at room temperature. Due to the low solubility of PTCDA, this solution was prepared by ultrasound-assisted dissolution of PTCDA in DMF and use of the clear solution after sedimentation of solid PTCDA.

## 2.2 Laser system

For this research project, a pulsed laser was used to pattern SAMs.

A schematic of a 1064 nm Nd:Vanadate laser system (Model IC 138, High Q laser, Austria) is presented in Figure 2.3. Inside the IC 138 laser box are seed laser, regenerative amplifier, post amplifier crystals and Pockels cells.

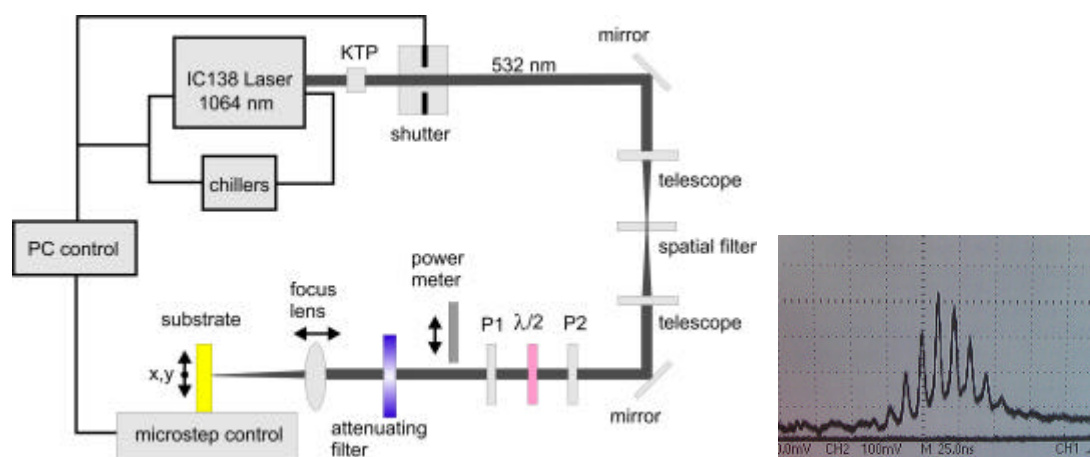


**Figure 2.3 (Left) Simplified diagram of laser scanning lithography (LSL) set up.** The microstepper controls the movement of the substrate in the XY plane, perpendicular to the laser beam. The energy used for LSL is measured by the power meter. The energy can be adjusted by rotating half-wave plate or polarizer P2. The laser beam was focused by a 0.5 cm focal length lens. The laser energy is attenuated before it is used for patterning. **(Right) Pulses train produced by the laser.**

The laser system used in this work is a special type of pulsed laser. Laser pulses are initiated at the seed laser. There are several amplifications and beam shaping steps before the laser beam passes through the aperture. The seed laser producing pulses with a 90 MHz frequency, which means it generates pulses (8-9 pulses here, each pulse has a different intensity.) every 11.1 nanoseconds. The beam is reflected by several mirrors

before it reaches the sample with a profile close to Gaussian distribution.

The laser beam can be switch on/off (pass/block) by a shutter, which is controlled by a computer programme (LABVIEW). Before the laser passes the shutter, its frequency is double by a KTP (Potassium Titanium Oxide Phosphate) crystal, which generates light of 532 nm from the 1064 nm of the laser. The microstepper controls the movement of the substrate sample in XY plane, perpendicular to the laser beam. The energy used for LSL is measured by the power meter before attenuating filters (neutral density glasses, Schott). The energy can be adjusted by rotating a half-wave plate. The laser beam is focused onto the substrate by a lens of 0.5 cm focal length.

Establishing the threshold for monolayer desorption involved a gradual reduction of the incident power from the damage threshold of the gold film until no desorption occurred. This was checked by performing electrochemical copper deposition onto a series of lines write at different laser power. As the laser energy varies from day to day, and the position of the focus of laser beam is judged by fixing it at a relative high energy which damages the surface, a series of patterns is always written at several energies to make sure the desired pattern is included in the series.

It is found that at faster scanning speed, higher laser energy is needed to damage the surface. It was also found that the threshold for monolayer desorption depended on the type of substrate. Higher energies are needed to desorb SAMs on Au/Mica substrate than that on Au/Si substrate.

Pattern definition was controlled by a LABVIEW Program. This program can write six kinds of patterns: (1) Zig-zag. (2) Single line. (3) Dashed lines. (4) Dash dot lines. (5) Lines with breaks. (6) Free definition. For example, 'lines with breaks' pattern can be defined by multiple rows of data.

***Format of data:***

***X-coordinate, x-speed, x-break, time-break, y-coordinate, y-speed, loops***

***500, 20, 20, t, 10, 50, 5***

***(t = 5, 10, 12, 14, 16, 18, 20, 25, 30, 35, 40, 45, 50, 55, 60)***

Here,  $x$ -coordinate is the total length of the line (micrometers); speed is typically 1-100  $\mu\text{m/s}$ .  $x$ -break is the length of dash while laser on. Time-break means laser off (ms).  $y$ -coordinate is the length of  $y$  coordinate. Loops define how often a single row of data is executed.

Continuous lines and zig-zag pattern were used to create passivation area.

***Format of data:***

***X-coordinate, x-speed, y-coordinate, y-speed, loops, laser on/off, sequence***

Laser on/off is defined by numbers from 0 to 3 (0 = laser off, 1 =  $x$  and  $y$  on, 2 =  $x$  on and  $y$  off, 3 =  $x$  off and  $y$  on). Sequence is also set by numbers from 0 to 3 (0 =  $x$  first, then  $y$ , 1 =  $x$  first, then  $y$ , 2 =  $x$  and  $y$  at the same time, 3 = *zig-zag*).

## **2.3 Electrochemistry**

In a three-electrodes cell as shown in Figure 2.4, the current passes between the working electrode (WE) and a counter electrode (CE). The potential of the working electrode is measured against a reference electrode (RE), most commonly on Ag/AgCl electrode. Cu wires can also be used as reference electrodes for electrochemical Cu deposition. The counter electrode can be made of any electrode material. However, it should be stable enough (no reaction or dissolution). A Pt wire is widely used. The device used to measure the potential difference between the working electrode and the reference electrode has a high input impedance so that only a very small current flows between reference and working electrodes.<sup>2</sup>

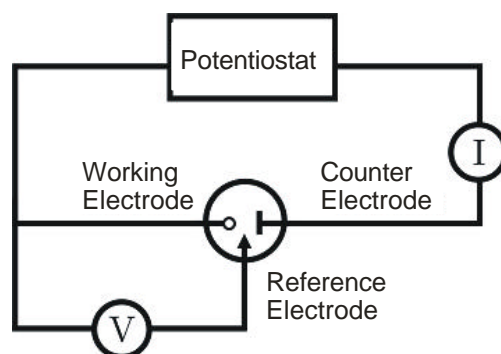


Figure 2.4 Sketch of a three-electrodes cell, which includes working, counter, and reference electrodes.<sup>2</sup>

To deposit Cu, we use either EG&G 283 potentiostat or Uniscan Instrument (model PG580) both controlled by a PC. Cu deposition on both bare Au surface (SAMs were removed by LSL) and patterned SAMs (after readsorption of another SAM) was accomplished in a three electrode cell with copper wires as counter electrode and reference electrode and 5 mM CuSO<sub>4</sub>/50 mM H<sub>2</sub>SO<sub>4</sub> electrolyte.

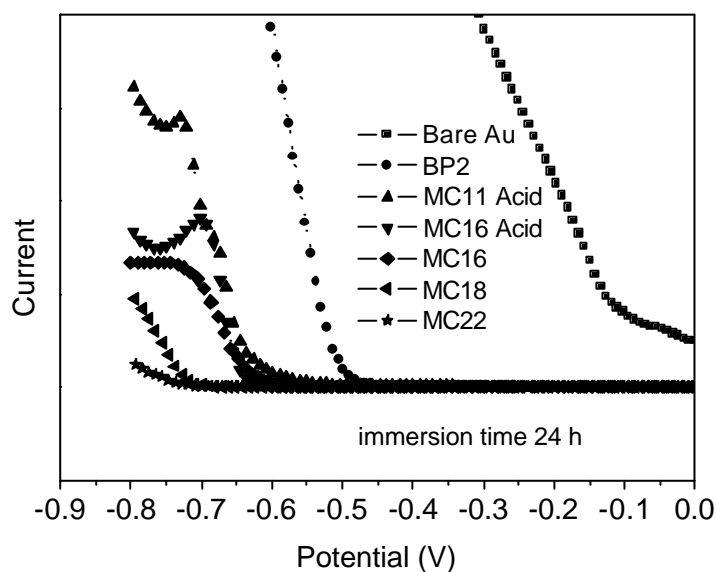


Figure 2.5 Linear sweep voltammograms for different SAMs on Au showing the onset of copper deposition in 5 mM CuSO<sub>4</sub>/50 mM H<sub>2</sub>SO<sub>4</sub> electrolyte. (Reference electrode: Cu wire).

Figure 2.5 shows linear sweep voltammograms for different SAMs on Au showing the onset for copper deposition. It was found that the initial copper deposition potential is different for different types of SAMs as the charge transfer rate is depending on the

chain length and molecular structures. For BP2, the initial copper deposition starts at about -0.45 V, while for the MC18, copper deposition occurs above -0.7 V. So, -0.48 V was chosen for selective deposition. Under such conditions, the copper only deposited on the regions covered by BP2, and not on the regions covered by MC18.

## 2.4 STM Measurements

STM measurements were carried out using a PicoPlus microscope (Molecular Imaging). STM images were recorded in constant current mode. All images are presented without filtering.

The STM measurements were carried out in three types of environments: in air, in organic solvent (hexadecane solution), and in water-based solutions (5 mM CuSO<sub>4</sub>/ 50 mM H<sub>2</sub>SO<sub>4</sub> electrolyte and 10 mM AuCl<sub>3</sub> electrolyte).

For experiments performed in air and hexadecane, cut tips were used. A teflon cell was used for experiments carried out in hexadecane solution.

For experiments performed in water-based solution, any influence of electrochemical currents at the tip must be avoided (typical electrochemical currents are of the order of  $\mu\text{A}$  or even higher, much too large to detect an underlying tunneling current down to nA or even pA). This is provided by a special tip coating which leaves merely the foremost part of the tip in contact with the liquid. The tip was first etched and then coated with hot glue, leaving only a small part of the apex uncovered. Such coated tip not only can be used as a tool for imaging, but also can be used a tool for manipulating (see section 4.4). In these experiments, patterns were first created by a coated tip using the PicoLITH programme, a commercial software from Molecular Imaging (see section 2.4.3). The same tip was then used to examine the surface during *in situ* metal deposition.

### 2.4.1 ECSTM Setup

Electrochemical scanning tunneling microscope (ECSTM) is designed to run in an electrochemical cell. It allows the *in situ* investigation of an electrochemical process. Figure 2.6 shows a set up model of an STM-tip dipped into an electrolyte-filled electrochemical cell. The probed sample (SAMs modified Au substrate) is the working electrode (WE). The reference electrode (RE) and the counter electrode (CE) ensure the control over electrochemical processes within the cell and at the working electrode surface. For the tunneling process a bias is applied between WE and the tip. Hence, the tip itself serves as a further electrode within the cell. This 4-electrode arrangement in the electrochemical cell is controlled by a bipotentiostat.

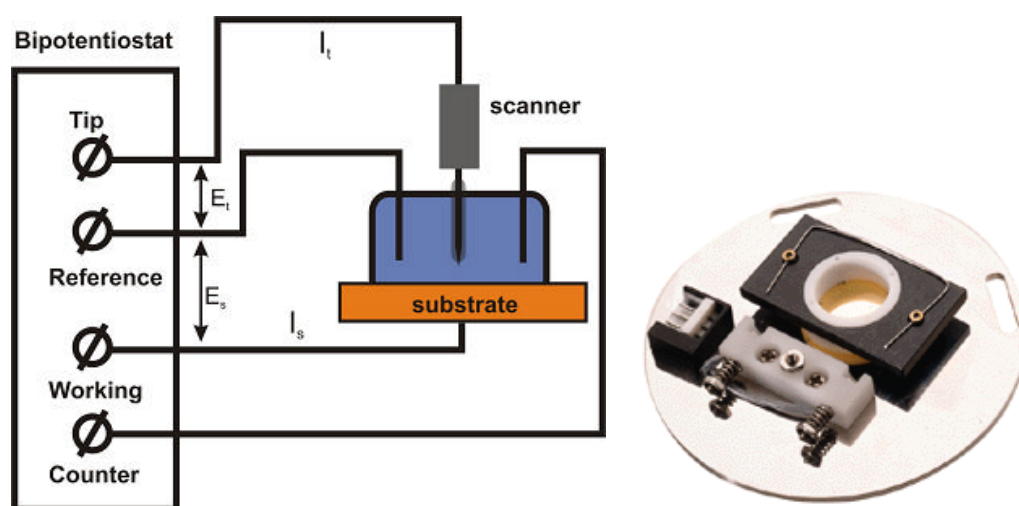


Figure 2.6 (a) Four-electrodes ECSTM set-up, the tip was etched and coated to minimize the leaking current. (b) Photograph of the electrochemical cell (Molecular Imaging).

Figure 2.7 shows the relationship between the probe potential (STM tip potential, TP), sample potential (SP), and sample bias (SB). The sample bias can be expressed by:

$$SB = SP - TP \quad (2 - 1)$$

Both TP and SP are referenced to reference electrode. In the experiments, SP is used to control the reaction at the SAM surface. For example, by changing SP from positive to negative, Cu can be deposited on the sample surface. Pulsing option can be used to control the deposition time (from 0.1 to 1000 seconds).

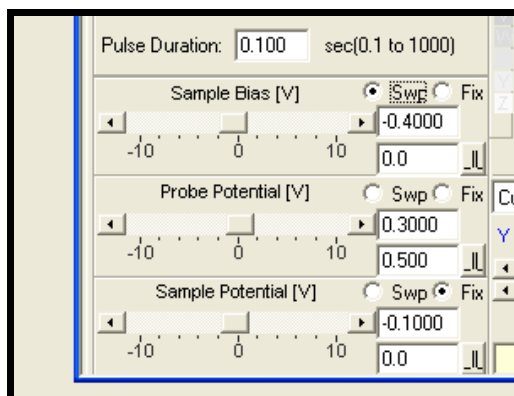


Figure 2.7 Window panel allowing control of potentials in ECSTM.

## 2.4.2 STM Tip Preparation

Tips were mechanically cut and electrochemically etched from a 0.25 mm Pt/Ir wire (8:2, Goodfellow). For the former, the tips are usually shaped by cutting the wire while pulling. The idea here is that the wire breaks apart the tip never touches the cutter, possible contamination of the tip is prevented. For the later, it is done by AC-etching the Pt/Ir wire in a 0.6 M KOH/2 M KSCN solution.<sup>3,4</sup> A Variac is set to about 7 V to etch the tip until the wire break into two parts. By electrochemically etching, one can get a sharp tip, which makes the coating easier. Figure 2.8 shows the cut, etched and coated tips.

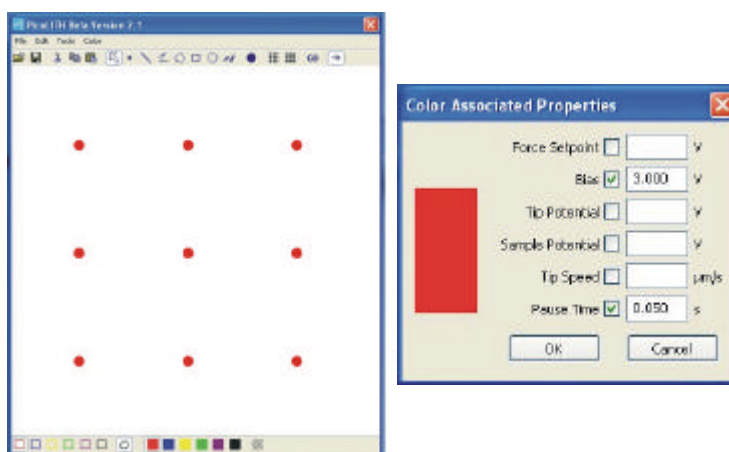


Figure 2.8 Optical micrographs of cut, etched and coated tips used for STM and ECSTM (coated tip) .

## 2.4.3 PicoLITH

PicoLITH is a software package that is integrated into the PicoScan software. It provides users with the tools necessary to perform lithography using an AFM or STM

tip. In STM mode, it defines bias, tip speed and pause time (the temporal duration that the tip remains at a point object) parameters to control the lithography. Patterns can be designed as lines, dots, or even more complicated patterns. Figure 2.9 shows an example of nine dots programmed by PicoLITH software.



**Figure 2.9** Nine dots are programmed by PicoLITH software. Parameters such as bias, tip speed, and pause time are used to control the shape of desired pattern.

## 2.5 XPS and NEXAFS Measurements

XPS and NEXAFS measurements and data evaluation were done through collaborations by Michael Zharnikov, Tobias Weidner, and Nirmalya Ballav. Information is provided here as results are part of the interpretation of systems. The XPS and NEXAFS measurements of C<sub>12</sub>SH, C<sub>12</sub>SCN (Michael Zharnikov and Tobias Weidner) and MUA (Michael Zharnikov and Nirmalya Ballav) were performed under UHV conditions (a base pressure  $< 1.5 \times 10^{-9}$  mbar) at the HE-SGM beamline of the synchrotron storage ring BESSY II in Berlin, Germany. The XPS spectra were acquired with a VG CLAM 2 analyzer in normal emission geometry. The energy resolution was  $\approx 0.4$  eV. The energy scale was referenced to the Au 4f<sub>7/2</sub> peak at a binding energy (BE) of 84.0 eV.<sup>5</sup> The spectra were fitted by symmetric Voigt functions and a Shirley-type background. To fit the S 2p<sub>3/2,1/2</sub> doublet, we used two peaks with the same full width at half-maximum (fwhm), the standard spin orbit splitting of  $\sim 1.18$  eV (verified by fit), and a branching ratio of 2 (S2p<sub>3/2</sub>/S2p<sub>1/2</sub>). The fits were performed self-consistently: the same fit parameters were used for identical spectral regions.

The acquisition of the NEXAFS spectra was carried out at the carbon *K*-edge in the partial electron yield mode with a retarding voltage of  $-150$  V. Linear polarized synchrotron light with a polarization factor of  $\approx 82\%$  was used. The incidence angle of the light was varied from  $90^\circ$  (*E*-vector in the surface plane) to  $20^\circ$  (*E*-vector nearly normal to the surface) in steps of  $10^\circ$ – $20^\circ$  to monitor the orientational order of the molecules within the films. This approach is based on the linear dichroism in X-ray absorption, i. e. the strong dependence of the cross-section of the resonant photoexcitation process on the orientation of the electric field vector of the linearly polarized light with respect to the molecular orbital of interest.<sup>6</sup> The raw NEXAFS spectra were normalized to the incident photon flux by division through a spectrum of a clean, freshly sputtered gold sample. The energy scale was referenced to the pronounced  $\pi_1^*$  resonance of highly oriented pyrolytic graphite (HOPG) at  $285.38$  eV.<sup>7</sup>

Thickness of MUA samples was determined from comparing the (C 1s/Au 4f) intensity ratio of MUA/Au samples with the analogous value for reference samples (MC12/Au, and MC16/Au).

## 2.6 IRRAS Measurements

Infrared reflection absorption spectroscopy (IRRAS) measurements were performed with a dry-air-purged Digilab FTS 7000 series spectrometer, equipped with polarization modulation (PM) and a liquid-nitrogen-cooled midband mercury cadmium telluride (MCT) detector. Spectra were acquired at a resolution of  $2\text{ cm}^{-1}$ , and 5 scans were accumulated in the PM mode.

## 2.7 Contact Angle Measurements

Equilibrium contact angle measurement was carried out with a KRUSS G10 contact angle goniometer. The contact angles were measured at different points on the surface with  $\text{H}_2\text{O}$  and the mean value was used.

## References:

- (1) Rong, H. T.; Frey, S.; Yang, Y. J.; Zharnikov, M.; Buck, M.; Wuhn, M.; Woll, C.; Helmchen, G. *Langmuir* 2001, 17, 1582-1593.
- (2) Bard, A. J.; Faulkner, L. R. *Electrochemical Methods*, 1981.
- (3) Xiao, X. Y.; Berenz, P.; Baltruschat, H.; Sun, S. *Journal of Electroanalytical Chemistry* 2001, 500, 446-452.
- (4) Sugimasa, M.; Inukai, J.; Itaya, K. *Journal of Electroanalytical Chemistry* 2003, 554, 285-291.
- (5) Moulder, J. F. S., W. E.; Sobol, P. E.; Bomben, K. D. *Handbook of X-ray Photo-electron Spectroscopy*; Perkin-Elmer Corp., 1992.
- (6) Stöhr, J. *NEXAFS Spectroscopy*; Springer-Verlag: Berlin, 1992.
- (7) Batson, P. E. *Physical Review B* 1993, 48, 2608-2610.

## Chapter 3 Self-assembled Monolayers as Templates for Micro/Nano Fabrication

### 3.1 Introduction

There are several methods for patterning a SAM-coated surface as mentioned in chapter 1.3. Here, laser lithography was applied as it has the advantage that it is an excellent tool for precise localized heating.<sup>1</sup> It can activate or accelerate endothermic chemical reactions.<sup>2</sup> The approach is a direct writing (the desired pattern is formed by the relative movement of laser beam and sample), noncontact lithography. Compared to electron beam and focused ion beam techniques, laser surface patterning has the advantage of simple setup, fast speed direct writing and large area processing,<sup>3</sup> while at the same time maintaining a sub-micro meter resolution.<sup>4,5</sup>

The gold-sulfur bond is unstable at elevated temperatures, causing a SAM to desorb.<sup>6</sup> It was observed that complete desorption of octadecanethiol adsorbed on Au(111) occurs at about 450 K, indicating that the Au-S bond is cleaved. The activation energy is reported to be 32 kcal/mol.<sup>7</sup> It is hence expected that localized heating of SAMs can break up the Au-S bond and produce bare regions of gold through thermal desorption. These bare gold regions can then be covered with a different type of thiol to modify the surface structure and properties, such as wetting or charge transfer.

Desorption of SAM by laser irradiation has been described as a thermal process.<sup>8</sup> Energy is absorbed by the substrate and provides a localized high temperature, which causes desorption of the SAM. This chapter reports on laser-induced desorption as a technique to pattern SAMs which are subsequently used as templates for metal electrodeposition. In contrast to this traditional way which uses the laser as a destructive/damaging tool, we found out that properly adjusted laser irradiation can also induce an opposite thermal effect, that is defects are annealed, thus making SAMs more resistant against metal deposition.

In the last part of this chapter, we demonstrate that superhydrophobic surfaces can be

fabricated by metal deposition onto patterned SAMs.

## 3.2 Laser Scanning Lithography

### 3.2.1 STM Investigation of Laser-Patterned Surfaces

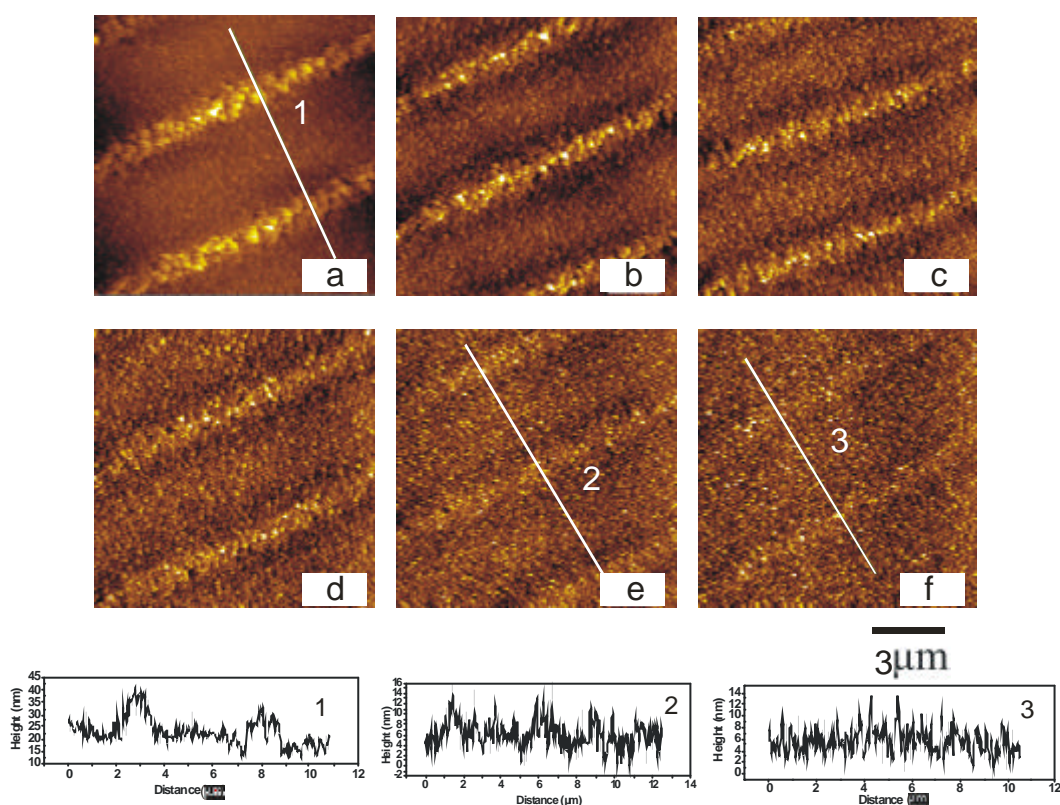


**Figure 3.1** STM images of MC18/Au/Si surfaces after LSL. (a) 7.0 mW, line width  $\sim 1.6 \mu\text{m}$ ; (b) 6.5 mW, line width  $\sim 1.4 \mu\text{m}$ ; (c) 6.0 mW, line width  $\sim 1.2 \mu\text{m}$ ; (d) 5.5 mW, line width  $\sim 1.1 \mu\text{m}$ ; (e) 5.0 mW, line width  $\sim 1.0 \mu\text{m}$ ; (f) 4.5 mW, line width  $\sim 0.8 \mu\text{m}$ . The cross section analysis of 1, 2, and 3 correspond to lines shown in (a), (e), and (f), respectively. STM tunneling parameters: 0.05 nA, 1.0 V. (power after filters: 0.48%).

A pulsed laser as described in Chapter 2 was used to pattern SAMs. A MC18/Au/Si substrate was used for patterning. The laser power was adjusted from 7 mW to 4.5 mW, with a step of  $-0.5 \text{ mW}$ . Lines were written at a spacing of  $5 \mu\text{m}^*$ . Figure 3.1 shows STM images of a MC18/Au/Si surface after laser irradiation. From (a) to (f), the power used

\* For experimental setup, see section 2.2.

for patterning was decreased from 7.0 mW<sup>#</sup> to 4.5 mW in steps of 0.5 mW. It was found that at a moderate laser power of 7.0 mW, materials (Au and Si) on the surface were not removed. On the contrary, they protruded from the surface by about 10 nm higher. With decreasing power, the high contrast also decreases. It was found that the width of the line decreased from 1.6 to 0.8  $\mu\text{m}$  as the power decreased from 7.0 mW to 4.5 mW, showing that the surface modification is very sensitive to the laser power. The fact that protrusions were seen instead of depressions (etch)<sup>4</sup> is due to the low power used for patterning, which is not sufficient to remove Au/Si material. The sudden increase in temperature causes expansion in the irradiated area, thus forming a loose structure on the surface.

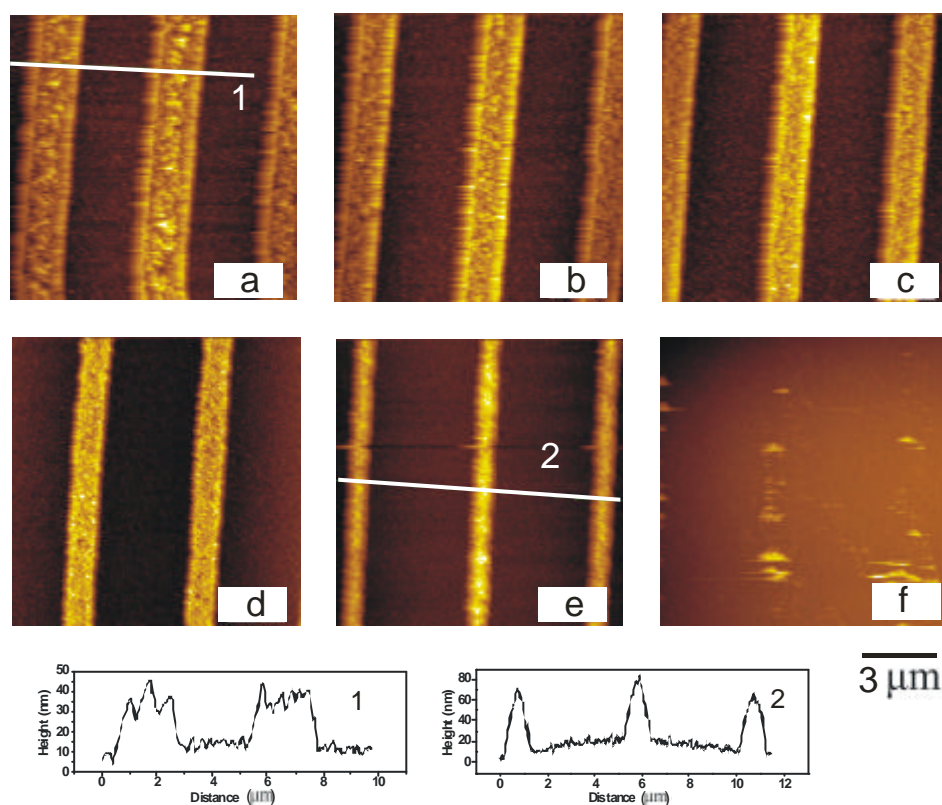


**Figure 3.2** STM images of copper deposited onto LSL areas, irradiated at different powers as shown in Figure 3.1. (a) 7.0 mW, line width  $\sim 1.9 \mu\text{m}$ ; (b) 6.5 mW, line width  $\sim 1.7 \mu\text{m}$ ; (c) 6.0 mW, line width  $\sim 1.4 \mu\text{m}$ ; (d) 5.5 mW, line width  $\sim 1.2 \mu\text{m}$ ; (e) 5.0 mW, line width  $\sim 0.9 \mu\text{m}$ ; (f) 4.5 mW, no visible lines. Copper deposition:  $-0.4 \text{ V}$  for 20 seconds. The cross section analysis of 1 and 2 corresponds to lines shown in (a) and (e), respectively. STM tunneling parameters: 0.05 nA, 1.0 V. (power after filters: 0.48%).

<sup>#</sup> Power used is measured before attenuating filters (neutral density glasses). Also, as the area of irradiation is difficult to calculate, power instead of power density was used.

Figure 3.2 shows Cu patterns formed after Cu deposited on the modified areas as shown in Figure 3.1. The copper line width from (a) to (e) is 1.9, 1.7, 1.4, 1.2 and 0.9  $\mu\text{m}$  respectively, which corresponds well to the patterns shown in Figure 3.1, thus, indicating that the copper deposition has a good confinement, i.e., Cu only deposits onto the damaged areas. The smallest copper lines created were about 900 nm wide as shown in (e) with an laser power of 5.0 mW. If the laser power is decreased down to 4.5 mW, no copper lines were seen anymore. However, this does not mean that there is no deposition as deposited Cu can be swept away by the STM tip. Although Cu can be deposited on the partially damaged SAMs covered area, they are not bond tightly to the Au surface and under STM scanning, can be swept away. This will be addressed in more detail in Chapter 4.

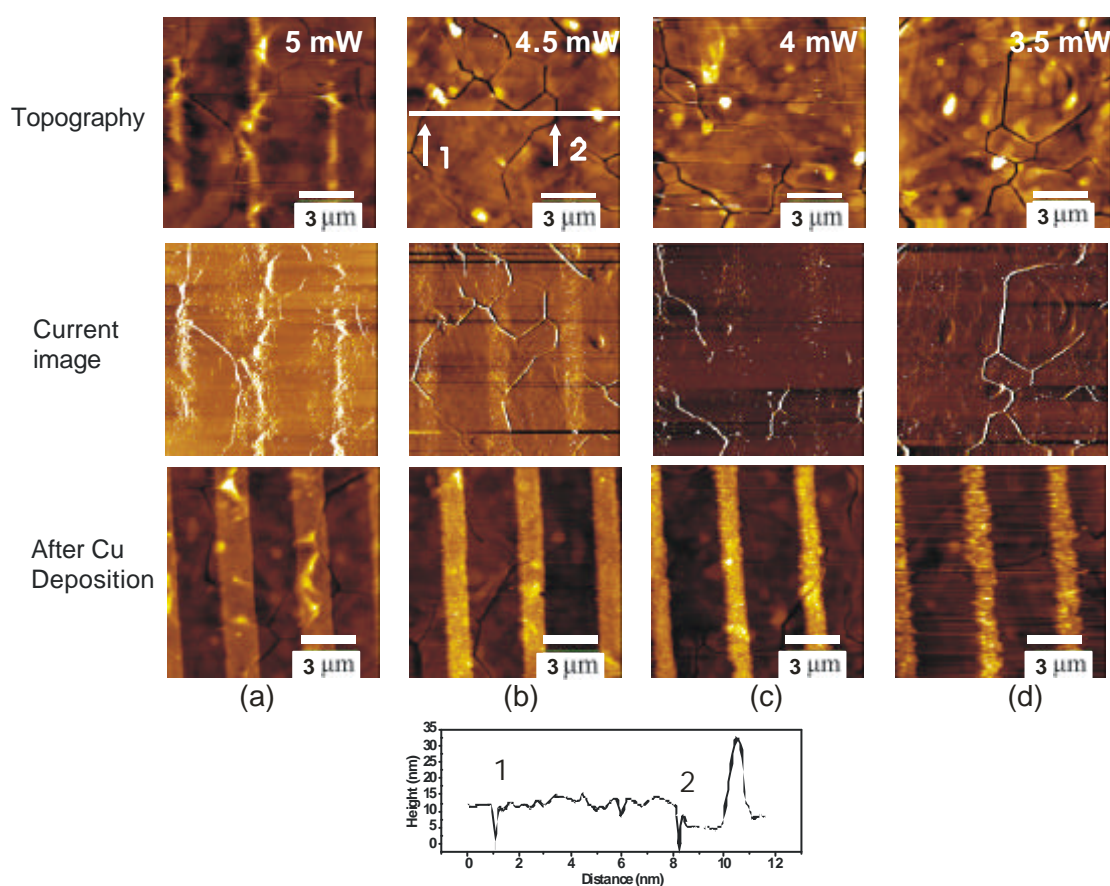


**Figure 3.3** STM images of MC11/Au/mica surfaces irradiated at different powers before (row 1) and after copper deposition (row 3). (a) 5.0 mW, line width (after copper deposition)  $\sim 1.8 \mu\text{m}$ ; (b) 4.5 mW, line width  $\sim 1.4 \mu\text{m}$ ; (c) 4.0 mW, line width  $\sim 1.1 \mu\text{m}$ ; (d) 3.5 mW, line width  $\sim 0.9\text{-}1.1 \mu\text{m}$ . Cross section analysis correspond to the line shown in (b). Copper deposition:  $-0.35 \text{ V}$  for 10 seconds. STM tunneling parameters: 0.1 nA, 1.0 V. (power after filters: 0.96%).

Surfaces of Au/Si are rough and molecular resolution structures are difficult to image on this kind of substrate. Therefore, patterning Au/Mica surfaces which are atomically flat can help us to obtain more information. Figure 3.3 shows patterns created on the surface of MC11/Au/Mica. The first row shows the STM topography images of the surface, which were imaged after laser scanning (before Cu deposition). The second row shows the corresponding current images. The third row shows the deposition of copper lines after electro deposition. The lines formed from (a) to (d) were patterned by varying the laser power from 5 mW to 3.5 mW, in decreasing steps of 0.5 mW. It was found that at 5 mW, the power is high enough to change the topography of the surface as shown in Figure 3.3(a). The topography and current images all show clearly the pattern lines. When the power was reduced to 4.5 mW, the pattern lines were invisible in the topography image; however, the current image clearly showed the pattern lines. Given that the STM is operated under constant current mode, no contrast in the current image should be seen. However, since the scanning speed is fast (2334 nm/s), and since the conduction inside the patterned area differs after irradiation (laser irradiation results in inhomogeneous structures, i.e. SAM partial damage, see Fig. 3.4), the feedback loop does not respond fast enough, thus the pattern can be seen. For the lines patterned at 3.5 mW, both topography and current images did not show the pattern lines. However, after copper deposition, thin copper lines still can be formed on the surface, showing that the laser still cause damage to the SAMs.

The reason why damage lines are not seen from the topography images might be due to the surface roughness of Au/Mica substrates. Au/Mica can have atomic flat surface in sub-micro/nano area. However, in large area (e.g. 10  $\mu\text{m}$  as shown in Fig. 3.3), they are significantly rougher than Au/Si substrates as shown in Fig. 3.1.

It is also interesting to note that the grain boundaries (see Fig. 3.3(b), marked as 1 and 2) do not have higher nucleation under electrochemical Cu deposition, although the depth of such depressions is about 10 nm.

To have a better understanding of the mechanism, we zoom into the lines. Figure 3.4 shows the irradiation area of Figure 3.3(b) at higher magnification. It was found that the

SAM was severely altered upon laser irradiation. However, there were still some patches of SAM with a striped structure remaining on the surface.<sup>9-11</sup> The space of these stripe structures is about 1.6 nm. Thus it is believed to be the lying down phase.

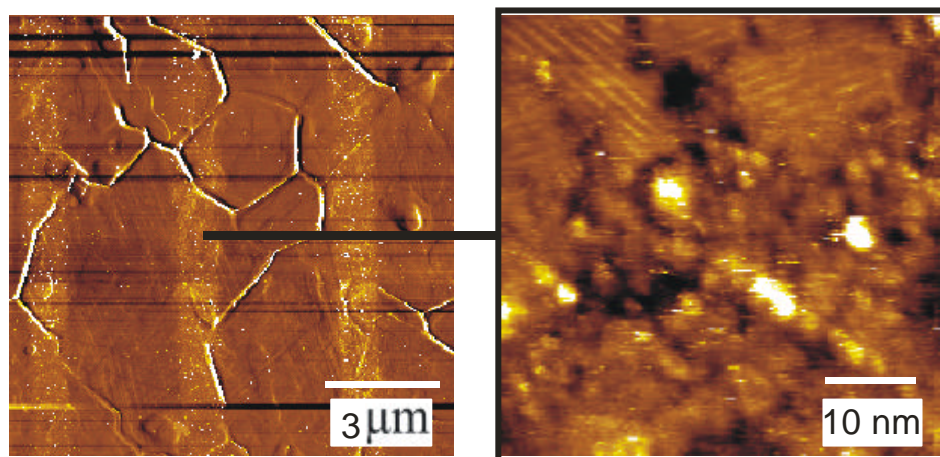


Figure 3.4 STM images showing area irradiated at laser power of 4.5 mW. Most of the molecules on the irradiated area were altered. However, some structures remained on the surface. (power after filters: 0.96%)

### 3.2.2 LSL Repeatability

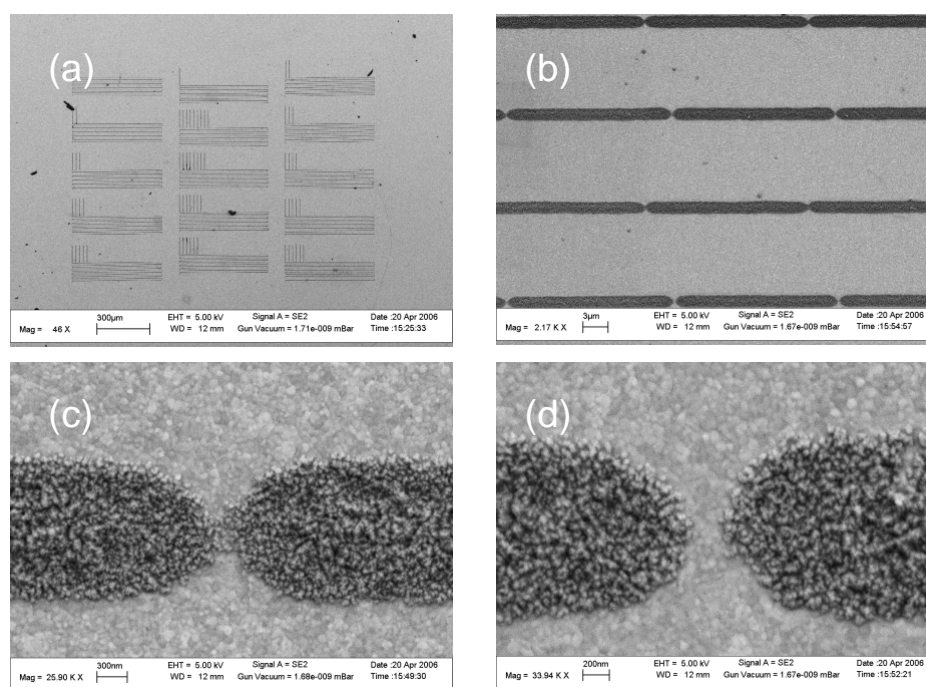


Figure 3.5 SEM image of laser irradiated MC18/Si sample after copper deposition (-0.3 V for 20 seconds). (a) An overview of patterns with different gap time break; (b) A pattern with a time break of 45 ms (gap vary from 0 to 0.2 μm). (c) and (d) show gap variations.

To explore how small structures can be generated by laser lithography, we wrote lines separated by a gap as shown in Figure 3.5. The gap distance can be adjusted by changing the time break during the writing of these lines as described in Chapter 2. However, there is some variation of the gap distance even under the same parameters (the same writing speed and the same break time). Figure 3.5 shows SEM images of a laser irradiated MC18 sample after copper deposition. (a) shows 15 patterns written by varying the gap distance; (b) shows a pattern written by a time break of 45 ms at speed of  $20\mu\text{m/s}$ . It was found that the gap vary from 0 to  $0.2\mu\text{m}$  as shown in (c) and (d).

From SEM, it was clear that the gap width varies from line to line. Even on the same line, gap distances vary. It was also found that all gap distances are smaller than the calculated from the parameters as shown in Table 3.1. There are several factors affecting the precision of the patterning. First, the laser scanning speed. As mentioned in chapter 2, the higher the speed, the higher the power is needed to desorb SAM, which means the laser can still damage the surface due to thermal diffusion even when the shutter was switched off. Second, it is also possible that during Cu deposition, Cu particles grow outwards and close the gap. Third, mechanical precision of the microstepper and the stability of the shutter also cause variations.

**Table 3.1 Relation between gap distances and time break**

Laser moving speed: $20\mu\text{m/s}$		
Time break (s)	Gap in theory ( $\mu\text{m}$ )	Gap in experiment ( $\mu\text{m}$ )
$t \leq 40$	0.8 or below	No gap (connected)
$t = 45$	0.9	0 to 0.2
$t = 50$	1.0	0.2 to 0.5
$t = 55$	1.1	0.3 to 0.5
$t = 60$	1.2	0.5 to 0.6

### 3.2.3 Lift Off

For applications as electrodes the metal patterns have to be transferred to an insulating surface. The presence of SAMs dramatically reduce adhesion between substrate and deposited metals.<sup>12</sup> Thus, deposited patterns can be transferred to an insulating substrate.<sup>13</sup> We prepared samples of MC18 SAM, exposed it to laser irradiation to selectively remove molecules, and finally immersed the sample into BP2 solution. After 30 minutes, the substrate was removed from the solution, rinsed with ethanol, and blown dry with nitrogen. A patterned SAM is then obtained as shown in Figure 3.6 (A).

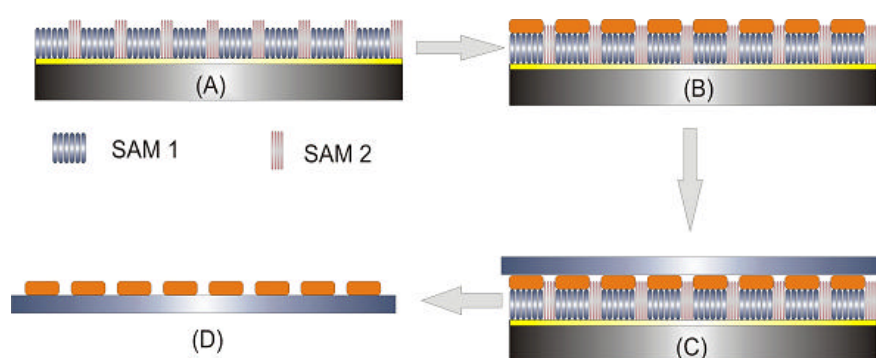


**Figure 3.6** Fabrication scheme of metal structures by electrochemical metal deposition and lift off. (A) A gold surface modified by a patterned SAMs. (B) Selective deposition of copper. (C) The deposited metal structure is adhered to an insulator. (D) Cu structure is detached from the substrate.

After electrochemical deposition ( $-0.3$  V for 20 s), the sample was removed from the cell, rinsed with copious amounts of de-ionized water, and blown dry with nitrogen. Transfer of the copper pattern to a glass slide was achieved by using cyanoacrylate adhesive. The whole procedure is shown in Figure 3.6(B) to (D).

Figure 3.7 shows the optical micrograph of Cu pattern on a glass produced by selective copper deposition and lift off according to the scheme shown in Figure 3.6. Copper lines are about  $10\ \mu\text{m}$  long and  $1.5\ \mu\text{m}$  wide. It was found that the transfer is complete since SAMs served as an antiadhesion layer. It was also found that some copper particles (marked by circles in Figure 3.7) were present beside the copper pattern. They were produced during copper deposition from defect sites in MC18, which were less blocking and thus were more prone to copper deposition.

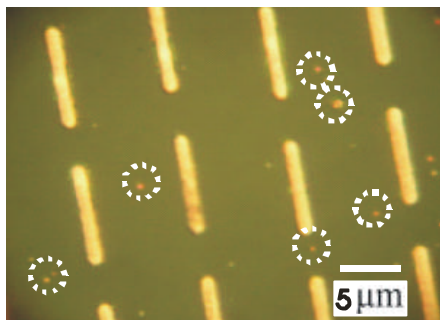


**Figure 3.7** Optical micrograph showing copper lines on a glass produced by selective copper deposition and lift off. Unwanted copper particles deposited are marked by circles.

### 3.2.4 Conclusion

Laser scanning lithography was used to pattern SAM modified Au surfaces. With this technique, localized molecules on the substrate are desorbed during laser irradiation. Thermal desorption occurs as a result of the large temperature rise produced by the laser. STM images show that after laser lithography, SAMs are altered and some molecules remain on the surface in a laying down phase. It was found that the surface is very sensitive to the laser power (variation of about 10% can cause Cu deposition and non-deposition). The minimum line width that can be produced by LSL is about 900 nm. There is still room to improve the resolution as the resolution is determined by the laser spot size, which depends on the focus system. Compared with other patterning technologies such as electron beam lithography, laser patterning has the advantage of simple setup, direct writing, and large area processing.

## 3.3 Laser-Induced Passivation

### 3.3.1 Introduction

Fabrication of smaller and more efficient structures in electronic and spintronic devices depends on better dielectric materials for nanofabrication. One approach is the use of SAMs, which can be well-ordered and thus are of interest as ultrathin dielectrics. SAMs have the potential to be used as ultrathin insulating layers in electronic elements, providing an alternative to commonly used oxide dielectrics such as  $\text{SiO}_2$  or  $\text{Al}_2\text{O}_3$ .<sup>14</sup>

The structures of SAMs are generally regarded as if they contained few defects. Yet, they are substantially more complex than commonly assumed as discussed in Chapter 1.<sup>15,16</sup> For many SAM applications, the quality of SAMs prepared under normal conditions (immersion at room temperature over night) is enough, but for others defects are a problem and the control of SAMs quality is a crucial point. Typical fields where high-quality SAMs are required are in electronics,<sup>17-25</sup> spintronics<sup>26,27</sup> and electrochemistry.<sup>28</sup>

In this section, we demonstrate that SAMs can become more passivating by irradiation at an appropriate laser power. This irradiation result in a more blocking behavior upon electrochemical deposition. Such blocking effect is believed to result from a reduction of defects. We propose that this effect is caused by thermal effect, which produces liquid phase SAMs on gold surface.

### 3.3.2 Passivation Effect

During LSL process, we observed the formation of passivated region adjacent to the patterned areas, i.e., an enhanced blocking behavior upon electrochemical metal deposition.

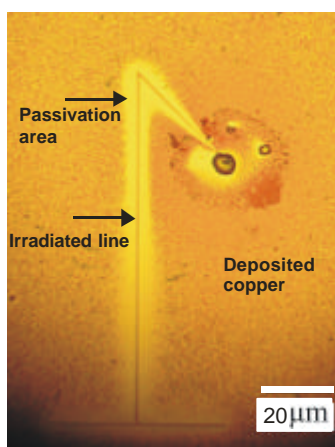


**Figure 3.8** Optical micrography of a pattern “1” written on MC18/Au/Mica by power of 4.0 mW with a speed of 50  $\mu\text{m/s}$ , followed by copper deposition at -0.3 V for 40 seconds. Passivation area can be identified near the pattern line. (power after filters: 0.96%).

This effect is illustrated in Figure 3.8 which shows an optical micrograph of a pattern

“1” written on a MC18/Au/Mica surface by laser and subsequently developed by copper deposition. The line width of the pattern “1” is about 1.2  $\mu\text{m}$ , and an extension of about 3-6  $\mu\text{m}$  passivation area can be easily spotted near the pattern, where no copper particles were found. One might argue that this is due to depletion of  $\text{Cu}^{2+}$  during electrodeposition process as the copper concentration reduces significantly near the pattern line (SAMs had been destroyed after the laser patterning). However, this was ruled out (see section 3.3.3) since passivation lines can be created by adjusting the laser power.

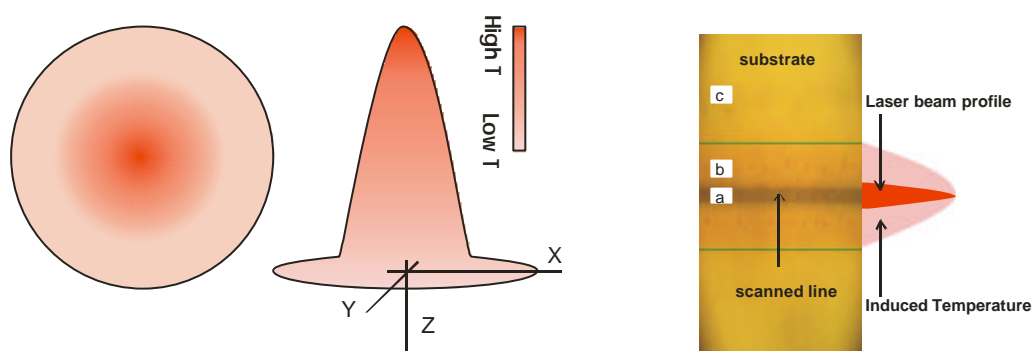


**Figure 3.9** Beam profile of the laser (left), and experimental optical micrograph of the Au surface scanned by the laser (right). The area of laser-induced temperature rise (area *b*) is much larger than the laser beam (area *a*). Area *c* is not affected by laser.

To understand this effect, let us have a look at the laser beam profile (Figure 3.9). The laser beam has a Gaussian profile with the highest temperature at the centre part. Depending on the output energy, the centre part can induce temperature higher than 1000  $^{\circ}\text{C}$  and even ablate gold.<sup>8,29</sup> However, simultaneously, the edge of the laser beam also induces an increase in the temperature of the surface that is high enough to modify the surface. Area *a* in Figure 3.9 corresponds to the centre part of the laser beam where the SAM is damaged, and area *b* is the part where the SAM is modified without loss of molecules. The width of area *a* is about 2  $\mu\text{m}$ , and the width of area *b* is about 6  $\mu\text{m}$ . In Figure 3.8, area *b* is thus the area showing passivation upon Cu deposition.

When the laser is scanning, the centre spot of the laser induces high temperature, which causes SAM desorption. Since gold has a good thermal conductivity (melting point of gold is 1064  $^{\circ}\text{C}$ ; thermal conductivity is 320  $\text{W m}^{-1} \text{K}^{-1}$ ), the heat is transferred

to nearby areas quickly, causing an abrupt temperature increase. The temperature decreases quickly as the laser spot is moved away. This may cause the gold and SAM structure in nearby area to rearrange.

### 3.3.3 Passivation Lines

As shown in Figure 3.8/3.9, passivation is induced in the outer areas of the laser spot and beyond. It is expected that passivation line can be created if the laser energy is reduced to a point in which the centre part of the laser energy is just sufficient for passivation and does not induce SAM desorption. Figure 3.10 shows optical micrographs of patterns written on MC22/Au/Mica surface. The lines were written in a sequence of 3.3 mW, 2.6 mW, and 3.3 mW. For lines written at power of 3.3 mW, the centre spot damaged the SAM, after electrodeposition, Cu was deposited on the area where laser scanned. However, a passivation effect was clearly seen on the edge of the line. Passivation lines can be created at a lower power of 2.6 mW. It was found that the line width (passivation area) written at 2.6 mW is smaller than the line width written at 3.3 mW. This is explained by the temperature effect. The higher the power, the further does the heated area extend. When the power was set back to 3.3 mW, passivation was again only observed at the edge of the line. It is important to note that the passivation effect is very sensitive to laser power.

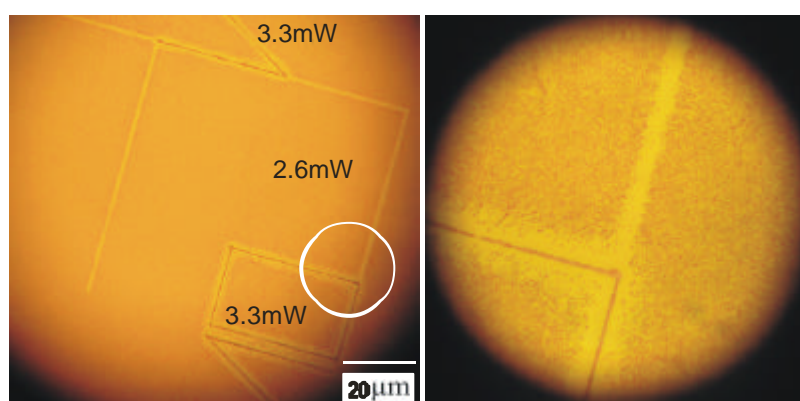


**Figure 3.10** Optical micrographs of pattern written on MC22/Au/Mica (after copper deposition at -0.4 V for 20 seconds). The optical micrograph on the right is a magnification of circled area shown on the left image. (power after filters: 0.96%).

Figure 3.11 shows another example where patterning/passivation lines can be created by choosing different laser power. Figure 3.11 (a) to (f) show six patterns written on MC18/Au/Mica surface using power of 3.3, 2.9, 2.6, 2.8, 3.0, and 3.2 mW, respectively.

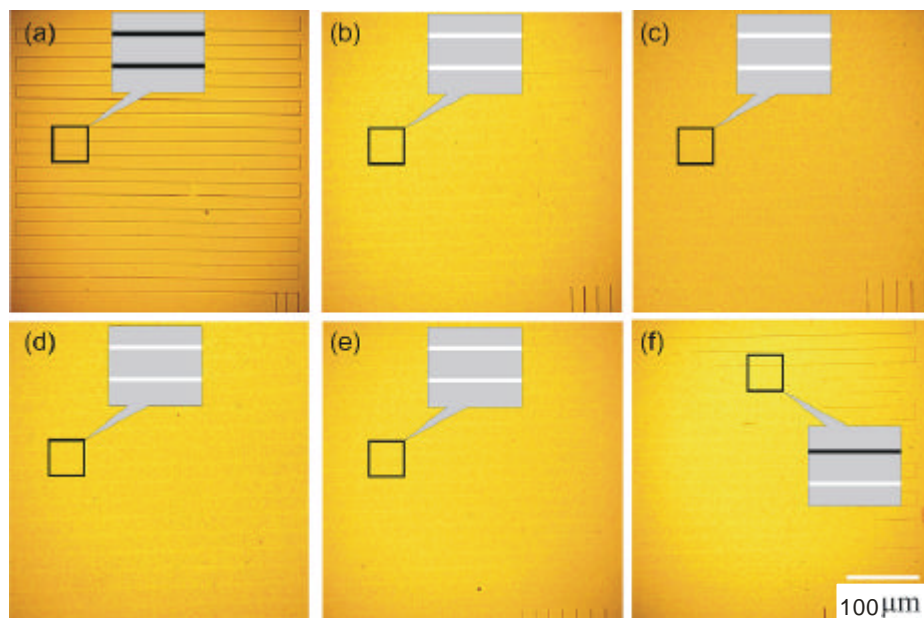


**Figure 3.11** Optical micrographs of patterns written on MC18/Au/Mica. The writing power from (a) to (f) are 3.3, 2.9, 2.6, 2.8, 3.0, and 3.2 mW respectively. The dark lines in insertions represent Cu lines; while the white lines represent passivation lines. The gap between two lines is 20  $\mu\text{m}$ , the scanning speed was 50  $\mu\text{m}/\text{s}$ . The size of each pattern is  $500 \times 400 \mu\text{m}^2$ . Copper deposition was -0.4 V for 40 seconds, then -0.48 V for another 5 seconds to increase the contrast. (power after filters: 0.96%).

For patterns written with even higher power of 3.3 mW, we observed the same effect as the one shown in Figure 3.8 with copper deposited onto the lines. It was found that the passivation occurred when the lines were written with the laser power between 2.6 mW and 3.0 mW ( see Figure 3.11 (b) to (e) ). In (f) the lines were written with power of 3.2 mW, partial passivation was seen and some area also exhibited damages (i.e. Cu deposit). This might be due to variation of the laser power or a tilt of the sample (sample is not perpendicular to the laser beam). This experiment clearly shows the sensitivity of the passivation to the laser power.

### 3.3.4 Large Area Passivation

Passivation may lead to practical applications if large area can be produced. This was accomplished by increasing the density of lines (i.e., by reducing the gap between two lines).

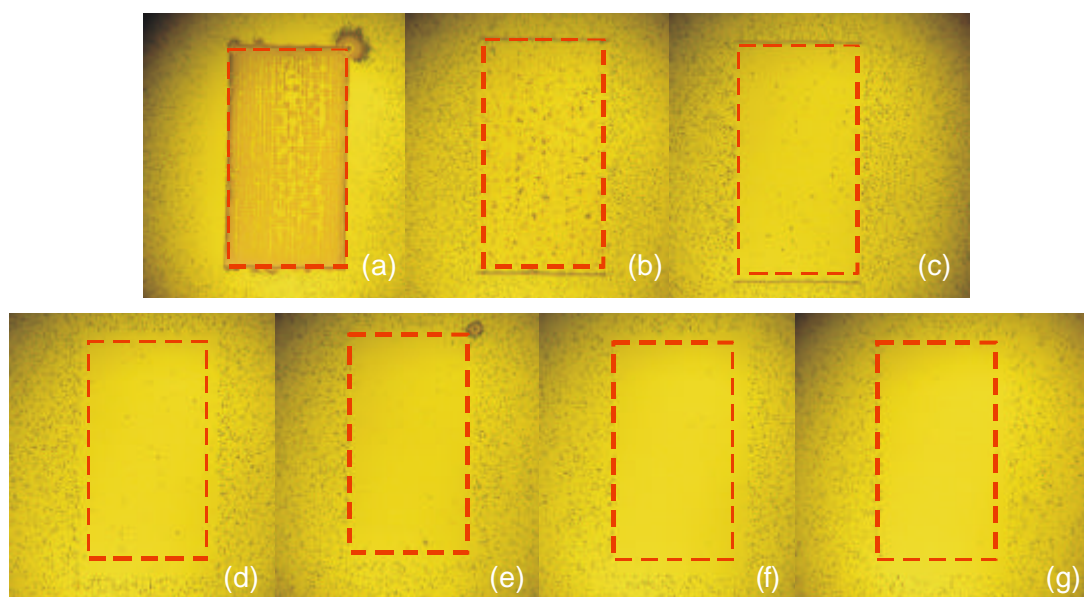


**Figure 3.12** Optical micrographs of patterns written on MUA/Au/Si. Copper deposition -0.5 V for 10 seconds. From a to g, the patterns were written with the power from 3.3 mW, 3.1 mW, 2.9 mW, 2.7 mW, 2.5 mW, 2.3 mW and 2.1 mW respectively. Each pattern is  $200 \times 100 \mu\text{m}^2$ , and line distance is  $5 \mu\text{m}$ . (power after filters: 0.96%).

Figure 3.12 shows rectangular patterns written on the MC18/Au/Si surface with power ranging from 3.3 mW to 2.1 mW, with steps of 0.2 mW. Patterns are about  $200 \times 100 \mu\text{m}^2$  and were formed by lines separated by  $5 \mu\text{m}$ . A power of 3.3 mW was high enough to damage SAM, hence Cu was deposited. However, when the power was reduced to 2.9 mW, the passivation effect became apparent. Less copper particles were found inside compared to the outside area. The passivation occurs for laser power ranging from 2.9 mW to 2.1 mW. Below 2.1 mW, the scanning area showed no difference from the outside area. This indicates that the power is too low to affect the SAM. Quantitative analysis of the passivation was done by comparing the percentage of the Cu coverage within the patterned area and in the surrounding areas. This was

done by using the scanning probe image processor (SPIP). Images were first flattened by a polynomial fit (degree: 3), and then a grain analysis was performed. The final values were made by comparing the original optical image with the modified image. Results are shown in Table 3.2.

**Table 3.2 Nucleation of Cu on MUA SAM ( Cu deposition parameters are: -0.5 V for 10 seconds). Sample shown in Figure 3.12.**

Power	3.3 mW	3.1 mW	2.9 mW	2.7 mW	2.5 mW	2.3 mW	2.1 mW
Irradiated area	83.9%	7.18%	0.9%	0.4%	0.32%	0.09%	0.07%
Nonirradiated area	6.50%						

At power of 2.1 and 2.3 mW, the nucleation sites are less than 0.1%. This is significantly smaller than the outside area (6.5%). It is noted that nucleation sites, both inside and outside the passivated area depend on the deposition potential.

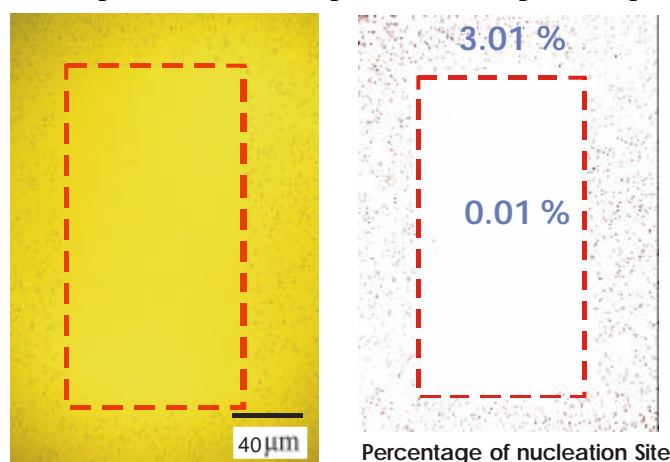
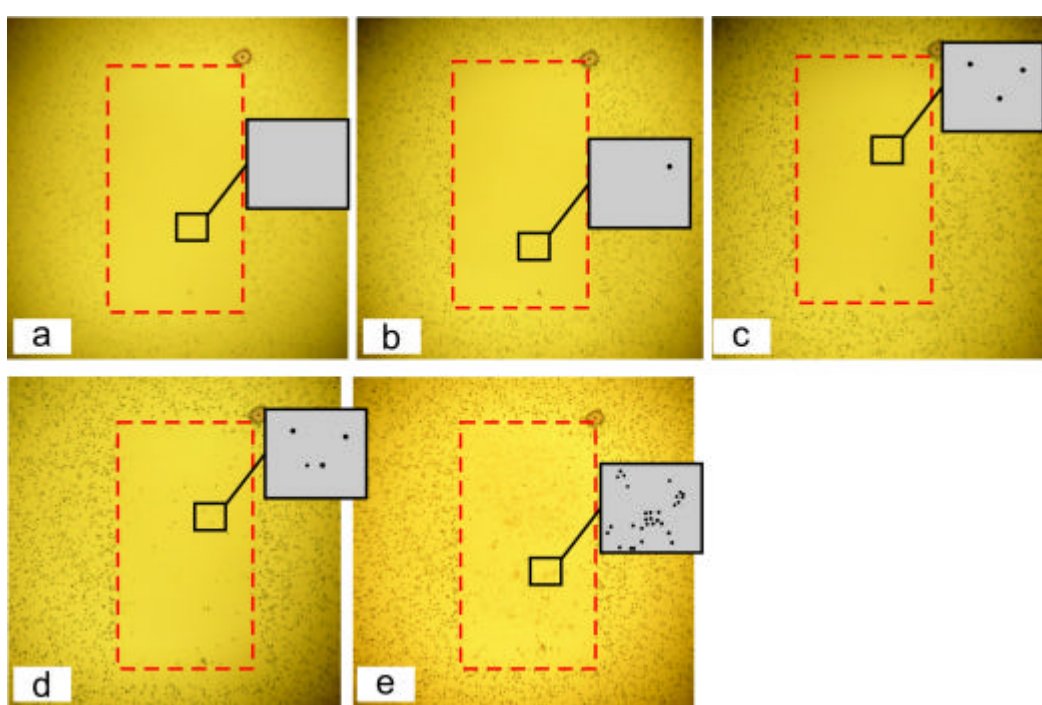


**Figure 3.13 Optical micrographs of patterns written on MUA/Au/Si. Copper deposition -0.4 V for 20 seconds. The pattern was written by a power of 2.1 mW with a scanning speed of 50  $\mu\text{m}$  /s. (power after filters: 0.96%).**

Figure 3.13 shows a passivation area scanned with power of 2.1 mW. The Cu coverage outside the rectangular area is 3.01%, while inside it is only about 0.01%, which is 2 orders of magnitude lower than the area without laser modification.

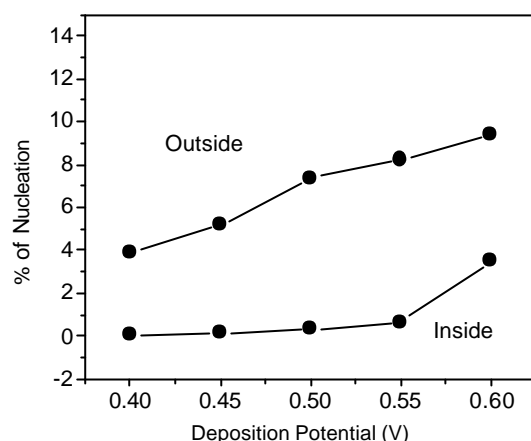
To investigate the effect of the potential during Cu deposition, we applied various

deposition potentials. Figure 3.14 presents optical micrographs of a sample after a series of Cu deposition. When Cu was deposited at  $-0.4$  V for 20 seconds, the passivation area was very clear. There were almost no Cu particles inside the rectangular area. As the potential was set more negative, the percentage of nucleation sites outside the passivation area increases significantly, while it was stable inside. However, when the potential reached  $-0.6$  V, there was a sudden increase in the density of nucleation sites in the passivated area, showing the “breakdown” of the passivation.



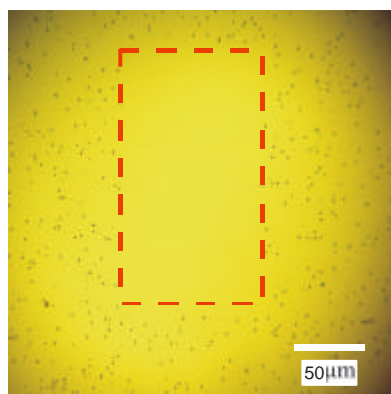
**Figure 3.14** Optical micrographs of rectangular patterns written on MC11/Au/Si. The power was 2.5 mW (power after filters: 0.96%). The copper deposition condition: (a)  $-0.4$  V 20 seconds; (b)  $-0.45$  V 10 seconds; (c)  $-0.5$  V for 10 seconds; (d)  $-0.55$  V for 10 seconds; (e)  $-0.6$  V for 10 seconds. The area of rectangle is  $100 \times 200 \mu\text{m}^2$ . The insets represent the nucleation sites in the selected area.

Figure 3.15 summarizes the percentages of nucleation sites of passivated area and outside area at different Cu deposition potential. It highlights the difference inside and outside the passivated area.



**Figure 3.15** Percentage of nucleation sites inside and outside the passivated area at different deposition potential (corresponds to Figure 3.14).

All samples discussed above were prepared at room temperature. Since the passivation is caused by thermal annealing, it is worth investigating samples prepared at elevated temperature. Figure 3.16 shows optical micrographs of MC18/Au/Si prepared at 72° for 2 days after laser treatment and Cu deposition. It was found that the passivation effect was still very pronounced. However, outside the passivated area, copper deposition was less dense compared to samples prepared at room temperature. This is because SAMs prepared at elevated temperature have less defects and are structurally more perfect.<sup>30</sup>



**Figure 3.16** Optical micrographs of a pattern written on MC18/Au/Si. The laser power is 2.2 mW (power after filters: 0.96%). Cu deposition conditions are -0.4 V for 40 seconds.

As shown before, the passivation effect is not restricted to CH<sub>3</sub>-terminal SAMs. It was also observed in COOH-terminal SAMs (MUA and MHA). Relationship between

SAM and passivation has been verified by measuring contact angle after laser irradiation. We irradiated an area of about  $1.5 \times 1.5 \text{ mm}^2$  and measured the contact angle before and after irradiation (MUA/Au/Si). Two pictures of contact angle measurements ( $\text{H}_2\text{O}$  drop) were shown in Figure 3.17. Before laser irradiation, the contact angle is about  $42^\circ$ , while after, the contact angle is about  $39^\circ$ . The difference is not very pronounced, which indicates that the structure does not change too much.

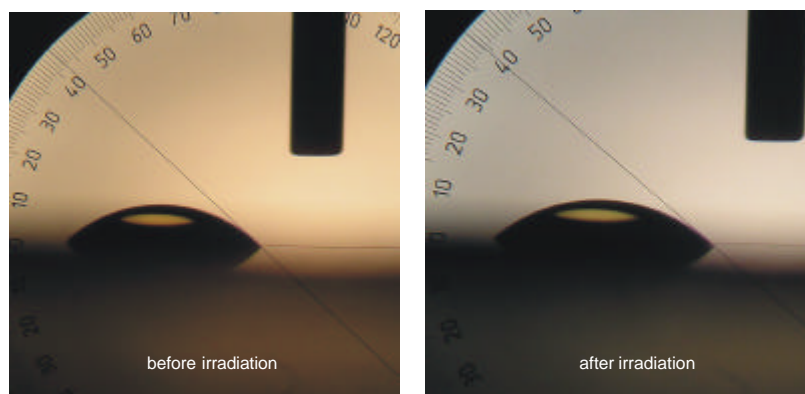


**Figure 3.17** Contact angles of  $\text{H}_2\text{O}$  drop on MUA/Au/Si before ( $\text{CA} = 42^\circ$ ) and after ( $\text{CA} = 39^\circ$ ) irradiation. The pattern was written by a power of 2.3 mW. (power after filters: 0.96%).

### 3.3.5 STM investigation of Laser Passivated Surfaces

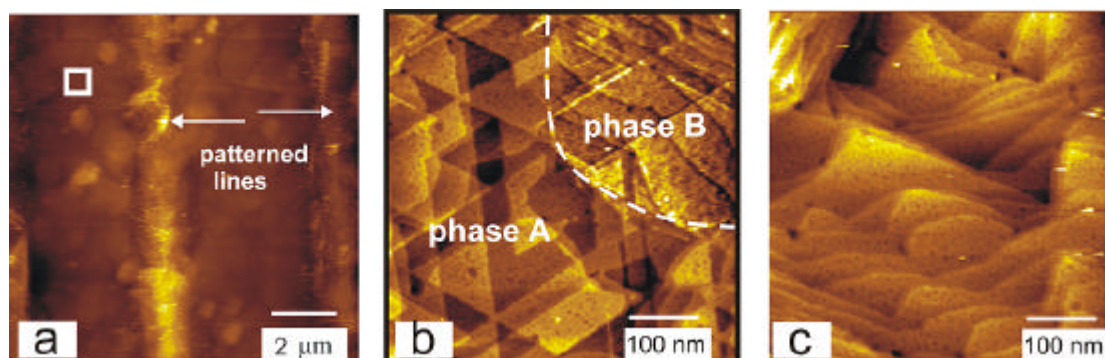


**Figure 3.18** (a) STM image of MC11/Au/Mica after laser irradiation (7.0 mW, power after filters: 0.48%,  $20 \mu\text{m/s}$ ). (b) STM image of a area selected in (a) (marked by a square). (c) STM image of a nonirradiated area of MC11.

To further investigate laser passivation, we imaged the sample with STM. Figure 3.18 (a) shows a large image of the surface structure after laser irradiation. A selected area as indicated by square is shown in (b). Two different structures were found (labeled A and B). Structure A is similar to the non irradiated area (see image (c)), while

structure B appears more uniform, which is believed to be the effect of irradiation. It has been reported that MC12 has phase transition at the temperature of about 323 K. At this temperature, there is coexistence between the solid and liquid phase.<sup>31</sup>

One should note that although passivated area block bulk Cu deposition, UPD still occurs. Some patches of UPD Cu monolayer were found on the surface after Cu deposition as shown in Figure 3.19(b).

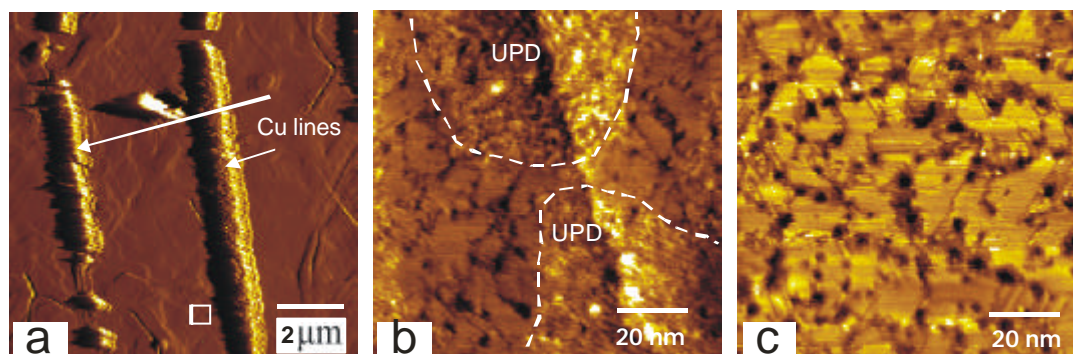


**Figure 3.19** (a) STM image of MC11/Au/Mica after irradiation and Cu deposition (5.0 mW, power after filters: 0.48%), areas between lines show passivation. A selected area as indicated by square is shown in (b). (c) Nonirradiated area.

### 3.3.6 Application of Passivation

Passivation can be used to enhance the contrast of Cu deposition. We can indeed write a second pattern inside the passivated area using higher laser power. This is shown in Figure 3.20.

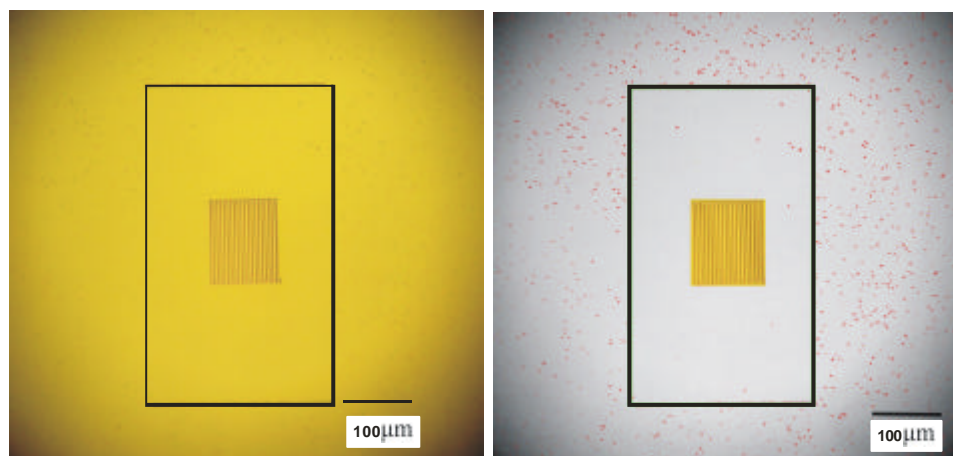


**Figure 3.20** Optical micrographs of a copper pattern written inside a passivated area (indicated by rectangular, 4.6 mW). The smaller pattern with Cu electrodeposited was irradiated by 6.2 mW. (power after filters: 0.48%). Left one is the original picture. Right one highlights the contrast.

By using a low laser power (4.6 mW), a large passivation area (indicated by the green box) is formed on MC18/Au/Si. On this passivated area, a second and smaller pattern is created by using a higher laser power (6.2 mW), which is just high enough to desorb the SAMs. After Cu electrodeposition, the Cu is deposited exclusively in the small pattern. This method allows us to reduce defects, and thus to significantly improve the SAM which is important for micro and nanoscale fabrication, where uncontrolled defects cannot be tolerated.

### 3.3.7 Conclusion

Laser-induced passivation on SAMs surface was investigated. The effect enhances the blocking capability upon electrochemical metal deposition. We observe the effect on MC22, MC18, MC14, MC11, MUA, BP12, BP5, and BP2 modified gold surface, regardless of the substrate type (Mica or Si). We suggest that passivation is induced by a thermal effect: during irradiation, high temperature is built up in the focus and the heat can transfer quickly to the edge, inducing rearrangement of SAMs structure and the annealing of defect sites. The effect blocks bulk copper deposition, but does not prevent UPD. By choosing appropriate laser power, large passivated area can be created, which can be used as substrate for further fabrication.

The passivation effect has also been observed on BPT ( $C_6H_5-C_6H_4-SH$ ) and BP12 modified Au surface after electron beam irradiation (300 eV).<sup>32</sup> It was found that after electrochemical Cu deposition, irradiated areas show better blocking behavior. In this case the aromatic moiety is responsible for this effect by cross linking each other, while irradiated alkanethiols show degradation under same treatment. In contrast the passivation effect observed here is believed to be a thermal effect as it was observed on both aromatic and alkanethiol SAMs.

However, a good stability of the laser power is fundamental. Indeed we showed before that small variation may induce damages in the SAMs, preventing formation of a passivated area.

## 3.4 Superhydrophobic Surface Built from SAM Templates

### 3.4.1 Introduction

In the previous section, we discussed passivation of SAMs by laser irradiation. The effect allows SAM to block metal electrodeposition by reducing the amount of defects acting as nucleation sites. However, defects can also be useful. In this section, it is shown how these defects can be used to generate a rough surface and hence form a superhydrophobic surface.

Superhydrophobic surfaces with a water contact angle (CA) larger than  $150^\circ$  have attracted a lot of interest from both fundamental and practical aspects.<sup>33,34</sup> Many biological surfaces, in particular plant leaves (e.g. lotus leaves), exhibit superhydrophobicity.<sup>35</sup> Wax crystals on lotus leaf create a very rough surface, which enhances the hydrophobicity. The wax crystals form pillars with micrometer-scale dimensions.<sup>36,37</sup> Many methods have been used to create rough surface,<sup>38-44</sup> or even to mimic<sup>37,45</sup> lotus leaves surface. Most of these modifications were carried out on the surfaces of plastics, as they are easier to handle. It would be very interesting to mimic such surface structures on metal surfaces. In a previous work<sup>13</sup> we have shown that SAMs can be used as template for fabricating metal microstructures. Here, we use hydrophobic SAMs as templates to grow a rough Cu structure in order to build a superhydrophobic metal surface.

### 3.4.2 Experimental

Patterned SAMs were produced by microcontact printing using a polydimethylsiloxane (PDMS) stamp with parallel lines of  $4\ \mu\text{m}$  width and  $8\ \mu\text{m}$  periodicity. The stamp was immersed in a 1 mM solution of 1-Octadecanethiol (MC18) in ethanol, blown dry in nitrogen and pressed gently onto the surface for 25 seconds. The stamp is then rotated by 90 degrees and pressed again on the substrate. A grid of MC18 is thus formed. The scheme is illustrated in Figure 3.21.

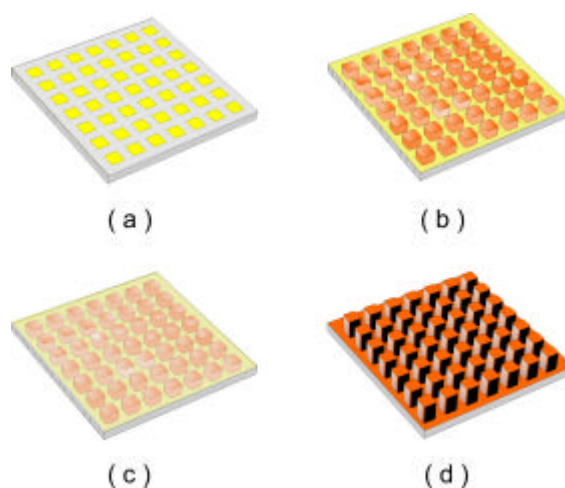


**Figure 3.21** Fabrication of superhydrophobic surface on Au surface using SAMs as templates. (a) SAM grid on substrate, which defines areas for copper deposition. (b) Copper deposited on the uncovered area. (c) SAM formation on freshly prepared copper islands. (d) Formation of a dense layer of copper on the substrate, followed by immersion into MC18.

To form the bumps on the surface, the SAM grid was mounted in the electrochemical cell for copper deposition. The deposition was done at  $-0.3$  V for 300 seconds. The sample was then removed from the cell, rinsed with ethanol and was immersed in the MC18 ethanol solution for 30 minutes at  $72^\circ$ . Since thiol binds easily on Cu,<sup>46,47</sup> a layer of MC18 formed on the Cu islands. After rinsing with ethanol and drying with nitrogen, the substrate was placed again in the cell and a second layer of Cu was deposited. The deposition finished in two steps:  $-0.75$  V for 20 seconds, and  $-0.5$  V for 300 seconds.

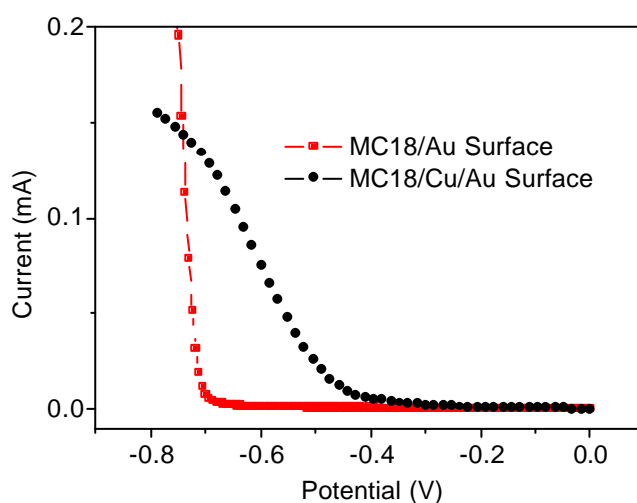


**Figure 3.22** Linear sweep voltammograms showing thresholds for Cu deposition on MC18/Au and MC18/Cu/Au. Starting at 0 V the potential is scanned at a rate of 50 mV/s.

As shown in Figure 3.22, Cu deposition for MC18/Au and MC18/Cu/Au starts at -0.7, -0.4, respectively. Thus after the deposition, copper films (grid areas) and copper islands cover the entire substrate. The sample is once again removed from the cell, and rinsed with ethanol. It was then immersed in the MC18 solution at 72° for 60 minutes. Finally, it is rinsed with ethanol and dried with nitrogen.

### 3.4.3 Results and Discussion

Figure 3.23(a) shows optical micrographs of copper structures formed in the SAM grid defined by micro-contact printing (area free of SAM was deposited by Cu). The inset shows the substrate (15 × 15 mm<sup>2</sup>). The shiny area (10 × 10 mm<sup>2</sup>) is the copper structure. Figure 3.23 (b) shows the microstructure of rough Cu structures formed by depositing a fully covered Cu layer onto the surface of (a). A final layer of MC18 was coated onto the surface. Such rough bumpy structure combined with the hydrophobic property of MC18 SAMs, makes Au substrate superhydrophobic as shown in Figure 3.23(b). Water droplet with a contact angle of 165° is achieved (see inset).

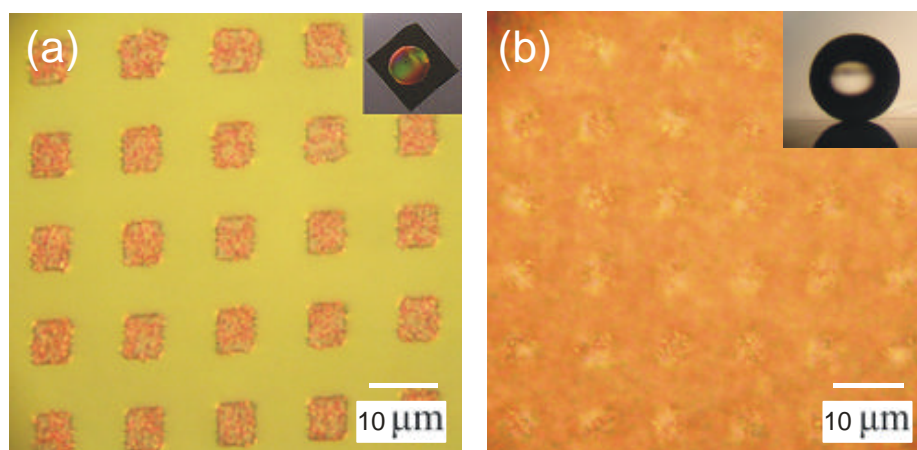


**Figure 3.23 (a)** Optical micrograph of the copper structure formed in the SAM grid defined by micro-contact printing. Area free of SAM was deposited by Cu (-0.3 V, 300 seconds). The inset shows the substrate (15 × 15 mm<sup>2</sup>). **(b)** Optical micrograph of the copper bumpy structure formed by depositing a layer of Cu onto the surface of (a). Cu deposition: -0.5 V for 300 second. A final layer of MC18 was formed on this surface. The inset shows the optical image of a water droplet on the surface. Contact angle of 165° is achieved. The volume of the water droplet is ~4 μl.

The MC18 SAM plays two different roles. First, the SAM acts as a template to define the copper deposition area and form the Cu islands structure. Such rough structure with nano copper particles reduces the contact area between water droplet and substrate.

As suggested in the literature,<sup>38,42</sup> the relationship between contact angle and surface structures can be evaluated by Cassie's law.<sup>48</sup>

$$\cos q_c = g(\cos q + 1) - 1 \quad (3 - 1)$$

$q_c$  is the superficial contact angle;  $q$  is the contact angle of the flat surface of water; and  $g$  is the surface area fraction of water.

This equation means that a superhydrophobic surface can be achieved with small  $g$  and large  $q$ . MC18 yields a large CA of about  $110^\circ$  for  $H_2O$  when absorbed on a Au surface. So we expect formation of a superhydrophobic surface if a small  $g$  can be obtained. From equation 3-1, when the contact angle is  $165^\circ$  (surface as shown in Figure 3.23), the value of  $g$  is 0.05. By comparison, the contact angle is only  $153^\circ$  if only rough copper was deposited on Au, and hence for  $g$  is 0.17, i.e., 3-4 times larger. Since the roughness of the structure can be controlled by adjusting the deposition condition, and the template shape, more complicated structures can be prepared by this method. The second role of the MC18 SAM is to form a hydrophobic monolayer on the whole metal surface.

The method described here can be used to form superhydrophilic surface by using a hydrophilic SAM such as MUA as reported by Jiang et al.<sup>40</sup>

### 3.4.4 Conclusion

We have demonstrated an effective way to prepare a superhydrophobic surface. By using self-assembled monolayer as template, a superhydrophobic surface with a contact angle of  $165^\circ$  can be obtained. By controlling the geometry of the metal pattern and electrochemical deposition parameters, we can control the surface roughness. This

method can be easily applied to other metals, such as silver. These superhydrophobic surfaces may lead to applications in the fields of microfluidic devices with electro-optical components,<sup>49</sup> electrowetting, and as supporting surface for optical tweezers operation, which needs a superhydrophobic surface for droplet movements.

## References:

- (1) Chang, W.; Choi, M.; Kim, J.; Cho, S.; Whang, K. *Applied Surface Science* 2005, 240, 296-304.
- (2) Friebel, S.; Aizenberg, J.; Abad, S.; Wiltzius, P. *Applied Physics Letters* 2000, 77, 2406-2408.
- (3) Hong, M. H.; Huang, S. M.; Luk'yanchuk, B. S.; Chong, T. C. *Sensors and Actuators a-Physical* 2003, 108, 69-74.
- (4) Chang, W. S.; Kim, J.; Cho, S. H.; Whang, K. H. *Japanese Journal of Applied Physics Part 1-Regular Papers Brief Communications & Review Papers* 2006, 45, 2082-2086.
- (5) Mullenborn, M.; Dirac, H.; Petersen, J. W. *Applied Physics Letters* 1995, 66, 3001-3003.
- (6) Schreiber, F. *Progress in Surface Science* 2000, 65, 151-256.
- (7) Shadnam, M. R.; Amirfazli, A. *Chemical Communications* 2005, 4869-4871.
- (8) Shadnam, M. R.; Kirkwood, S. E.; Fedosejevs, R.; Amirfazli, A. *Langmuir* 2004, 20, 2667-2676.
- (9) Fitts, W. P.; White, J. M.; Poirier, G. E. *Langmuir* 2002, 18, 1561-1566.
- (10) Fitts, W. P.; White, J. M.; Poirier, G. E. *Langmuir* 2002, 18, 2096-2102.
- (11) Staub, R.; Toerker, M.; Fritz, T.; Schmitz-Hubsch, T.; Sellam, F.; Leo, K. *Langmuir* 1998, 14, 6693-6698.
- (12) Azzaroni, O.; Schilardi, P. L.; Salvarezza, R. C. *Electrochimica Acta* 2003, 48, 3107-3114.
- (13) Thom, I.; Hahner, G.; Buck, M. *Applied Physics Letters* 2005, 87, 024101.
- (14) Aswal, D. K.; Lenfant, S.; Guerin, D.; Yakhmi, J. V.; Vuillaume, D. *Analytica Chimica Acta* 2006, 568, 84-108.
- (15) Love, J. C.; Estroff, L. A.; Kriebel, J. K.; Nuzzo, R. G.; Whitesides, G. M. *Chemical Reviews* 2005, 105, 1103-1169.
- (16) Vericat, C.; Vela, M. E.; Salvarezza, R. C. *Physical Chemistry Chemical Physics* 2005, 7, 3258-3268.
- (17) Burtman, V.; Ndobe, A. S.; Vardeny, Z. V. *Journal of Applied Physics* 2005, 98, 034314.
- (18) Cho, J. H.; Lim, J. A.; Han, J. T.; Jang, H. W.; Lee, J. L.; Cho, K. *Applied Physics Letters* 2005, 86, 171906.
- (19) Parashkov, R.; Becker, E.; Riedl, T.; Johannes, H. H.; Kowalsky, W. *Advanced Materials* 2005, 17, 1523-1527.
- (20) Zhou, C. Z.; Nagy, G.; Walker, A. V. *Journal of the American Chemical Society* 2005, 127, 12160-12161.
- (21) Maisch, S.; Buckel, F.; Effenberger, F. *Journal of the American Chemical Society* 2005, 127,

- 17315-17322.
- (22) Rawlett, A. M.; Hopson, T. J.; Amlani, I.; Zhang, R.; Tresek, J.; Nagahara, L. A.; Tsui, R. K.; Goronkin, H. *Nanotechnology* 2003, *14*, 377-384.
- (23) Nitzan, A.; Ratner, M. A. *Science* 2003, *300*, 1384-1389.
- (24) Gutierrez, R.; Fagas, G.; Richter, K.; Grossmann, F.; Schmidt, R. *Europhysics Letters* 2003, *62*, 90-96.
- (25) Burtman, V.; Ndobé, A. S.; Jiang, X.; Vardeny, Z. V. *Synthetic Metals* 2005, *154*, 329-332.
- (26) Emberly, E. G.; Kirczenow, G. *Chemical Physics* 2002, *281*, 311-324.
- (27) Tai, Y.; Shaporenko, A.; Noda, H.; Grunze, M.; Zharnikov, M. *Advanced Materials* 2005, *17*, 1745-1749.
- (28) Schneeweiss, M. A.; Hagenstrom, H.; Esplandiu, M. J.; Kolb, D. M. *Applied Physics a-Materials Science & Processing* 1999, *69*, 537-551.
- (29) Shadnam, M. R.; Kirkwood, S. E.; Fedosejevs, R.; Amirfazli, A. *Journal of Physical Chemistry B* 2005, *109*, 11996-12002.
- (30) Cyganik, P.; Buck, M. *Journal of the American Chemical Society* 2004, *126*, 5960-5961.
- (31) Fenter, P.; Eisenberger, P.; Liang, K. S. *Physical Review Letters* 1993, *70*, 2447-2450.
- (32) Felgenhauer, T.; Yan, C.; Geyer, W.; Rong, H. T.; Golzhauser, A.; Buck, M. *Applied Physics Letters* 2001, *79*, 3323-3325.
- (33) Song, X. Y.; Zhai, J.; Wang, Y. L.; Jiang, L. *Journal of Physical Chemistry B* 2005, *109*, 4048-4052.
- (34) Yu, X.; Wang, Z. Q.; Jiang, Y. G.; Zhang, X. *Langmuir* 2006, *22*, 4483-4486.
- (35) Barthlott, W.; Neinhuis, C. *Planta* 1997, *202*, 1-8.
- (36) Cheng, Y. T.; Rodak, D. E.; Angelopoulos, A.; Gacek, T. *Applied Physics Letters* 2005, *87*, 194112.
- (37) Vogelaar, L.; Lammertink, R. G. H.; Wessling, M. *Langmuir* 2006, *22*, 3125-3130.
- (38) Zhang, G.; Wang, D. Y.; Gu, Z. Z.; Mohwald, H. *Langmuir* 2005, *21*, 9143-9148.
- (39) Li, M.; Zhai, J.; Liu, H.; Song, Y. L.; Jiang, L.; Zhu, D. B. *Journal of Physical Chemistry B* 2003, *107*, 9954-9957.
- (40) Jiang, Y. G.; Wang, Z. Q.; Yu, X.; Shi, F.; Xu, H. P.; Zhang, X. *Langmuir* 2005, *21*, 1986-1990.
- (41) Wang, S. T.; Feng, L.; Jiang, L. *Advanced Materials* 2006, *18*, 767-770.
- (42) Hosono, E.; Fujihara, S.; Honma, I.; Zhou, H. S. *Journal of the American Chemical Society* 2005, *127*, 13458-13459.
- (43) Erbil, H. Y.; Demirel, A. L.; Avci, Y.; Mert, O. *Science* 2003, *299*, 1377-1380.
- (44) Qian, B. T.; Shen, Z. Q. *Langmuir* 2005, *21*, 9007-9009.
- (45) Han, J. T.; Xu, X. R.; Cho, K. W. *Langmuir* 2005, *21*, 6662-6665.
- (46) Azzaroni, O.; Vela, M. E.; Fonticelli, M.; Benitez, G.; Carro, P.; Blum, B.; Salvarezza, R. C. *Journal of Physical Chemistry B* 2003, *107*, 13446-13454.
- (47) Ron, H.; Cohen, H.; Matlis, S.; Rappaport, M.; Rubinstein, I. *Journal of Physical Chemistry B* 1998, *102*, 9861-9869.
- (48) Cassie, A. B. D.; Baxter, S. *Trans. Faraday Soc.* 1944, *40*, 546-561.
- (49) Meldrum, D. R.; Holl, M. R. *Science* 2002, *297*, 1197-1198.

## Chapter 4 SAM Manipulation and Modification by STM

### 4.1 Introduction

Control of the growth of binary phase SAMs is critical for many applications,<sup>1-4</sup> such as wettability control,<sup>5</sup> bio-specific surfaces,<sup>6-9</sup> and molecular electronic devices.<sup>10,11</sup> There are several ways to form multicomponent SAMs: (1) from a solution containing a mixture of molecules,<sup>1,12-15</sup> (2) by simple immersion and replacement,<sup>16-18</sup> (3) by insertion of individual molecules into a matrix layer (usually an alkane thiol SAMs),<sup>1,2,16</sup> (4) by patterning.<sup>19-30</sup> Patterning technologies such as micro-contact printing, photolithography, laser beam lithography, scanning near-field photolithography, electro-beam lithography and scanning probe lithography (SPL) have been explored to form binary phase of SAMs on various substrates. Scanning probe microscopy (SPM) has two roles in the field of nanotechnology: the first one is the ability to 'see' molecules in a straightforward way; the other one is that the probe tip can be used to manipulate atoms/molecules on the surface. Both scanning tunnelling microscopy and atomic force microscopy (AFM) can be used to generate patterns of very high resolution that are usually not achievable by other technologies. For example, single atom manipulation can be performed in UHV at low temperature with STM.<sup>31</sup> Surface modification using STM has been extensively investigated in the past two decades.<sup>28,32-41</sup> Most of the work relies on forcing the probe to penetrate into the SAMs (i.e. by increasing current/reducing tip-sample bias), and using the mechanical force between the tip and the SAMs to modify the surface as shown in Figure 4.1.<sup>37</sup> Another way to modify the surface is by applying a high voltage pulse (several volts) to the tip, which removes material from the substrate.<sup>25,26,35,42</sup> For example, holes can be produced in a graphite surface by applying short voltage pulses (3–8 V, 10–100  $\mu$ s) across the tunneling gap. These operations remove one or more layers of graphite in a small region directly below the tip due to weak bonding between the layers.<sup>39</sup> Also a

SAM covered Au surface can be modified by applying a high voltage pulse. The pulse results in material transfer between the substrate and the tip, which is believed to be an electric field effect.<sup>25,26,35,42</sup> Patterns created by these two type of operations can be used for assembling a second type of SAM by immersing into the respective solution.<sup>27</sup> One of the aims here is to investigate how small the structures are we can generate, i.e., how much smaller is the addressable length scale compared to laser or microcontact printing discussed in the previous chapter. STM is used to generate nanostructures under several modes of operations: mechanical force (sweeping mode, high current and low voltage), electric-field-induced damage (punching mode, high voltage), and replacement (nanografting). In the last part of this chapter, we also investigated metal deposition on STM patterned SAM *in situ* in order to elucidate the behaviour of metal deposition at the nano-scale.

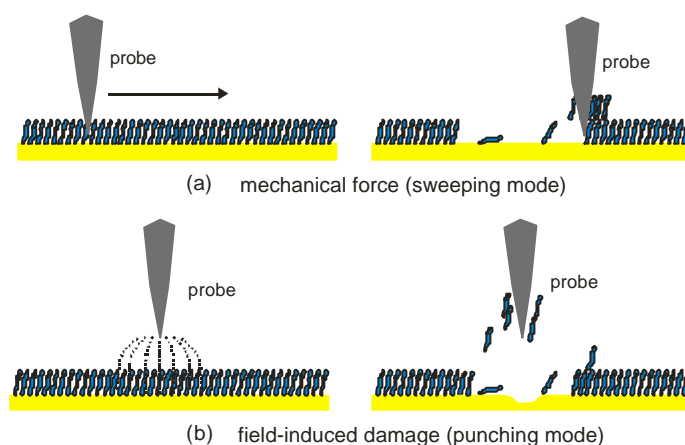


**Figure 4.1** Schematic diagram showing two modes of modification on a SAM covered surface. (a) Sweeping mode, achieved by scratching the SAM with STM (high current and low voltage) or with AFM (high load). (b) Field-induced damage (punching mode), achieved by applying a high voltage pulse (2.5 – 5 V) between tip and substrate.

## 4.2 Sweeping Effect

### 4.2.1 STM Modification of Electrodeposited Metal Clusters on SAMs

#### 4.2.1.1 Alkane thiol SAMs

During the imaging of the line pattern as described in the previous chapter, we found that if the pattern was written at low laser power, the copper deposited onto these lines can be swept away during STM imaging.

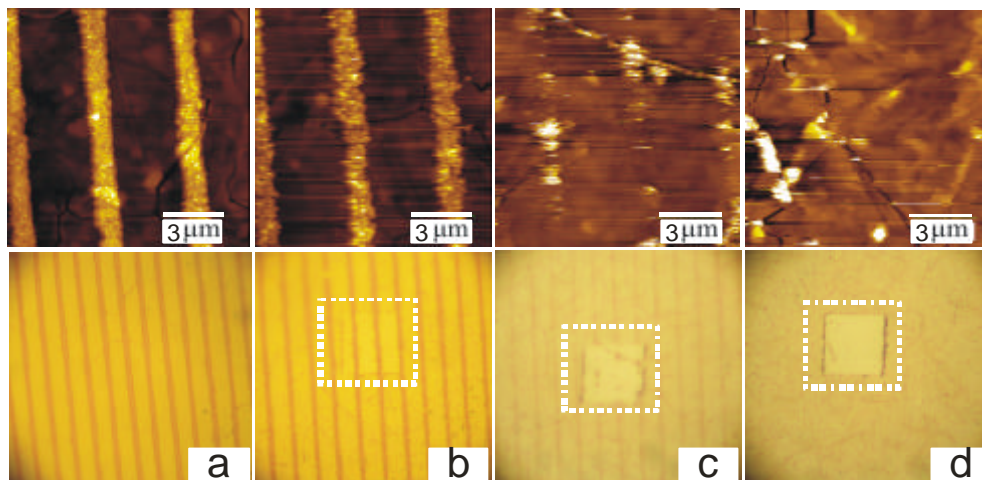


**Figure 4.2** STM images (upper row) and optical micrographs (lower row) showing Cu lines on LSL modified MC11/Au/Mica surface during and after STM scanning. Laser power used for LSL patterning was 4 mW, 3.5 mW, 3 mW, and 2.5 mW for (a), (b), (c) and (d), respectively. The rectangles indicated in the optical micrographs correspond to the STM scanned area. Copper deposition: -0.35 V for 10 seconds. STM image parameters are 100 pA and 1.0 V.

As shown in Figure 4.2, the power used to write the patterns (a), (b), (c), and (d) were 4, 3.5, 3, and 2.5 mW respectively. Cu was deposited onto these laser irradiated areas. Samples were then imaged (scanned) by STM at a combination of 100 pA and 1.0 V.

It was seen that the power of 4 mW was high enough to damage the SAM. Cu deposition occurs onto the bared Au region. Hence the Cu lines were strongly connected to the Au surface and cannot be removed by the STM tip when imaged with 1.0 V and 100 pA. This was confirmed by comparison of the optical micrograph with the STM image, which shows no difference between scanned and outside areas. When the laser power was reduced to 3.5 mW, the pattern lines become thinner. This is because MC11 was only partially damaged in the patterned lines and thus the deposited Cu lines had less direct contact with Au due to remaining MC11. In this case, Cu lines can be swept away by the tip. This phenomenon was more pronounced when the LSL power was reduced to 3 mW as shown in (c). For 2.5 mW, no Cu lines were deposited as the laser power was too weak to damage the SAMs. However, in the optical micrograph,

a square almost free of copper particles was created in the STM scanned area. These copper particles were swept to the edge of the scanning area as seen in (d) and a clean, “copper free” area was created.

To confirm the influence of the STM tip on the electrodeposited Cu particles, we did another scanning experiment. We scanned an entire image once and then only 30% during reverse scan (see Figure 4.3). It was found that after the first scan most Cu particles are swept by the tip (area A). The partial reverse scan pushes remaining Cu particles to the middle of the area where the scan was stopped. This confirms that Cu particles were indeed moved by the tip.

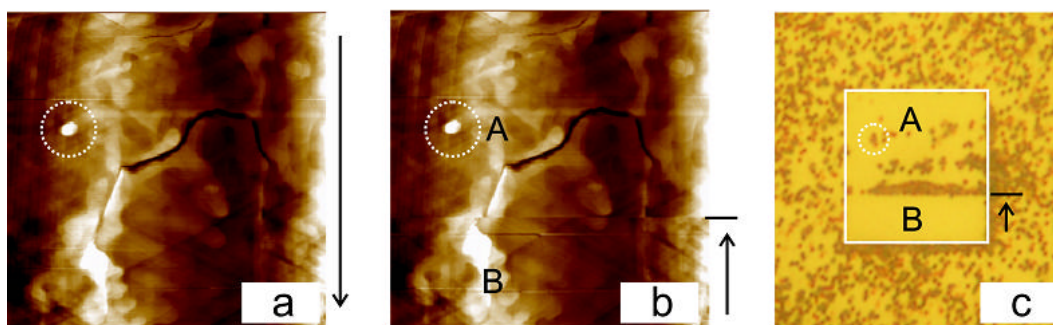


**Figure 4.3** STM images (a and b,  $10 \times 10 \mu\text{m}^2$ ) and Optical micrograph (c) showing the sweeping on MC11/Au surface. It was found that after a first scanning (a), some copper particles remain on the scanned area (see upper part of c, area A). After a partial reverse scan, the area is clean of Cu (see lower part of c, area B). Arrows show STM scanning directions. The circles indicate the same area. Copper deposition:  $-0.35 \text{ V}$  for 80 seconds. STM scanning parameters are  $5 \text{ pA}$  and  $1.0 \text{ V}$ .

If we have a look at how copper deposits on SAMs, we can have a better understanding of this effect. Copper deposition on SAMs involves at least three processes<sup>43</sup> as shown in Figure 4.4 (more details of Cu deposition will be discussed in section 4.5). These are: (1) deposition on top of the SAMs; (2) penetration into SAM and growth like a mushroom; (3) deposition at SAM-substrate interface results in a buried layer. The on-top metal only has weak interaction with the SAMs depending on the type of function group the SAM has. Such particles should be easily swept by the STM tip. The mushroom grown Cu is also not stable on the surface. As it has been shown before, because of such a weak interaction Cu can be easily peeled off/lifted off.<sup>44</sup> Thus it is not surprising that under STM scanning “necks” breaks and Cu is swept

away. One should note that in the optical micrograph of Fig. 4.3(c), area (A) clearly shows copper particles, while there is no visual particle within STM image. This means that these particles are not connected to the Au surface and are left behind the tip during the sweeping.

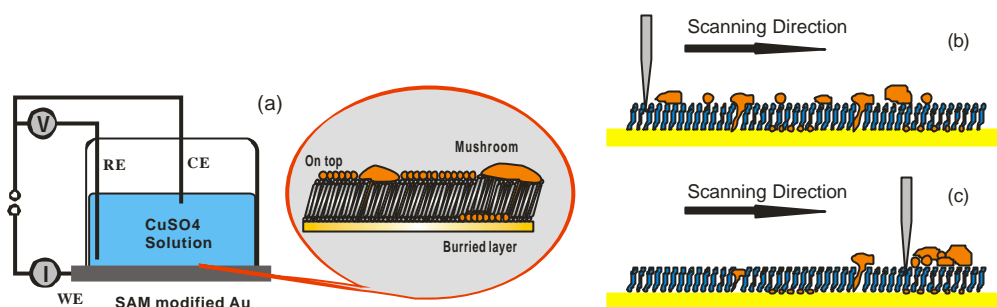


**Figure 4.4** Sketch illustrating the sweeping effect. There are several possibilities of copper deposition on a SAM modified Au surface as shown in (a). At least two are related to the sweeping effect: one is the copper sitting on top of the SAMs, the other one is the mushroom type, in which copper particles are connected with the gold surface via copper wires. In the right (b and c), cartoon shows that “on top” and “mushroom” type Cu particles can be swept away by scanning.

As the tip- substrate gap can be adjusted by changing the current, bias or the combination of both, one can expect that by changing these parameters, the sweep effect would be different. Figure 4.5 shows that for different tunneling currents, the sweeping effect is different. The square sweep by the tip at a current set to 100 pA has less copper particles than the area swept at 30 pA. At 100 pA, the STM tip is closer to the surface and friction forces between tip and copper particles are higher.

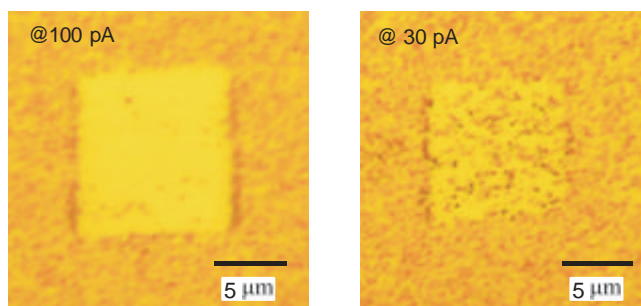


**Figure 4.5** Optical micrographs of Cu deposited on MC11/Au showing that at 100 pA sweeping is more pronounced than at 30 pA (bias kept constant at 1.0 V). Copper deposition: -0.35 V for 20 seconds.

## 4.2.1.2 Other SAMs

SAMs of different chain length and terminal groups show different blocking behaviour. It was shown that vapour deposited Al reacts with  $-\text{CO}_2\text{CH}_3$ ,  $-\text{COOH}$  terminal thiol to form organoaluminum complexes, but penetrates to the Au/S interface for  $\text{CH}_3$  terminated thiols.<sup>45,46</sup> Vapour-deposited copper on  $-\text{CH}_3$ ,  $-\text{OH}$ ,  $-\text{CO}_2\text{CH}_3$ , and  $-\text{COOH}$  terminal alkane thiol have also been investigated.<sup>47</sup> It was found that for  $-\text{OH}$ ,  $-\text{COOH}$ , and  $-\text{CO}_2\text{CH}_3$ , there is a competition between Cu atom bonding onto C-O bonds and penetration to the Au/S interface, while for  $-\text{CH}_3$ , the copper only penetrates to the Au/S interface. These experiments indicate that the tip sweeping effect may depend on the type of SAM as well.

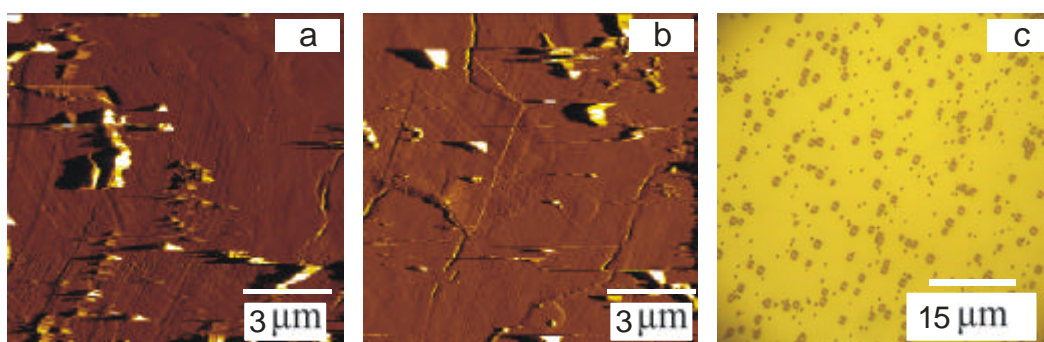


**Figure 4.6** Sweeping effect on MUA/Au/Mica surface. (a) STM image scanned with 1.0 V and 50 pA. (b) Scanned under 1.0 V and 100 pA. (c) Optical micrograph. Under both conditions, copper particles can be seen both in STM images and optical micrograph. Copper deposition is -0.4 V (Cu wire as reference) for 80 seconds. The Cu particles shown are about tens of nm higher than the SAM/Au surface.

To verify this hypothesis, sweeping was performed on the surface of MUA/Au surface. Figure 4.6 shows MUA/Au/Mica scanned by STM at a tunneling current of 50 pA (a), and 100 pA (b), respectively. Copper particles are still stable in both cases. This is due to the functional terminal group  $\text{COOH}$ , which can trap the bulk copper and forms stable structure that cannot be removed under the imaging conditions.<sup>48</sup> However, the situation is different for alkane thiols and biphenyl thiols, which show a dependence on the molecular length. Figure 4.7 and Table 4.1 illustrate the sweeping of Cu particles on DT, BP0, BP1, BP2, BP3, BP4, BP5, BP12, MC11, MC18, MC22, MUA, and MHA

modified Au surface. The molecules chosen are based on the consideration of chain length (short chain, BP0, BP1 and long chain BP12, MC18, and MC22) and of the terminal functional group ( $\text{CH}_3$  and  $\text{COOH}$ ). The three left columns in Figure 4.7 show optical micrographs and the three right columns are STM topography images. It was found that for DT, BP0, and MC6, after electrochemical deposition, the surfaces were smooth, and no metal particles were visible. For long molecules, Cu particles were observed. These experiments indicate that long chain SAMs can block metal deposition. Metal particles deposited are either grown from defect sites of the SAM or by other mechanism such as electron tunneling. These particles can be swept away by the STM tip. For short chain thiol, they cannot block the Cu deposition. Cu penetrates the SAM and grows at the Au-S interface. The results are summarized in Table 4.1.

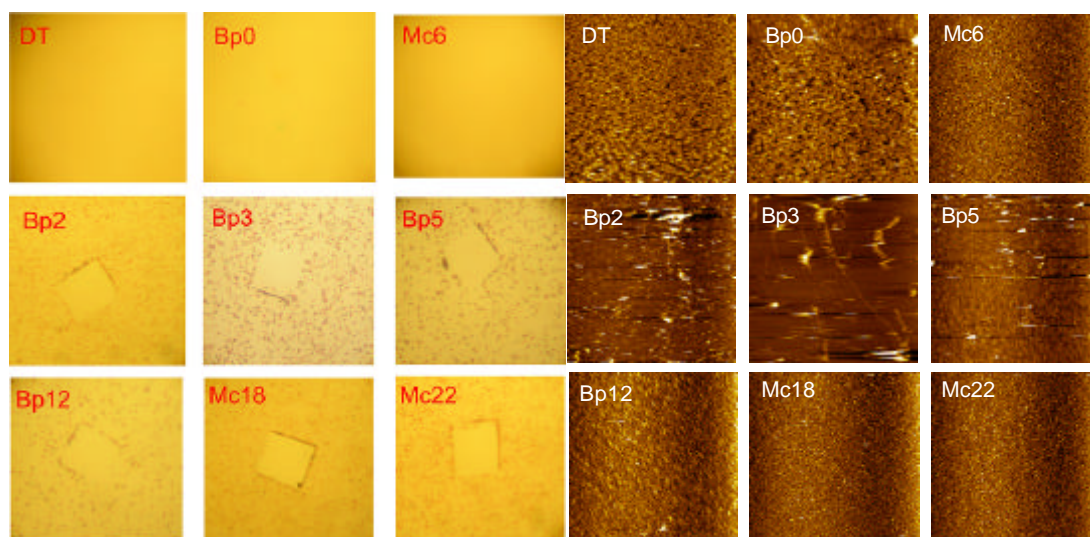


**Figure 4.7** Sweeping effect on different type of SAMs (Au/Si), the three left columns are optical micrographs and the three right columns are STM images (scan range is  $10 \times 10 \mu\text{m}^2$ ). Patterns (square) correspond to STM scan range. Copper deposition was  $-0.4 \text{ V}$  for 20 seconds or 40 seconds depending on the copper particles quantity. The STM sweeping parameters were  $0.1 \text{ nA}$  and  $1.0 \text{ V}$ . Note that uniform layers of Cu were deposited on the surface of DT, BP0, and MC6.

Because the metal deposition mechanism differs, the sweeping effect is also different depending on the type of SAMs. Table 4.1 lists several types of SAMs that shown different sweeping effect under the same scanning conditions.

**Table 4.1** Copper deposited on different types of SAMs show different sweeping effect. Samples were prepared on Au/Si in ethanol at  $345 \text{ K}$  overnight. Copper deposition was achieved by keeping

the sample at -0.4 V for 20 seconds or 40 seconds depending on the observed growth rate. Tunneling parameters were 0.1 nA and 1.0 V.

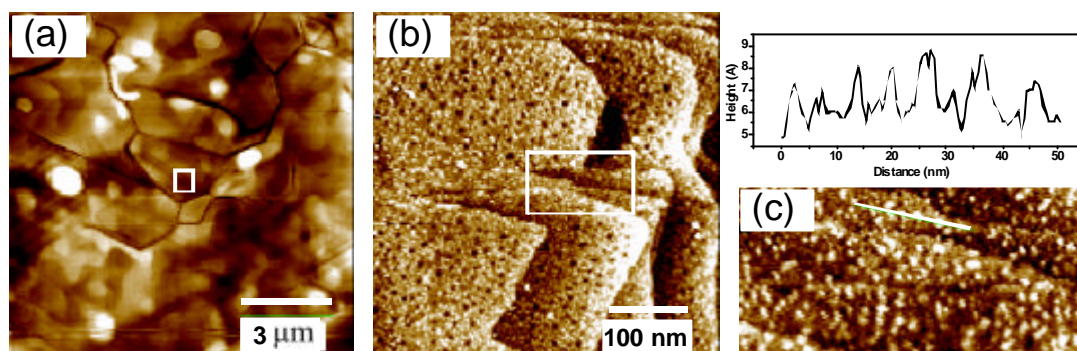
Type of SAMs	STM image shows big particles?	Optical micrograph shows STM sweeping area?
DT	No	No
BP0	No	No
BP1	Some	Some
BP2	Some	Yes
BP3	Some	Yes
BP5	Some	Yes
BP12	No	Yes
MC11	Some	Yes
MC18	No	Yes
MC22	No	Yes
MUA	Yes	No
MHA	Yes	No

We classify the molecules into four categories: (1) DT, BP0, and MC6 SAMs do not block the copper penetration. The Cu deposited was well connected to the gold surface and appears uniform. Deposited Cu is very stable and cannot be removed by STM tip. (2) BP12, MC18, and MC22 prevent Cu penetration. Deposited Cu particles are on top of the SAMs, and are easily swept by the tip. (3) MUA and MHA, which have acid terminal groups can coordinate with Cu and thus copper is observed. (4) BP1, BP2, BP3, BP5, and MC11 SAMs can block the copper penetration to some extent. However, some copper penetrates through the SAMs and forms mushroom-type copper structures. STM can image some big particles (mushroom structures), while the majority of particles is easily swept away.

## 4.2.2 Sweeping Effect at the Nanoscale

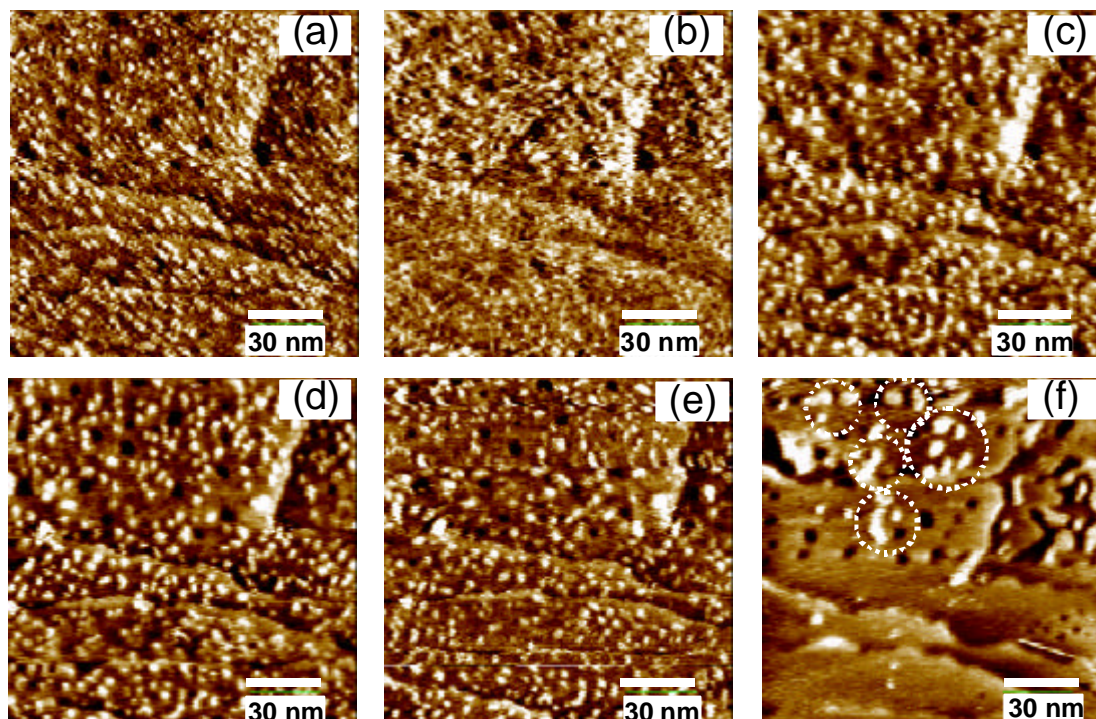
### 4.2.1.1 Sweeping on Cu Deposited SAM Surfaces

The sweeping effect described above was in the scale of micrometer range. Now we further investigate this effect on the nanoscale.



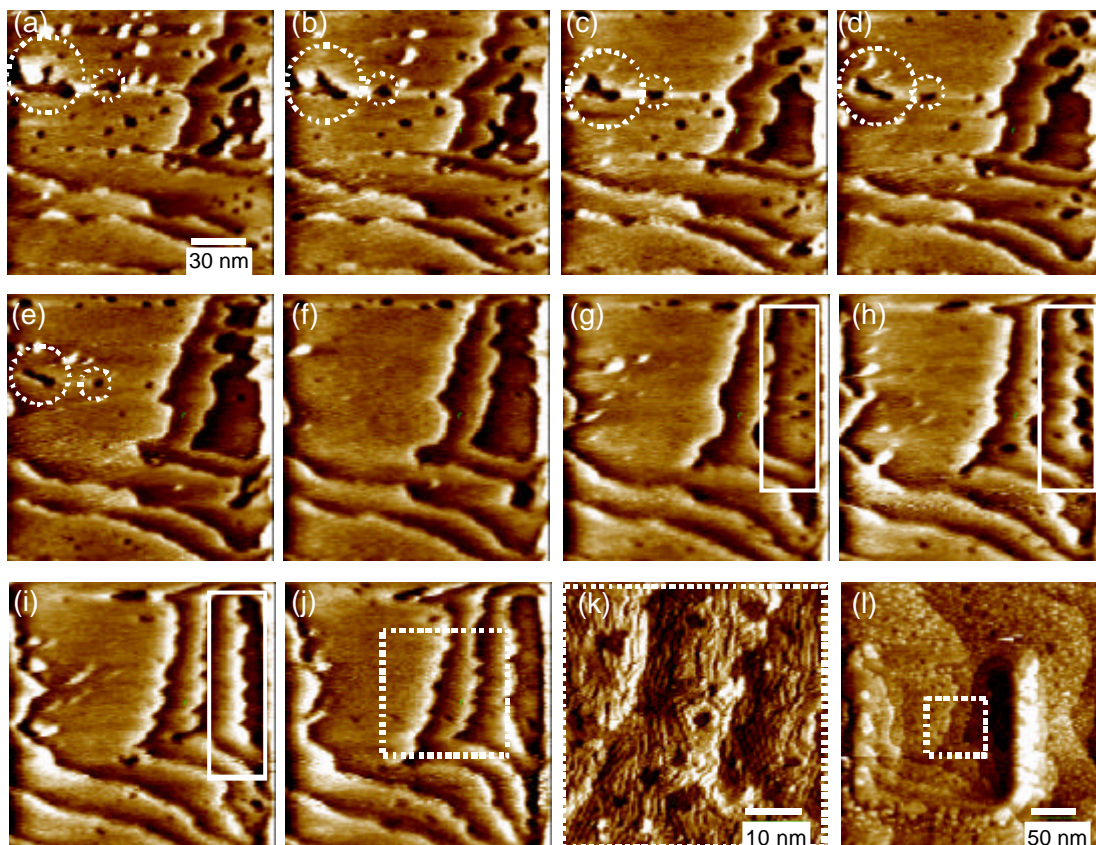
**Figure 4.8** (a) STM images of bulk Cu on MC11/Au after two pre-scanning at 0.1 nA and 1.0 V; (b) STM image selected from (a) (see white square). (c) STM image selected from (b) (see white rectangle). (b) and (c) were recorded with 3 pA and 1.0 V. The sample was prepared by immersing Au/Mica into ethanol solution at 345 K for overnight. Copper deposition was done at -0.35 V (vs. Cu wire) for 80 seconds. The sample was then immersed into MC11 to reabsorb MC11 to prevent Cu oxidation.

Figure 4.8 (a) shows an STM image of a Cu/MC11/Au sample after two STM scans. Bulk copper has been removed completely. At high resolution (see (b) and (c)), a large number of small islands were observed. These islands have a diameter of 1-3 nm and a height of 2-3 Å. They are assigned to UPD nanoislands.<sup>49,50</sup> They remain on the surface after more than 10 scans at 3 pA and 1.0 V. As illustrated in Figure 4.4, these islands were buried underneath the original SAM. Therefore they are more stable than bulk copper under the same scanning conditions. However, these nanoislands were swept away at higher tunneling currents (see Figure 4.9). From (a) to (e), the tunneling current was 10 pA, 100 pA, 1 nA, 2 nA, and 3 nA (bias at 1.0 V) respectively. It was found that these islands were moved as the current increases. However, sweeping was not as efficient as in the case of bulk particles. Sweeping became more efficient when the bias was reduced from 1.0 V to 0.1 V. It was found that not only copper islands were removed, but also the Au surface was etched under these parameters as shown in (f). At the right edge of (f), a Au layer was removed combined with copper islands. At the same time, some bigger islands were formed on the surface as indicated by circles. These islands have a diameter of several nanometers and a height of ~5 Å, which could be a mixture of Au and Cu.



**Figure 4.9** STM images showing the dynamic process of sweeping on MC11/Au. From (a) to (e), the tunneling current was 0.01 nA, 0.1 nA, 1 nA, 2 nA, and 3 nA, respectively (bias at 1.0 V). Sweeping is slow if only the tunneling current was adjusted. However, a sudden etching (f) happens when the bias was reduced to 0.1 V (keeping the current at 3 nA).

Images scanned after (f) are shown in Figure 4.10. The etching continues from the edge of the right side and the motif at the center was removed to the edge as shown from (a) to (d). It was found that etching of Au proceeds layer by layer. As shown in (g) and highlighted by the rectangle, etching started from the edge of the scan range and small holes were created first. From (h) and (i), the holes get bigger and the depth of this depression is about one Au atom. (k) shows an image corresponding to the area shown in (j). The image was recorded at 5 pA and 1.0 V so that the scan allows imaging but do not further etch the surface. Striped structures were observed on the surface and were confirmed to be the SAM molecules as will discuss later. Image (l) shows an STM image at large scale. A clear depression was found in the scanned area. Rows of accumulated material were seen on the edges.



**Figure 4.10** STM images scanned after (f) in Figure 4.9 showing the evolution of etching process. Parameters used from (a) to (e) are 3 nA and 0.1 V. From (f) to (j): 3 nA and 0.01 V. (k) is recorded at 5 pA and 1.0 V. (k) reveals a striped structure. (l) shows the same location but with a larger scan range.

During etching, there was another phenomenon happening at the same time, as shown in Figure 4.10 from (a) to (f). It was clearly seen that some holes (marked by circles) originally at the surface are filled. This might be due to a SAMs-Au complex being trapped in these pits during the scanning. A similar effect was also reported by McCarley et al.<sup>51</sup>

Figure 4.10(k) reveals a striped structure after the sweeping. This could be the result of molecules and possibly Au and Cu diffusing back and forming a new low density structure.<sup>52</sup> A larger area of  $1000 \times 1000 \text{ nm}^2$  was scanned to check this hypothesis since it provides more chance to observe the surface with more details and it provides a flatter surface after modification.

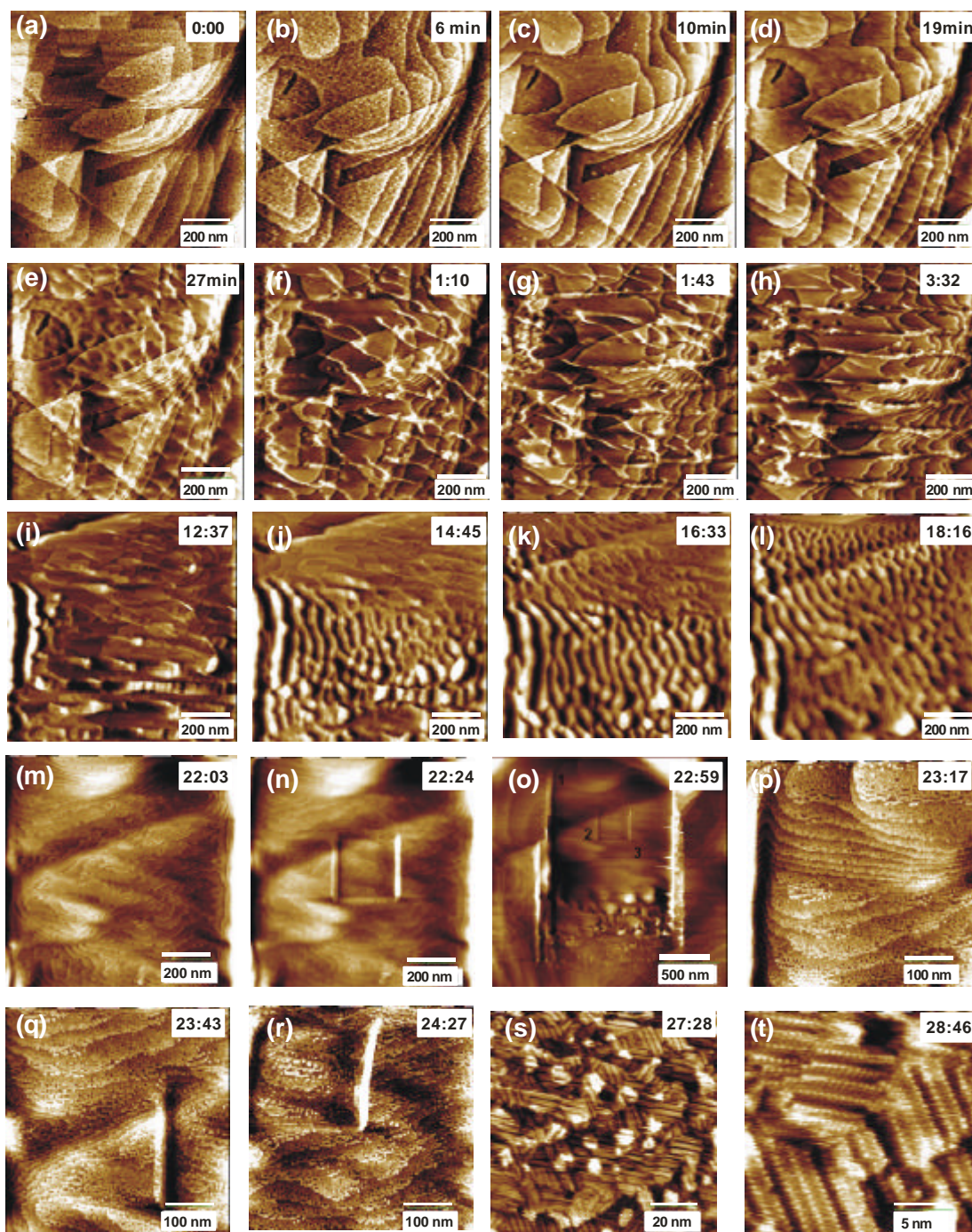


**Figure 4.11** STM images of MC11/Au/Mica showing the dynamics of the sweeping effect. (a) an area scanned by imaging mode (0.01 nA and 1.0 V). Images from (b) to (m) were scanned by modifying mode (3 nA and 0.01 V). Images from (o) to (t) were recorded at imaging mode (0.01 nA and 1.0 V). A  $250 \times 250 \text{ nm}^2$  square was swept (3 nA, 0.01 V) in the center as shown in (n). (p), (q), and (r) corresponds to the area 1, 2, and 3 in (o), respectively. (s) and (t) show the molecular structure on (r).

Figure 4.11 shows STM etching in a  $1000 \times 1000 \text{ nm}^2$  area. (a) shows the area under

imaging mode (10 pA, 1.0 V). It was then changed to modifying mode with parameters of 3 nA, 0.01 V. Changing from imaging to modifying condition immediately triggers displacement of material at the surface as shown in (b). After two scans copper islands all disappear as shown in (d). A close look at (d) reveals that something was moving from left to right. Material was travelling so far that it can be easily distinguished between two subsequent STM images with the time passed between them is about 4 minutes. Images from (e) to (m) show a competition of sweeping and back diffusion. It was found that after more than 20 hours of modification, the original surface was completely changed. The triangular shape as shown in (a) has disappeared. The area of  $250 \times 250 \text{ nm}^2$  shown in (n) was also etched (under the same scanning parameters (3 nA, 1.0 V)). Two rows of material can be found at the edge of the scanned area. (o) shows the zoom out of (n), and two rows of particles were observed on the edge of the modified area. Images (p), (q), and (r) correspond to the area labelled as 1, 2, 3 as shown in (o), which show striped structures. (s) and (t) showed the molecular resolution of area 3. Small islands with diameters of about 2-3 nm were observed on the surface (see (s)). It was found that the structure is different to a native SAM of MC11. Figure 4.12 shows molecularly resolved structures after etching. Line *a* indicates that the height difference between the island and the surrounding area is about  $2.5 \text{ \AA}$ . Thus these could be isolated Au(Cu) islands buried under the SAM. Along line *b*, the distance between two molecules is  $6 \text{ \AA}$ . The structure is unusual as for alkane thiol assembled on Au(111) where the nearest distance is  $5 \text{ \AA}$ . It is not sure at the present whether this is caused by the drift during scanning. Along line *c*, the distance between two rows is about  $12 \text{ \AA}$ . Between rows, some molecules are also visible. These are about  $0.6$  to  $1.0 \text{ \AA}$  lower than the surrounding structure. The striped structure is probably a loosely packed SAM after sweeping. In summary, the molecularly resolved structure seen after heavily etching/sweeping clearly demonstrates the high mobility of the SAM on the substrate.

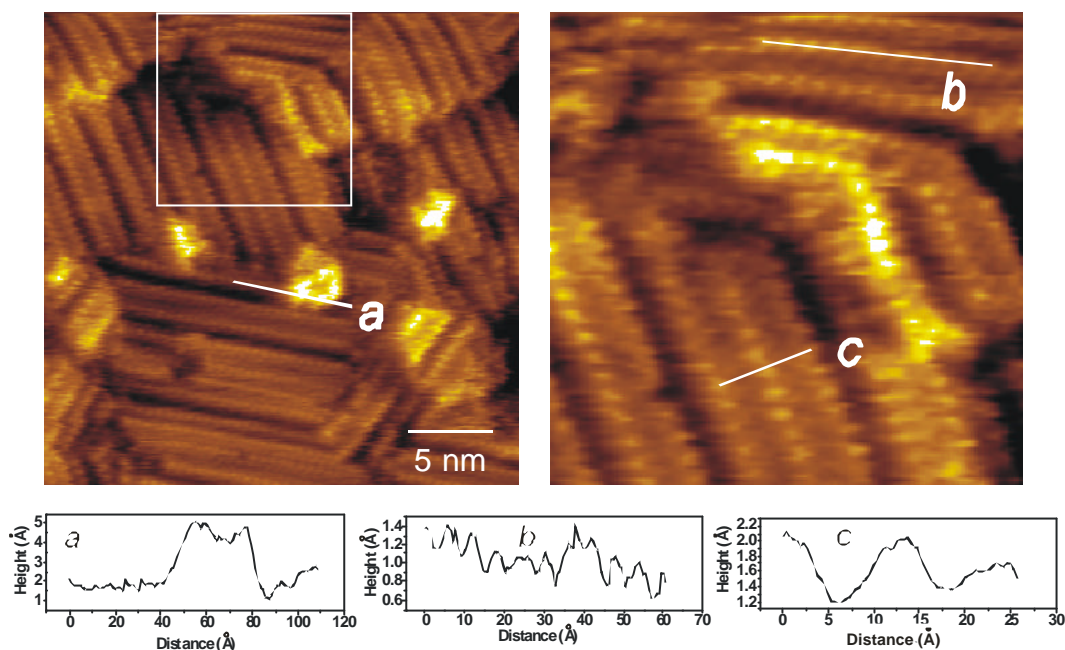


**Figure 4.12** High resolution images of MC11/Au/Mica surface after etching as shown in Figure 4.11. Line *a* shows the height difference of the protrusion is about 2.5 Å, indicating a Au or Cu island. Along line *b*, the distance between two molecular is 6 Å. Along line *c*, the distance between two rows is about 12 Å.

#### 4.2.1.2 Sweeping on SAM Surfaces

We also investigated the STM sweeping effect on MC11/Au surface without Cu modification as shown in Figure 4.13. After etching, several holes were created in the scanned area. These are marked by a square in (b). Two rows of material accumulated on the edge of the scanned area. These two rows of accumulated material are likely to be gold atoms moved from the scanned area by the STM tip. High resolution images (see (c) and (d)) of the etched area show that molecules cover the surface. The cross section shows that the distance between molecules is 5 Å, which fits the distance of upright standing MC11 molecules on the Au(111) surface. This strongly suggests that the SAMs diffused back after the sweeping. What is surprising is that the re-assembly of the molecules is very quick as inferred from image (c) which was taken just 5 minutes after etching. This may be due to two reasons. First, molecules pushed to the edge of the scanned area diffuse easily back to the newly created Au surface to

minimise the surface energy. Second, in confined nanoscale areas, the surrounding SAM assists reassembly in the etched area. This confinement assisted assembly will also be discussed in the following section.

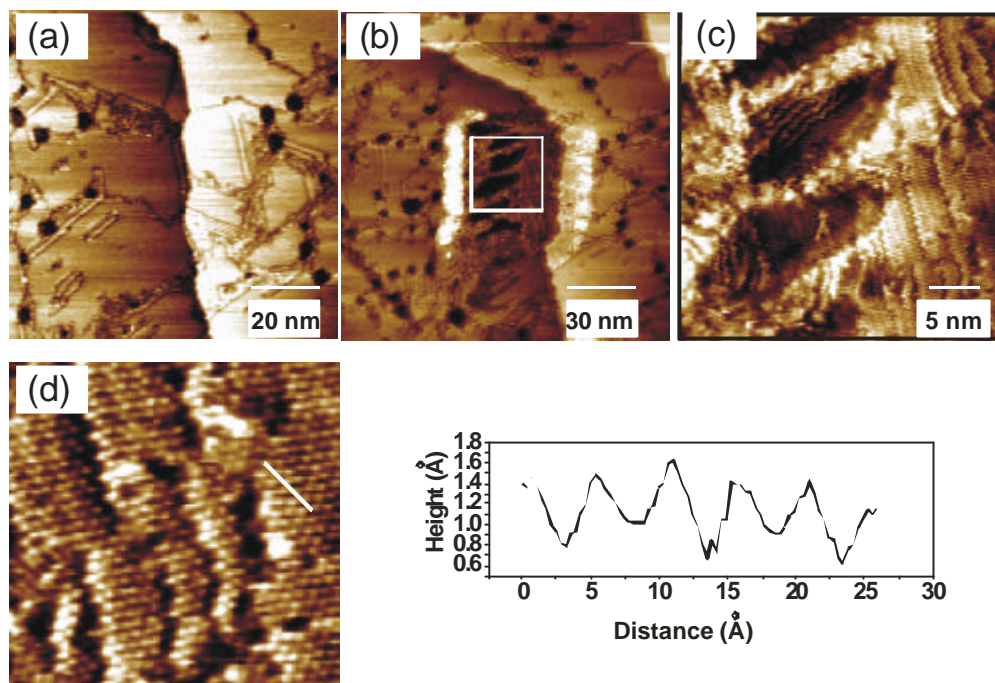


**Figure 4.13** STM images showing STM sweeping on MC11/Au surface. After sweeping (0.9 nA, 0.8 mV, 12 lines/s), two rows of material are seen at the edge of the scanned area (b). The molecular structure can be clearly identified in the swept area (c). (d) shows a high resolution STM image of the molecular structure. The cross section shows that the nearest distance between molecules is 5 Å. Images were recorded with 0.01 nA and 1.0 V.

### 4.2.3 Discussion

It has been reported that STM sweeping/etching also happens on other materials. A single SnSe<sub>2</sub> layer can be removed with a tunneling current of 0.66 nA and a bias of 480 mV (slow etching is also observed for tunneling as low as 50 pA and bias of 50 mV).<sup>34</sup> Similar etching can also happen on the surface of TiSe<sub>2</sub> and NbSe<sub>2</sub>. The authors proposed four possible mechanisms. (1) Reactive species produced by the electric field and/or current flow between tip and sample attack the most reactive sites (defects or step edges). This results in volatile products. However, this mechanism is unlikely since etching also occurs in He atmosphere.<sup>34</sup> (2) Heat or power dissipation in the

confined region of the current flow induces etching. However, no clear dependence on bias or current was observed suggesting that this is also not the explanation.<sup>53</sup> In addition, the heat produced by the current is believed to be negligible.<sup>54</sup> (3) Field-assisted evaporation. Since etching occurs at both positive and negative biases the mechanism is unlikely. Moreover, in our case, since the etching is more efficient at low bias, the mechanism cannot be valid. (4) Abrasion of the surface via direct tip-sample contact.<sup>55,56</sup> This mechanism is more likely.

Abrasion-induced damage is commonly used for nanografting with AFM.<sup>57,58</sup> Similar etching processes have also been observed on SAM-modified Au surfaces by STM.<sup>33,36,37</sup> It is interesting to note that, without adsorbed SAM, the Au surface is not etched by the STM tip.<sup>32,38</sup> Here, for the first time, we show direct evidence that the SAMs diffuse back onto etched/swept area. A review of how SAMs bind to the gold surface can help to understand this effect. For a number of years, it was believed that the adsorption sites of the sulfur are threefold hollow sites of the bulk terminated Au(111) surface. However, in 2003, Kondoh et al. found that for CH<sub>3</sub>S, the binding position is at the atop position of the defect-free Au(111) surface by scanned-energy and scanned-angle photoelectron diffraction.<sup>59</sup> Based on STM measurements and density-functional theory calculations, Maksymovych et al. proposed a new structural mode for the lowest-coverage SAM of alkane thiols on Au(111) as pairs of RS species bonded via a Au adatom (RS-Au-SR).<sup>60</sup> The result is in agreement with Yu and Wang's work which proposed that alkylthiolate SAMs on Au(111) involve Au-thiolate moieties, rather than thiulates bonded directly to the atomically flat substrate.<sup>61,62</sup> The same behaviour was also observed in a totally different complex phase of tertiary butylthiolate on Au(111) showing that the adatom-thiolate moiety can also occur other than n-alkane thiols.<sup>61</sup> S binds strongly to Au atoms and therefore weakens the bonds between the attached Au atoms and their neighbours.<sup>63,64</sup> It is indeed suggested that adsorption of thiol results in a significant reduction in binding energy between the two top layers of gold atoms.<sup>33</sup> Thus, under the influence of the tip, the first layer of gold atoms, together with the adsorbed molecules, can be easily removed. Once the top layer

of gold and the adsorbed molecules are removed, the second layer of bare gold becomes the top layer. The net effect is that gold thiolate is pushed to the edge of the etched area, where Au atoms become incorporated into the substrate while the molecules diffuse back to the scanned area, and trigger a further etching. Figure 4.14 shows a schematic illustration of the etching effect.

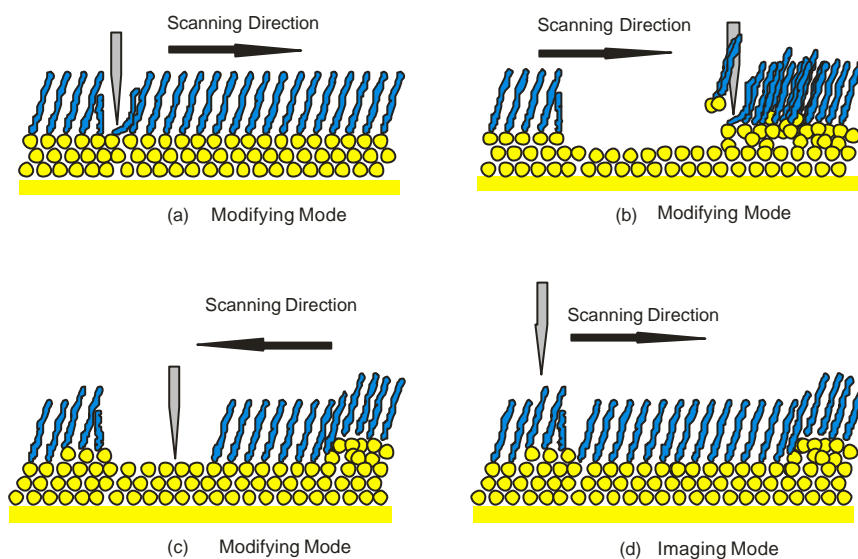


**Figure 4.14** Cartoon illustrating the sweeping effect. The tip penetrates the SAMs in the modifying mode (high current and low voltage). The top layer of Au atoms is easily removed by mechanical interaction as shows in (b). However, when the tip scans back, molecules diffuse back to the exposed area as shown in (c) and (d).

#### 4.2.4 Conclusions

For metal deposition onto SAM modified substrates, the blocking behaviour depends on the molecular length and on the terminal functional group. (1) DT, BP0, and MC6 SAMs do not block copper penetration. The Cu deposited was well connected to the gold surface and appears uniform. Deposited Cu is very stable and cannot be removed by STM tip; (2) BP12, MC18, and MC22 prevent Cu penetration. Deposited Cu particles are on top of the SAMs, and are easily swept by the tip; (3) MUA and MHA, which have acid terminal groups can coordinate with Cu and thus copper is observed;

(4) BP1, BP2, BP3, BP5, and MC11 SAMs can block the copper penetration to some extent. However, some copper penetrate through the SAMs and forms mushroom-type copper structures. STM can image some big particles (mushroom structures), while majority of particles are easily swept away by STM tip.

The sweeping effect can be adjusted by changing the I/V parameters, which control the tip-sample gap. Sweeping is more efficient for smaller tip-sample distance. Molecularly resolved images confirm that after sweeping, the scanned area remains covered by molecules in a mechanism of diffusion. Such process can repeat and result in a layer by layer etching.

## 4.3 Displacement Patterning

### 4.3.1 Introduction

Substrates bearing a SAM pattern created by lithography can be used for assembling another SAM by immersion into a second SAM solution.<sup>27</sup> SPM offers several advantages such as patterning and imaging at the same time at high resolution and in solution. However, the twofold use of SPM as analytical instrument and modification tool requires different sets of parameters for the two modes.

Displacement patterning based on SPM has mostly been done with AFM in the past.<sup>27,57,58,65-67</sup> By applying a relatively large load, the AFM tip can remove molecules. The process is usually called nanoshaving and is described in Chapter 1. The smallest structures demonstrated so far are 10 nm lines with a separation of 20 nm, and island of about 32 molecules of MC18 in a MC10 matrix.<sup>68</sup>

STM was been used for displacement patterning by applying high voltage pulses (several volts, “punching mode”) to the tip. The pulses remove substance (SAMs/metal atoms) between the tip and the substrate.<sup>25,26,35,42</sup> However, only a few studies<sup>25,26,28,41,42</sup> have been reported and the types of SAMs investigated are quite limited. The smallest features obtained are typically in the range of 10-30 nm

depending on the applied voltage<sup>25</sup> and patterns usually do not show uniform replacement.

So far, thiols used most as displacing species are ferrocenylundecanethioacetate SAM (FcC11SAc)<sup>25,41,42</sup> or a thiol with similar properties as the matrix layer (i.e. MC10/MC12)<sup>27,69</sup>. It was observed that when thiols were used in replacement lithography, a larger amount of adventitious replacement occurred at defect sites.<sup>27</sup> The reason is that different thiols have different driving forces to assemble onto the gold substrate which can cause replacement of one type by the other. Therefore, it is crucial to use a high quality SAM for patterning, such as the high temperature phase of BP2.<sup>70</sup> The following section discusses the punching mode as a method to create nanopatterns. We also found a new patterning method that operates at moderate bias and current, which can potentially lead to high resolution patterns. We analyze the mechanism behind the replacement process by using different molecules.

### 4.3.2 Patterning by Punching Mode

In contrast to the previous section where a mechanical removal of SAMs at low bias was presented, the present chapter deals with modification at high bias. By applying a high voltage between the STM tip and the sample, a SAM can be locally removed. We found that positive bias (sample positive) damages the surface more than a negative (sample negative) one as shown in Figure 4.15.

For (a), the sample bias was kept at 0.5 V before punching. A positive pulse of 3.5 V results in a hole as deep as 1 nm. For (b), the sample bias was also kept at 0.5 V and the pulse was -3.5 V. The area of damage is as large as in (a), but the depth is significantly less. For (c), both voltages were negative and the damage was even smaller. Cross section analysis clearly shows the difference between these three holes. The difference between (b) and (c) can be explained that for (b), in order to switch from the positive to negative bias, the tip has to cross the zero point, which brings the tip to the surface, can cause more damage than (c).

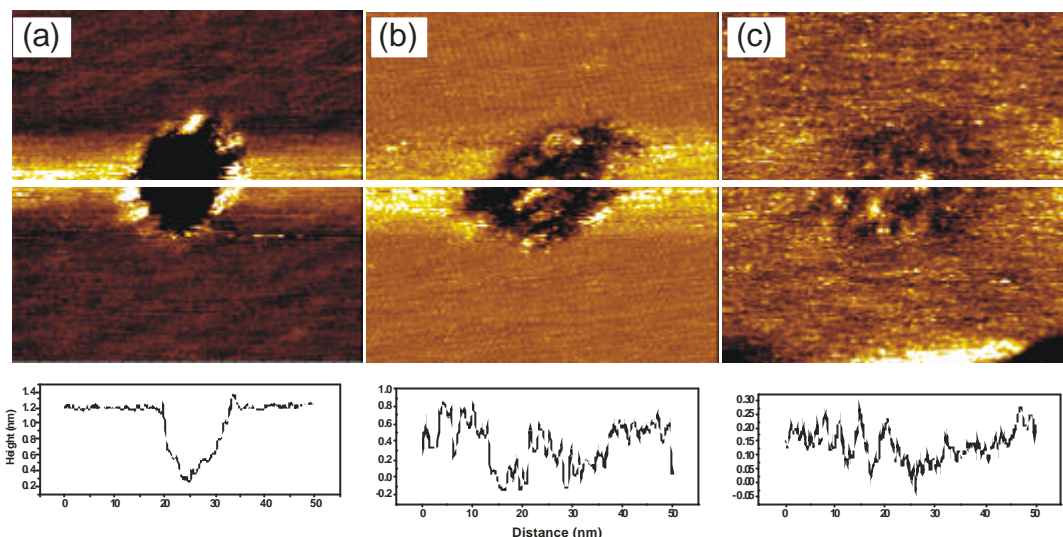


**Figure 4.15** STM images show damage created on a BP2/Au surface under different bias and voltage pulses. (a) Imaging bias = 0.5 V and pulse = 3.5 V for 50 ms. (b) Imaging bias = 0.5 V and pulse = -3.5 V for 50 ms. (c) Imaging bias = -0.5 V and pulse = -3.5 V for 50 ms. Line profiles show the depth of the holes.

One should note that the damage not only relates to the bias, but also to the current. Under the same bias, a higher current moves the tip closer to the surface, thus, causes bigger damage.

Writing speed also plays a role when patterning lines (see Figure 4.16). The lines shown in (a), (b), and (c) were written at 4 V, with increasing speed from 0.1  $\mu\text{m/s}$  to 1.25  $\mu\text{m/s}$ . The line width decreases from about 15 nm to about 8 nm. High quality pattern lines are obtained by combining a voltage of 5 V with a speed of 2  $\mu\text{m/s}$  (see Figure 4.16 (d)).

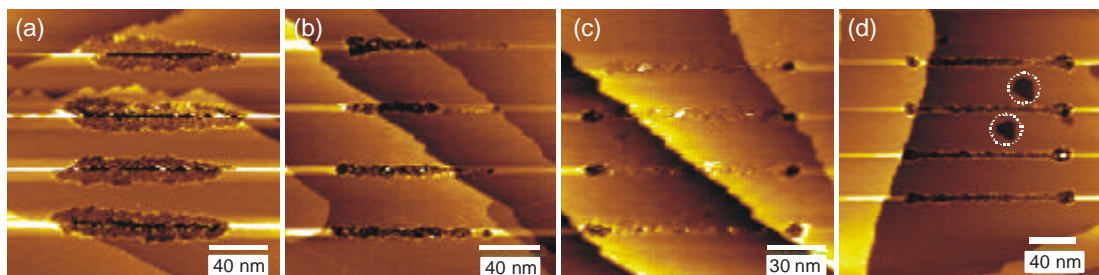


**Figure 4.16** STM images showing lines created on a BP2 SAM with different parameters. (a) Pulse = 4 V, written speed 0.1  $\mu\text{m/s}$ . (b) Pulse = 4 V, written speed 1  $\mu\text{m/s}$ . (c) Pulse = 4 V, written speed 1.25  $\mu\text{m/s}$ . (d) Pulse = 5 V, written speed 2  $\mu\text{m/s}$ . Depressions marked by circles are Au vacancy islands.

By controlling the timing of pulses an array of holes can be generated as shown in Figure 4.17. Holes are about 10 nm wide and about 5 Å deep, which corresponds to about two atomic Au layers.

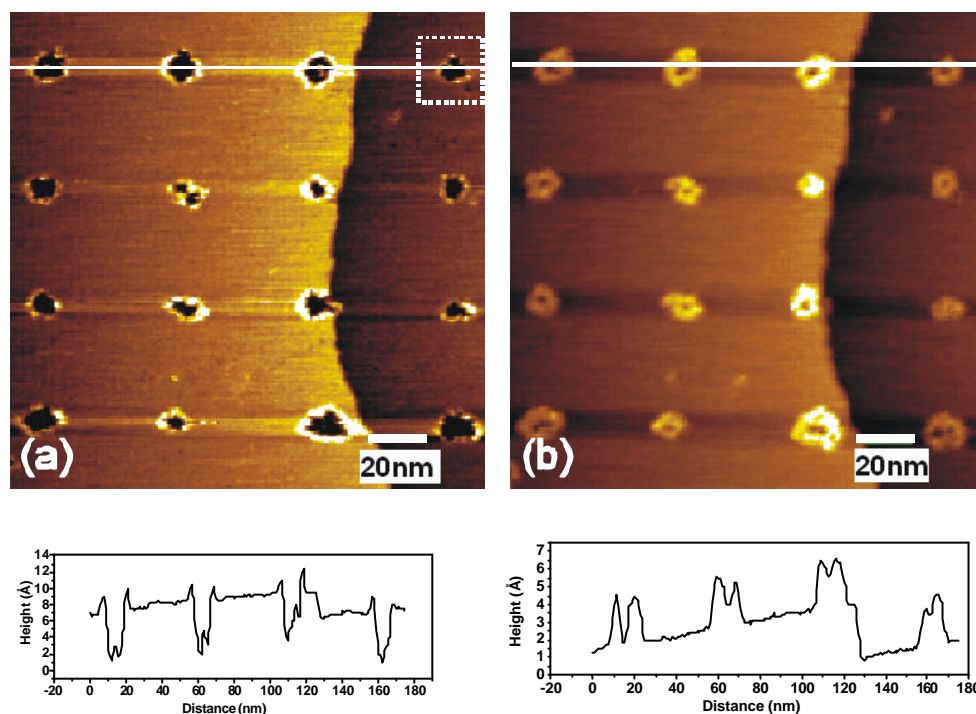


**Figure 4.17** (a) STM images showing a hole array generated on BP2/Au surface in BP3/hexadecane solution by pulses under 3.0 V for 50 ms. (b) Holes can be filled by BP3 molecular in hexadecane solution. Image was taken after 5 hours. The line profiles show the change in height difference upon BP3 assembling into the punched holes.

In contrast to air or vacuum environment, punching in solution allows replacement of molecules *in situ*. Figure 4.17(b) shows the STM image of holes backfilled by BP3 (after 5 hours). The line profile shows that they are now about 2-3 Å higher than the surrounding area, in sharp contrast to the line profile right after the punching. However, it was interesting to find that some of the holes are not completely filled as revealed by the line profiles (also ref. to 3D image in Figure 4.18). Small holes can easily be filled, while bigger holes are more difficult to be filled. This unexpected behaviour is not clear at present, but an explanation could be that replacement is more difficult in the centre of the hole due to ordered SAM compared to the edge area.

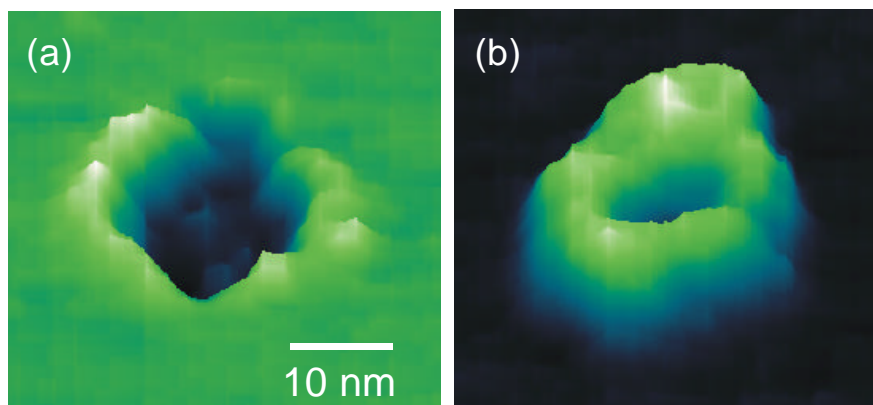


**Figure 4.18** 3D images of a hole selected from Figure 4.17 (marked by square). (a) The hole right after punching. (b) The hole after BP3 filling.

Adjusting the parameters allow the creation of a 1 nm sized “hole” (see Figure 4.19). Figure 4.19(a) shows an area selected for patterning (bright spot as label). (b) and (c) were obtained after applying pulses of 2.6 V for 50 ms and 2.7 V for 50 ms, respectively. No holes were created under these parameters. (d) shows that a 1 nm sized “hole” generated by a pulse of 2.8 V for 50 ms. However, a close look at this hole shows that it is only about 2 Å deep, which suggests that the BP2 molecule is still occupying the area. The simple explanation could be that the terminal CH<sub>3</sub> group broke from the molecular. Another explanation could be that the thiol complex is trapped by the surrounding BP2 molecular during the popping out as a result of insufficient bias (not enough to excite the SAMs or Au atoms or both). As the conductance of such disconnect/weakly bonded motif is weaker than the normal SAMs nearby, so in constant current mode, the topography shows this area is deeper than the surrounding area.

Similar results with holes as small as 2 nm were obtained by W. Mizutani et al. in UHV.<sup>35</sup> Compared with UHV, the advantage of punching in hexadecane is that it is a simple method and pattern (holes) created can be filled *in situ* if a second SAM present in the hexadecane solution as shown in Figure 4.17.

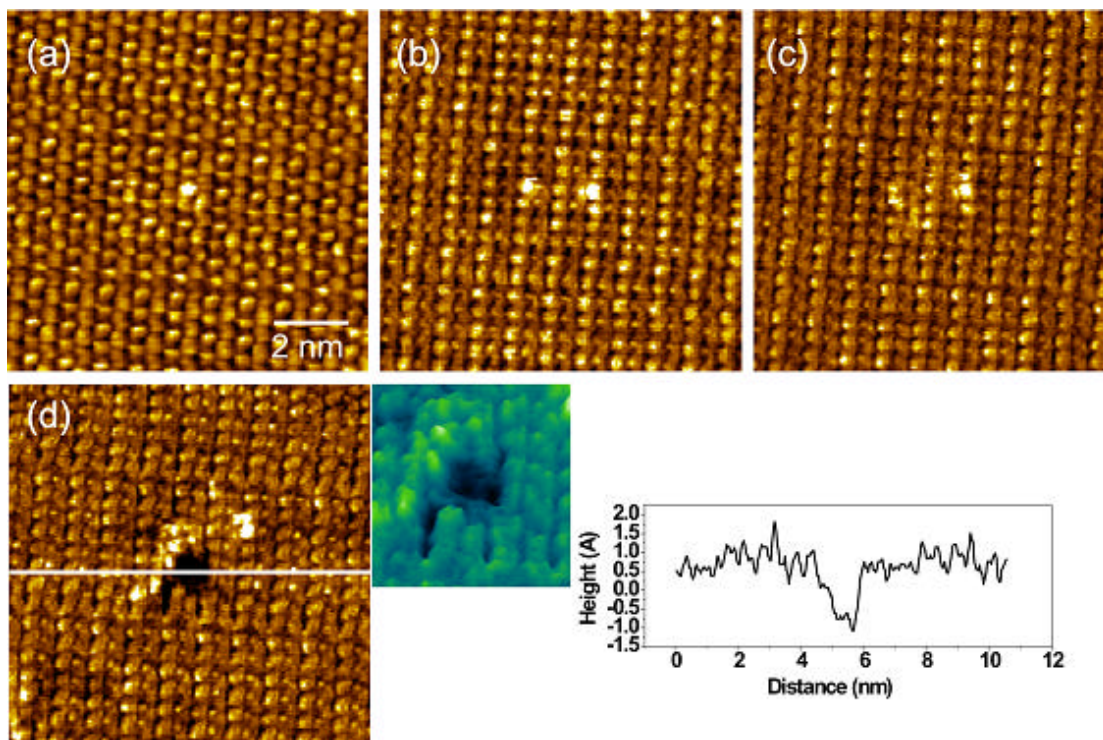


**Figure 4.19** STM images showing that 1 nm “hole” created on BP2/Au surface by punching in hexadecane solution. (a) shows a selected area for patterning (a bright spot as a label). (b) and (c) were obtained by applying pulses of 2.6 V for 50 ms and 2.7 V for 50 ms respectively, which showed that inefficient pulse cannot create a hole. (d) shows that a 1 nm “hole” can be created when the bias was increased to 2.8 V for 50 ms, the inset shows the 3D image of the hole. The cross section analysis shows the “hole” is about 2 Å deep. All images were obtained at  $I = 6$  pA, bias = 0.5 V.

However, if the voltage used is too high, dots will be generated instead of holes as shown in Figure 4.20. Arrays of dots of about 30 nm large and 5 nm high were formed at a voltage of 5 V. These dots are believed to be a combination of Au atoms, BP2 molecules and Pt/Ir coming from the STM tip (one way to clean the STM tip is by applying a high voltage on the STM tip to make it sharp, usually several volts).

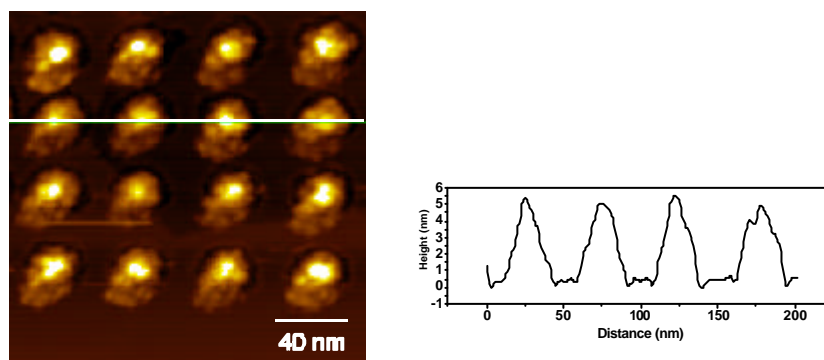


**Figure 4.20** STM image (in air) showing that arrays of dots instead of holes were generated on BP2/Au/Mica surface by applying pulses of higher voltage bias (5 V for 5 ms).

In summary, a positive (sample positive, tip negative) high voltage (2.5–5 V) applied on the surface of a BP2 SAM can locally damage the SAM and lead to generation of holes. The damage depends on the bias and on the current. Damaged areas can be filled by a second thiol (e.g. BP3) in hexadecane solution. However, small pulses do not create holes big enough to trigger any replacement. For too high pulses, islands are formed.

### 4.3.3 Nanografting

#### 4.3.3.1 Nanografting on Uniform SAMs

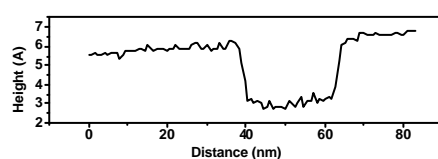
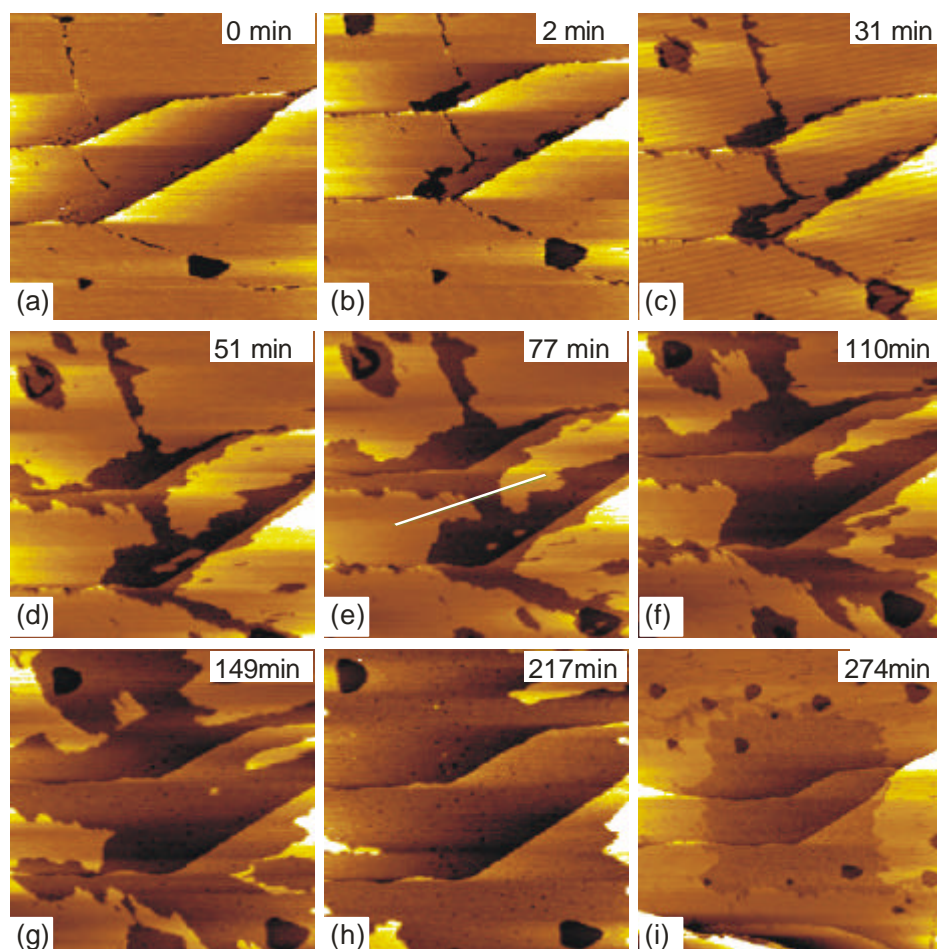


**Figure 4.21** STM images showing SAM of BP2 (matrix layer) “etched” in MC12/hexadecane solution. The etching started at the domain boundaries and defect sites as shown in (a). The etched area expanded and covered the whole surface (scanned area,  $250 \times 250 \text{ nm}^2$ ) as shown from (a) to (h) which takes about 260 minutes. (i) shows a large area around the region scanned in (a-h) ( $I = 50 \text{ pA}$ , bias =  $0.5 \text{ V}$ ). The cross section analysis shows that the height difference is about  $2.5 \text{ \AA}$ .

During experiments on punching and backfilling in hexadecane solution, we found that only particular types of thiols such as BP1, BP3 filled the holes but did not replace the BP2 SAM. However, if MC12 was used, the situation is different as shown in Figure 4.21. It was seen that the surface was “etched”, which started from the domain boundary of the BP2 layer and expanded across the whole area that was scanned by the STM tip. One should note that this effect was observed at a bias/current combination which is usually used for imaging in air.

It was found that etching happens as soon as the area was scanned by the tip. From (b) to (h), it was clearly shown that domain boundaries, step edges and depressions are the trigger points of the etching. After about 4 hours scanning, the whole area was totally changed. This was confirmed by scanning a larger area ( $500 \times 500 \text{ nm}^2$ ) as shown in (i), a  $250 \times 250 \text{ nm}^2$  square pattern was found in the previously scanned area. As the parameters used to obtain the image of (i) are the same as the “etching” parameters, some “etching” was also happening outside the  $250 \text{ nm}$  square area. If the tip keeps scanning at those parameters, a new  $500 \times 500 \text{ nm}^2$  area of new pattern (MC12) will be created. (To avoid unwanted “etching”, one can withdraw the tip by reducing the current, see section 4.3.3.3). It was found that some small pits (vacancy islands) were formed during this process. This represents a typical process of assembly of alkane thiols on Au(111).<sup>71</sup> We ruled out that the process displayed in Figure 4.21 was a simple removal of BP2 (removal of BP2 leaving clean gold) as the cross section shown that the height difference between these two area is about  $2.5 \text{ \AA}$ . Also, we ruled out a tip induced change of the BP2 structure as in pure hexadecane or in the BP2/hexadecane solution, under the same parameters, no etching happens. Furthermore, SAM structure is confirmed in the displacement area (see Figure 4.23). We found out that this was a process of displacement as we later observed molecular structures of both areas.

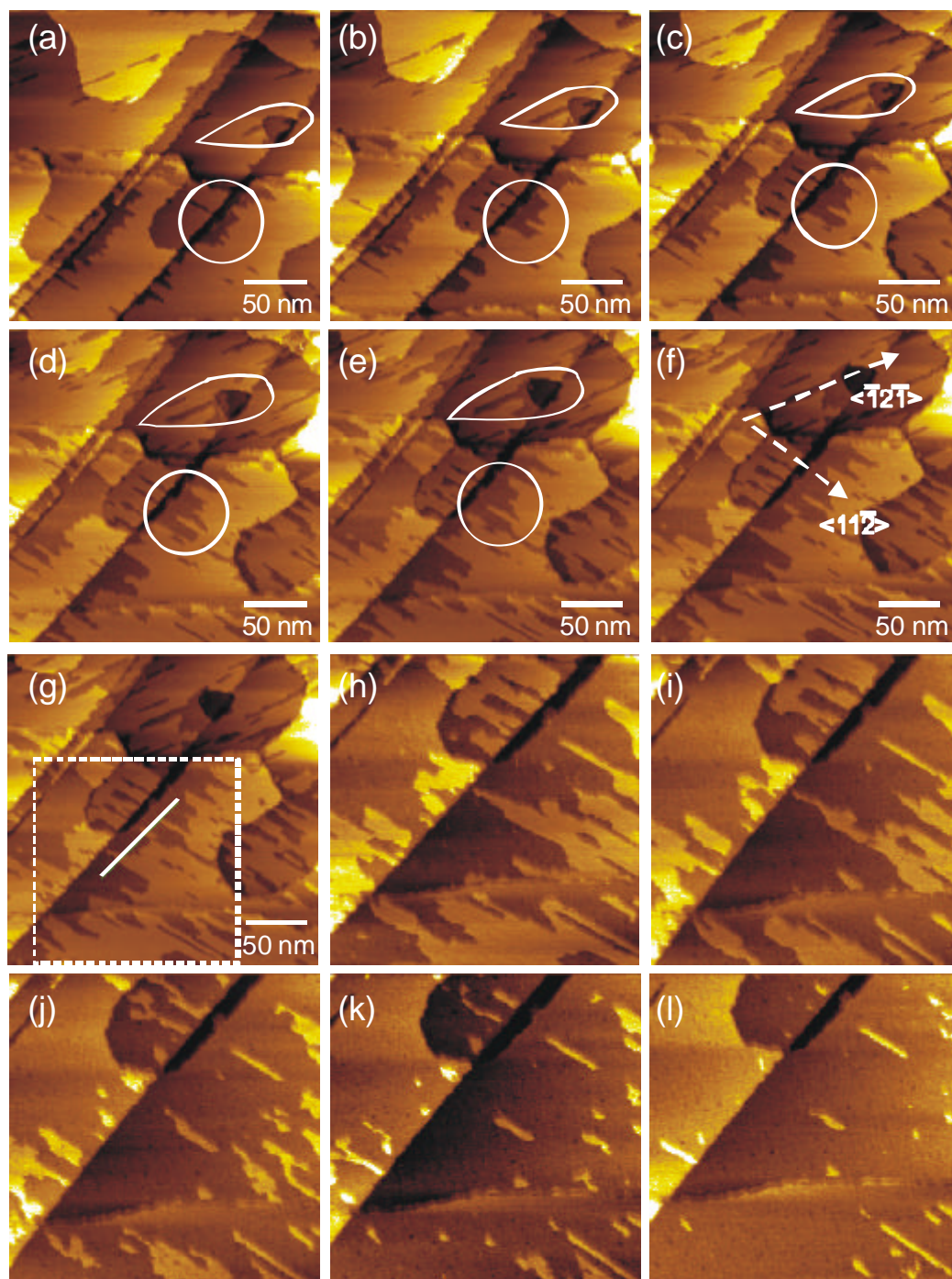


**Figure 4.22** STM images showing BP2 (matrix layer) replaced by MC6 in hexadecane solution. The replacement starts at domain boundaries and defect sites as shown in (a), similar to the

replacement of BP2 by MC12 (see Figure 4.21). (h) to (i) is the selected area in (g) as indicated by a square. The replacement from (a) to (g) takes about 37 minutes under the parameters of 0.05 nA and 0.5 V. From (h) to (i) takes about 21 minutes under the parameters of 0.075 nA and 0.2 V. The line profile corresponds to the line in (g).

Interestingly, an MC12 layer in BP2/hexadecane solution is not replaced. Also, BP2 SAM is not replaced by BP3 (see Figure 4.17). However, a BP2 SAM is replaced by MC6 (see Figure 4.22). Figure 4.22 shows STM images of a BP2 SAM (matrix layer) replaced by MC6 in hexadecane solution. Again, the replacement starts at domain boundaries and defect sites, similar to the replacement of BP2 by MC12 (see Figure 4.21). It is interesting that the replacement happens mainly in two directions,  $\langle 11\bar{2} \rangle$  and  $\langle \bar{1}2\bar{1} \rangle$  as shown from (a) to (e) indicated by circles. To understand this, molecular resolution structures are needed as shown in Figure 4.23.

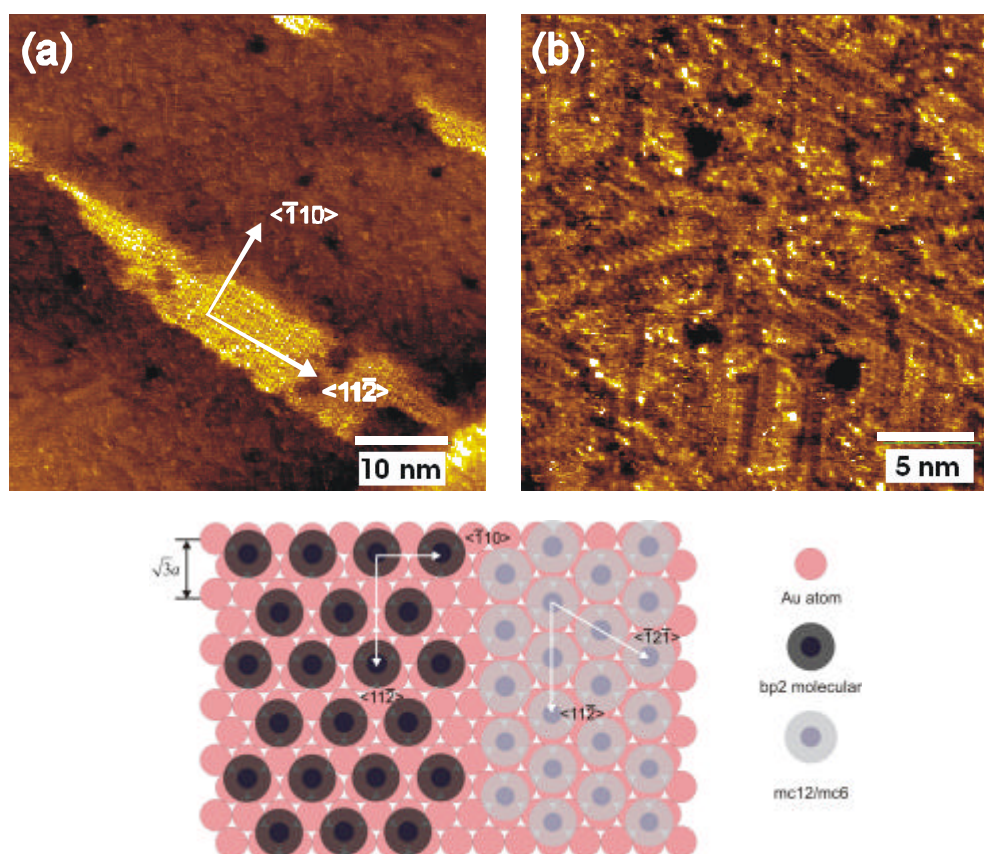


**Figure 4.23** STM images showing replacement of BP2 by MC6 in hexadecane. Two different structures can be clearly seen in (a). Brighter part is (a) BP2, and the darker part is MC6. The height difference is 2.5 Å. High resolution image of the MC6 structure is shown in (b). Images are obtained at 0.075 nA, 0.2 V. The schematic shows BP2 and alkane thiol assembled on Au(111).

In Figure 4.23, molecular resolution of both replacing molecules (MC6) and matrix

molecules (BP2) are shown in the same image. Bright region is BP2 and dark region is MC6. Etch pits are formed during self assembly of MC6, similar to what was seen for MC12. It was interesting to find that a very sharp edge is created along the  $\langle 11\bar{2} \rangle$  direction. The directional preference is related to the Au(111) structure as illustrated in the schematic in Figure 4.23. This might be due to the fact that molecules are more compact along  $\langle \bar{1}10 \rangle$  direction, while more open along  $\langle 11\bar{2} \rangle$  direction. This directional preference for replacement might be used for precisely controlling the pattern shape.

The line profile in Figure 4.22(g) shows that the height difference of BP2 and the MC6 is about 2.5 Å. It is the same difference as the BP2/MC12 even though molecular length of MC12 and MC6 are about 13 Å and 6.3 Å. BP2 is about 8.1 Å long (considering the tilt angle 30° for MC6 and MC12, and 45° for BP2)<sup>72</sup>. The height difference of the BP2/MC12 has been suggested to be the effect of solvent.<sup>40</sup> The height contrast will be reversed if the solvent between the tip and the SAM had a higher transconductance than the SAM. However this cannot explain the height difference of BP2/MC6 as MC6 is shorter than BP2. So these differences have to take into account the difference in the conductivities of the molecules.<sup>12,73</sup>

The conductance of a molecular wire can be expressed by the exponential law<sup>73,74</sup>:

$$G = G_0 \exp(-\beta d) \quad (4 - 1)$$

where  $G_0$  is the contact conductance,<sup>12</sup>  $\beta$  is the molecule-dependent decay constant, and  $d$  is the molecular length. For biphenyl part in BP2, the value of  $\beta$  is about 0.5 Å<sup>-1</sup>,<sup>75</sup> while for alkenes chain, the value varies from 0.6 to 1 Å<sup>-1</sup>,<sup>73,75-80</sup> (although most values are around 0.9 – 1 Å<sup>-1</sup>)<sup>75,80</sup>. However, quantitative calculations based on these values are only valid when the patterned SAMs have the same structure as when directly assembled on clean Au, e.g. the MC12 patterned in the matrix layer might not have a tilt angle of 30°. Also, the conductance of the solvent compared to the SAMs and where the tip is exactly positioned<sup>81</sup> have to be taken into account, this makes the quantitative calculation more difficult. However, qualitatively the height contrast can

be easily understood. As these images were taken under the constant current mode (0.05 nA, 0.5 V), the tip moves up and down across the surface to adjust the distance of the gap between the SAMs and the tip to keep the current constant. Assume that the tip is right on top of the BP2. To keep the same parameters when the tip move to MC12 molecules, the tip has to move down to the gold surface as the conductivity of biphenyl is better than alkane thiol. The result is that the tip is scanning smoothly on top of the BP2, but once it encounters the MC12, the tip has to move down and penetrate into the MC12 SAMs. For the MC6/BP2, as the MC6 molecule is shorter than BP2, while the conductivity of them is almost the same. So the tip can move smoothly on both BP2 and MC6. This can also explain that under the 0.05 nA, 0.5 V parameters, the STM can get the clear image of both BP2 and MC6, but cannot get the clear molecular resolution of MC12 as the tip penetrates into the molecule layer. Withdrawing the tip (reduce the current and increase the bias), enables molecular resolution of both MC12 and BP2.

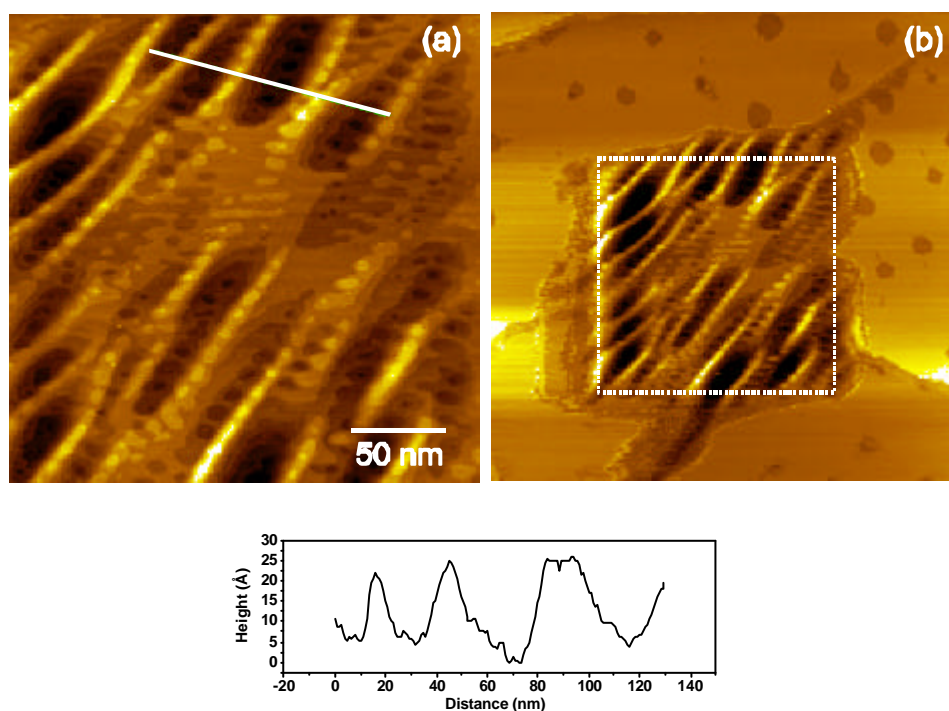


**Figure 4.24** STM images showing a BP2 layer replaced by MUA in hexadecane solution. (a) A rough surface is created after 90 minutes replacement. (b) Zoom out of (a) showing only the scanned area is ‘etched’. STM parameters are  $I = 50$  pA, bias = 0.5 V.

It is interesting to note that the replacement depends on the type of molecules used.

The replacement in MUA/hexadecane is very different from CH<sub>3</sub>-terminal alkane thiols as shown in Figure 4.24. It was found that the replacement is not uniform. Some areas appear several Au layers deep (see cross section analysis in (a)). This again clearly shows the molecular dependence of the replacement. This difference can be attributed to the double layer formation (hydrogen bonding) (see chapter 5.2, MUA assembling). However, how it exactly affects the replacement is still unknown at this stage.

#### 4.3.3.2 Patterned SAMs by Nanografting

Since replacement always starts at defects, we tested the stability of BP2 against replacement by performing the *in situ* experiment (see Figure 4.25). Several holes were punched (3.5 V, 50 ms) on a BP2 SAM as shown in (b). The scanned area was then reduced to focus on only four of them as shown in (c) and scanning continued on the same area as shown from (c) to (n). It was found that the holes created by punching expand under STM scanning as time goes on. After about 30 minutes, the holes are connected and the scanned area is replaced by MC18. A large image (o) reveals that all other holes are intact. This shows that tip scanning is necessary for the replacement. The replacement by MC18 is similar to the replacement by MUA as shown in (l - n). This might be due to the lower conductivity of MC18, which forces the tip into the SAM and etch the scanned area. This is the same effect as the sweeping effect (see 4.2.2).

This experiment clearly shows that the BP2 is very stable against unwanted replacement.

It is interesting to note that the depression area (step edge in the native SAM) (marked by an ellipse as shown in Fig. 4.25(c)) is quite stable. The area is almost not affected as shown in images from (c) to (h). However, an intrinsic defect (Impurities originated from Au substrates occupy in these defects. It was marked by a solid circle as shown in Fig. 4.25(c)) is less stable under STM tip scanning. This clearly shows that step edges are not serious defects, but intrinsic defects are more vital to determine the

quality of a SAM.

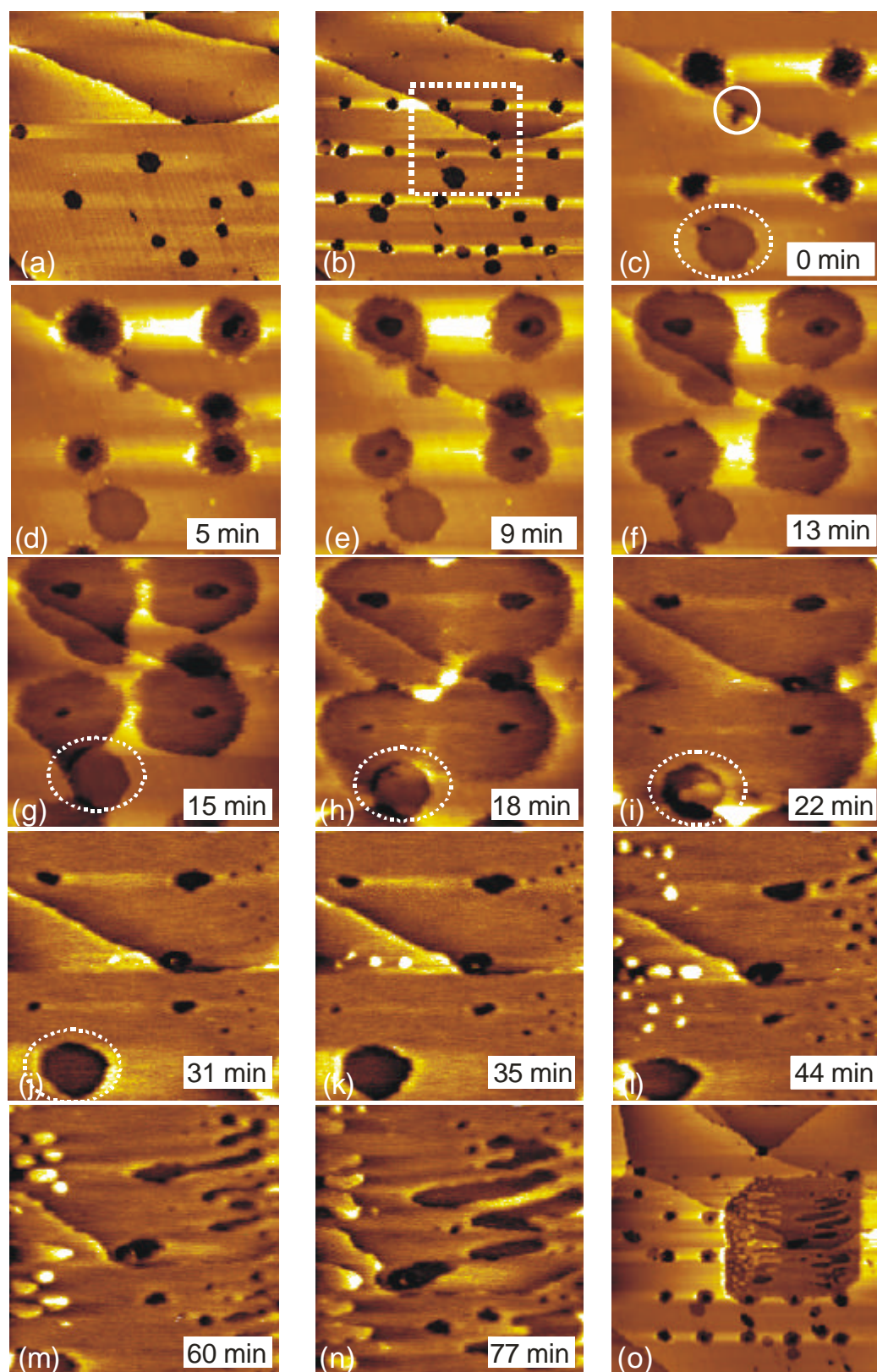


**Figure 4.25** STM images showing replacement of BP2 by MC18 in hexadecane solution. (a) BP2 surface before punching ( $250 \times 250 \text{ nm}^2$ ). (b) Holes punched by applying pulses of 3.25 V for 50 ms for each hole. (c) STM tip scanning only four of the holes as indicated in (b) by square. (d) to (n)

show the dynamic replacement process in the chose area. (o) shows the zoom out of the scanned area. All images were obtained at 0.05 nA, 0.5 V.

The relationship of replacement area and the time can be expressed by  $A(\text{area}) = 240 - 0.87 t + 0.0018 t^2$  ( $t \geq 264$ ) as shown in Figure 4.26. The linear replacement in terms of radius shows that the replacement occurs all along the edge of the replaced area. Note that this difference by MC6 where replacement is directional. This could results from a stronger ability of MC18 to replace BP2.

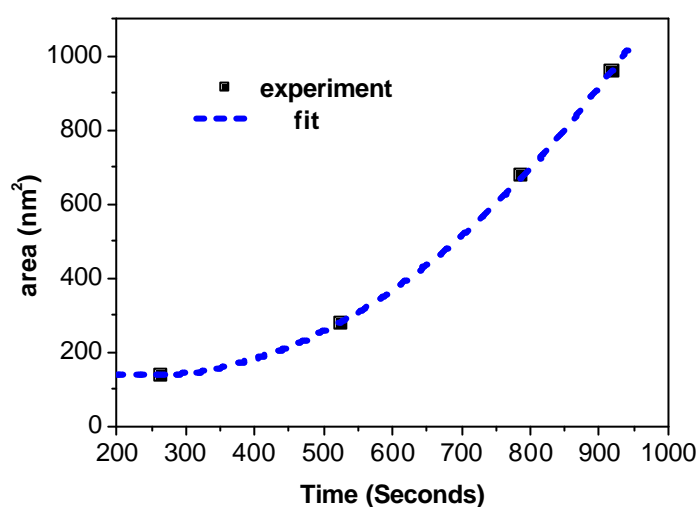


**Figure 4.26** Relationship between the replacement area and time. Evaluation was performed by selecting the top right hole as shown in Fig. 4.25(c).

#### 4.3.3.3 Discussion

Surface modification induced by SPM tip has produced many interesting effects,<sup>34,82,83</sup> with some of the mechanisms still unknown. Tip induced change of nanostructure has been observed by Berenz et al. in clean and ethene covered Pt(111) surface with Cu UPD.<sup>54</sup> They observed a displacement of organic adsorbate (ethene) followed by Cu UPD, scanning under similar conditions over the surface free of ethene, but covered by UPD Cu also leads to a nanostructure formation. In these experiments, no nanostructure was formed in the absence of  $\text{Cu}^{2+}$  ions, and longer scanning time led

to a higher nanostructure. Such nanostructures are believed to be an alloy of Cu and Pt based on the fact that they are still stable even at the potential of 250 mV vs Cu/Cu<sup>2+</sup>. The authors rule out the effect of temperature increased by friction or by electric heating, but could not propose a mechanism for the formation of such nanostructure.

The nanografting described here is different from the sweeping effect discussed in section 4.2.2. Sweeping occurs for high current and low voltage mode (e.g. 0.9 nA, 0.8 mV). Obviously, it is also different from the punching mode, which uses high voltage. So far, we observed nanografting on BP2 for BP<sub>m</sub> with  $m \geq 4$ . For BP3 and BP1, no or only very slow replacement is observed. Alkane thiols such as MC6, MC11, MC12, MC18 and MUA are all capable to displace the BP2 layer. Nanografting on MC11 SAM requires a significantly longer alkanethiol. It was found that MC18 can replace MC11, but MC6 cannot replace the MC11. Nanografting on a more complicated matrix SAM (bpp-SH) does not work in the presence of MC11 or MC12. However, nanografting was observed in the presence of MC14 or MC18 in hexadecane solution. Such replacements show that at least two factors are required for the nanografting:

1. The replacing molecule should have a stronger ability to assemble than the matrix SAM.
2. Defects are required either by the layer itself or by punching, such punching does not necessary create a visible hole, but only weakens the interactions in the SAM such as van der Waals forces among molecules. Once the SAM stability of the area is decreased, the original SAM can be replaced by a stronger one.

Similar results can be found in the work of Gorman, et al.<sup>40</sup> It was found that when longer chain thiols ( dodecanethiol, hexadecanethiol) were used to replace shorter chain thiols (decanethiol), the pattern was always bigger than for the opposite operation. Also more defects can be found nearby the pattern showing sign of replacement. However, they did not address this issue.

Xie and Kolb observed a spatially confined copper dissolution by STM tip in 50 mM H<sub>2</sub>SO<sub>4</sub> + 1 mM CuSO<sub>4</sub> in which Cu can be dissolved at potentials at which Cu dissolution should normally not happen (for example, Cu dissolved at  $E_{\text{sample}} = -50$  mV

vs  $\text{Cu}/\text{Cu}^{2+}$ ).<sup>84</sup> The dissolution was also observed to relate to the current, for example, at  $E_{\text{sample}} = -60$  mV,  $I = 0.2$  nA, the tip has no influence. However, when the current is increased to 2-50 nA, the etching rate increases by a factor of 2, showing the sensitivity of the tip-substrate distance. They proposed that the dissolution of Cu is due to the electron transfer from Cu directly into the empty states of the tip, which has a lower Fermi level than that of the sample. However, this mechanism is less likely to be the case of our experiment as the replacement happened in hexadecane and the sign of the bias (positive or negative) does not affect the replacement. It is also unlikely that an ionic species desorbs as in electrochemistry

It has been shown that even at low tunnelling current (6 pA), the tip can induce molecular restructuring. It was pointed out that the local heating due to the tunnelling current is not a factor in this transformation.<sup>54</sup> However, the transformations induced by the tip with 6 pA are suggested to be at least as big as those induced by an AFM tip at 30 nN force.<sup>85</sup> To explain this phenomenon, we propose another model. As the distance between the tip and the substrate is very small (~1 nm), the electric field is huge ( $10^7$  V/cm), SAM-solvent mixture in between can solidify. This electrorheological effect<sup>86-89</sup> would explain the etching by just a simple friction effect. If this model is true, then it would also explain our results as SAMs dissolved in hexadecane can also become solid under such high electric fields. This model can explain why COOH-terminal SAM has a stronger etching/replacement effect, as the intermolecular hydrogen bond can increase the electrorheological effect.<sup>86</sup> There might be another possibility, since the STM tip is made of Pt/Ir (8:2), so the SAM can also assemble on the surface of the tip in the hexadecane solution. Such SAM modified tip may have different properties and working like a brush, this can cause the nanografting effect. However, this explanation cannot explain why for other thiols, such as BP1, BP2, BP3, there is not such effect.

At this point, the STM manipulation principles are briefly summarized with Figure 4.27 listing several manipulation mechanisms. (a) is the sweeping mode, which operates at high current and low bias by bringing the tip very close to the surface. (b) is

the normal working mode. Electrons tunnel between the tip and the sample. (c) is the punching mode, where a high voltage pulse is applied. (d) field-induced electrons. This occurs when the bias voltage exceeds the work function of the tip.

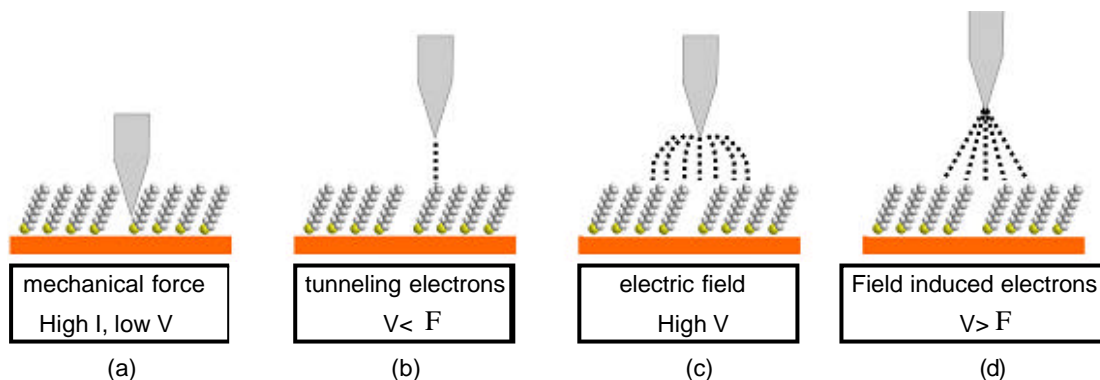


**Figure 4.27** Schematic showing four manipulation mechanisms with STM.<sup>90</sup>  $V$  is the bias and  $F$  is the work function of the sample. (a) Sweeping mode, which operates with high current and low bias and brings the tip very close to the surface. (b) Normal working mode, electrons tunnel between the tip and sample. (c) Punching mode, which is operated by applying a high voltage pulse. (d) Field-induced electrons.

Sweeping mode (a) and punching mode (c) were discussed in the previous sections and are not responsible for the nanografting effect discussed above. The field-induced electron also does not apply since it requires a very high voltage. Tunnelling electrons generated under normal working mode might be the reason for the nanografting. Tunnelling-electron-induced desorption is indeed well documented.<sup>65,90-93</sup> In addition, since the electrons are confined to the apex of the STM tip, molecular resolution can be obtained. Tunnelling-electron-induced desorption should occur independent on the bias polarity.<sup>94</sup> We observed the same here. However, Tunnelling-electron-induced desorption should occur at a relative high current, usually several nA. This is in sharp contrast with our result as displacement even happens at a tunnelling current of 8 pA.

Regardless of the mechanism of the nanografting effect, it was surprising how fast the replacement takes place. This can be attributed to the spatial confinement effect. For normal SAMs assembled on Au surface, it takes at least several hours at elevated temperature to form such crystalline structure. The self-assembly involves at least two steps.<sup>22</sup> The first step is a low coverage phase formation which takes place in few

seconds to several minutes and the second step is to maximize the density of molecules and minimize the defects in the SAMs, a process which requires several hours. For the replacement happening here, the edge of the host molecule provides a supporting cell for the assembly of guest molecules, which assemble on the surface without going through the first step of the low coverage, flat lying phase. This confined space assisted assembling was observed by Liu et al. by AFM.<sup>66,69</sup>

The advantage of nanografting is that it is more confined and more uniform compared with the sweeping and punching modes. Very sharp edge and flat surface are formed. No gold atoms are pushed to the edge as it is the case for the sweeping (high current, low voltage).

#### 4.3.3.4 Conclusion

STM nanografting was studied in hexadecane solution\* under normal STM imaging parameters, which is different from the sweeping (high current) and punching (high voltage) modes. It was found that long chain thiols can replace short chain thiols; alkane thiols can replace biphenyl thiols, i.e., the SAMs in hexadecane solution should have a stronger ability to assemble than the matrix SAM. A defect is the trigger point from which the replacement starts and expands across the whole area covered by the scanned range of the STM tip. Several mechanisms were proposed to explain this nanografting effect. The BP2 high temperature phase is a very suitable matrix for nanopatterning due to its stability and lack of defects in large areas, which is very important for nanopatterning. The speedy replacement by nanografting also minimises unwanted exchange reactions.

---

\* The effect is not limited to hexadecane and was also observed in toluene. The solvent does not play a big role during nanografting as soon as it is a poorly conducting and non-volatile solvent.

## 4.4 Metal Deposition on STM Modified SAMs

### 4.4.1 Introduction

Depositing metals on SAM modified substrates is another interesting topic. The jump-to-contact method has been demonstrated to be capable of depositing metallic dots on substrates.<sup>95-97</sup> Metal was deposited on the tip and then the metal-loaded tip was forced to touch the substrate by switching off the feedback loop. However, this method has less control on the SAM covered surface as the interaction between the metal dots and SAMs is weak, and it was found unwanted metal islands also deposited on the surface.<sup>98</sup> Zamborini et al. successfully showed that Ag can be deposited into holes created by punching in air.<sup>99</sup> This was attributed to the role of the water condensation between the tip and substrate, which completes a two electrode nanoelectrochemical cell. Such nanoelectrochemical cell may help to localize the Ag metal bulk deposition and limit the UPD process to the areas addressed by the tip. One important issue of our project is to localize metal growth on patterns created in SAMs, which is an important step towards a SAM based generation of low dimensional metal nanostructures,<sup>100-107</sup> and eventually metal-SAM-metal nanostructures<sup>108-112</sup>. Deposition of metal on the nanoscale may be very different to the one at micrometer scale due to interfacial and quantisation effects.<sup>95,113</sup> Therefore, an investigation of metal deposition on SAMs patterned on the nanoscale is important.

Underpotential deposition of Cu on Au surface always happens before bulk metal deposition starts. It is important to investigate the underpotential deposition of metal on the nanoscale and *in situ*. The electrochemical scanning tunnelling microscope (ECSTM) has proven to be a very important tool to investigate structural changes during the UPD process.<sup>114,115</sup> It has been suggested that UPD of Cu induces monoatomic high islands. They were assigned to the formation of Cu thiolate after the penetration of Cu ions through the SAM layer. However, there is still some controversy over the mechanism of the UPD, whether a complete Cu monolayer is formed is under

debate. Recently, our group demonstrated that defects originated from impurities of Au substrate trigger UPD.<sup>50</sup> A complete Cu monolayer formed underneath the SAM starts from these defects. Given that type of defect and growth mechanism, it is interesting to generate defects on purpose and to investigate the UPD process *in situ*.

#### 4.4.2 Results and Discussion

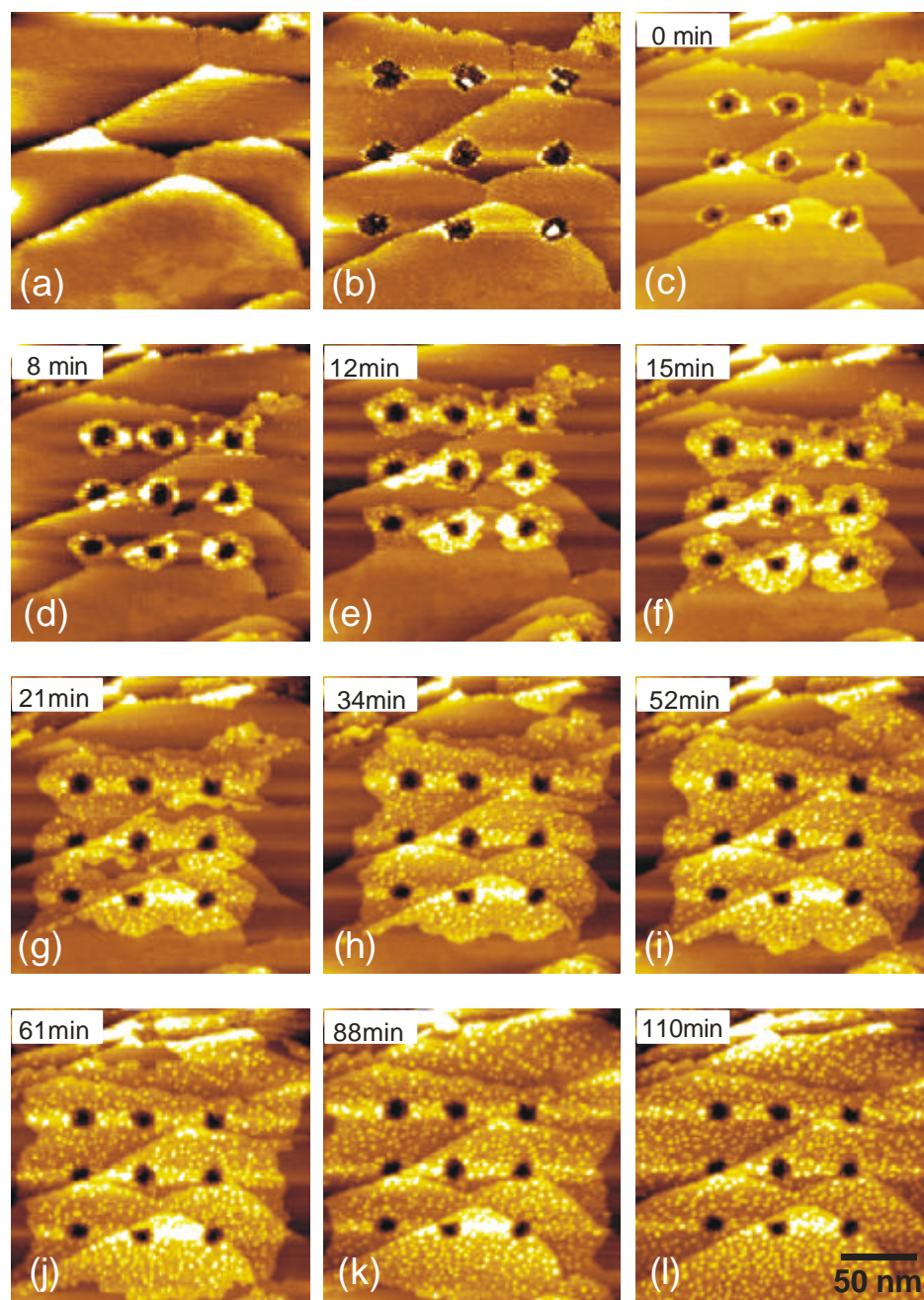


**Figure 4.28** STM images showing the process of Cu UPD growth on BP2/Au(111). (a) shows the area before creating holes by high voltage punching. (b) shows that nine holes were created by

applying a voltage of 3.5 V for 50 ms for each hole. (c) shows the same area in 5 mM  $\text{CuSO}_4$  and 50 mM  $\text{H}_2\text{SO}_4$  solution under the potential of 0.3 V (vs.  $\text{Cu}/\text{Cu}^{2+}$ ). From (d) to the (l), UPD area expands and covers the full area as the potential is changed from +0.3 V to +0.2 V.

Figure 4.28 shows the *in situ* UPD growth of Cu from tip-induced defects. (a) shows the area in air prior to modification. (b) shows nine holes created by applying voltage pulses of 3.5 V for 50 ms. A coated tip was used since it was subsequently used in the same experiment for in situ monitoring of Cu UPD. (c) shows the same area in 5 mM  $\text{CuSO}_4$  / 50 mM  $\text{H}_2\text{SO}_4$  solution at +0.3 V (vs.  $\text{Cu}/\text{Cu}^{2+}$ ). From (d) to the (l), the UPD area expands as the potential was changed from 0.3 V to 0.2 V. Interestingly, after the potential was set to -0.1 V, i.e., into the OPD region, no bulk Cu growth was observed. Even though the damage of the SAM was considerable, the surface essentially retains passive. The sample was kept at -0.1 V for about 1 hour. This should be long enough for the growth of bulk Cu metal. To explain the absence of bulk Cu, one could suggest at first that the diffusion of UPD copper was faster than the nucleation of bulk Cu particles. However, this can be ruled out since no Au particle grows into holes in  $\text{AuCl}_3$  electrolyte, where no UPD can occur with Au substrate.

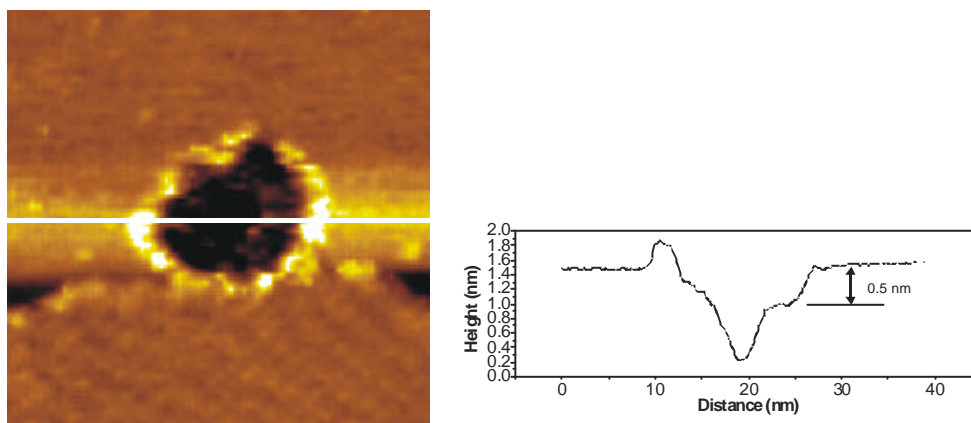


**Figure 4.29** Cross section analysis of one hole prior UPD. The depth of the hole is about 1.3 nm with a step of about 5 Å which is about 2 gold atoms deep in Au(111) surface.

A close look at the punched holes in (b) showed that it has a depth of about 1.3 nm with a clear step of about 0.5 nm (see Figure 4.29). The step gives very important

information as 5 Å is about 2 gold atoms deep on the Au(111) surface. It was shown by Frey et al. that cleavage by low energy electrons of thiolate-substrate bonds in biphenyl SAMs is not accompanied by the removal of the complete molecules.<sup>116</sup> Vandeweert et al. showed that electron-induced desorption is in competition with the formation of a carbon-rich residual film on the surface, either as a form of intact molecules or as fragments (thiolate).<sup>117</sup> Although the mechanism of cleavage of molecules might be different in our case as voltage pulses are applied, these experiments showed that molecules can still intact under harsh conditions. Binding energies of S-C bond and Au-S bond are about 74 kcal/mol and 40-45 kcal/mol, respectively.<sup>118,119</sup> Since these energies are of the same order of magnitude, cleavage can happen in both cases when a high voltage pulse is applied. We conclude that the voltage pulses excite gold atoms, while the SAMs remains on the area or diffuse back quickly to cover the exposed area. Figure 4.30 shows a schematic of the proposed model.

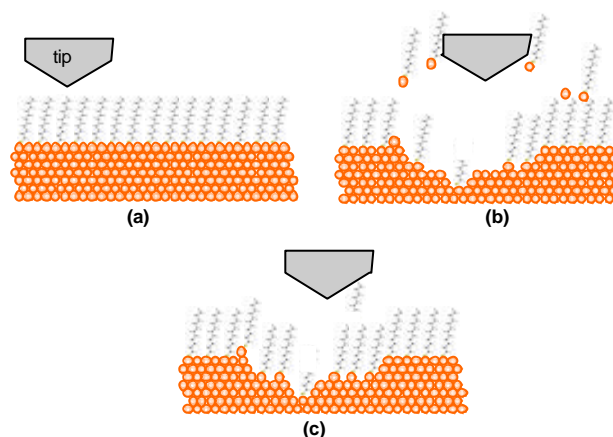


**Figure 4.30** Schematic illustrating high voltage punching. Au atoms and SAMs/gold complex are excited. The motif diffuses back very quickly and recovers the exposed area.

To further understand how defects created by punching affect the metal deposition, we carried out another experiment on the MUA/Au/Mica surface. Figure 4.31 is another example showing that holes created by punching are not serious defects as what we thought it should be. The hole is 30 nm large with a depth of about 6 nm was punched in air at 5 V on the MUA/Au(111) surface (see Figure 4.31(a)). The sample was then exposed to CuSO<sub>4</sub> solution. The potential was kept at +0.25 V at the beginning.

When the potential was moved to +0.15 V, UPD starts. It was found that UPD started from a defect along one step edge (see Figure 4.31(b)) and not from the punched hole. These defects are known to act as nucleation and growth sites for Cu UPD.<sup>50</sup> Thus if other defects are in the vicinity of punched holes, nucleation is more likely in the natural defects. Note that at -0.05 V, no Cu OPD was observed.

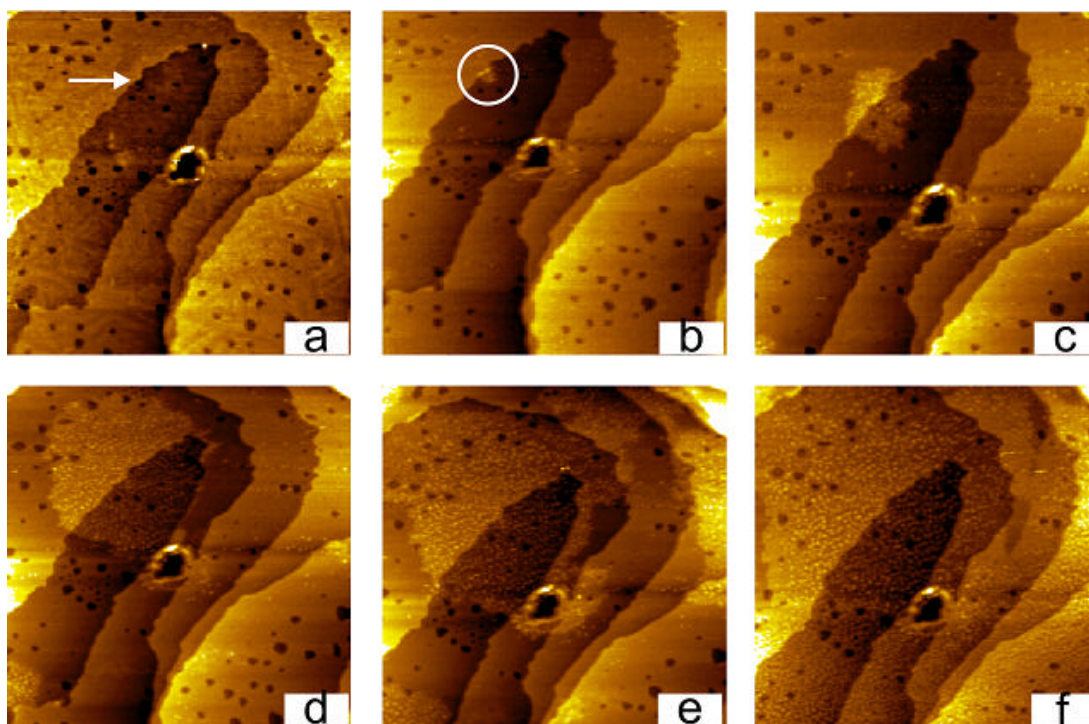


**Figure 4.31** *In situ* STM images showing Cu UPD on MUA/Au(111). A hole of 30 nm large and 6 nm deep was punched at 5 V (a). (b) and (c) show that UPD started from a defect (indicated by white circle in (b)). From (c) to (f), UPD expanded until covering the entire area. Potential from (a) to (f) are +0.25 V, +0.15 V, +0.15 V, +0.1 V, 0 V, and -0.05 V, respectively (vs. Cu wire).

Figure 4.32 shows another example of how intrinsic and extrinsic (punched) defects affect the metal deposition. A hole was punched in the middle of the scanned area. Again, it was found that the UPD starts at the defect located at a step edge as indicated by the arrow in (a). UPD also nucleates from the punched hole about 40 minutes later (see (b)) at the potential of -0.05 V. No OPD is observed at -0.1 V (see (c)). From these experiments, it was found that UPD on BP2 (see Figure 4.28) and MUA (see Figure 4.31) is different. For BP2, the punched holes are the nucleation points for Cu UPD due to the well-ordered structure of the high temperature phase.<sup>70,120</sup> For MUA, the layer is

less perfect and more defects exist on the surface. These are more favourable for UPD. These experiments suggest that punched holes are refilled by molecules but possibly in a less ordered way. Punched holes are UPD nucleation sites for perfect SAM, but are in competition with other defects when the layer is less perfect.

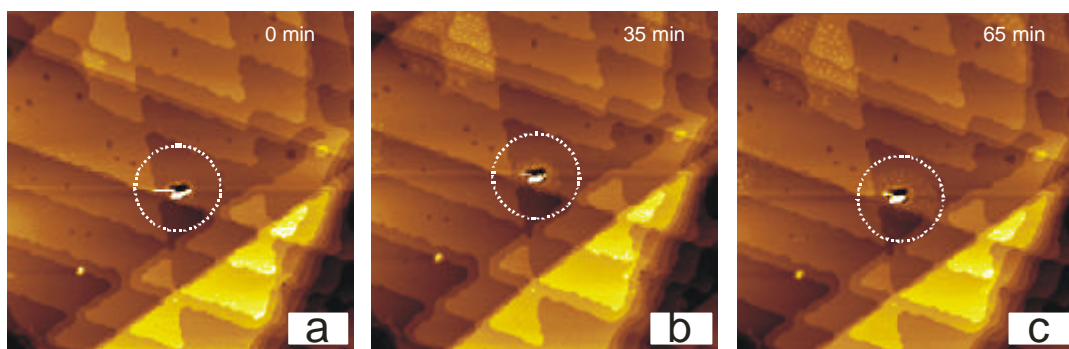


**Figure 4.32** *In situ* STM images showing UPD growth on MUA/Au(111). A hole was punched in the middle of the scanned area as indicated by circle. UPD starts from an intrinsic defect as indicated by the arrow in (a). UPD growth takes about 1 hour from (a) to (c). (Scan range is  $500 \times 500 \text{ nm}^2$ ). Potentials in a, b, and c are 0, -0.05, and -0.1 V, respectively. No bulk copper growth is observed.

Despite enormous efforts to grow bulk metal from punched defect by using different SAMs, it has not been successful so far. Figure 4.33 completes the series of images shown in Figure 4.32.

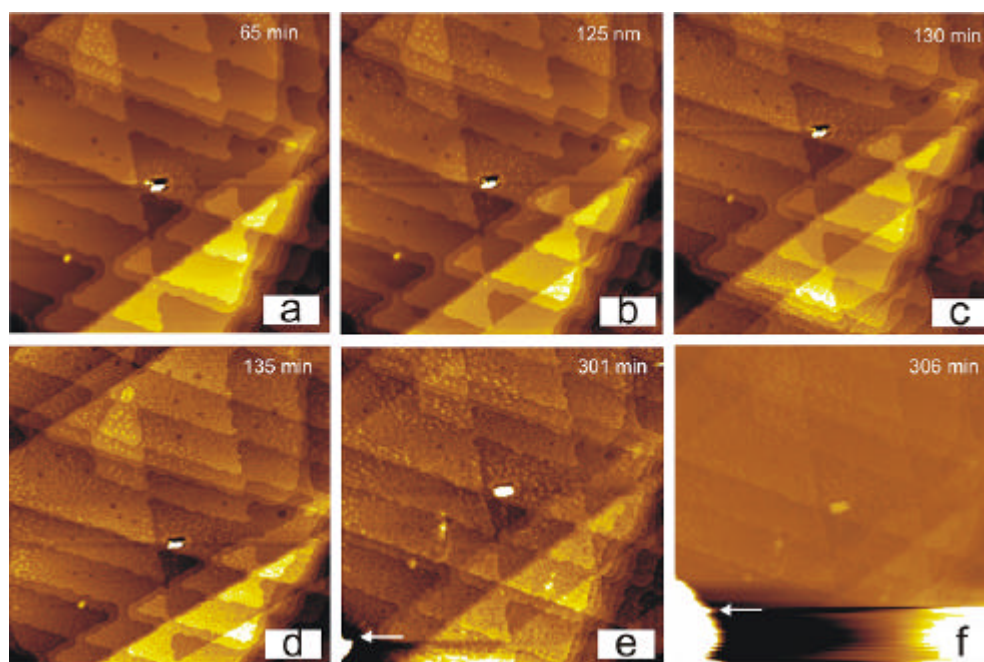


**Figure 4.33** *In situ* STM images showing the tip effect during metal deposition (images are from the same series as in Figure 4.32). UPD growth is slow from (a) to (b) (~1 hour). The UPD coverage increases significantly after the tip was withdrawn 100 nm away from the surface for 2 minutes (c).

(e) and (f) show bulk copper OPD (see arrows). Potential is  $-0.1$  V for all images. Images are  $500 \times 500$  nm<sup>2</sup>.

UPD growth was very slow from (a) to (b), ( $\sim 1$  hour). However, after withdrawing the tip by  $100$  nm for  $2$  minutes, we observed a significant expansion of UPD area (see (c)). Bulk copper was also observed in the lower left corner in images (e) and (f) after more than  $2$  hours at  $-0.1$  V. This experiment indicates that the tip hinders UPD and OPD. This is further addressed in Figure 4.34.

To avoid UPD, we used a solution of  $10$  mM  $\text{AuCl}_3$ . Again, no OPD was observed in the punched defects. However, bulk Au was observed. It grew from outside the scanned area as shown in Figure 4.34. From (a) to (e), the potential was kept at  $-0.15$  V (vs. Au wire). Bulk Au growth is continuous. (a) and (b) show an area of  $500 \times 500$  nm<sup>2</sup>. Bulk Au growth is marked by arrows. From (c) to (f), the scan range is  $1000 \times 1000$  nm<sup>2</sup>. It was found that Au grew from outside to scanned area until the area was filled as shown in (f). This result is similar to Gilbert's observation for Cu OPD on decanethiol-covered Au(111).<sup>121</sup>

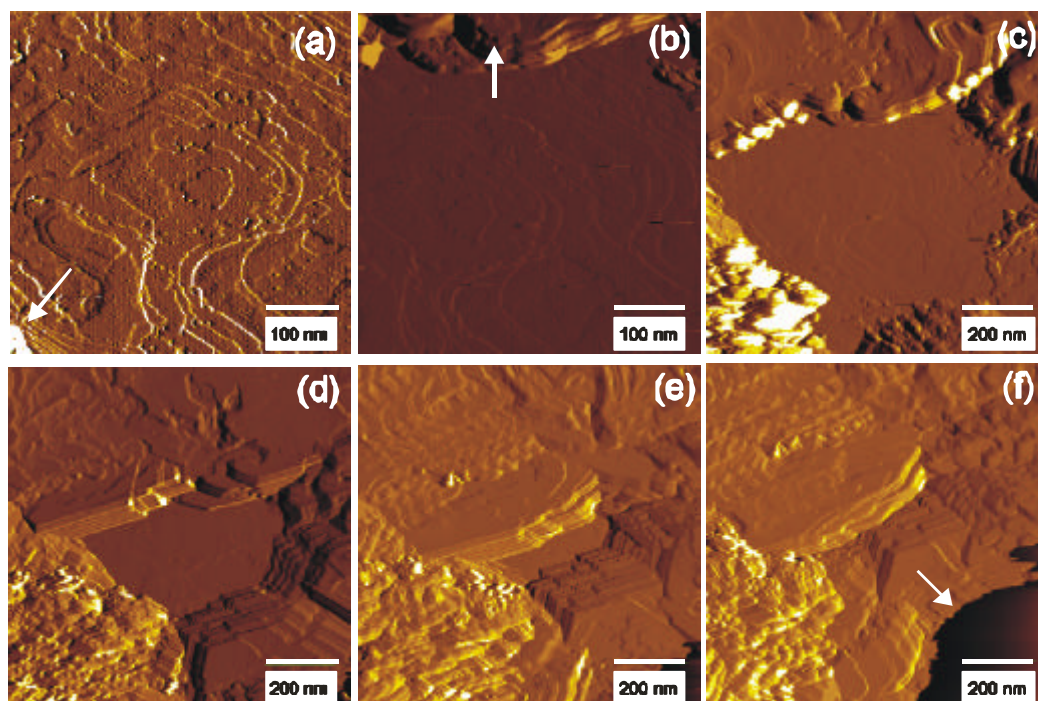


**Figure 4.34** *In situ* STM images showing the bulk Au deposition on BP2/Au(111) in  $10$  mM  $\text{AuCl}_3$ . It was found that the bulk Au grew from outside the scanned area. From (a) to (e), the potential was kept at  $-0.15$  V. Arrows indicate Au growth. The height of the Au layer deposited in (d) is about  $25$  nm. The reference electrode is Au wire. Imaging parameters are  $0.05$  nA and  $-0.15$  V.

All these experiments clearly show that the STM tip hinders the metal deposition. The bulk metal grows faster outside the scanned area and then creep into the patterned area despite punched defect in center area. Same tip effect was observed during Cu deposition onto the MUASAM (see Figure 4.33). We propose that the coating on the tip reduces metal concentration around the tip in water solution, given its hydrophobic surface. In addition, a coating tip occupies a huge space compared with the patterned area.

To avoid tip interference with metal growth, we performed similar experiments by withdrawing the tip (see Figure 4.35). (a) shows a hole (2 nm deep, 25 nm wide) was punched on a MUA/Au surface. After imaging the defect, the tip was withdrawn 100 nm away from the surface, and prior to applying a pulse at -0.2 V for 1s, the sample potential was set at 0.0 V.

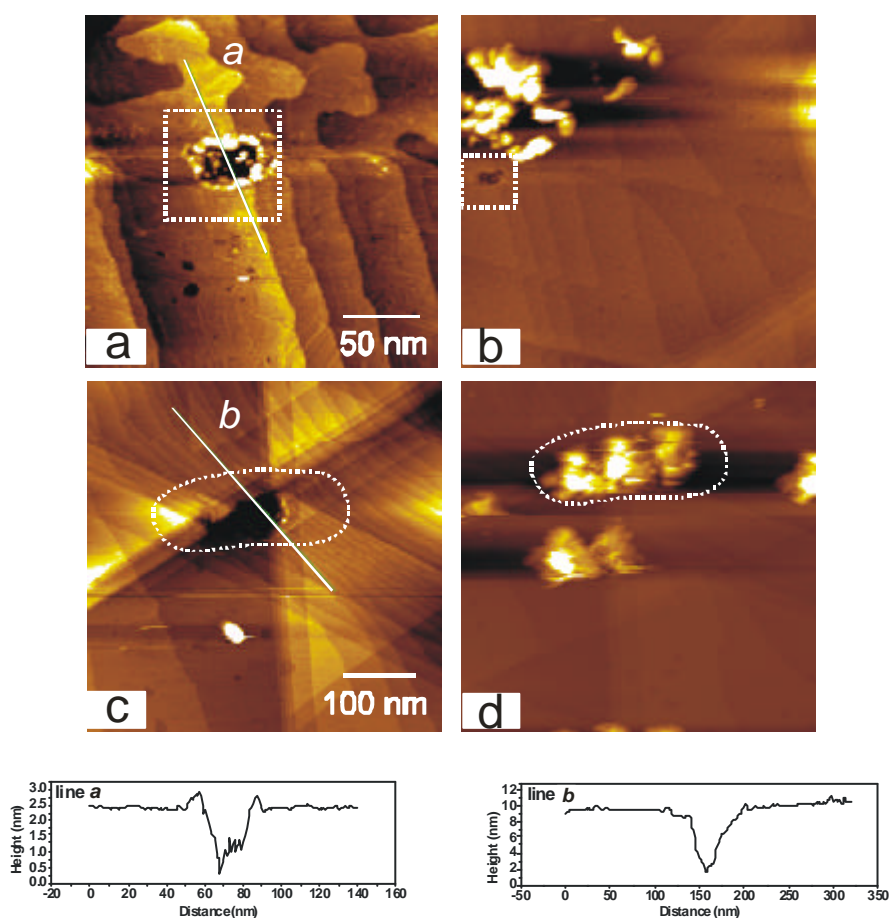


**Figure 4.35** *In situ* STM images showing the bulk Cu deposition on MUA/Au(111). (a) A hole (2 nm deep, 25 nm wide). (b) Metal particles grow on defect sites but not on the punched area. (c) A

**bigger defect was punched (7 nm deep and 50 nm wide). (d) Bulk Cu grows on the punched area as well as on other defect sites.**

The sample potential then returns to 0.0 V to avoid dissolution of bulk metal in case any deposition has occurred and the cell potential is switched off. After deposition, we found that some Cu particles are present on the surface (see (b)). Surprisingly, there was no copper in the punched hole. In another experiment (shown in (c) and (d)), a bigger defect was punched (7 nm deep and 50 nm wide). After the same deposition scheme, we found bulk Cu deposited in the punched area. But some random and unwanted particles were also observed at other defects sites.

### 4.4.3 Conclusions

Defects (punched holes) were created purposely on SAM covered Au surfaces and *in situ* STM was used to observe UPD and OPD processes. Several conclusions are inferred from our experiments.

- (1) Holes punched with high voltage pulses are surprisingly passive. This possibly results from the presence of molecules diffusing back in the punched area.
- (2) Punched holes trigger UPD nucleation in “perfect” SAM, such as the high temperature phase of BP2. However, in the presence of other defects, punched holes are only a secondary source of nucleation site
- (3) The STM tip may hinder metal UPD and OPD for *in situ* experiments.
- (4) Bulk metal deposition on punched holes depends on the size. A large hole (e.g. 7 nm deep and 50 nm wide) can trigger bulk deposition. However, a smaller one (e.g. 2 nm deep and 25 nm wide) does not trigger any bulk deposition. In summary, small scale patterning by punching is sufficient for applications based on UPD but not for bulk metal OPD.

## References:

- (1) Lewis, P. A.; Donhauser, Z. J.; Mantooh, B. A.; Smith, R. K.; Bumm, L. A.; Kelly, K. F.; Weiss, P. S. *Nanotechnology* 2001, *12*, 231-237.
- (2) Giuseppina Pace, A. P., Marie-Noelle Lalloz-Vogel, Jack Harrowfield, Jean-Marie Lehn, Paolo Samori *Angew. Chem. Int. Ed.* 2008, *47*, 2484-2488.
- (3) Smith, R. K.; Lewis, P. A.; Weiss, P. S. *Progress in Surface Science* 2004, *75*, 1-68.
- (4) Senaratne, W.; Andruzzi, L.; Ober, C. K. *Biomacromolecules* 2005, *6*, 2427-2448.
- (5) Xia, Y. N.; Qin, D.; Yin, Y. D. *Current Opinion in Colloid & Interface Science* 2001, *6*, 54-64.
- (6) Reynolds, N. P.; Janusz, S.; Escalante-Marun, M.; Timney, J.; Ducker, R. E.; Olsen, J. D.; Otto, C.; Subramaniam, V.; Leggett, G. J.; Hunter, C. N. *Journal of the American Chemical Society* 2007, *129*, 14625-14631.
- (7) Holmlin, R. E.; Chen, X. X.; Chapman, R. G.; Takayama, S.; Whitesides, G. M. *Langmuir* 2001, *17*, 2841-2850.
- (8) Haussling, L.; Michel, B.; Ringsdorf, H.; Rohrer, H. *Angewandte Chemie-International Edition in English* 1991, *30*, 569-572.
- (9) Nelson, K. E.; Gamble, L.; Jung, L. S.; Boeckl, M. S.; Naeemi, E.; Golledge, S. L.; Sasaki, T.; Castner, D. G.; Campbell, C. T.; Stayton, P. S. *Langmuir* 2001, *17*, 2807-2816.
- (10) Donhauser, Z. J.; Mantooh, B. A.; Kelly, K. F.; Bumm, L. A.; Monnell, J. D.; Stapleton, J. J.; Price, D. W.; Rawlett, A. M.; Allara, D. L.; Tour, J. M.; Weiss, P. S. *Science* 2001, *292*, 2303-2307.
- (11) Mizutani, W. *Japanese Journal of Applied Physics Part 1-Regular Papers Short Notes & Review Papers* 1999, *38*, 7260-7263.
- (12) Lussem, B.; Muller-Meskamp, L.; Karthaus, S.; Waser, R.; Homberger, M.; Simon, U. *Langmuir* 2006, *22*, 3021-3027.
- (13) Li, L. Y.; Chen, S. F.; Jiang, S. Y. *Langmuir* 2003, *19*, 3266-3271.
- (14) Shevade, A. V.; Zhou, J.; Zin, M. T.; Jiang, S. Y. *Langmuir* 2001, *17*, 7566-7572.
- (15) Bumm, L. A.; Arnold, J. J.; Charles, L. F.; Dunbar, T. D.; Allara, D. L.; Weiss, P. S. *Journal of the American Chemical Society* 1999, *121*, 8017-8021.
- (16) Fuchs, D. J.; Weiss, P. S. *Nanotechnology* 2007, *18*, 044021.
- (17) Hobara, D.; Sasaki, T.; Imabayashi, S.; Kakiuchi, T. *Langmuir* 1999, *15*, 5073-5078.
- (18) Kakiuchi, T.; Iida, M.; Gon, N.; Hobara, D.; Imabayashi, S.; Niki, K. *Langmuir* 2001, *17*, 1599-1603.
- (19) Leggett, G. J. *Chemical Society Reviews* 2006, *35*, 1150-1161.
- (20) Ducker, R. E.; Janusz, S.; Sun, S. Q.; Leggett, G. J. *Journal of the American Chemical Society* 2007, *129*, 14842-14843.
- (21) Sun, S. Q.; Leggett, G. J. *Nano Letters* 2007, *7*, 3753-3758.
- (22) Love, J. C.; Estroff, L. A.; Kriebel, J. K.; Nuzzo, R. G.; Whitesides, G. M. *Chemical Reviews* 2005, *105*, 1103-1169.
- (23) Mendes, P. M.; Preece, J. A. *Current Opinion in Colloid & Interface Science* 2004, *9*,

- 236-248.
- (24) Sun, S. Q.; Chong, K. S. L.; Leggett, G. J. *Nanotechnology* 2005, 16, 1798-1808.
- (25) Williams, J. A.; Gorman, C. B. *Langmuir* 2007, 23, 3103-3105.
- (26) Lewis, M. S.; Gorman, C. B. *Journal of Physical Chemistry B* 2004, 108, 8581-8583.
- (27) Xu, S.; Miller, S.; Laibinis, P. E.; Liu, G. Y. *Langmuir* 1999, 15, 7244-7251.
- (28) Kramer, S.; Fuierer, R. R.; Gorman, C. B. *Chemical Reviews* 2003, 103, 4367-4418.
- (29) Ballay, N.; Schilp, S.; Zharnikov, M. *Angewandte Chemie-International Edition* 2008, 47, 1421-1424.
- (30) Ballav, N.; Weidner, T.; Rossler, K.; Lang, H.; Zharnikov, M. *Chemphyschem* 2007, 8, 819-822.
- (31) Reed, M. *Science* 1993, 262, 195-195.
- (32) Guo, Q. M.; Yin, F.; Palmer, R. E. *Small* 2005, 1, 76-79.
- (33) Keel, J. M.; Yin, J.; Guo, Q.; Palmer, R. E. *Journal of Chemical Physics* 2002, 116, 7151-7157.
- (34) Parkinson, B. *Journal of the American Chemical Society* 1990, 112, 7498-7502.
- (35) Mizutani, W.; Ishida, T.; Tokumoto, H. *Langmuir* 1998, 14, 7197-7202.
- (36) Schoer, J. K.; Zamborini, F. P.; Crooks, R. M. *Journal of Physical Chemistry* 1996, 100, 11086-11091.
- (37) Schoer, J. K.; Crooks, R. M. *Langmuir* 1997, 13, 2323-2332.
- (38) Wang, Z. H.; Moskovits, M. *Journal of Applied Physics* 1992, 71, 5401-5409.
- (39) Albrecht, T. R.; Dovek, M. M.; Kirk, M. D.; Lang, C. A.; Quate, C. F.; Smith, D. P. E. *Applied Physics Letters* 1989, 55, 1727-1729.
- (40) Gorman, C. B.; Carroll, R. L.; He, Y. F.; Tian, F.; Fuierer, R. *Langmuir* 2000, 16, 6312-6316.
- (41) Gorman, C. B.; Carroll, R. L.; Fuierer, R. R. *Langmuir* 2001, 17, 6923-6930.
- (42) Fuierer, R. R.; Carroll, R. L.; Feldheim, D. L.; Gorman, C. B. *Advanced Materials* 2002, 14, 154-157.
- (43) Schneeweiss, M. A.; Hagenstrom, H.; Esplandiu, M. J.; Kolb, D. M. *Applied Physics a-Materials Science & Processing* 1999, 69, 537-551.
- (44) SondagHuethorst, J. A. M.; Fokkink, L. G. J. *Langmuir* 1995, 11, 4823-4831.
- (45) Fisher, G. L.; Walker, A. V.; Hooper, A. E.; Tighe, T. B.; Bahnck, K. B.; Skriba, H. T.; Reinard, M. D.; Haynie, B. C.; Opila, R. L.; Winograd, N.; Allara, D. L. *Journal of the American Chemical Society* 2002, 124, 5528-5541.
- (46) Walker, A. V.; Tighe, T. B.; Cabarcos, O. M.; Reinard, M. D.; Haynie, B. C.; Uppili, S.; Winograd, N.; Allara, D. L. *Journal of the American Chemical Society* 2004, 126, 3954-3963.
- (47) Nagy, G.; Walker, A. V. *Journal of Physical Chemistry B* 2006, 110, 12543-12554.
- (48) Colavita, P. E.; Doescher, M. S.; Molliet, A.; Evans, U.; Reddic, J.; Zhou, J.; Chen, D.; Miney, P. G.; Myrick, M. L. *Langmuir* 2002, 18, 8503-8509.
- (49) Nishizawa, M.; Sunagawa, T.; Yoneyama, H. *Langmuir* 1997, 13, 5215-5217.
- (50) Silien, C.; Buck, M. *Journal of Physical Chemistry C* 2008, 112, 3881-3890.
- (51) McCarley, R. L.; Dunaway, D. J.; Willicut, R. J. *Langmuir* 1993, 9, 2775-2777.
- (52) Stranick, S. J.; Parikh, A. N.; Allara, D. L.; Weiss, P. S. *Journal of Physical Chemistry* 1994,

- 98, 11136-11142.
- (53) Flores, F.; Echenique, P. M.; Ritchie, R. H. *Physical Review B* 1986, 34, 2899-2902.
- (54) Berenz, P.; Xiao, X. Y.; Baltruschat, H. *Journal of Physical Chemistry B* 2002, 106, 3673-3680.
- (55) Munuera, C.; Barrena, E.; Ocal, C. *Nanotechnology* 2007, 18, 125505.
- (56) Ryu, S.; Schatz, G. C. *Journal of the American Chemical Society* 2006, 128, 11563-11573.
- (57) Liu, G. Y.; Xu, S. *Abstracts of Papers of the American Chemical Society* 1997, 214, 29-Iec.
- (58) Xu, S.; Liu, G. Y. *Langmuir* 1997, 13, 127-129.
- (59) Kondoh, H.; Iwasaki, M.; Shimada, T.; Amemiya, K.; Yokoyama, T.; Ohta, T.; Shimomura, M.; Kono, S. *Physical Review Letters* 2003, 90, 066102.
- (60) Maksymovych, P.; Sorescu, D. C.; Yates, J. T. *Physical Review Letters* 2006, 97, 146103.
- (61) Yu, M.; Bovet, N.; Satterley, C. J.; Bengio, S.; Lovelock, K. R. J.; Milligan, P. K.; Jones, R. G.; Woodruff, D. P.; Dhanak, V. *Physical Review Letters* 2006, 97, 166102.
- (62) Wang, Y.; Hush, N. S.; Reimers, J. R. *Journal of the American Chemical Society* 2007, 129, 14532-14533.
- (63) Trevor, D. J.; Chidsey, C. E. D. *Journal of Vacuum Science & Technology B* 1991, 9, 964-968.
- (64) Trevor, D. J.; Chidsey, C. E. D.; Loiacono, D. N. *Physical Review Letters* 1989, 62, 929-932.
- (65) Liu, G. Y.; Xu, S.; Qian, Y. L. *Accounts of Chemical Research* 2000, 33, 457-466.
- (66) Xu, S.; Laibinis, P. E.; Liu, G. Y. *Journal of the American Chemical Society* 1998, 120, 9356-9361.
- (67) Garno, J. C.; Zangmeister, C. D.; Batteas, J. D. *Langmuir* 2007, 23, 7874-7879.
- (68) Liu, G. Y.; Amro, N. A. *Proceedings of the National Academy of Sciences of the United States of America* 2002, 99, 5165-5170.
- (69) Yu, J. J.; Tan, Y. H.; Li, X.; Kuo, P. K.; Liu, G. Y. *Journal of the American Chemical Society* 2006, 128, 11574-11581.
- (70) Cyganik, P.; Buck, M. *Journal of the American Chemical Society* 2004, 126, 5960-5961.
- (71) Choi, Y.; Jeong, Y.; Chung, H.; Ito, E.; Hara, M.; Noh, J. *Langmuir* 2008, 24, 91-96.
- (72) Rong, H. T.; Frey, S.; Yang, Y. J.; Zharnikov, M.; Buck, M.; Wuhn, M.; Woll, C.; Helmchen, G. *Langmuir* 2001, 17, 1582-1593.
- (73) Bumm, L. A.; Arnold, J. J.; Dunbar, T. D.; Allara, D. L.; Weiss, P. S. *Journal of Physical Chemistry B* 1999, 103, 8122-8127.
- (74) Magoga, M.; Joachim, C. *Physical Review B* 1997, 56, 4722-4729.
- (75) Wold, D. J.; Haag, R.; Rampi, M. A.; Frisbie, C. D. *Journal of Physical Chemistry B* 2002, 106, 2813-2816.
- (76) Slowinski, K.; Fong, H. K. Y.; Majda, M. *Journal of the American Chemical Society* 1999, 121, 7257-7261.
- (77) Wold, D. J.; Frisbie, C. D. *Journal of the American Chemical Society* 2001, 123, 5549-5556.
- (78) Cui, X. D.; Zarate, X.; Tomfohr, J.; Sankey, O. E.; Primak, A.; Moore, A. L.; Moore, T. A.; Gust, D.; Harris, G.; Lindsay, S. M. *Nanotechnology* 2002, 13, 5-14.
- (79) Wang, W. Y.; Lee, T.; Reed, M. A. *Reports on Progress in Physics* 2005, 68, 523-544.
- (80) Holmlin, R. E.; Ismagilov, R. F.; Haag, R.; Mujica, V.; Ratner, M. A.; Rampi, M. A.; Whitesides, G. M. *Angewandte Chemie-International Edition* 2001, 40, 2378-2382.

- (81) Su, G. J. J.; Aguilar-Sanchez, R.; Li, Z. H.; Pobelov, I.; Homberger, M.; Simon, U.; Wandlowski, T. *Chemphyschem* 2007, 8, 1037-1048.
- (82) Hla, S. W. *Journal of Vacuum Science & Technology B* 2005, 23, 1351-1360.
- (83) Suez, I.; Backer, S. A.; Frechet, J. M. J. *Nano Letters* 2005, 5, 321-324.
- (84) Xie, Z. X.; Kolb, D. M. *Journal of Electroanalytical Chemistry* 2000, 481, 177-182.
- (85) Touzov, I.; Gorman, C. B. *Journal of Physical Chemistry B* 1997, 101, 5263-5276.
- (86) Wen, W. J.; Huang, X. X.; Sheng, P. *Soft Matter* 2008, 4, 200-210.
- (87) Shen, C.; Wen, W. J.; Yang, S. H.; Sheng, P. *Journal of Applied Physics* 2006, 99, -.
- (88) Hao, T. *Advanced Materials* 2001, 13, 1847-1857.
- (89) Ma, H. R.; Wen, W. J.; Tam, W. Y.; Sheng, P. *Advances in Physics* 2003, 52, 343-383.
- (90) Ho, W. *Accounts of Chemical Research* 1998, 31, 567-573.
- (91) Stipe, B. C.; Rezaei, M. A.; Ho, W.; Gao, S.; Persson, M.; Lundqvist, B. I. *Physical Review Letters* 1997, 78, 4410-4413.
- (92) Rezaei, M. A.; Stipe, B. C.; Ho, W. *Journal of Chemical Physics* 1999, 110, 4891-4896.
- (93) Guohua Yang, N. A. A., Gang-yu Liu *Proceedings of SPIE* 2003, 5220, 52.
- (94) Bartels, L.; Wolf, M.; Klamroth, T.; Saalfrank, P.; Kuhnle, A.; Meyer, G.; Rieder, K. H. *Chemical Physics Letters* 1999, 313, 544-552.
- (95) Kolb, D. M.; Ullmann, R.; Will, T. *Science* 1997, 275, 1097-1099.
- (96) Schindler, W.; Hofmann, D.; Kirschner, J. *Journal of Applied Physics* 2000, 87, 7007-7009.
- (97) Li, W.; Hsiao, G. S.; Harris, D.; Nyffenegger, R. M.; Virtanen, J. A.; Penner, R. M. *Journal of Physical Chemistry* 1996, 100, 20103-20113.
- (98) Kolb, D. M.; Engelmann, G. E.; Ziegler, J. C. *Solid State Ionics* 2000, 131, 69-78.
- (99) Zamborini, F. P.; Crooks, R. M. *Journal of the American Chemical Society* 1998, 120, 9700-9701.
- (100) Baunach, T.; Ivanova, V.; Scherson, D. A.; Kolb, D. A. *Langmuir* 2004, 20, 2797-2802.
- (101) Thom, I.; Hahner, G.; Buck, M. *Applied Physics Letters* 2005, 87, 024101.
- (102) Geissler, M.; Wolf, H.; Stutz, R.; Delamarche, E.; Grummt, U. W.; Michel, B.; Bietsch, A. *Langmuir* 2003, 19, 6301-6311.
- (103) Park, M. H.; Jang, Y. J.; Sung-Suh, H. M.; Sung, M. M. *Langmuir* 2004, 20, 2257-2260.
- (104) Joachim, C.; Gimzewski, J. K.; Aviram, A. *Nature* 2000, 408, 541-548.
- (105) Rawlett, A. M.; Hopson, T. J.; Amlani, I.; Zhang, R.; Tresek, J.; Nagahara, L. A.; Tsui, R. K.; Goronkin, H. *Nanotechnology* 2003, 14, 377-384.
- (106) Schilardi, P. L.; Dip, P.; Claro, P. C. D.; Benitez, G. A.; Fonticelli, M. H.; Azzaroni, O.; Salvarezza, R. C. *Chemistry-a European Journal* 2005, 12, 38-49.
- (107) Menke, E. J.; Thompson, M. A.; Xiang, C.; Yang, L. C.; Penner, R. M. *Nature Materials* 2006, 5, 914-919.
- (108) Maisch, S.; Buckel, F.; Effenberger, F. *Journal of the American Chemical Society* 2005, 127, 17315-17322.
- (109) Burtman, V.; Ndobe, A. S.; Vardeny, Z. V. *Journal of Applied Physics* 2005, 98, 034314.
- (110) Fendler, J. H. *Chemistry of Materials* 2001, 13, 3196-3210.
- (111) Selzer, Y.; Cabassi, M. A.; Mayer, T. S.; Allara, D. L. *Nanotechnology* 2004, 15, S483-S488.
- (112) Reed, M. A.; Zhou, C.; Muller, C. J.; Burgin, T. P.; Tour, J. M. *Science* 1997, 278, 252-254.
- (113) Kolb, D. M. *Angewandte Chemie-International Edition* 2001, 40, 1162-1181.

- (114) Hagenstrom, H.; Schneeweiss, M. A.; Kolb, D. M. *Langmuir* 1999, 15, 2435-2443.
- (115) Epple, M.; Bittner, A. M.; Kuhnke, A.; Kern, K.; Zheng, W. Q.; Tadjeddine, A. *Langmuir* 2002, 18, 773-784.
- (116) Frey, S.; Rong, H. T.; Heister, K.; Yang, Y. J.; Buck, M.; Zharnikov, M. *Langmuir* 2002, 18, 3142-3150.
- (117) Vandeweert, E.; Bastiaansen, J.; Vervaecke, F.; Lievens, P.; Silverans, R. E.; Cyganik, P.; Postawa, Z.; Rong, H. T.; Buck, M. *Applied Physics Letters* 2003, 82, 1114-1116.
- (118) Zhong, C. J.; Porter, M. D. *Journal of the American Chemical Society* 1994, 116, 11616-11617.
- (119) Nuzzo, R. G.; Zegarski, B. R.; Dubois, L. H. *Journal of the American Chemical Society* 1987, 109, 733-740.
- (120) Cyganik, P.; Buck, M.; Strunskus, T.; Shaporenko, A.; Wilton-Ely, J. D. E. T.; Zharnikov, M.; Woll, C. *Journal of the American Chemical Society* 2006, 128, 13868-13878.
- (121) Gilbert, S. E.; Cavalleri, O.; Kern, K. *Journal of Physical Chemistry* 1996, 100, 12123-12130.

## Chapter 5 Self-Assembled Monolayers

### General

The most studied and most widely used system of SAMs is alkanethiol on metals. As mentioned in chapter 1, self-assembling surfactant molecule can be divided into three parts: head group, molecular chain, and terminal functional group. Modifications based on these three parts can result in SAMs with new properties. In this chapter, we explored different types of SAMs including thiocyanate (head group is SCN instead of SH for thiol), carboxylic acid terminal group ( $-\text{COOH}$ , polar functional group), and bis(pyrazolyl)pyridine terminal group of interest for metal coordination.

### 5.1 Self-Assembled Monolayers of Dodecyl Thiocyanate

#### 5.1.1 Introduction

Adsorption of organosulfur compounds is a standard way to form self-assembled monolayers (SAMs) on coinage metals, in particular on gold and it is the ease of preparation and flexibility in the design of the molecular structure which enables the tailoring of surface properties for a diversity of applications in (bio)sensors, nanotechnology or electrochemistry.<sup>1-5</sup> While thiols have been most popular they are not an optimal choice from the chemical point of view as they are prone to oxidation to disulfides which in the case of dithiols can seriously affect formation of SAMs<sup>6</sup> or makes the quality of the resulting SAMs critically dependent on the details of the preparation conditions.<sup>7,8</sup> In search for alternatives a number of other options based on precursors have been explored including acetyl protected thiols<sup>7,9-11</sup> or Bunte salts, i.e., organic thiosulfates.<sup>12,13</sup> Common features of these approaches is that the layers, even though chemical analysis shows that they consist of thiolates, are either of poor structural quality and/or experimental conditions are very critical. Another route has

more recently been reported by Ciszek et al.<sup>14,15</sup> who demonstrated that thiocyanates form thiolate SAMs through cleavage of the S-CN bond. Compared to other self-assembling organosulfur compounds, this approach promises to be less critical with respect to preparation conditions as thiocyanates are more stable than thiols and no deprotection steps are required. The thiocyanate assembly on gold has been shown to yield thiolate SAMs and a surface mediated cleavage of the S-CN bond and subsequent desorption of  $[\text{Au}(\text{CN})_2]^-$  has been suggested.<sup>14,15</sup> However, comparison with SAMs formed from thiols showed an inferior quality of the monolayer for the thiocyanate analogues as revealed by cyclic voltammetry,<sup>15</sup> sum frequency generation<sup>16</sup> and STM<sup>16</sup> where the latter did not reveal any ordered structure. In contrast, a very recent study of octyl thiocyanates demonstrated that ordered SAMs can be formed but this depends strongly on the preparation conditions.<sup>17</sup> While solution based preparation at room temperature did not yield ordered SAMs, extended areas of crystalline order were observed for preparation at elevated temperature and adsorption from the vapour phase. However, the overall structural quality of the SAMs is still far from the one of SAMs formed directly from thiols. Furthermore, high resolution STM revealed a structure very different from the  $\sqrt{3} \times \sqrt{3}$  based structures of alkane thiols and a missing row structure was suggested. It appears that, so far, it has proven difficult to establish alternatives to thiols or disulfides which yield thiolate SAMs of high quality.

In this section, we investigate the preparation conditions of thiocyanate. High quality of SAM is obtained on Au, which is promising as an alternation of thiols.

## 5.1.2 Results and Discussion

### 5.1.2.1 STM characterization

Initial experiments with dodecyl thiocyanate used as purchased produced poor quality SAMs as demonstrated by Figure 5.1.

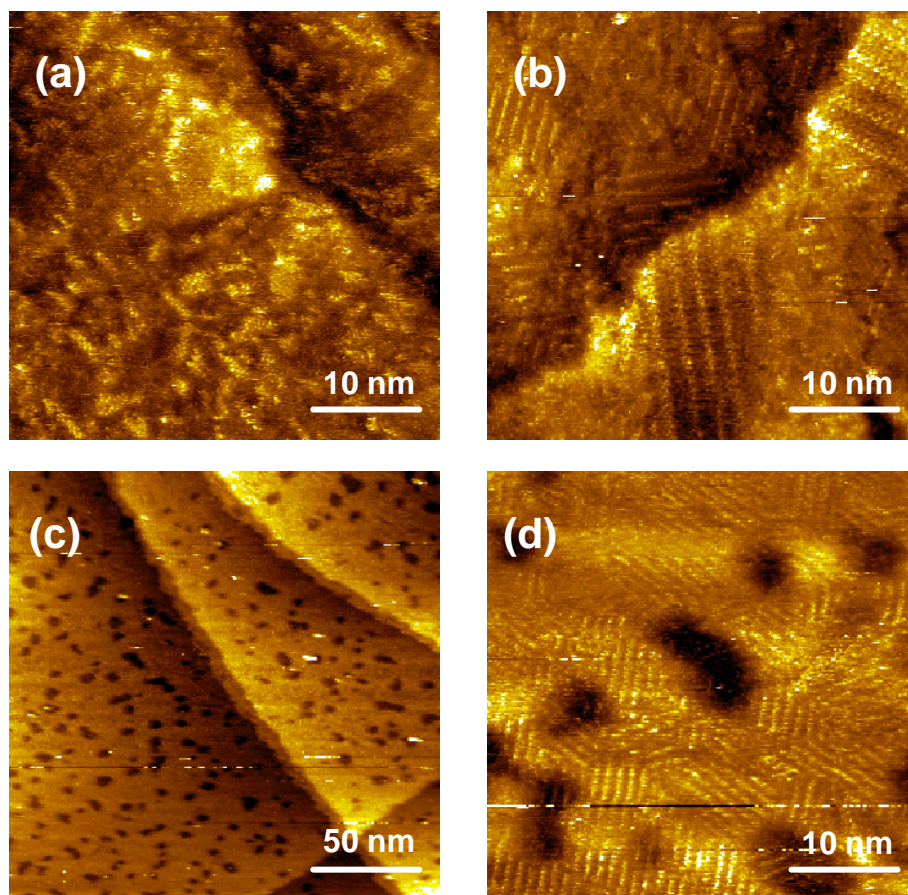


**Figure 5.1** STM images of a Au(111)/mica sample immersed into a 15 mM non-purified C12SCN fresh solution in ethanol. Samples prepared at (a) room temperature for 13 hours, (b) 345 K for 48 hours and (c,d) 345 K for 96 hours (c,d).

Samples prepared at room temperature (Fig. 5.1a) showed no sign of an ordered structure in agreement with the work of Dreesen *et al.*<sup>16</sup> At elevated temperature which is known to improve the structural quality of thiol layers<sup>18-21</sup> ordered features become indeed discernible (Fig. 5.1b). Striped structure are seen which are oriented parallel to the  $\langle 1\bar{1}0 \rangle$  direction and which are separated between 1.3 and 3 nm. With longer immersion times the striped structure becomes more regular and extends over larger areas. After immersion for 96 h a reasonably well-organized layer was obtained with stripes regularly separated by about 1.4 nm (Fig. 5.1d). Height profiles along the stripes reveal a height modulation with  $\sim 5$  Å periodicity. The structure looks like the one reported for octyl thiocyanate (C8SCN).<sup>17</sup> While for C8SCN a missing row structure was suggested, the dimensions and the resemblance to STM images of low coverage

phases of alkane thiols<sup>22,23</sup> is also compatible with a lying down phase of alkane thiols and/or thiocyanates. For reasons which become clear below we did not investigate this structure in more detail. Another interesting observation relates to the appearance of vacancy islands. These monoatomic deep defects of monoatomic depth in the Au-substrate, which are a characteristic feature of alkane thiol SAMs,<sup>24</sup> only appear after prolonged immersion times as seen from the comparison of Figs. 5.1b - d. However, despite the emergence of vacancy islands and an improved order for longer immersion times, no features indicating a  $\sqrt{3} \times \sqrt{3}$  based structure of densely packed, upright-standing thiols were observed.

While the film formation just described was observed for samples prepared from a fresh solution of dodecyl thiocyanate as purchased, immersion of substrates into an identical but aged one, i.e., a solution which has been repeatedly used before to prepare SAMs, produced markedly different results. Au substrates immersed into such an aged solution of C12SCN as purchased yield a SAM virtually identical to one formed from dodecane thiol. As seen from Fig. 5.2, such a SAM exhibits the characteristic extended domains and monoatom deep depressions in the substrate (vacancy islands). The high resolution image shows the molecular arrangement characteristic for an alkane thiolate SAM and described by a  $(4 \times 2)$  unit cell.

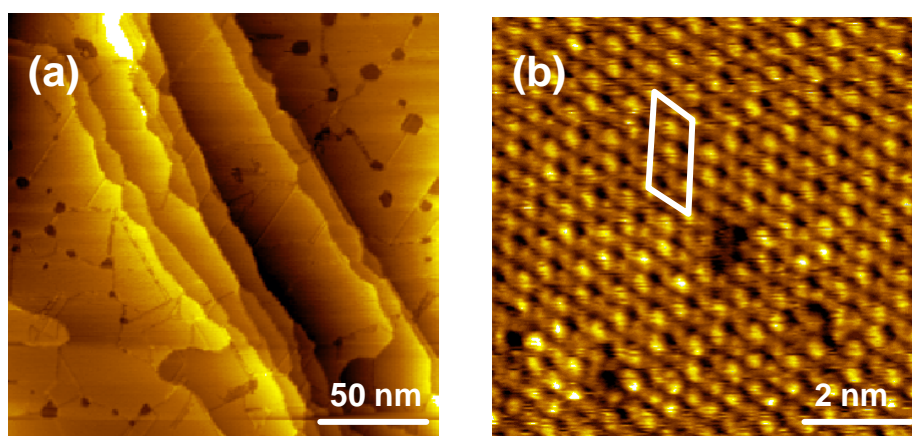


**Figure 5. 2** STM images of a Au(111)/mica sample prepared from a 15 mM non-purified C12SCN aged solution in ethanol at 345 K for 48 h. (a) Large scale image showing vacancy islands. (b) High resolution image with the  $c(4 \times 2)$  unit cell indicated.

Thermal annealed samples revealed the typical structure observed in alkanethiols.<sup>25,26</sup> After annealing at 383 K for 10 h, the depressions in the gold terraces fuse with each other (Fig. 5.3(a)). Stripe structures were formed after annealing at 393 K for 10 h (Fig. 5.3 (b), (d)). However, sample annealing at 418 K results in a damaged layer (c).

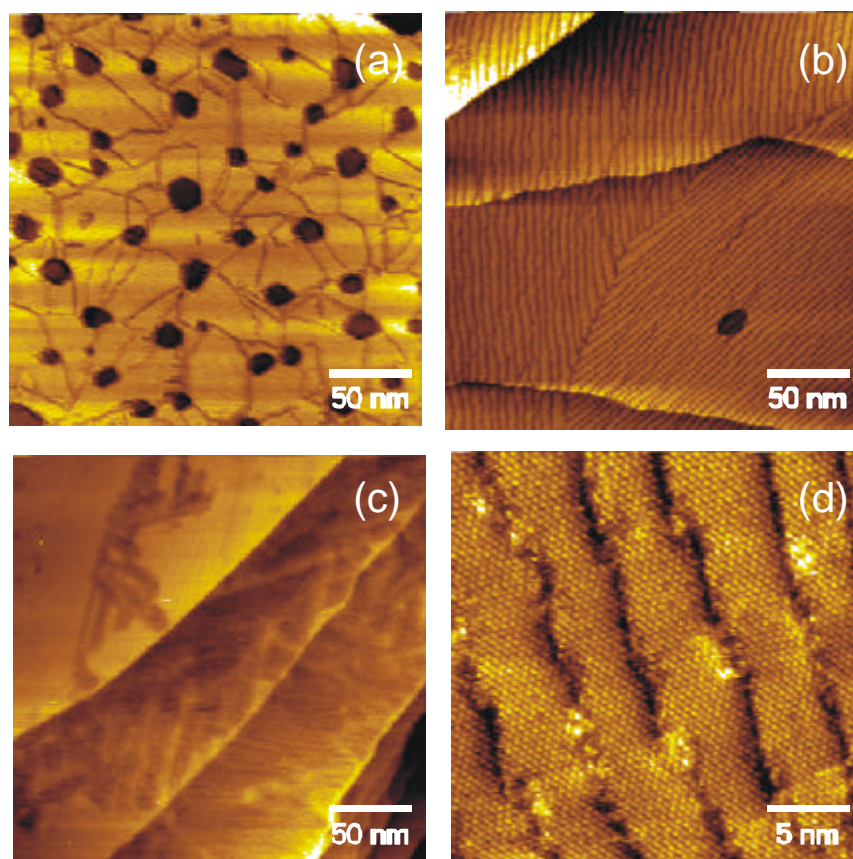


**Figure 5.3** STM images of samples annealed at 383 K(a), 393 K(b) and 418 K(c) for 10 h in  $N_2$  atmosphere. (d) shows high resolution structure of (b).

Two possible explanations can account for the observation of SAM formed on Au(111). One (model I) is that the substance as purchased contains impurities which adsorb preferentially and impede adsorption of the thiocyanate and its conversion to thiolates. Through repeated use of the same solution impurities would be removed, thus, resulting in a facilitated adsorption of the thiocyanate and subsequent conversion to thiolate. An alternative explanation (model II) would be an enrichment of disulfide in the solution caused by exchange processes between species in solution and on the surface<sup>27</sup>. Through adsorption of thiocyanates, conversion to thiolates on the Au

substrate and subsequent desorption as disulfides, which would be facilitated by elevated preparation temperatures, repeated use of the same solution for several Au substrates should result in an enrichment of disulfides. In this case formation of the thiol-like SAM would be essentially due to the adsorption of disulfides present in low concentration and not due to thiocyanates. In order to test which of the mechanisms applies, experiments with purified C12SCN were performed and results cross checked by a number of control experiments.

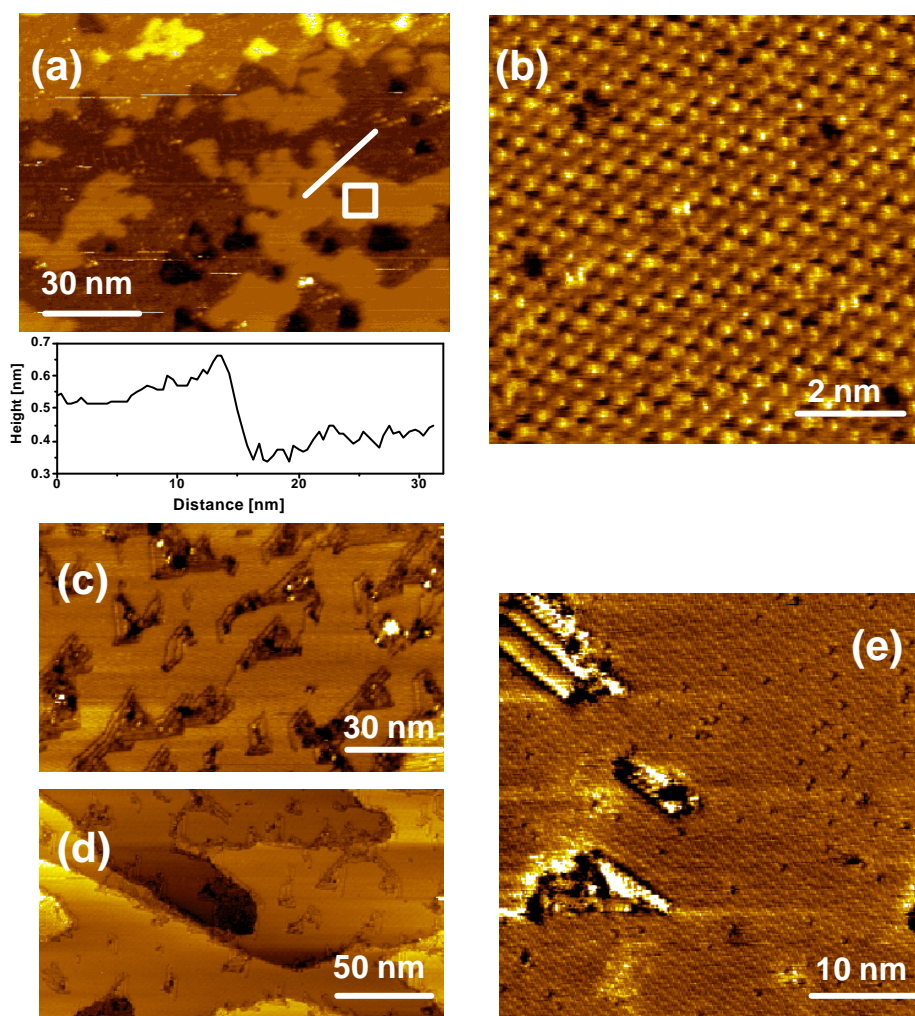


**Figure 5. 4** STM images of a Au(111)/mica sample immersed into a 15 mM purified C12SCN fresh solution in ethanol. Preparation at room temperature for 13h (a), 345 K/13h (c) and 345K/48h (d) large scale image showing vacancy islands. (b) High resolution image with the  $c(4 \times 2)$  unit cell indicated. Height profile in (a) is along the line, and the square defines the area of the high resolution image (b). (e) High resolution image of (d).

As demonstrated by Fig. 5.4, purification changes the picture quite dramatically. SAMs prepared under identical conditions as the one shown in Fig. 5.1a, i.e., room temperature and 13 h immersion time, appear very different (Fig. 5.4a). Patches which cover a substantial part of the surface and appear higher by about 2.5 Å, some striped features and 2.5 Å deep depressions are discernible. Magnifying the bright patches (Fig. 5.4b) reveals a structure identical to the  $\sqrt{3} \times \sqrt{3}$  arrangement of a thiol SAM. Interestingly, molecular resolution was only obtained on the patches which appear higher and not from the surrounding area. The appearance of a densely packed phase already at room temperature, which does not form from the non-purified, non-aged solution, already suggests that it is not the enrichment of disulfide in the bulk solution through thiocyanate-thiolate conversion and desorption (model II) but rather the impurities present in the original substance which prevent formation of a densely packed layer (model I).

The ordered patches seen for samples prepared at room temperature grow substantially in size for preparation at elevated temperature and longer immersion times as seen from Figs. 5.4c-e and any striped phases disappear. However, small disordered areas remain. Immersion at 345 K for even more than 96 h still does not eliminate them. A very interesting point is that the ordered areas consist of very large domains with disordered patches interspersed. It seems that ordered domains grow around these patches which means that once the structureless patches have formed thiolate SAM formation in these areas is inhibited. Suspecting that the disordered areas may originate from a small amount of residual contamination still present even after purification, we applied the same procedure as above for the non-purified substance, i.e., several fresh gold substrates were consecutively used to remove impurities. Preparation from such an aged solution for 48 hours eliminates the residual disordered areas as seen in Fig. 5.4d and leads to formation of a SAM of stunning quality as illustrated by Figs. 5.5a and 5.5b.

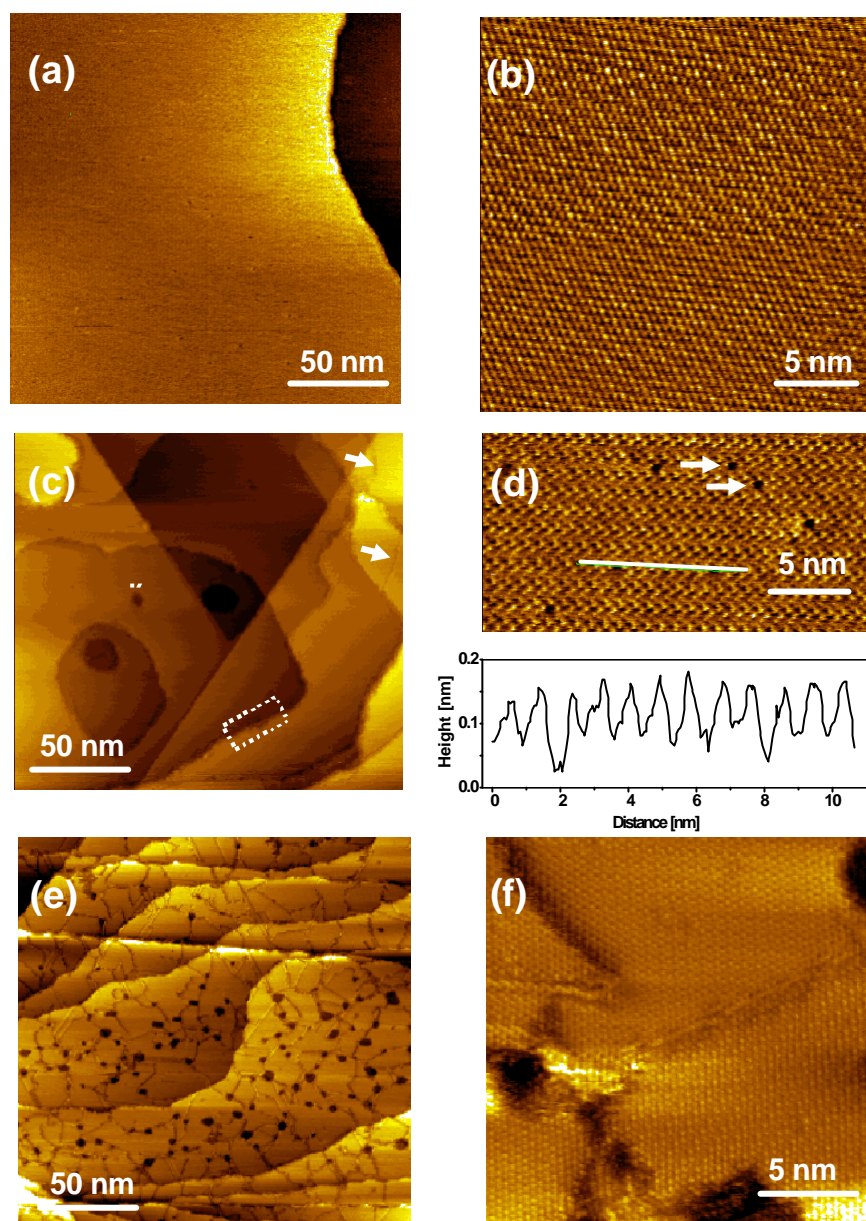


**Figure 5.5** (a-d) STM images of a Au(111)/mica sample immersed into a 15 mM purified and aged C12SCN solution in ethanol. Preparation at 345 K/48h. (e,f) Images of an C12SH SAM prepared at 345 K/48h. Arrows in (d) mark domain boundaries, dotted circle and rectangle highlight a vacancy island and a defect area, respectively. Arrows in (d) mark molecule sized defects. For details see text. Height profile in (d) is defined by the line.

Domains exceeding 200 nm in diameter are regularly observed. Another feature is the absence of vacancy islands in the STM images of Figs 5.5a and 5.5b which is striking when compared to a SAM prepared from C12SH under otherwise identical conditions (Fig. 5e,f). While the structural perfection of the layer shown in Figs. 5a and 5b is quite commonly observed areas of slightly lower quality are also present in other

locations of the same sample. This is illustrated by Figs. 5.5c where some residual vacancy islands (marked by dotted circle), domain boundaries (marked by arrows) and small areas of defects (marked by dotted rectangle) can be seen. Another type of defect which is characteristic for SAMs formed from C12SCN is revealed by the high resolution image shown in Fig. 5.5d. Molecular sized depressions about 0.5 Å deep are seen in some areas. The same type of depression is seen at somewhat higher density for the sample shown in Fig. 5.4e. Occasionally we also see analogous depressions extended over a few molecules. Since in these cases individual molecules can be clearly resolved we conclude that the depressions are not caused by missing molecules. At present we can only speculate about the origin of these contrast variation. Possible reasons could be contaminations at the interface or a molecular species with no or different head group trapped in the film. The latter would be consistent with a very small signal of a non-thiolate species sometimes seen in XPS (see below).

Since the quality of the layer is so critically dependent on impurities present in the solution we paid utmost attention to possible artifacts which could result in high quality monolayers from species other than the thiocyanate. Obvious candidates are thiols/disulfides as already mentioned above. To establish, that these species are not generated in the bulk solution by simple conversion of thiocyanates due to the elevated temperatures and extended periods of time, the purified C12SCN solution (no substrate immersed) was stored at the temperature and for the duration which result in high quality layers. After that a substrate was immersed into the solution for overnight and no high quality layers were obtained. Another control experiment was to use a purified aged solution and produce a high quality layer such as the one shown in Fig. 5.5. Subsequently it was mixed in a 1:1 ratio with an unpurified fresh solution which results in a layer of poor quality as an unpurified fresh solution (see Fig. 5.6(a)). A further control experiment was the addition of C12SH to the as-purchased C12SCN. A SAM prepared from this mixture showed the typical good quality of a thiolate SAM (see Fig. 5.6 (b)).

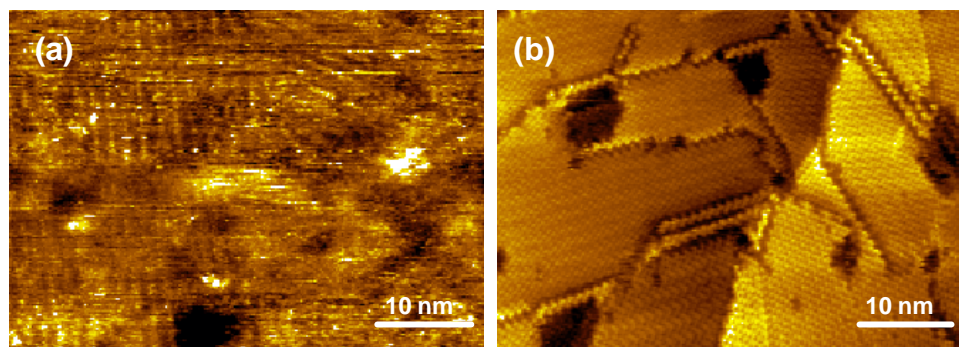


**Figure 5.6** (a) STM image of a Au(111)/mica sample immersed into mixture of purified aged C12SCN solution and unpurified fresh C12SCN solution (1:1 ratio) at 345 K for 13 h. (b) STM image of a Au(111)/mica sample immersed into C12SH solution and unpurified fresh C12SCN solution (1:1 ratio) at 345 K for 13 h.

All these tests demonstrate that a high quality layer is not generated by species converted from isocyanates due to high temperatures and extended preparation times but by thiocyanates directly. All experiments taken together reveal a striking sensitivity of thiocyanate based SAM formation to impurities. Unfortunately, we have no information about the detailed nature of the impurity in the as-purchased C12SCN beyond the presumption that it might be an oxidised sulfur species (see XPS below).

### 5.1.2.2 XPS and NEXAFS Spectroscopy

XPS and NEXAFS measurements and data evaluation were done through collaborations by Michael Zharnikov and Tobias Weidner. Information is provided here as results are part of the interpretation of systems. The influence of the solution purity was further elucidated by XPS in which we compared SAMs prepared by immersion of the Au/mica substrates in either a fresh (sample I) or aged (sample II) solution of purified C12SCN in ethanol. Fig. 5.7 compares the C 1s and S 2p spectra of the two types of samples. The C 1s spectra are very similar with the main peak at 284.8 eV, related to the alkyl chain, and a small shoulder at higher BE (286.5-287 eV), related to a contamination (CO) and clearly visible only for sample I. The FWHM of the main peak for sample II is noticeably smaller than that for sample I (1.38 eV vs. 1.54 eV) suggesting a higher structural homogeneity of the former. The S 2p spectra of both

samples are dominated by the doublet with a BE of 162.0 eV (S 2p<sub>3/2</sub>) characteristic of thiolate-type sulfur bonded to the metal surfaces. For sample II, this doublet is accompanied by a low-intensity one at 163.8 eV (S 2p<sub>3/2</sub>) which has also been reported (164 eV) in the study of octane thiocyanate<sup>17</sup> and which could be assigned to unbound sulfur species<sup>28</sup>. In contrast, the S 2p spectrum of sample I exhibits a quite intense peak at 168.83 eV (S 2p<sub>3/2</sub>) related to an oxidised sulfur species (167.6 and 169.8 eV are observed for SO<sub>3</sub><sup>-</sup> and SO<sub>4</sub><sup>-</sup>, respectively).<sup>29</sup> As mentioned in the STM section this feature could be a signature of the species adsorbed in the patches where no thiolate SAMs is formed (e.g. Fig. 5.4d).

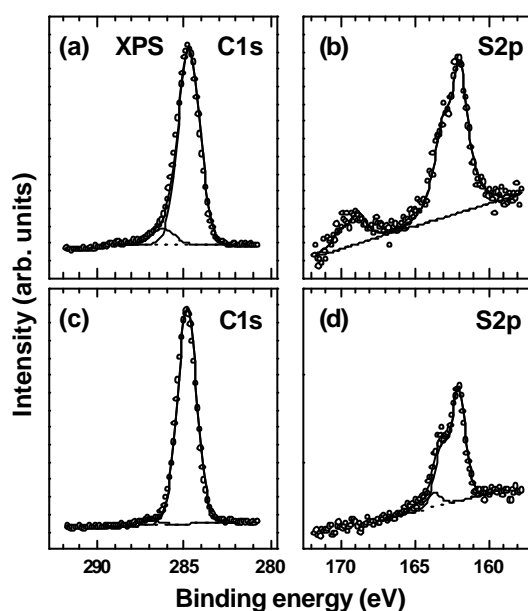


**Figure 5. 7** C 1s (a,c) and S 2p (b,d) XPS spectra of Au(111)/mica samples immersed into a fresh (a,b) and aged (c,d) solution of purified C12SCN (15 mM) in ethanol. The spectra were acquired at a photon energy of 400 eV.

The N 1s and O 1s regions were also measured (not shown). No N1s signal was detected for sample II, whereas a very small trace of nitrogen was observed for sample I. Very small O1s signals could be detected from both samples, which, however, was stronger for sample I than II. Summarising, the XPS data fully support the conclusion drawn from the STM images that high quality thiolate SAMs can be formed from C12SCN provided contaminations are removed by the ageing procedure.

The formation of a well organized layer is further corroborated by analysis of the NEXAFS spectra of sample II shown in Fig. 5.8. These spectra exhibit characteristic absorption resonances of extended alkyl chains in *all trans* conformation, namely a sharp R\* resonance at  $\approx 287.7$  eV, attributed to the excitations into C-H\* valence orbitals and/or Rydberg states,<sup>30-34</sup> and two broader resonances at  $\approx 293.4$  eV and  $\approx 301.6$  eV, related to valence, antibonding C-C  $\sigma^*$  and C-C'  $\sigma^*$  orbitals, respectively.<sup>30,35</sup> All the above resonances exhibit a clear linear dichroism, suggesting a high orientational order in the respective sample (Fig. 5.8).

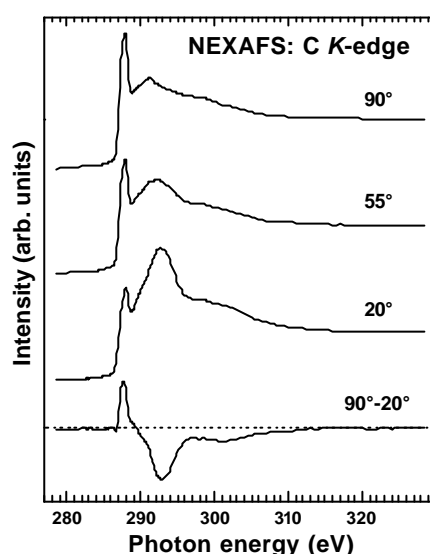


**Figure 5. 8** NEXAFS spectra of a Au(111)/mica sample immersed into an aged solution of purified C12SCN (15 mM) in ethanol. The spectra were acquired at X-ray incidence angles of 90°, 55°, and 20°. The bottom curve represents the difference between the 90° and 20° spectra. The dotted line corresponds to zero and is a guide to the eye.

### 5.1.2.3 IRRAS characterization

Fig 5.9 shows the IR spectra of SAMs prepared from two types of solution: a fresh solution with unpurified C12SCN and an aged solution of purified C12SCN. In agreement with the XPS data, no C-N vibration peak between 2100 and 2200  $\text{cm}^{-1}$  was observed in both cases (not shown). The sample prepared in fresh solution exhibits the characteristic symmetric and asymmetric stretch vibrations of  $\text{CH}_2$  groups at 2854 and 2925  $\text{cm}^{-1}$ , respectively, while a sample prepared in the aged solution shows these

vibrations at 2852 and 2920  $\text{cm}^{-1}$ . According to literature data,<sup>36-38</sup> a shift of these peaks towards lower frequencies is a fingerprint of a higher orientational and conformational order of the aliphatic chains in the latter sample.

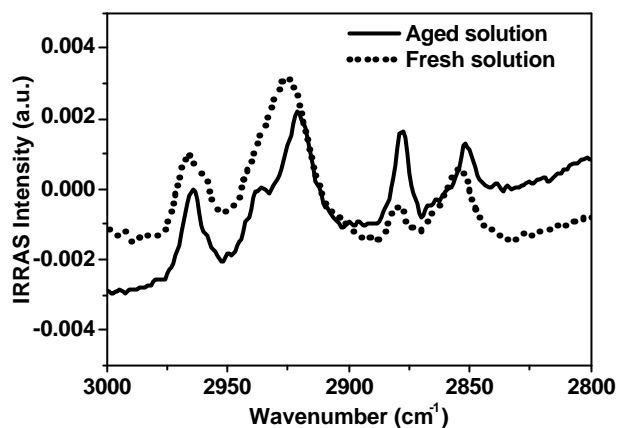


Figure 5. 9 IRRAS spectra of SAM on Au(111)/mica prepared from a 15 mM non-purified C12SCN fresh solution (dotted line) and a 15 mM purified C12SCN aged solution (solid line).

### 5.1.3 Conclusion

Thiolate SAMs formed from C12SCN are structurally identical and of at least the same structural quality to those obtained from the respective alkane thiol. It is important to note that the influence of the preparation parameters, besides temperature and immersion time, the purity of the substance is particularly critical. In contrast to thiols which can easily displace contaminations<sup>39</sup> it seems that dissociative adsorption of thiocyanates is very effectively inhibited by contaminations. While it is unclear at present which of the elementary steps are affected, the difference to thiols can be speculated to originate from differences in the initial sticking coefficient of the thiocyanate and the activation barrier for S-CN bond cleavage of the adsorbed thiocyanate. Cleavage of the rod-like moiety can be expected to be sterically much more demanding than S-H or S-S bond cleavage as an orientation of the SCN moiety parallel to the surface might be required. High quality SAM of C12SCN is promising as an alternative to thiols.

## 5.2 Self Assembled Monolayers of MUA Prepared by Physical Vapour Deposition

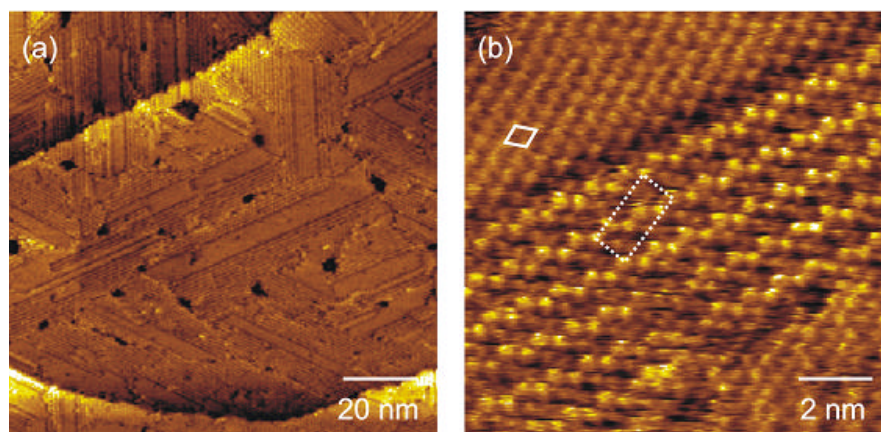
### 5.2.1 Introduction

Carboxylic acid ( $-\text{COOH}$ ) terminated surfaces are of interest for a wide range of applications in electrochemistry, sensor development, nanoparticles and biology<sup>40-44</sup>. In case of the alkanethiols ( $\text{CH}_3$  termination), the adsorption process leads to the formation of a highly ordered, crystalline adlayer<sup>3,45</sup>. Unlike  $\text{CH}_3$ -terminated SAMs, high quality  $\text{COOH}$ -terminated SAMs are harder to form due to the formation of hydrogen bonding between two molecules.<sup>46,47</sup> As a result, a wide range of contact angles ( $10 - 70^\circ$ ) has been reported.<sup>48-50</sup> Several methods have been proposed to improve the quality of  $\text{COOH}$ -terminated SAMs, such as disrupting the interplane hydrogen bonds by adding  $\text{CF}_3\text{COOH}$ <sup>51</sup> or acetic acid<sup>48</sup> and rinsing the sample by base solution. However, a high quality monolayer is still difficult to obtain.

To avoid possible solvent effect and to reduce the hydrogen bond formations during adsorption, we use physical vapour deposition (PVD) method to form ordered, highly crystalline carboxylic acid group terminal structures on Au(111).

### 5.2.2 Results and Discussion

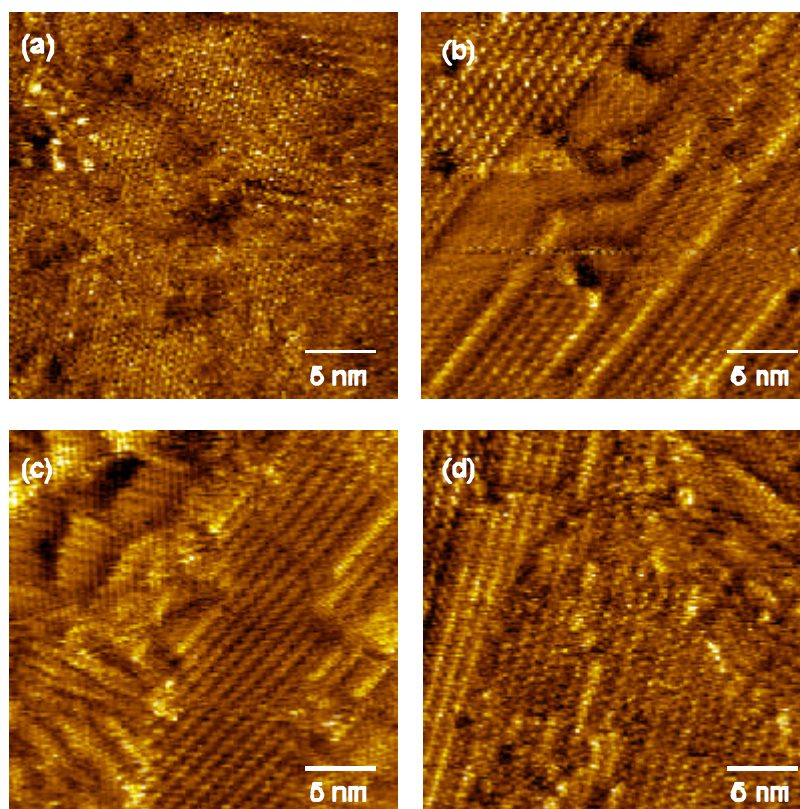
#### 5.2.2.1 STM and contact angle characterizations



**Figure 5.10** STM images of MUA SAM prepared at 323 K for 5 hours showing the large scale (a) and molecular scale structure of MUA (b). Two different structures are seen. One is  $\sqrt{3} \times \sqrt{3}$  (marked by solid lines), the other one is the  $4 \times 2$  superlattice structure (marked by dotted lines).

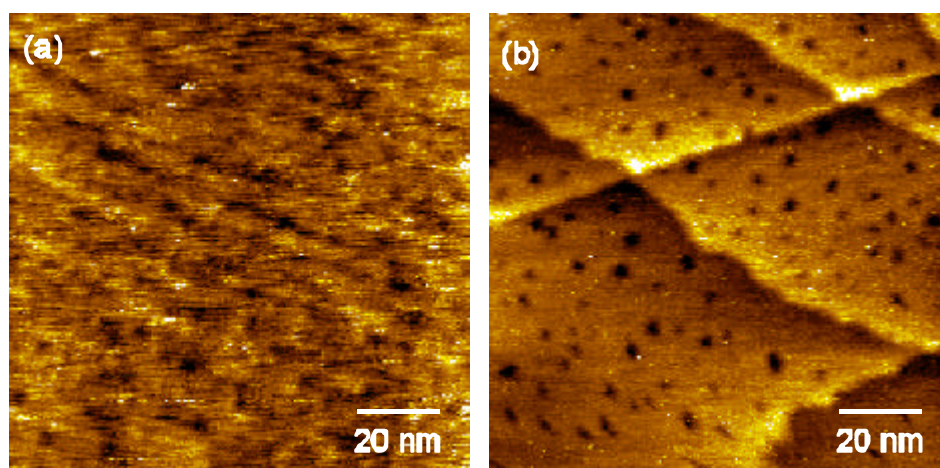
Fig 5.10 shows STM images of SAM of MUA prepared by PVD at 323 K for 5 hours. The reason for choosing 323 K is that the melting point of MUA is about 318-323 K. By using a higher temperature than the melting point, one would expect the MUA molecules transfer more easily to the Au substrate due to higher vapor pressure.

It was found that sample prepared by PVD has a crystalline structure as shown in Fig 5.10 (a) compared with the samples prepared in ethanol solution as shown in Fig 5.12. The MUA assembled on the Au(111) has a preference to grow along a certain direction. There are clearly two different structures on the surface as shown in Fig 5.10 (b). One is the  $\sqrt{3} \times \sqrt{3}$  (marked by solid lines), the other one is the  $4 \times 2$  superlattice structure (marked by dotted lines). This  $4 \times 2$  structure suggests that during this PVD assembly process, the Au-S bonding and the molecular chain determine the orientation of the SAMs, while the terminal group has a minor role.



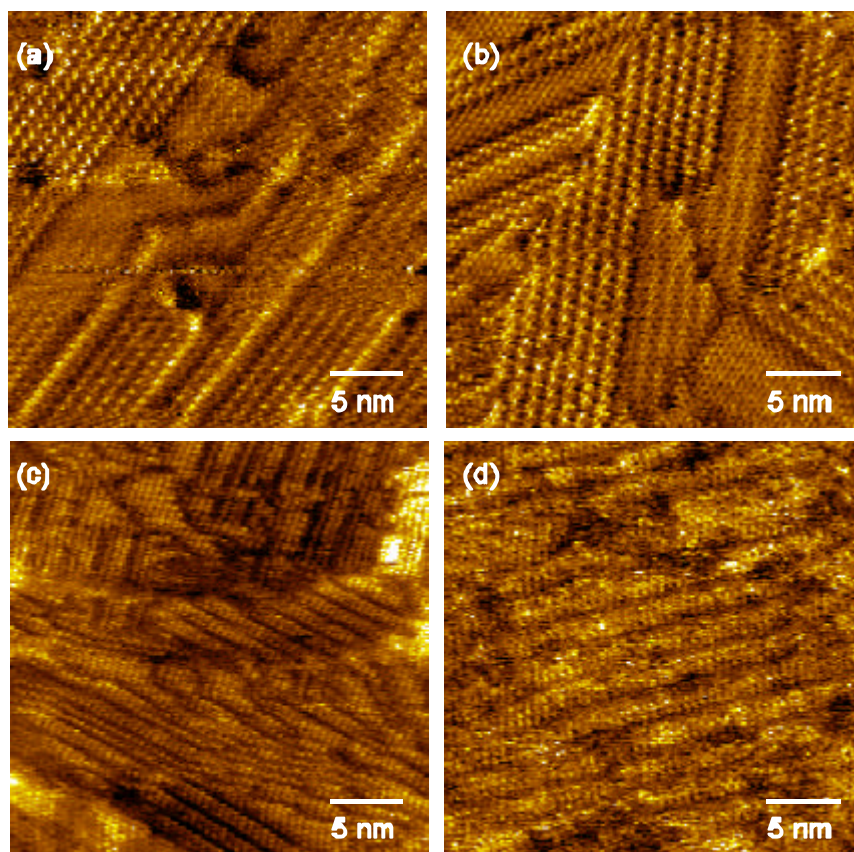
**Figure 5.11** STM images of MUA prepared at 333 K. (a) 2.5 hours; (b) 5 hours; (c) 15 hours; (d) 30 hours.

Fig 5.11 shows the STM images of MUA SAMs prepared at 333 K for various incubation times. Fig 5.11(a) shows that the molecule transfer is quick, after 2.5 hours incubation, the MUA has already covered the entire Au surface, and molecular resolution can be obtained, but the layer quality is still poor at this stage. By increasing the incubation time to 5 hours, a better quality SAM can be formed as shown in Fig. 5.11(b). This SAM shows clearly two different structures as what had seen in Fig 5.10. Further increase of the incubation time to 15 and 30 hours does not change the structures too much (Fig 5.11 (c),(d)). For comparison, we also prepared SAMs of MUA from ethanol solution with MUA concentrations of 1 mM and 0.1 mM. STM images in Fig 5.12 shows that SAMs of MUA prepared in ethanol solution have a poor quality and no molecular resolution can be observed.



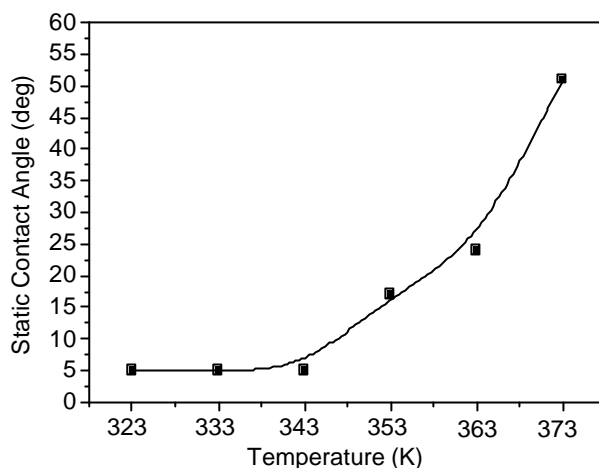
**Figure 5. 12** STM images of MUA prepared in ethanol solution at 333 K for 5 hours. (a) 1 mmol; (b) 0.1 mmol.

Fig 5.13 shows the STM images of SAMs of MUA prepared at various temperatures. It was found that samples prepared at 333 and 343 K have similar structures (Fig. 5.13 a,b). A double row structure was observed as the temperature increased to 353 K (Fig. 5.13c). These striped structures are about 1 nm wide, correspond to two MUA molecule distance across the surface, and are believed to be the formation of dimers due to intermolecular hydrogen bonding. Further increase of the temperature to 363 K makes the layer more disordered (Fig. 5.13d).



**Figure 5. 13** STM images of MUA prepared at 333, 343, 353, and 363 K for 5 hours as shown in (a), (b), (c) and, (d), respectively.

This result is consistent with the contact angle measurement as shown in Fig 5.14. The contact angle of MUA prepared at 323, 333 and 343 K have a low contact angle of  $5^\circ$  (in fact, it is only a rough measurement as the water droplet spreads quickly and makes a precise measurement difficult). For sample prepared at 353 and 363 K, the contact angle is  $16^\circ$  and  $22^\circ$  respectively. A contact angle of about  $50^\circ$  for samples prepared at 373 K might be due to desorption of MUA SAM. These contact angles are relatively small compared with the contact angle of SAMs prepared in ethanol solution. The contact angle of SAMs of MUA prepared from 1 mM and 0.1 mM ethanol solution at 333 K for 5 hours is  $55^\circ$  and  $34^\circ$ , respectively. Extending the incubation time from 5 hours to 15 hours results in higher contact angle of  $64^\circ$  and  $53^\circ$  for 1 mM and 0.1 mM solution, respectively. This strongly suggests the formation of hydrogen bonding between MUA molecules.



**Figure 5. 14** Contact angles of MUA prepared by PVD on Au/Si substrate at various temperatures for 5 hours.

### 5.2.2.2 Electrochemical characterization

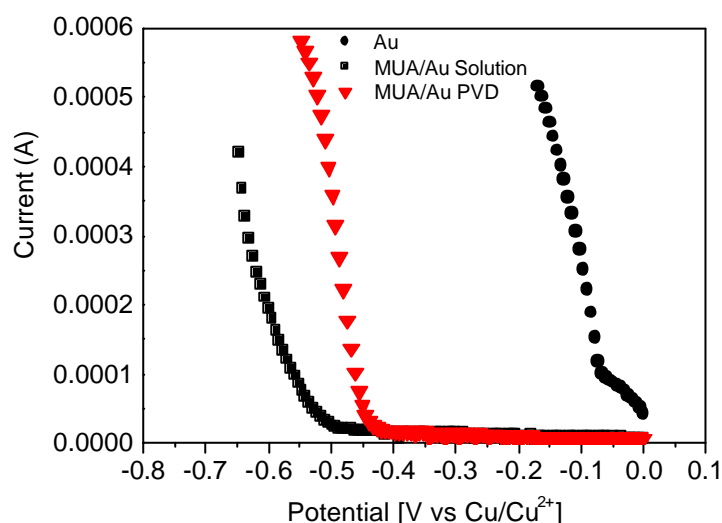


**Figure 5. 15** Copper deposition on a Au/Si electrode, and Au/Si electrode modified by MUA prepared in solution and prepared by PVD at 333 K for 5 hours. The copper solution is 50 mM H<sub>2</sub>SO<sub>4</sub> and 5 mM CuSO<sub>4</sub>.

Examinations of MUA SAMs were further carried out by electrochemical characterization. Fig 5.15 shows copper deposition on bare Au and MUA modified Au surfaces prepared in ethanol solution and prepared by PVD. It was found that after modification, the onset of deposition has been shifted negatively for both MUA SAMs, which shows that both layers have fully covered the Au surface. For sample prepared in

solution, the initial deposition potential is about  $-0.5$  V, while for sample prepared by PVD, the initial deposition potential is about  $-0.44$  V, which is  $0.06$  V more positive than for the sample prepared in solution. This is not because of the SAM quality prepared from PVD is less good as SAM prepared from solution, but might be due to the formation of double layers for samples prepared from solution (see XPS data in section 5.2.2.4).

### 5.2.2.3 IRRAS characterization

Fig 5.16 shows the IR spectroscopy of both samples prepared in solution and prepared by PVD. It has been previously shown that single, non-hydrogen bound carboxyl groups at  $\sim 1740$   $\text{cm}^{-1}$ , carboxyl groups hydrogen-bound with one hydrogen bond or hydrogen bonds to two different neighboring molecules at  $\sim 1720$   $\text{cm}^{-1}$ , and completely dimerized carboxyl groups with two hydrogen bonds to one neighboring molecule at  $\sim 1700$   $\text{cm}^{-1}$ .<sup>52,53</sup> It was found that both samples have a broad peak cover the range of  $1720$  and  $1740$   $\text{cm}^{-1}$ , which indicated that both samples have single carboxyl group and hydrogen-bound group. This suggests that sample prepared by PVD also has hydrogen bonding, which might be formed between two MUA molecules or due to the presence of adsorbed water.

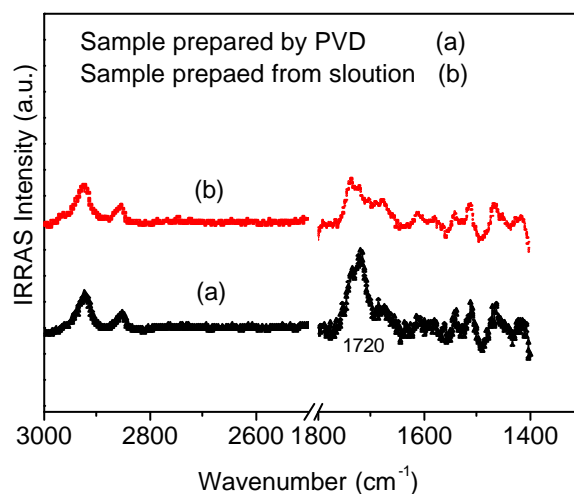


**Figure 5. 16 IR spectroscopy of MUA prepared by PVD and prepared in ethanol solution at 333 K for 5 hours.**

## 5.2.2.4 XPS and NEXAFS Spectroscopy

XPS and NEXAFS measurements and data evaluation were done through collaborations by Michael Zharnikov and Nirmalya Ballav. Information is provided here as results are part of the interpretation of systems. Fig 5.17 shows XPS spectra of samples prepared by PVD and immersion in solution. (a) is the O 1s spectra, the peak positions for both samples are all at about 532.4 eV. (b) is the C 1s spectra, it was found that for samples prepared by PVD, there is one peak at 284.9 eV, which is a characteristic of densely packed and contamination-free alkanethiol SAMs; For samples prepared from solution, show a higher binding energy of 285.3 eV. These two peaks are related to the alkyl chain. Both samples have a second peak at 289.3 eV due to the carboxylic acid moiety. (c) shows the S 2p spectra. Both samples show S 2p doublet at positions of 162.1 and 163.7 eV. The peak at 162.1 eV is similar to the CH<sub>3</sub>-terminated alkanethiol SAMs adsorbed on Au substrates, indicating that this can be assigned to the S atom bound to the Au surface.<sup>54</sup> The peak at 163.7 eV is related to unbound sulfur due to disulfide moieties (R-S-S-R).<sup>55-57</sup> However, for samples prepared from solution, there is a minor peak at 164.2 eV, which can be assigned to the SH group.<sup>58</sup> It is noted that the intensities of both O 1s and C 1s are stronger for samples prepared from solution than samples prepared from PVD. Quantitative analysis revealed that double layer of MUA was obtained for samples prepared from solution, while monolayer was obtained from PVD.

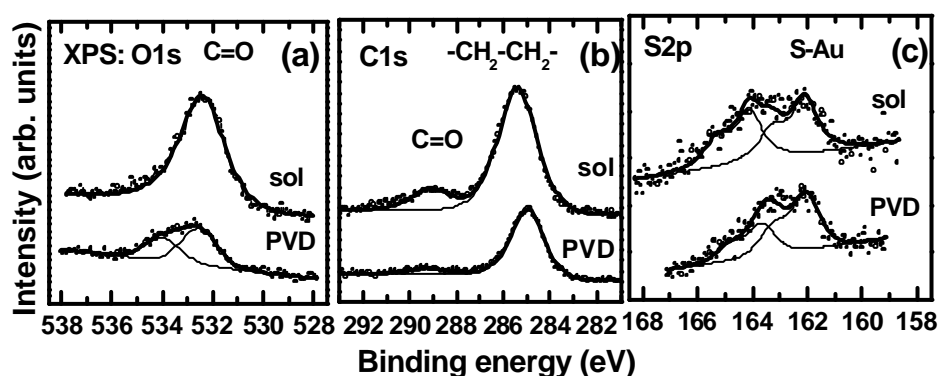


Figure 5. 17 C 1s, O 1s, and S 2p XPS spectra of MUA/Au(111)/Mica samples prepared by PVD and immersed in solution.

Fig 5.18 shows the NEXAFS spectra of samples prepared by PVD and prepared from solution. C K-edge NEXAFS spectra of both samples have a pronounced absorption resonance at 287.7 eV, which is attributed to the excitations into C-H\* valence orbitals and/or Rydberg states; absorption at 293.4 eV is related to valence, antibonding C-C  $\sigma^*$  orbital.<sup>59</sup> However, there is a weak absorption at 285.1 eV for sample prepared from solution which is not found in sample prepared by PVD. This absorption at 285.1 eV is characteristic of C=C bonds ( $\pi^*$  resonance), which might be due to some impurities. O K-edge NEXAFS spectra show that for sample prepared by PVD, the absorption is at 532.6 eV, while for sample prepared from solution, the absorption is at 532.8 eV. Both are related to  $\pi^*$  C=O. The broad feature at the range of 540-550 eV is assigned to a  $\sigma^*$  orbital between the C and O atoms.<sup>53</sup>

All the resonances exhibit a clear linear dichroism, suggesting a high orientation; however, the sample prepared by PVD shows a better order than sample prepared from solution.

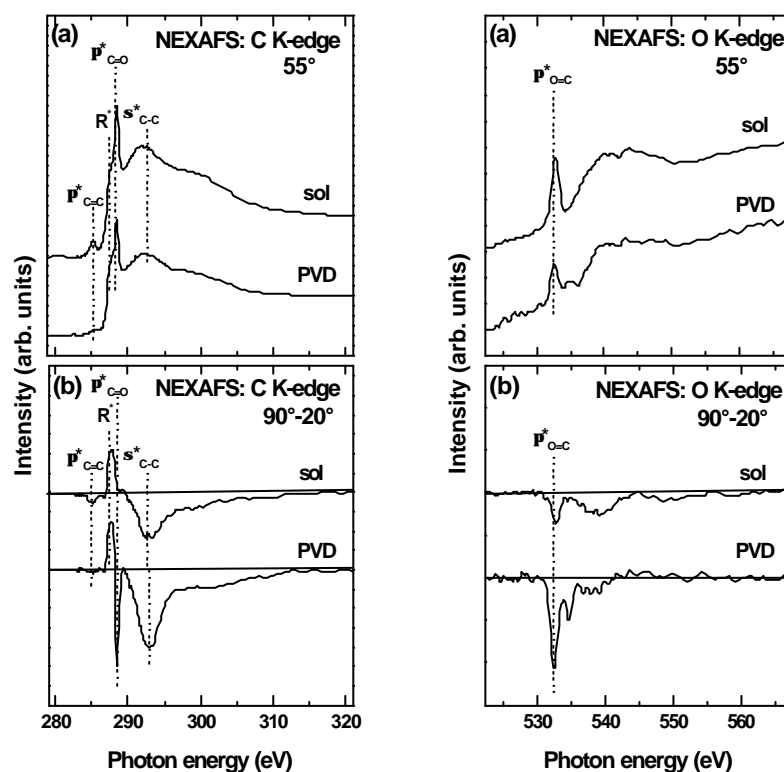


Figure 5. 18 NEXAFS spectra of samples prepared by PVD and prepared from solution. The spectra were acquired at X-ray incidence angles of  $90^\circ$ ,  $55^\circ$ , and  $20^\circ$ . The bottom curve represents the difference between the  $90^\circ$  and  $20^\circ$  spectra.

A quantitative analysis yields a thickness of 14.5 Å for sample prepared from PVD and 28.5 Å for sample prepared from solution, indicating the sample prepared by PVD is a monolayer, while sample prepared from solution is a double layer. Quantitative evaluation of the angular dependence of the resonance intensity, as shown in Fig 5.19 for R\*-resonance yields a tilt angle of the hydrocarbon chain of 34° for sample prepared by PVD, which is a typical value for alkanethiol, while for sample prepared from solution, the tilt angle is about 60.5°, indicating a less ordered structure. Also, the  $\pi^*_{C=O}$ -resonance yields a tilt angle of 39° for sample prepared by PVD, while for sample prepared from solution, poor data were obtained.

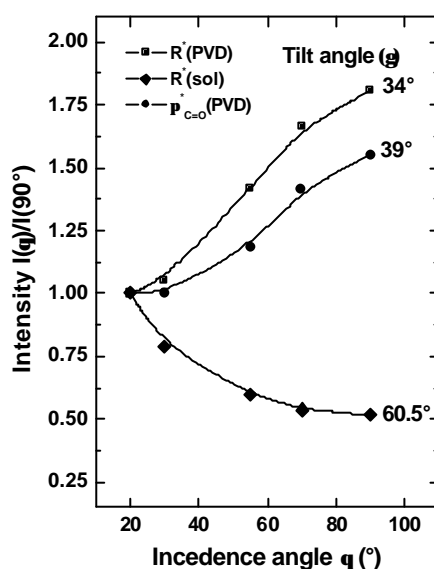


Figure 5. 19 Angular dependence of the R\* and  $\pi^*_{C=O}$  resonance intensity ratio.

### 5.2.3 Conclusion

We investigated the self-assembly of MUA SAM on Au(111) by a simple physical vapor deposition. Well-ordered MUA layers are formed in a few hours at the temperature range of 323-363 K. STM images with molecular resolution show clearly two different structures described by a  $\sqrt{3} \times \sqrt{3}$  unit cell and (4×2) superlattice, respectively. This is in sharp contrast to samples prepared in ethanol solution which show disordered structure. Contact angle measurements reveal that MUA prepared by

PVD has a contact angle as low as 5°. XPS, NEXAFS, IR and electrochemical methods are applied to examine the MUA SAMs. It is revealed that sample prepared by PVD is a monolayer, while sample prepared from solution forms a double layer.

## 5.3 Bis(pyrazol-1-yl)pyridine-terminated SAMs on Au(111)

### 5.3.1. Introduction

A SAM bearing bis(pyrazolyl)pyridine (bpp) moieties can serve as a flexible platform for complexation and as a template for the controlled assembly of more complex structures such as metal coordinated multilayers or metal-organic frameworks.<sup>60,61</sup> However, substantial hurdles have to be overcome in order to realize this concept, such as precise control of the arrangement and addressing of the molecular entities. It is not yet clear to what degree the structure of SAMs consisting of laterally complicated  $\pi$ -systems<sup>62-66</sup> can be controlled. SAMs of a related class of molecules, terpyridyl-based thiols, have been used as starting layer to grow films in a layer by layer fashion using bis(terphenyl)-metal coordination<sup>67-69</sup> but no detailed structural characterisation of the initial monolayer was reported.<sup>70,71</sup>

In this section, we have begun to study the process of films formation of bpp-SH and bpp-SCN molecules (see Fig. 5.20) on Au(111) by STM.

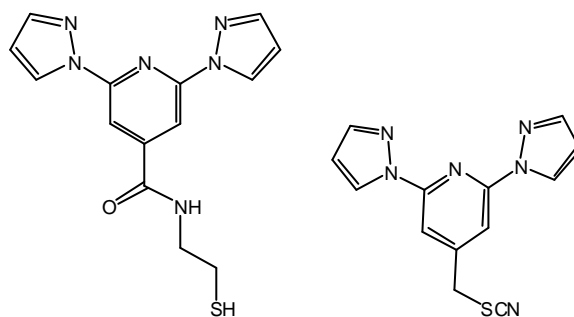
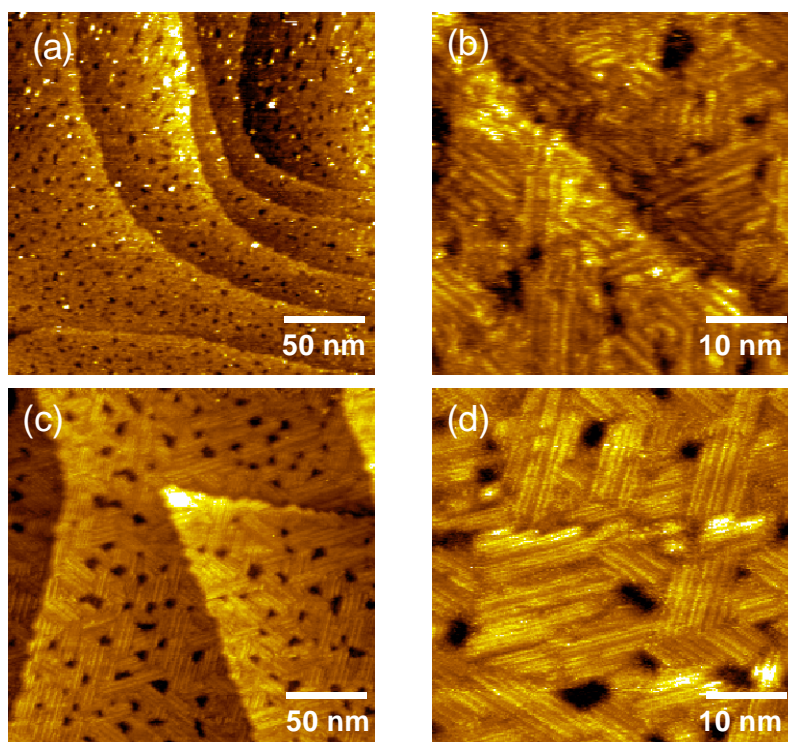


Figure 5.20 Structures of bpp-SH and bpp-SCN.

### 5.3.2 STM characterization of bpp-SH

Since ethanol is most commonly used for thiol SAM preparation, samples were initially prepared from this solvent. Immersion at room temperature resulted in SAMs of low structural quality with an indication of an ordered arrangement of molecules in small areas only. The order improved significantly for preparation at elevated temperatures and extended immersion times.



**Figure 5.21** STM images of **bpp-SH** on **Au(111)/mica**. Preparation from ethanol at 345 K for 5 days (a, b) and from DMF solution at 363 K for 15 hours (c,d).

On a large scale (Fig. 5.21a) the surface is characterised by depressions  $\sim 2.5$  Å deep and about 2-6 nm in size which are the so-called vacancy islands in the gold substrate well known from thiols where the sulfur head group is tethered to an alkane chain.<sup>19,24</sup> A magnified image (Fig. 5.21b) reveals stripes  $\sim 1.5$  nm apart indicative of ordered structures. In attempts to further improve the structure, DMF was used as solvent as its boiling point of 426 K allows higher preparation temperatures than ethanol. A significantly better ordered SAM was obtained at 363 K as suggested by the striped features in the large scale image of Fig. 5.21c which are shown at higher resolution in

Fig. 5.21d. However, reproducibility was relatively poor as the ratio of ordered and disordered areas varied significantly from sample to sample. While the reason for this is not clear at present we suspected that low levels of impurities adsorbing preferentially or bpp-SH molecules adsorbing in a flat lying geometry due to the interaction of the aromatic system with the substrate might inhibit formation of a well-ordered layer. To reduce a possible interaction of the aromatic moieties with the substrate, bpp-SH was adsorbed onto a substrate already precoated with an organic layer. Attempts to adsorb bpp-SH by displacement of short chain alkanethiols such a butane thiol, similar to long chain alkane thiols which replace shorter ones,<sup>72-74</sup> did not result in any improvement of the film quality.

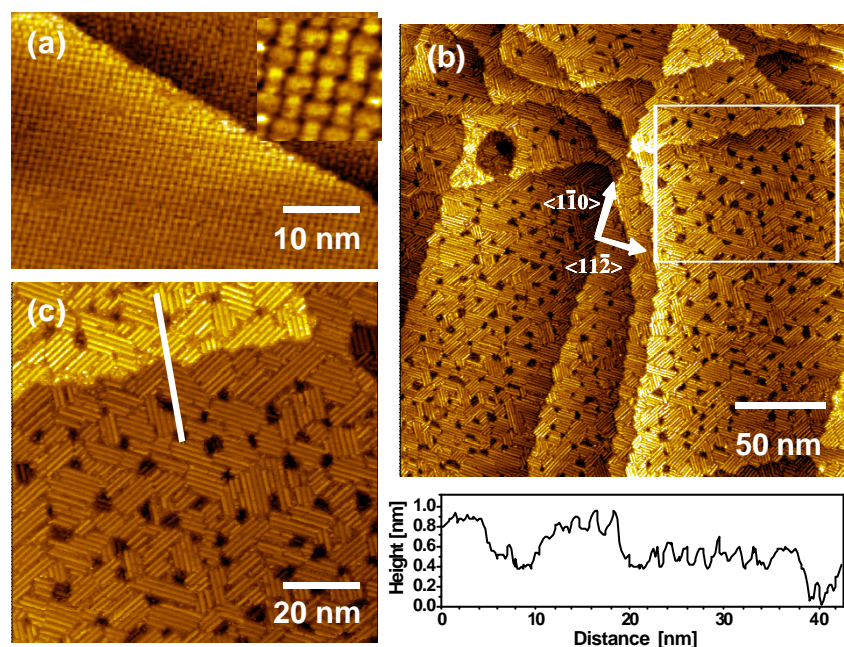


**Figure 5.22** STM images of PTCDA (a) and bpp-SH SAM (b,c) on Au(111)/mica. PTCDA layer and bpp-SH SAM were prepared from DMF solutions at room temperature/5 min immersion time and 363 K/15h, respectively. Inset in (a) shows PTCDA layer at high magnification. Inset in (b) shows large scale image with area of high magnification indicated by white rectangle.

However, a substantial improvement was found for a different type of adsorbate, namely perylene-3,4,9,10-tetracarboxylic-3,4,9,10-dianhydride (PTCDA). These molecules form highly ordered layers on the Au surface with its molecular plane parallel to the surface (Fig. 5.22a).<sup>75,76</sup> This type of precoating resulted in bpp-SH SAMS of reproducible quality with very well ordered domains of stripes aligned along

the  $\langle 11\bar{2} \rangle$  direction as seen in Fig. 5.22b,c. The height profile defined by the line in Fig. 5.22c which runs across a step and a depression of identical height, reveals the latter is indeed one of the above mentioned vacancy islands. In a substantial fraction of the depressions the ordered structure of the SAM is identified, analogous to alkane thiols.<sup>77</sup> The most prominent feature of the STM images of Fig. 5.22b,c is the striped structure suggesting a symmetry of the molecular arrangement which is different from the threefold one of gold substrate. This conflict in symmetry which is similar to biphenylhexane thiol (Fig. 7 in ref<sup>19</sup>), causes packing problems where differently oriented domains meet. Interestingly, the vacancy islands are usually located at domain boundaries. Another notable feature of the bpp-SH SAM is the pronounced faceting of the steps along the  $\langle 1\bar{1}0 \rangle$  direction clearly seen in Figs. 5.22b and c. Again, similar to biphenyl alkane thiols<sup>21</sup> the molecule alters the energetics of the interface in a way that the  $\langle 11\bar{2} \rangle$  directions become energetically more favourable.

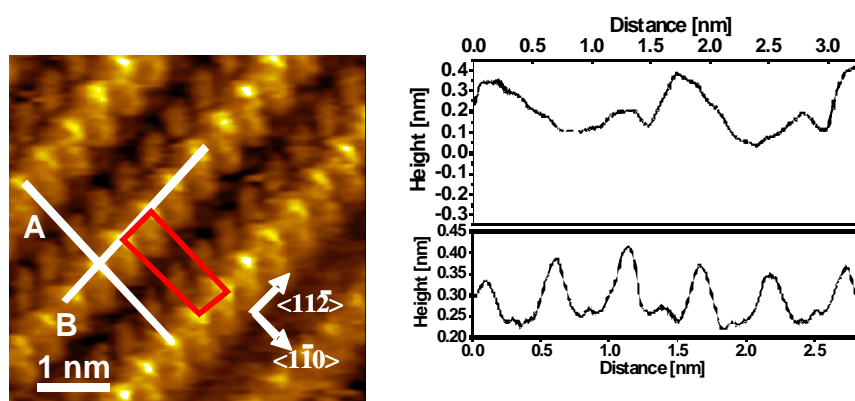


**Figure 5.23** High resolution STM image of a bpp-SH SAM on Au(111)/mica prepared from DMF solutions at 363 K for 15 h. Line A, B mark the respective height profiles. The  $3 \times 5$  unit cell is indicated by the red rectangle.  $U_{\text{tip}} = 1\text{V}$ ,  $I = 25\text{ pA}$ .

The highly ordered SAMs obtained by use of precoated substrate allows also recording of STM images at molecular resolution. The magnified images of Fig. 5.23 reveal that the stripes consist of protrusions which are  $\sim 5\text{ \AA}$  apart (profile B) and that the distance between the stripes is  $\sim 15\text{ \AA}$  (profile along line A). The corrugation is significantly more pronounced along  $\langle 1\bar{1}0 \rangle$  compared to  $\langle 11\bar{2} \rangle$ . Within one

period the profile along A shows two clear maxima of different height and a minimum about half way in between. From the dimension of the unit cell a commensurate  $5 \times \sqrt{3}$  structure is derived with one molecule per unit cell. This corresponds to an area of  $75 \text{ \AA}^2$  which is more than three times the value of  $21.6 \text{ \AA}^2$  found for alkane thiols. The long side of the unit cell fits well to the long axis of the molecule, thus, strongly suggesting that the bpp moieties form stacks.

### 5.3.3 STM characterization of bpp-SCN

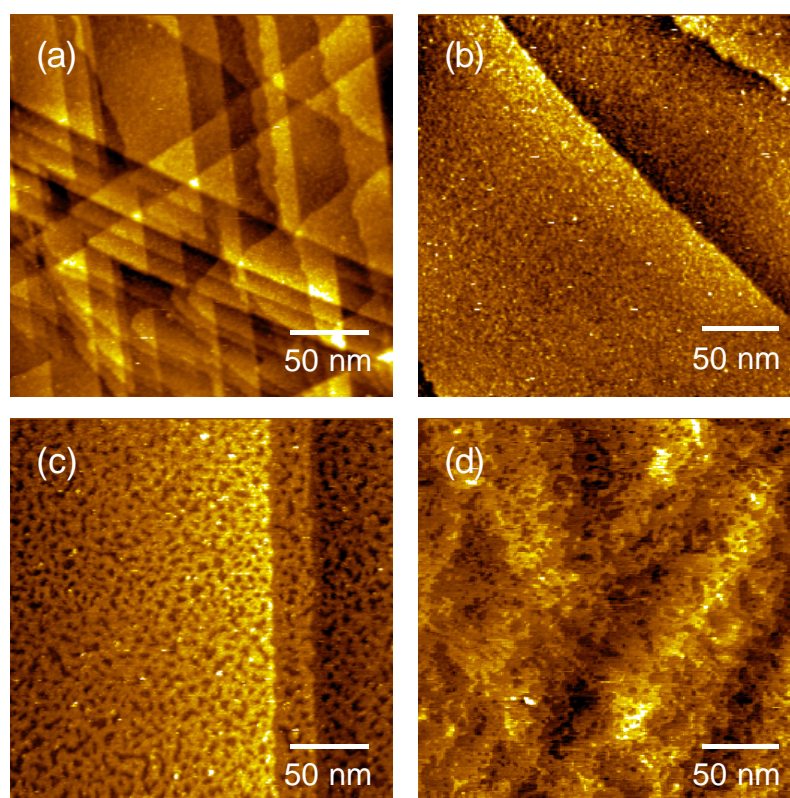


**Figure 5.24** STM images of bpp-SCN on Au(111)/mica samples prepared by immersion in ethanol. Samples prepared at 345 K for 2 h(a), 16 h(b), 48 h (c), and 88 h(d).

Figure 5.24 shows samples prepared from ethanol solution at 345 K for various times. Au surfaces all showed modification after incubation. However, no ordered structures were found on the surfaces. Samples prepared at 345 K for 16 h (see Fig. 5.24 (b)), which are normal preparation conditions for biphenyl SAMs, showed a rough surface with disorder structures. Decreasing the incubation time (see Fig. 5.24 (a)) or

increasing the incubation time (see Fig. 5.24 (c),(d)) result in a flatter or rougher surface.

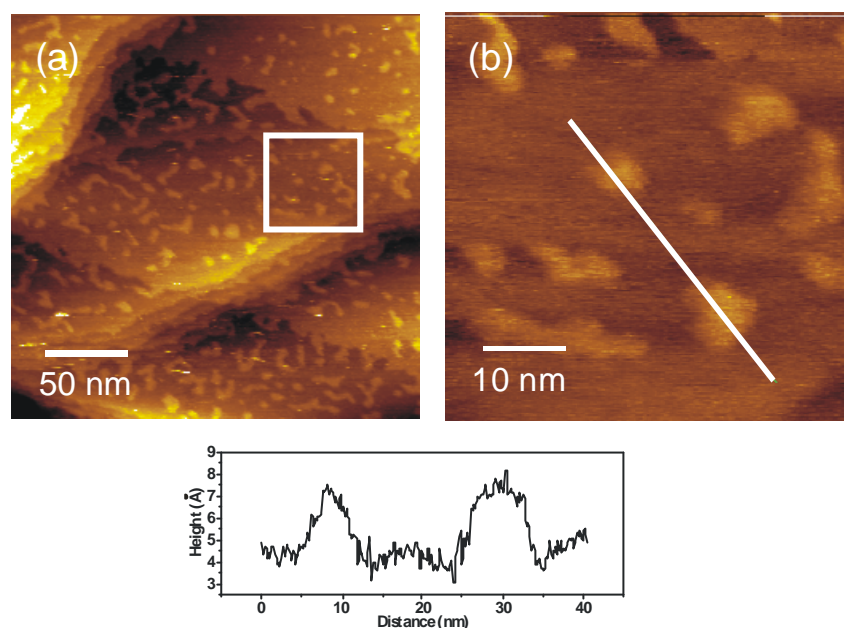


**Figure 5.25** (a) STM images of Au(111)/mica sample immersed into bpp-SCN solution in DMF at 345 K for 48 h. (b) STM image of selected area as indicated by square in (a). The cross section shows the height difference is  $\sim 2.5$  Å.

Sample prepared from DMF solution at 345 K for 48 h (see Fig. 5.25) also showed similar surface topography as prepared from ethanol solution. Islands were randomly distributed across the Au surface. These islands are about one Au atom high (see cross section analysis in Fig. 5.25). Au vacancy islands are observed on surfaces after the adsorption of organothiol. However, large amount of random islands are found here indicating a strong interaction/reaction between Au surface and substances on them. It is well-known that Au can be oxidized in cyanide solution to a soluble complex of  $[Au(CN)_2]^-$  (see equation 5-1).



However, as discussed in section 5.1, we do not observed such rough surface after adsorption of C12SCN, indicating that other factors also play a role.

Raisanen, et. al. found that 4-pyridinethiol dissolved Au in alcohol solutions in the presence of oxygen.<sup>78</sup> This is surprising as thiols are usually used as etch resists for Au.

They proposed that the solvent (alcohol in their case) can provide a suitable proton source to the pyridinethiolato nitrogen and assist the detachment of Au complex. However, such dissolution of Au was not observed in the preparation of bpp-SH, which has a similar pyridine structure as bpp-SCN. These experiments show that both SCN and the pyridine structure contributed to the dissolution of Au in our case, although the exact mechanism is unknown to us at the moment.

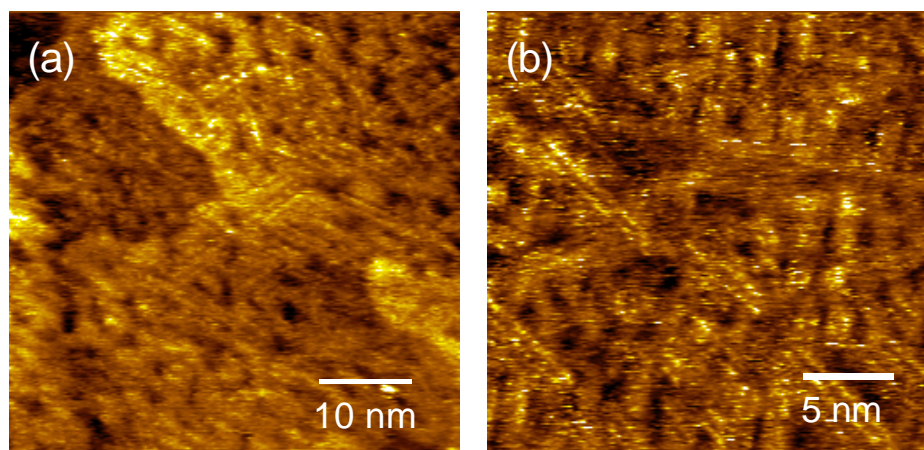


**Figure 5.26** STM images of Au(111)/mica samples immersed into bpp-SCN solution in DMF at 277 K for 24 h (a) and 48 h (b).

We found that preparation at room temperature or even below can inhibit the dissolution process and allowing order structures of bpp-SCN formed on Au surface. Figure 5.26 show striped structures which were formed on Au(111) surface by preparing in DMF solution at 277 K. However, more ordered structures still cannot be obtained by preparing from solution.

Inspired by the preparation of MUA SAM, we prepared samples by the PVD method. Striped structures were formed on Au(111) surface as shown in Figure 5.27. There is coexistence of ordered and disordered of phases for samples prepared from 363-383 K.

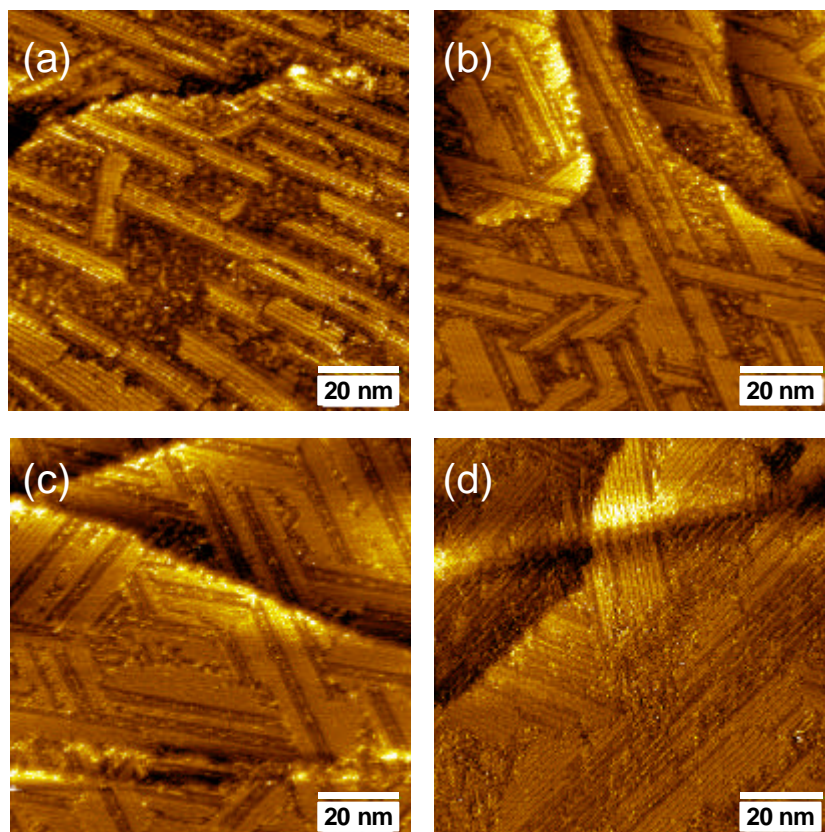


Figure 5.27 STM images of Au(111)/mica samples prepared by PVD method. (a) 363 K for 12 h. (b) 363 K for 24 h. (c) 373 K for 24 h. (d) 383 K for 24 h.

Highly crystalline structures were successfully obtained by preparing at 393 K for 12 h (see Figure 5.28). However, defect lines (missing rows) are clearly visible on the surface. These lines are about 3 nm wide and range from tens of nanometer to more than 100 nm. They are running exclusively along the  $\langle 11\bar{2} \rangle$  directions.

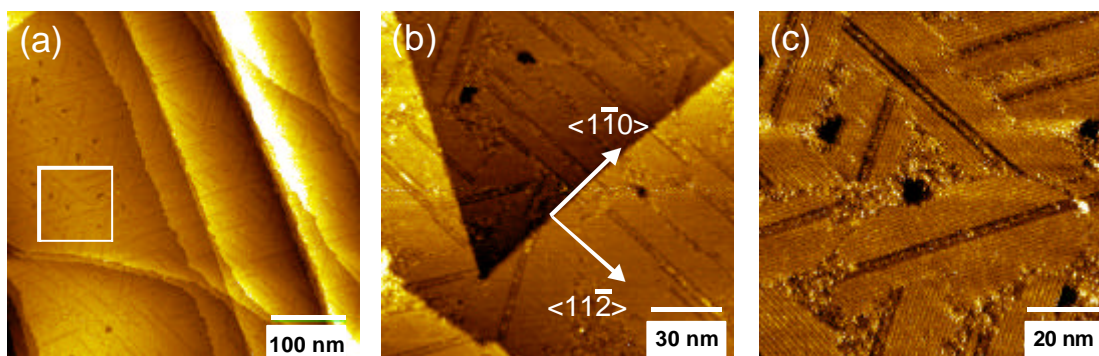
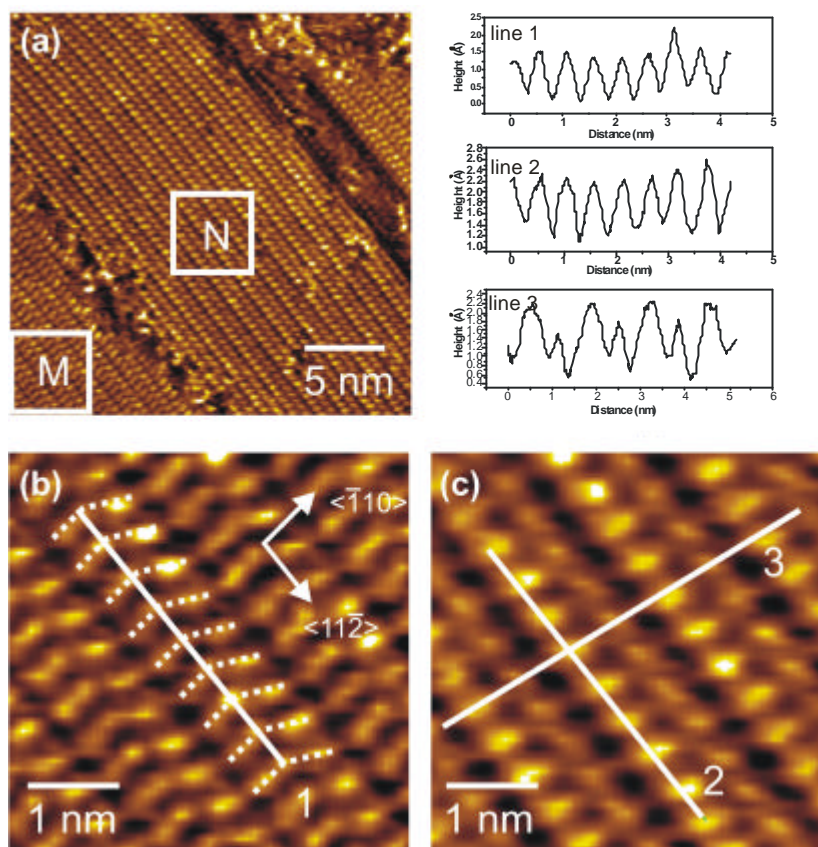


Figure 5.28 (a), (b) STM images of Au(111)/mica samples prepared by PVD method at 393 K for 12 h. (c) selected area as indicated by square in (a).

Molecular resolution images were also obtained as shown in Figure 5.29. Two different structures were found as labelled with M and N. The magnified image (see

Figure 5.29 (b)) of structure M reveals that the stripes consist of protrusions which are  $\sim 5 \text{ \AA}$  apart (line 1) and that the distance between the stripes is  $\sim 13 \text{ \AA}$ , which fits a bpp-SCN molecule. It is noted that the three bright spots are not in a line (see dot lines in (b)), indicating that there is a bend or a tilt of rings. The line profiles reveal that the stripes in N are also  $\sim 5 \text{ \AA}$  apart (line 2) and that the distance between the stripes is  $\sim 13 \text{ \AA}$  (line 3). However, there are only 2 spots for a molecule instead of 3 that has been seen for structure M. It has been proposed that only parts of molecules interacting with surface would contribute to the STM contrast although exact reasons are still unclear.<sup>79,80</sup>



**Figure 5.29** (a) STM images of Au(111)/mica samples prepared by PVD method at 393 K for 12 h. (b) Selected area as indicated by square in (a), structure M (c) Selected area as indicated by square in (a), structure N.

Indeed, we found that structure M can “transfer” to structure N simply because of tip effect. Figure 5.30 shows two subsequent images. There was a clearly change of tip as indicated in Figure 5.30(b) (labelled by dashed line). It was found that structure N as shown in 5.30(a) changed to structure M as soon as the tip changes.

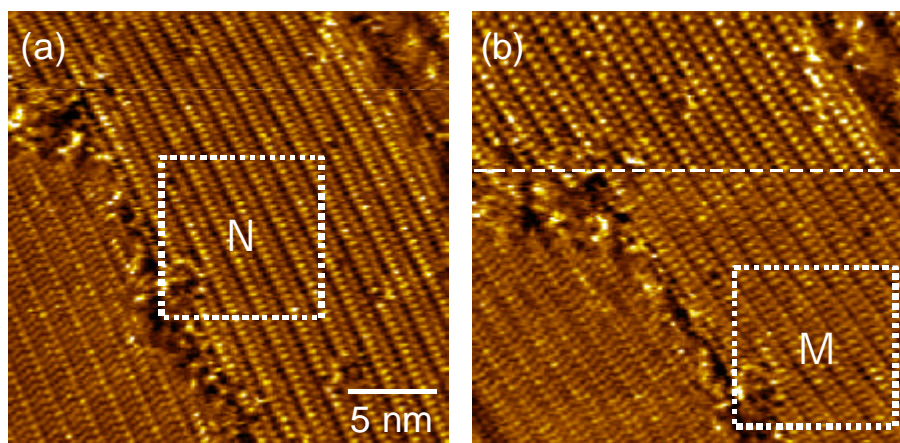


Figure 5.30 STM images showing the structure transition. (a) Scanning up; (b) Scanning down.

### 5.3.4 Conclusions

Self-assembled monolayers of a bis(pyrazol-1-yl)pyridine-substituted thiol (bpp-SH) and thiocyanate (bpp-SCN) on Au(111)/mica were studied with STM. Preparation conditions such as temperature, solvent, and contamination affect the formation of SAMs on Au(111) much more than when using other common thiols such as alkanethiols and biphenylthiols. For bpp-SH, using substrates which were precoated with PTCDA, preparation at elevated temperatures yields highly ordered layers whose structure is described by a rectangular ( $5 \times \sqrt{3}$ ) unit cell containing one molecule. For bpp-SCN, an ordered structure cannot be obtained from solution (ethanol, DMF) as bpp-SCN can etch the Au surface, but can be obtained by PVD. However, further studies are needed to elucidate the reason for the difference. Moreover, one should note that the repeatability of forming this SAM is low. Possible reason might be contamination of other SAMs on Au surface inhibit the adsorption of bp-SCN (as discussed in section 5.1, thiocyanate is sensitive to contaminations). Also, traced oxygen, water, and the variation of vapour pressure may also affect the repeatability.

## References:

- (1) Mrksich, M. *Chemical Society Reviews* 2000, 29, 267-273.
- (2) Gooding, J. J.; Mearns, F.; Yang, W. R.; Liu, J. Q. *Electroanalysis* 2003, 15, 81-96.
- (3) Love, J. C.; Estroff, L. A.; Kriebel, J. K.; Nuzzo, R. G.; Whitesides, G. M. *Chemical Reviews* 2005, 105, 1103-1169.
- (4) Schilardi, P. L.; Dip, P.; Claro, P. C. D.; Benitez, G. A.; Fonticelli, M. H.; Azzaroni, O.; Salvarezza, R. C. *Chemistry-a European Journal* 2005, 12, 38-49.
- (5) Thom, I.; Hähner, G.; Buck, M. *Appl. Phys. Lett.* 2005, 87, 024101.
- (6) Tour, J. M.; Jones, L.; Pearson, D. L.; Lamba, J. J. S.; Burgin, T. P.; Whitesides, G. M.; Allara, D. L.; Parikh, A. N.; Atre, S. V. *Journal of the American Chemical Society* 1995, 117, 9529-9534.
- (7) Azzam, W.; Wehner, B. I.; Fischer, R. A.; Terfort, A.; Woll, C. *Langmuir* 2002, 18, 7766-7769.
- (8) Tai, Y.; Shaporenko, A.; Rong, H. T.; Buck, M.; Eck, W.; Grunze, M.; Zharnikov, M. *Journal of Physical Chemistry B* 2004, 108, 16806-16810.
- (9) Shaporenko, A.; Elbing, M.; Baszczyk, A.; von Hanisch, C.; Mayor, M.; Zharnikov, M. *Journal of Physical Chemistry B* 2006, 110, 4307-4317.
- (10) Niklewski, A.; Azzam, W.; Strunskus, T.; Fischer, R. A.; Woll, C. *Langmuir* 2004, 20, 8620-8624.
- (11) Kang, Y. K.; Won, D. J.; Kim, S. R.; Seo, K. J.; Choi, H. S.; Lee, G. H.; Noh, Z. S.; Lee, T. S.; Lee, C. J. *Materials Science & Engineering C-Biomimetic and Supramolecular Systems* 2004, 24, 43-46.
- (12) Lukkari, J.; Meretoja, M.; Kartio, I.; Laajalehto, K.; Rajamaki, M.; Lindstrom, M.; Kankare, J. *Langmuir* 1999, 15, 3529-3537.
- (13) Lusk, A. T.; Jennings, G. K. *Langmuir* 2001, 17, 7830-7836.
- (14) Cizek, J. W.; Tour, J. M. *Chemistry of Materials* 2005, 17, 5684-5690.
- (15) Cizek, J. W.; Stewart, M. P.; Tour, J. M. *Journal of the American Chemical Society* 2004, 126, 13172-13173.
- (16) Dreesen, L.; Voleke, C.; Sartenaer, Y.; Peremans, A.; Thiry, P. A.; Humbert, C.; Grugier, J.; Marchand-Brynaert, J. *Surface Science* 2006, 600, 4052-4057.
- (17) Choi, Y.; Jeong, Y.; Chung, H.; Ito, E.; Hara, M.; Noh, J. *Langmuir* 2008, 24, 91-96.
- (18) Bumm, L. A.; Arnold, J. J.; Charles, L. F.; Dunbar, T. D.; Allara, D. L.; Weiss, P. S. *Journal of the American Chemical Society* 1999, 121, 8017-8021.
- (19) Cyganik, P.; Buck, M.; Azzam, W.; Woll, C. *Journal of Physical Chemistry B* 2004, 108, 4989-4996.
- (20) Cyganik, P.; Buck, M. *Journal of the American Chemical Society* 2004, 126, 5960-5961.
- (21) Cyganik, P.; Buck, M.; Strunskus, T.; Shaporenko, A.; Wilton-Ely, J. D. E. T.; Zharnikov, M.; Woll, C. *Journal of the American Chemical Society* 2006, 128, 13868-13878.
- (22) Poirier, G. E.; Fitts, W. P.; White, J. M. *Langmuir* 2001, 17, 1176-1183.
- (23) Poirier, G. E. *Langmuir* 1999, 15, 1167-1175.
- (24) Edinger, K.; Golzhäuser, A.; Demota, K.; Woll, C.; Grunze, M. *Langmuir* 1993, 9, 4-8.
- (25) Poirier, G. E.; Tarlov, M. J. *Abstracts of Papers of the American Chemical Society* 1995, 209,

## 49-Coll.

- (26) Delamarche, E.; Michel, B.; Kang, H.; Gerber, C. *Langmuir* 1994, 10, 4103-4108.
- (27) Schlenoff, J. B.; Li, M.; Ly, H. *Journal of the American Chemical Society* 1995, 117, 12528-12536.
- (28) Ishida, T.; Choi, N.; Mizutani, W.; Tokumoto, H.; Kojima, I.; Azehara, H.; Hokari, H.; Akiba, U.; Fujihira, M. *Langmuir* 1999, 15, 6799-6806.
- (29) Wang, M. C.; Liao, J. D.; Weng, C. C.; Klauser, R.; Shaporenko, A.; Grunze, M.; Zharnikov, M. *Langmuir* 2003, 19, 9774-9780.
- (30) Stöhr, J. *NEXAFS Spectroscopy*; Springer-Verlag: Berlin, 1992.
- (31) Bagus, P. S.; Weiss, K.; Schertel, A.; Woll, C.; Braun, W.; Hellwig, C.; Jung, C. *Chemical Physics Letters* 1996, 248, 129-135.
- (32) Vaterlein, P.; Fink, R.; Umbach, E.; Wurth, W. *Journal of Chemical Physics* 1998, 108, 3313-3320.
- (33) Weiss, K.; Bagus, P. S.; Woll, C. *Journal of Chemical Physics* 1999, 111, 6834-6845.
- (34) Scholl, A.; Fink, R.; Umbach, E.; Mitchell, G. E.; Urquhart, S. G.; Ade, H. *Chemical Physics Letters* 2003, 370, 834-841.
- (35) Outka, D. A.; Stohr, J.; Rabe, J. P.; Swalen, J. D. *Journal of Chemical Physics* 1988, 88, 4076-4087.
- (36) Snyder, R. G.; Strauss, H. L.; Elliger, C. A. *Journal of Physical Chemistry* 1982, 86, 5145-5150.
- (37) Porter, M. D.; Bright, T. B.; Allara, D. L.; Chidsey, C. E. D. *Journal of the American Chemical Society* 1987, 109, 3559-3568.
- (38) Nuzzo, R. G.; Dubois, L. H.; Allara, D. L. *Journal of the American Chemical Society* 1990, 112, 558-569.
- (39) Buck, M.; Eisert, F.; Fischer, J.; Grunze, M.; Trager, F. *Applied Physics a-Materials Science & Processing* 1991, 53, 552-556.
- (40) Cattabriga, M.; Ferri, V.; Tran, E.; Galloni, P.; Rampi, M. A. *Inorganica Chimica Acta* 2007, 360, 1095-1101.
- (41) Laibinis, P. E.; Lee, S. W. *Abstracts of Papers of the American Chemical Society* 2000, 219, U572-U572.
- (42) Bertilsson, L.; Potje-Kamloth, K.; Liess, H. D.; Liedberg, B. *Langmuir* 1999, 15, 1128-1135.
- (43) Auer, F.; Scotti, M.; Ulman, A.; Jordan, R.; Sellergren, B.; Garno, J.; Liu, G. Y. *Langmuir* 2000, 16, 7554-7557.
- (44) Patel, N.; Davies, M. C.; Hartshorne, M.; Heaton, R. J.; Roberts, C. J.; Tandler, S. J. B.; Williams, P. M. *Langmuir* 1997, 13, 6485-6490.
- (45) Vericat, C.; Vela, M. E.; Salvarezza, R. C. *Physical Chemistry Chemical Physics* 2005, 7, 3258-3268.
- (46) Arnold, R.; Azzam, W.; Terfort, A.; Woll, C. *Langmuir* 2002, 18, 3980-3992.
- (47) Himmel, H. J.; Terfort, A.; Woll, C. *Journal of the American Chemical Society* 1998, 120, 12069-12074.
- (48) Mendoza, S. M.; Arfaoui, I.; Zanarini, S.; Paolucci, F.; Rudolf, P. *Langmuir* 2007, 23, 582-588.
- (49) Michael, K. E.; Vernekar, V. N.; Keselowsky, B. G.; Meredith, J. C.; Latour, R. A.; Garcia,

- A. J. *Langmuir* 2003, 19, 8033-8040.
- (50) Wang, M. S.; Razatos, A. *Abstracts of Papers of the American Chemical Society* 2004, 227, U832-U833.
- (51) Wang, H.; Chen, S. F.; Li, L. Y.; Jiang, S. Y. *Langmuir* 2005, 21, 2633-2636.
- (52) Smith, E. L.; Alves, C. A.; Anderegg, J. W.; Porter, M. D.; Siperko, L. M. *Langmuir* 1992, 8, 2707-2714.
- (53) Willey, T. M.; Vance, A. L.; van Buuren, T.; Bostedt, C.; Nelson, A. J.; Terminello, L. J.; Fadley, C. S. *Langmuir* 2004, 20, 2746-2752.
- (54) Gonella, G.; Cavalleri, O.; Terreni, S.; Cvetko, D.; Floreano, L.; Morgante, A.; Canepa, M.; Rolandi, R. *Surface Science* 2004, 566, 638-643.
- (55) Ishida, T.; Hara, M.; Kojima, I.; Tsuneda, S.; Nishida, N.; Sasabe, H.; Knoll, W. *Langmuir* 1998, 14, 2092-2096.
- (56) Ito, E.; Konno, K.; Noh, J.; Kanai, K.; Ouchi, Y.; Seki, K.; Hara, M. *Applied Surface Science* 2005, 244, 584-587.
- (57) Pasquali, L.; Terzi, F.; Zanardi, C.; Pigani, L.; Seeber, R.; Paolicelli, G.; Suturin, S. M.; Mahne, N.; Nannarone, S. *Surface Science* 2007, 601, 1419-1427.
- (58) Xu, D. S.; Sun, L.; Li, H. L.; Zhang, L.; Guo, G. L.; Zhao, X. S.; Gui, L. L. *New Journal of Chemistry* 2003, 27, 300-306.
- (59) Ballav, N.; Weidner, T.; Zharnikov, M. *Journal of Physical Chemistry C* 2007, 111, 12002-12010.
- (60) Auditore, A.; Tuccitto, N.; Marzanni, G.; Quici, S.; Puntoriero, F.; Campagna, S.; Licciardello, A. *Chemical Communications* 2003, 2494-2495.
- (61) Cizek, J. W.; Keane, Z. K.; Cheng, L.; Stewart, M. P.; Yu, L. H.; Natelson, D.; Tour, J. M. *Journal of the American Chemical Society* 2006, 128, 3179-3189.
- (62) Krings, N.; Strehblow, H. H.; Kohnert, J.; Martin, H. D. *Electrochimica Acta* 2003, 49, 167-174.
- (63) Perepichka, D. F.; Kondratenko, M.; Bryce, M. R. *Langmuir* 2005, 21, 8824-8831.
- (64) Xu, Q. M.; Ma, H.; Yip, H.; Jen, A. K. Y. *Nanotechnology* 2008, 19, 135605.
- (65) Dou, R. F.; Ma, X. C.; Xi, L.; Yip, H. L.; Wong, K. Y.; Lau, W. M.; Jia, J. F.; Xue, Q. K.; Yang, W. S.; Ma, H.; Jen, A. K. Y. *Langmuir* 2006, 22, 3049-3056.
- (66) Nilsson, D.; Watcharinyanon, S.; Eng, M.; Li, L. Q.; Moons, E.; Johansson, L. S. O.; Zharnikov, M.; Shaporenko, A.; Albinsson, B.; Martensson, J. *Langmuir* 2007, 23, 6170-6181.
- (67) Kosbar, L.; Srinivasan, C.; Afzali, A.; Graham, T.; Copel, M.; Krusin-Elbaum, L. *Langmuir* 2006, 22, 7631-7638.
- (68) Maskus, M.; Abruna, H. D. *Langmuir* 1996, 12, 4455-4462.
- (69) Nishimori, Y.; Yamanoi, Y.; Kume, S.; Nishihara, H. *Electrochemistry* 2007, 75, 770-776.
- (70) Shekhah, O.; Wang, H.; Strunskus, T.; Cyganik, P.; Zacher, D.; Fischer, R.; Woll, C. *Langmuir* 2007, 23, 7440-7442.
- (71) Biemmi, E.; Scherb, C.; Bein, T. *Journal of the American Chemical Society* 2007, 129, 8054-8055.
- (72) Ishida, T.; Nishida, N.; Tsuneda, S.; Hara, M.; Sasabe, H.; Knoll, W. *Japanese Journal of Applied Physics Part 2-Letters* 1996, 35, L1710-L1713.
- (73) Nishida, N.; Hara, M.; Sasabe, H.; Knoll, W. *Japanese Journal of Applied Physics Part*

- I-Regular Papers Short Notes & Review Papers 1997, 36, 2379-2385.*
- (74) Kim, Y. K.; Koo, J. P.; Ha, J. S. *Applied Surface Science* 2005, 249, 7-11.
- (75) Chen, W.; Huang, H.; Chen, S.; Chen, L.; Zhang, H. L.; Gao, X. Y.; Wee, A. T. S. *Applied Physics Letters* 2007, 91, -114102
- (76) Nicoara, N.; Roman, E.; Gomez-Rodriguez, J. M.; Martin-Gago, J. A.; Mendez, J. *Organic Electronics* 2006, 7, 287-294.
- (77) Poirier, G. E. *Chemical Reviews* 1997, 97, 1117-1127.
- (78) Raisanen, M. T.; Kemell, M.; Leskela, M.; Repo, T. *Inorganic Chemistry* 2007, 46, 3251-3256.
- (79) Jung, T. A.; Schlittler, R. R.; Gimzewski, J. K.; Tang, H.; Joachim, C. *Science* 1996, 271, 181-184.
- (80) Pinheiro, L. S.; Temperini, M. L. A. *Surface Science* 2000, 464, 176-182.

## Chapter 6 Conclusions

Laser scanning lithography was used to pattern SAM modified Au surfaces. With this technique, localized molecules on the substrate are desorbed during laser irradiation. Thermal desorption occurs as a result of the large temperature rise produced by the laser pulses. STM images show that after laser lithography, SAMs are altered and some molecules remain on the surface in a lying down phase. It was found that the surface is very sensitive to the laser power (variation of about 10% makes the difference between Cu deposition and non-deposition). The minimum line width produced by LSL is about 900 nm. There is still room to improve the resolution as the resolution is determined by the laser spot size, which depends on the focus system. LSL is noncontact, flexible, and can be applied to other systems such as SAMs on silicon or even on polymeric substrates. Compared with other patterning technologies such as electron beam lithography, laser patterning has the advantage of simple setup, direct writing, and large area processing.

Along with laser patterning, laser-induced passivation of SAMs was also observed. This effect enhances blocking capability of SAMs upon electrochemical metal deposition. We observe the effect on MC22, MC18, MC14, MC11, MUA, BP12, BP5, and BP2 modified gold surfaces, regardless on the substrate type (mica or Si). We suggest that the passivation is induced by a thermal effect: during irradiation, high temperature is built up in the focus and the heat can transfer quickly to the edge, inducing rearrangement of SAMs structure and annealing of defects. The effect blocks bulk copper deposition, but does not prevent UPD. By choosing appropriate laser power, large passivated area can be created which can be used as a substrate for further fabrication where high quality of SAM is needed.

We have demonstrated an effective way to prepare a superhydrophobic surface. By using self-assembled monolayers as template for electrochemical metal deposition, a superhydrophobic surface with a contact angle of  $165^\circ$  can be obtained. By controlling the geometry of the metal pattern and electrochemical deposition parameters, we can

control the surface roughness. This method can be easily applied to other metals, such as silver. These superhydrophobic surfaces may lead to applications in the fields of microfluidic devices, electrowetting, and as supporting surface for optical tweezers operation, which needs a superhydrophobic surface for droplet movements.

For electrochemical metal deposition onto SAM modified substrates, the blocking behaviour depends on the molecular length and on the terminal functional group. (1) DT, BP0, and MC6 SAMs do not block copper penetration. The Cu deposited was well connected to the gold surface and appears uniform. Deposited Cu is very stable and cannot be removed by STM tip. (2) BP12, MC18, and MC22 prevent Cu penetration. Deposited Cu particles are on top of the SAMs, and are easily swept away by the tip. (3) MUA and MHA, which have acid terminal groups can coordinate with Cu and thus result in stronger adhesion. (4) BP1, BP2, BP3, BP5, and MC11 SAMs can block the copper penetration to some extent. However, some copper penetrates through the SAMs and forms mushroom-type copper structures. STM can image some big particles (mushroom structures), while the majority of particles is easily swept away.

Aiming for the generation of smaller structures, STM is used as a tool to pattern SAMs. Several phenomena observed in STM based manipulation of SAMs are addressed. The first one is sweeping effect. Deposited metal particles on top of SAM and molecules are swept by STM tip by choosing appropriate I/V parameters. The closer the tip (higher current, lower bias), the more effective it is. Molecularly resolved images confirm that after sweeping, the scanned area is still covered by SAM molecules. This is explained by diffusion. The sweeping process can be repeated, thus, resulting in a layer by layer etching. The second effect is field-induced desorption. Positive (sample positive, tip negative) voltage pulses (2.5 – 5 V) applied on the surface of a BP2 SAM can locally damage the SAM and lead to generation of holes. The damage depends on the bias and on the current. Damaged areas can be filled by a second thiol (e.g. BP3) in hexadecane solution. However, small pulses do not create holes big enough to trigger any replacement. For too high pulses, islands are formed. Defects (punched holes) were created purposely on SAM covered Au surfaces and *in*

*situ* STM was used to observe UPD and OPD processes. The third effect is nanografting. STM nanografting was studied in hexadecane solution under normal STM imaging parameters, which is different from the sweeping (high current) and punching (high voltage) modes. It is found that long chain thiols can replace short chain thiols; alkane thiols can replace biphenyl thiols, i.e. the SAMs in hexadecane solution should have a stronger ability to assemble than the matrix SAM. A defect is the trigger point from which the replacement starts and expands across the whole area covered by the scanned range of the STM tip. Several mechanisms were proposed to explain this nanografting effect. The BP2 high temperature phase is a very suitable matrix for nanopatterning due to its stability and lack of defects in large areas, which is very important for nanopatterning. The speedy replacement by nanografting also minimises unwanted exchange reactions.

Several conclusions can be drawn from our experiments. (1) Holes punched with high voltage pulses are surprisingly passive. This possibly results from the presence of molecules diffusing back in the punched area. (2) Punched holes trigger UPD nucleation in “perfect” SAM, such as the high temperature phase of BP2. However, in the presence of other defects, punched holes are only a secondary source of nucleation site. (3) The STM tip may hinder metal UPD and OPD for *in situ* experiments. (4) Bulk metal deposition on punched holes depends on the size. A large hole (e.g. 7 nm deep and 50 nm wide) can trigger bulk deposition. However, a smaller one (e.g. 2 nm deep and 25 nm wide) does not trigger any bulk deposition. In summary, small scale (~10 nm) patterning by punching is sufficient for applications based on UPD but not for bulk metal OPD.

Several SAMs assembled on Au(111) surface (1-mercaptoundecanoic acid (MUA), dodecyl thiocyanate (C12SCN) and bis(pyrazol-1-yl)pyridine-substituted thiol) were investigated with the aim to expand the type of SAMs that can be used as template for further application, such as metal coordination.

Assembly of C12SCN from ethanol solution onto Au(111)/mica substrates was investigated by STM, NEXAFS, XPS and IRRAS. Contrary to previous reports,

thiolate monolayers formed by cleavage of the S-CN bond can be obtained whose quality is at least as good as that of self-assembled monolayers formed directly from the thiol analogue of C12SCN, dodecanethiol. However, the achievable quality is strikingly dependent on the purity of the thiocyanate with even low levels of contamination impeding formation of structurally well-defined monolayers. High quality SAM of C12SCN is promising as an alternative to thiols.

Well-ordered MUA layers are formed in a few hours at the temperature range of 323-363 K by PVD. STM images with molecular resolution show clearly two different structures described by a  $\sqrt{3} \times \sqrt{3}$  unit cell and  $(4 \times 2)$  superlattice, respectively. This is in sharp contrast to samples prepared in ethanol solution which show disordered structure. Contact angle measurements reveal that MUA prepared by PVD has a contact angle as low as 5°. XPS, NEXAFS, IR and electrochemical methods are applied to examine the MUA SAMs. It is revealed that sample prepared by PVD is a monolayer, while sample prepared from solution forms a double layer.

Self-assembled monolayers of a bis(pyrazol-1-yl)pyridine-substituted thiol (bpp-SH) and thiocyanate (bpp-SCN) on Au(111)/mica were studied with STM. Preparation conditions such as temperature, solvent, and contaminations affect the formation of SAMs on Au(111) much more than other when using common thiols such as alkanethiols and biphenylthiols. For bpp-SH, using substrates which were precoated with perylene-3,4,9,10-tetracarboxylic dianhydride, preparation at elevated temperatures yields highly ordered layers whose structure is described by a rectangular  $(5 \times \sqrt{3})$  unit cell containing one molecule. For bpp-SCN, an ordered structure cannot be obtained from solution (ethanol, DMF) as bpp-SCN can etch the Au surface, but can be obtained by PVD. The formation of these well-ordered SAMs is the first step towards the controlled assembly of more complex structures such as metal coordinated multilayers or metal-organic frameworks.